UNIVERSITÀ DEGLI STUDI DI PADOVA
DIPARTIMENTO DI INGEGNERIA CIVILE, EDILE E AMBIENTALE
Department Of Civil, Environmental and Architectural Engineering

Master's Degree in Environmental Engineering,
Soil Protection and Water Management

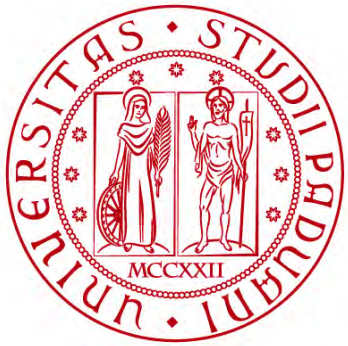

MASTER'S THESIS

Geostatistical analysis of pollutant concentrations in the groundwater systems of Vicenza Province.

Supervisor :
PROF. PIETRO TEATINI

Candidate: Laura Fabrello
2089021

Academic year 2023/2024

ABSTRACT

The following thesis aims to depict the spatio-temporal evolution of underground water quality in the high to middle plain area of the Vicenza Province.

Monitoring groundwater quality is crucial for safeguarding environmental health and protecting citizens from any sources of water pollution, especially since many private wells are present in the study area. This study is contextually significant as it results from a scholarship awarded by Viacqua S.p.A., a company responsible for water supply in 68 municipalities within the Vicenza province.

A comprehensive database recorded between 1981 and 2023 was provided and divided into two hydrogeologic systems of the Vicenza plain: the Agno valley and the plain to the north of Vicenza municipality. They are divided by a hillock system, making them hydraulically independent from each other.

The domain is characterized by extensive industrial and agricultural activities, necessitating the consideration of pollutants related to these sectors. The pollutants analyzed include the sum of PCE (perchloroethylene), TCE (trichloroethylene), collectively referred as “total solvents” related to industrial activities, nitrates and pesticides associated with agricultural activities, and sulphates and chlorides from both natural and industrial sources.

The analyses conducted were initially statistical and then geostatistical, with a particular focus on the ordinary kriging interpolation method. Maps showing the evolution of the contamination plumes over time, if present, and graphs representing the data trends are primary tools used to study the evolution of groundwater quality.

Table of Contents

List of Figures

List of Tables

1. INTRODUCTION

Underground water represents a major source of drinking water in Italy, making its safeguard imperative.

In the integrated water cycle, numerous stakeholders play critical roles, underscoring the importance of maintaining water quality throughout every stage of the cycle. For underground water, pollution can occur either through direct contamination after use or by contaminants being washed from the soil into aquifers.

Notably, the primary source of pollution is anthropogenic activity, which is increasing daily.

This thesis focuses on the quality of underground water in the Vicenza province, and is the result of an internship experience at VIacqua S.p.a, the authority managing water supply across 68 municipalities in the Veneto region. The study area is made of two sub-domains: a smaller one, the Agno Valley, with a dataset collected from 1998 to 2023 and covering 9 municipalities, and a larger one represented by high to middle plain north of Vicenza city, with data spanning the time frame between 1981 and 2023 and extended over 37 municipalities.

The dataset is not only extensive in terms of spatio-temporal coverage but also in the variety of pollutants analyzed. A thorough understanding of the domain and historical contamination events is crucial to identifying key contaminants for this study. Therefore, the focus was placed on total solvents, nitrates, pesticides (DACT), chloride, and sulphates.

A preliminary statistical analysis of the records was conducted using Microsoft Excel. Then, the spatial and temporal range of the dataset provides an ideal foundation for implementing a spatio-temporal study using geostatistical methods. Among these, the Kriging interpolation method is particularly effective for analyzing groundwater quality datasets within the same aquifer system. This study employs ArcGIS Pro and QGIS for geostatistical analysis, while RStudio is used for a better understanding of the ArcGIS Pro mathematical background.

The results of the Kriging method include maps showing the distribution of pollutant concentrations in the high plain of Vicenza area for a number of representative times. To

assess the reliability of these outcomes, error information associated to the expected values is provided through maps, graphs, and statistical values—key features of the chosen geostatistical method.

This thesis follows a logical structure to facilitate a comprehensive understanding of the study and its outcomes, as outlined below:

1. Review of the geological and hydrogeological settings of the domain;
2. Description of the analyzed pollutants, including their chemical characteristics, sources of pollution, environmental behavior, impact on human health, and relevant regulations;
3. Description of the methods used, with an overview of data quality, sampling methods, and statistical and geostatistical analyses performed;
4. Presentation of the results;
5. Discussion of the outcomes, leading to final conclusions.

2. STUDY AREA; HYDROGEOLOGICAL SETTING

2.1. THE VENETIAN PLAIN FEATURES

The area under investigation covers part of the Vicenza Province and can be divided into two subdomains: the Agno Valley, and the wider area of the plain above the city of Vicenza.

Before examining these subareas locally, it is important to start with a broader look at the hydrogeological characteristics of the Po Plain. To better understand the features of the Venetian Plain, it is necessary to consider its formation.

Its origin lies in the Tertiary (65.5 – 2.58 million years ago), during which the Alps rising caused the depression of the pre-Alpine area. Subsequently, during the Quaternary (since 2.58 million years ago until the present), the newly formed lower part of the Veneto region began to be filled with alluvial material transported by rivers and marine transgression phenomena, which alternated during that period. The Pleistocene (starting 2.58 million years ago) and the Holocene (from 11 700 years ago to the present) exhibited phases of glacio-eustatic changes.

The close correlation between sedimentation processes and the genesis of the plain is evidenced by the presence of megafan structures. These structures, shown in Figure 1, with their folding fan shape, reflect the changes in river paths during the area metamorphosis. It is possible to recognize the megafans related to sediment transport by rivers, often interpenetrating with each other. Typically, these structures are characterized by gravelly soils at their top, which mix with marine deposits toward the coast.

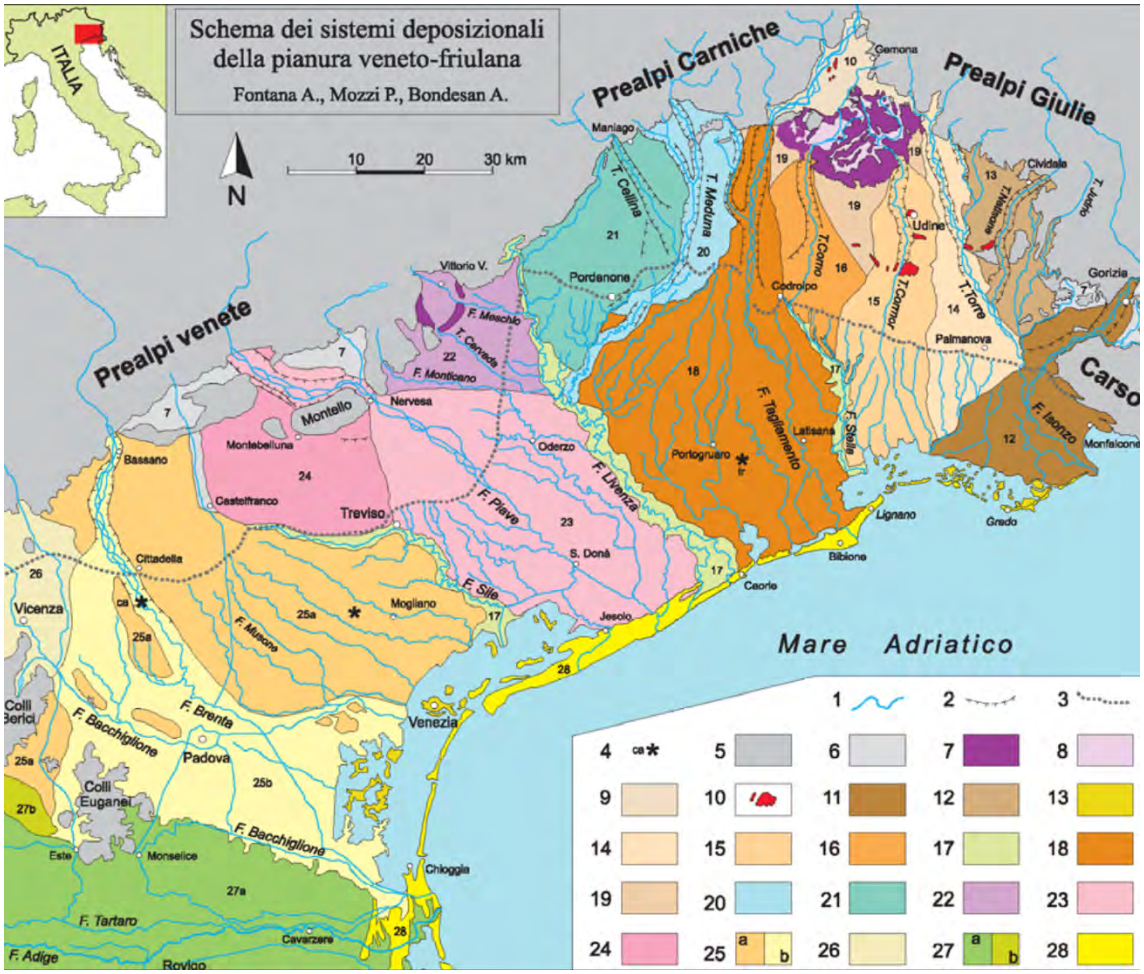

Figure 1. Deposition structures in Venetian plain (Bondesan, et al., 2004). KEY: 1) rivers; 2) corner of fluvial scarp; 3) upper limit of springs line; 4) points of known stratigraphy; 5) Prealps, Berici and Euganean Hills; 6) alluvial area related to prealpine rivers; 7) Morainic lines of the amphitheater of Piave and Tagliamento rivers; 8) intermorinic depressions; 9) Osoppo plain; 10) tectonic shelves of the high friulan plain; 11) megafan of Isonzo-Torre river; 12) conoid of Natisone-Judrio; 13) lagoon islands; 14) megafan of Torre river; 15) megafan of Cormor river; 16) megafan of the Corno of San Daniele mountain (?); 17) systems related to the principal rivers coming from springs (Stella, Livenza, Sile), locally cut; 18) megafan of Tagliamento river; 19) areas between megafan belonging to the Tagliamento sandur; 20) megafan of the Meduna river; 21) Cellina conoide; 22)conoidi of Montican, Cervada and Meschio rivers and of the rivers coming from glacial areas to Vittorio Veneto; 23) megafan of the Piave of Nervesa river; 24)megafan of Piave of Montebelluna river; 25) Brenta system: a) Pleistocene sector (Megafan of Bassano), b) holocene plain of Brenta with Bacchiglione contributes; 26) conoid of Astico; 27) Adige system: a) holocene plain with Po contributes; b) pleistocene plain; 28) coast and delta river systems.

Furthermore, the entire regional plain, being characterized by the same construction processes, shows uniform features. From the hydrogeological point of view, it is represented by three peculiar settings, mainly elongated with a ESE-WNW direction: the High, the Middle and the Low plain (Boscolo , et al., 2008).

The High plain area is characterized by thick gravelly soil overlying bedrock layer. The gravel percentage of this soil is up to one-third of the total, while the remaining part is composed of finer materials. This area typically extends 5 to 15 km from the Prealps.

Moving seaward, it is possible to run into the Middle plain, a transitional zone where the highly permeable materials of the High plain decrease in quantity, with the presence of silty-clayey soils. This 5 to 10 km wide area has a significant role as it is where springs occur. Finally, the Low plain extends from the Middle plain to the Adriatic coastline and the southern part of the Po River, with a width of 20 km. Here, sandy permeable layers alternate with clayey-silty deposits, which can be assumed as almost impermeable.

The peculiar hydrogeological characteristics of the Po Plain derive directly from the geological features. In fact, the High plain, which is characterized by highly permeable soils, is home of a thick phreatic aquifer. The Middle and Low plain zones are characterized by the presence of a well-developed multi-aquifer system. The system thickness reaches up to 400 m along the coastland, where a series of fresh-water aquifers are located, and decreases northwestward toward the spring band where the shallowest layers reach the ground level (Boscolo , et al., 2008).

It is important to note that multi-aquifer system in the coastal area is hydraulically connected to the phreatic aquifer in the High plain. This information highlights the importance of the system recharge in the upper plain, which impacts the groundwater availability and quality also in coastal areas far from the recharge zone. The regime of the phreatic aquifer recharge zone is quite uniform, with a unimodal fluctuation over time between a maximum value in early autumn and a minimum in early spring to the west of the Berici-Euganei Hills, and a bimodal behavior in the easter part associated to the pre-Alpine river regime with two maxima in the late spring and autumn. Indeed, especially in the High plain, the groundwater regime in the phreatic aquifer is significantly influenced by the regime of the rivers, which represent a main recharge source, with a delay factor between surface and subsurface extremes quantified in approximately 20-30 days (Boscolo , et al., 2008).

2.2. THE HIGH-MIDDLE PLAIN TO THE NORTH OF VICENZA

The first area under investigation, as already mentioned, is the one that extends to the north of the city of Vicenza and is comprised within the domain of the AATO (Autorità di Ambito Territoriale Ottimale – Optimal Territorial Area Authority) Brenta-Bacchiglione. It is bounded by the Alps foothills to the northeast, the Astico River valley to the north, the Lessinian Mountains to the northwest, and the city of Vicenza to the South, as shown in Figure 2. Here, the three geological settings of high, middle and low plain that characterize the Venetian plain can be observed, although the high plain setting prevails.

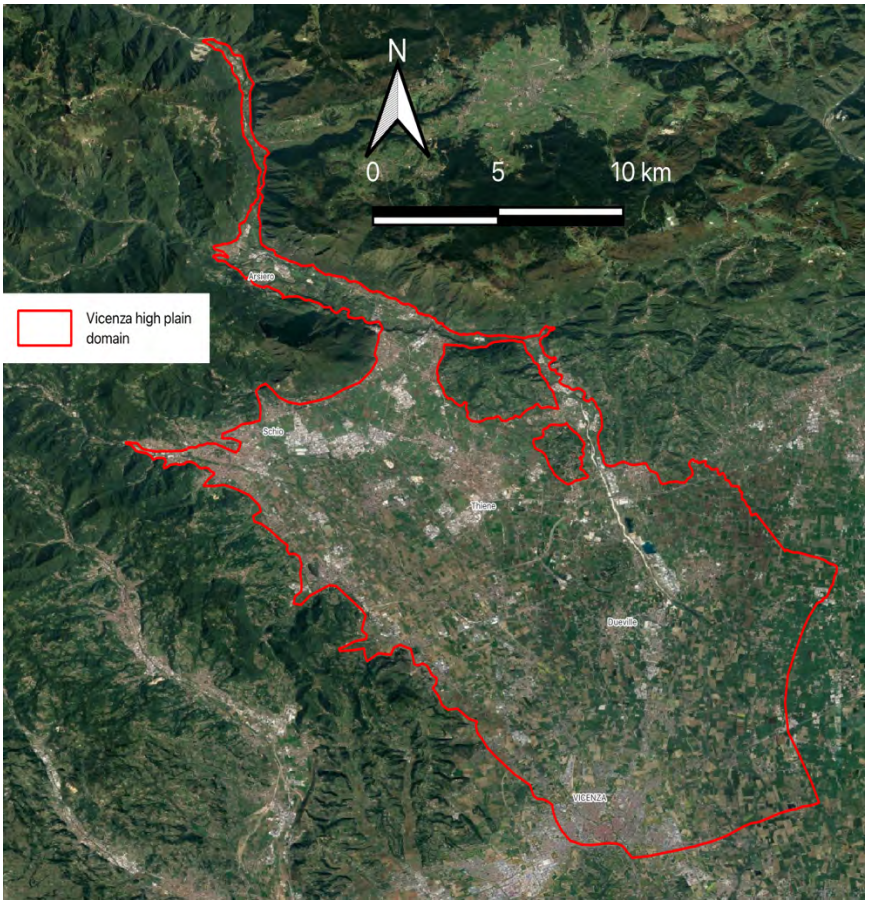

Figure 2. Boundary of the first sub-domain covering the plain to the north of Vicenza.

The high plain shows a slope of 1.5%. Moving in NW-SE direction and reaching the middle plain, the slope decreases, with elevations varying from 64 m.a.s.l. to 30 m.a.s.l over a distance of 2 to 10 km. Particularly, the multi-aquifer system shows 7 impermeable

units defining 8 aquifers, the upper of which is an unconfined aquifer (Centro di Idrologia "Dino Tonini", Università degli Studi di Padova, 2021) . Their thicknesses and depth vary in the area, on average, they are located at depths of 30, 50, 90, 120, 160 and 210 m below the land surface (Bonollo s.r.l., et al., 2003).

Notice in Figure 3 the pinch-out setting of the multi-aquifer system in the northest direction, with the vanishing of the impermeable layers due to the decrease of their thickness reaching the highly-permeable undifferentiated layer characterizing the High plain system (Centro di Idrologia "Dino Tonini", Università degli Studi di Padova, 2021). It is also important to underline that faults in NNW-SSE and N-S directions divide the area into different basins, contributing differently to the final hydrogeological balance (Bonollo s.r.l., et al., 2003). A sketch of the stratigraphical setting of the aquifer system from the High to the Low plain is provided in Figure 3.

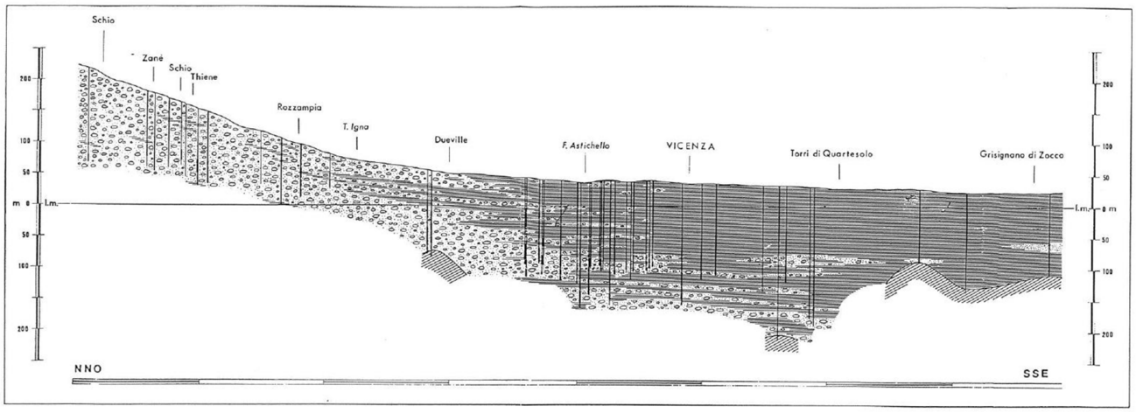

Figure 3. Soil stratigraphy of the domain along the axis Schio-Grisignano di Zocco (Bonollo s.r.l., et al., 2003)

From a hydrogeological point of view, the High and the Middle plain areas to the north of Vicenza are well known for being highly productive, particularly referring to the third, fourth and fifth aquifer layers of the multi-aquifer system. This is evidenced by the high production of springs, which in 2002 has shown an annual mean flow of 15 m^3/s. An evidence of this occurrence is highlighted by the water table risen upstream of the springs line in 2010 and 2014, with the phreatic aquifer that caused flood events (ARPAV, 2019). The underground flow is highly dependent on the rivers' regimes, with larger oscillations in the High plain area, where aquifers are more sensitive to variations in inputs. The main flow direction is from NNW to SSE, therefore following the direction of the faults. This is related to the dispersion effect of rivers. In the domain, as it can be observed in Figure

4, two main directions related to the Leogra-Timonchio and Astico systems can be recognized (Bonollo s.r.l., et al., 2003).

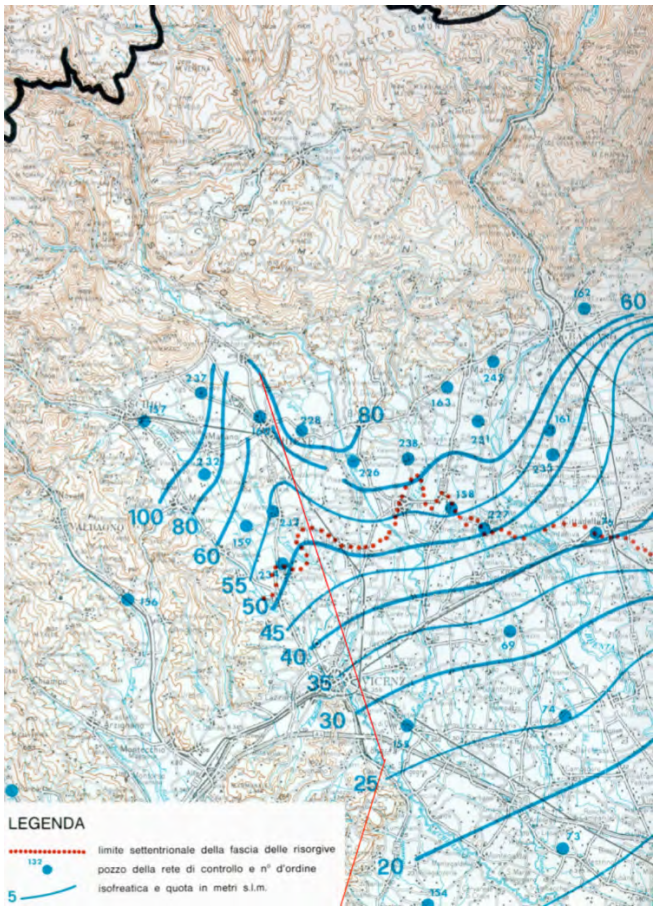

Figure 4. Average iso-phreatic map (m above msl) in the plain to the northeast of Vicenza. The values refer to the last decades (Tamà, 2013).

The hydraulic conductivity of the soil is a main parameter to be investigated as pollutants tend to infiltrate with water from the land surface, eventually reaching aquifers. Figure 5 provides a map of the saturated hydraulic conductivity K_{sat} of the least permeable soil in the upper 1.5 m. To properly interpret the map, it is important to note that the least permeable soil regulates the behavior of the entire thickness. Notice that the majority of the study area is characterized by a moderate permeability.

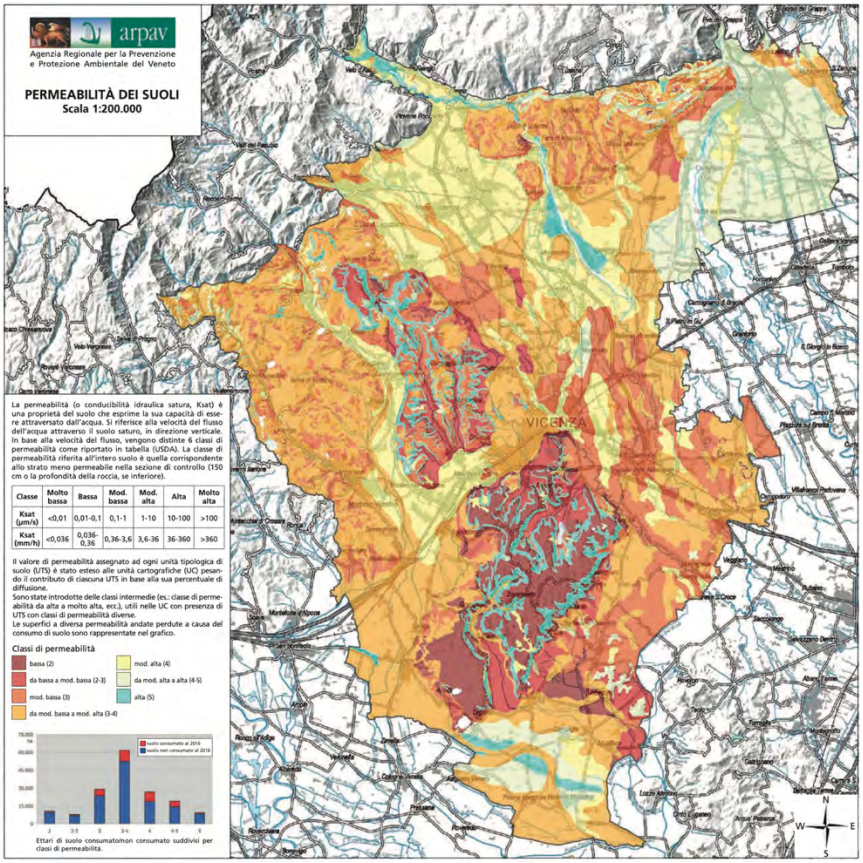

Figure 5.Soil permeability in saturated condition around Vicenza (Dalla Rosa, et al., 2018).

In the area under investigation, many private pumping wells are located, confirming the high quality of the groundwater and the productivity of the aquifer system. A census led by CIN (Centro Idrico Novoledo) in 1997-1998 reported that the total volume of pumped groundwater in the municipalities of Bolzano Vicentino, Bressanvido, Caldogno, Costabissara, Dueville, Monticello Conte Otto, Quinto Vicentino, Sandrigo, Torri di Quartesolo, Villaverla, and Vicenza was of about 20×10^6 m^3/year. Furthermore, water withdrawal from the aquifers system is conducted by industrial activities as well (Bonollo s.r.l., et al., 2003).

Figure 6 provides the land cover of the study area. A significant part is covered by structures for both industrial activities and private uses, but the largest portion of the entire domain is devoted to agricultural purposes.

Productive activities pose a threat to underground water quality, often lowering it and making it unsuitable for potable uses. According to historical records by ARPAV in 2019, the most critical pollutants are halogenated solvents. Additionally, the concentration of

the glyphosate pesticide – and its metabolite aminomethylphosphonic acid (AMPA) – as well as PFAS, are worryingly increasing (ARPAV, 2019).

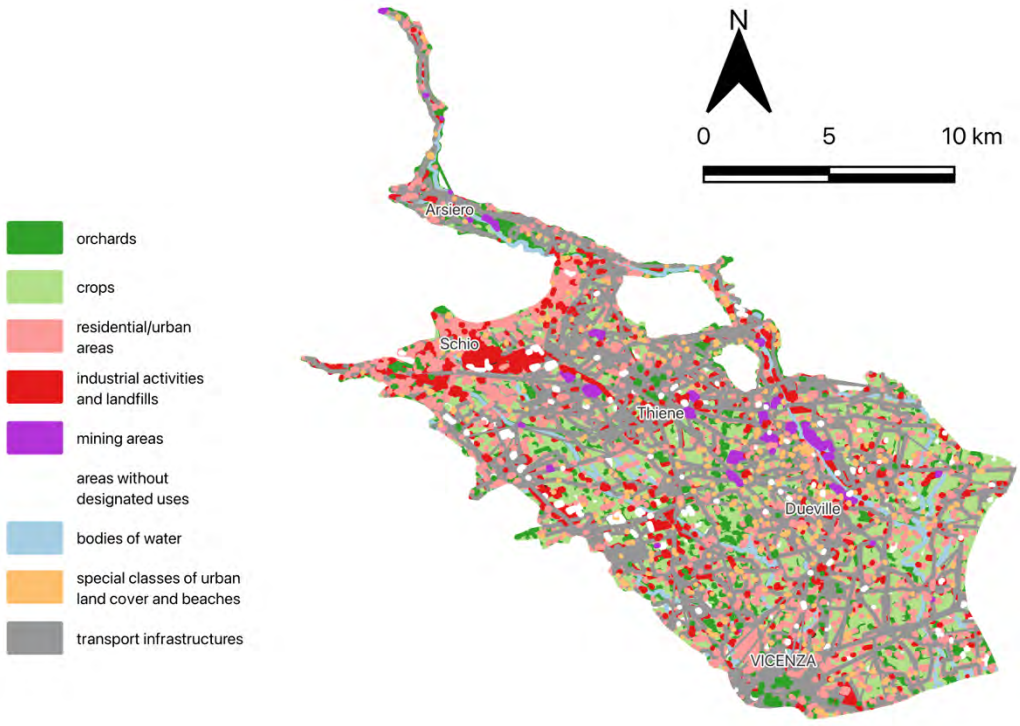

Figure 6. Land cover of the high plain of Vicenza (Geoportale Regione Veneto).

2.3. THE AGNO VALLEY

The Agno valley is the right branch of the Agno-Chiampo valley, located to the west of Vicenza. The area under consideration conveys water with a catchment surface of 261 km^2 (Bonollo s.r.l., et al., 2003). It has an average elevation is 85 m.a.m.s.l., with a mean slope of 2.5% (Mazzola, et al., 2013) toward the S and SE directions. Delimitations of the second sub-domain is displayed in Figure 7.

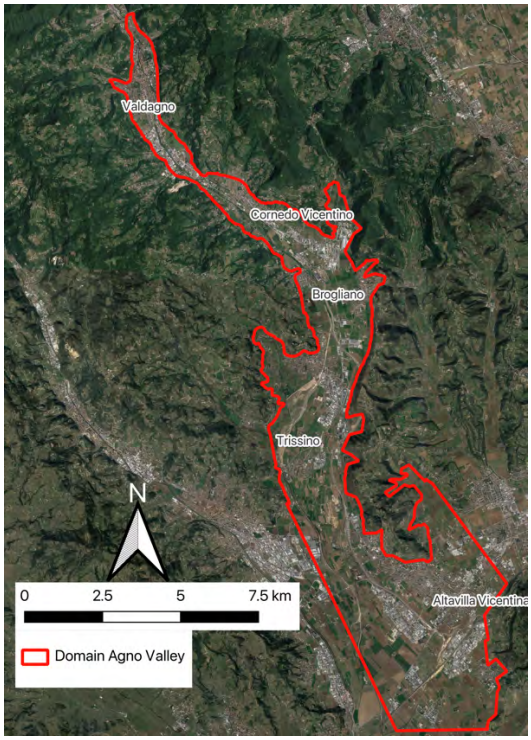

Figure 7.Boundary of the second sub-domain encompassing the Agno River valley.

The study area exhibits typical characteristics of the High plain with gravelly soil that reaches depths of up to 100 m in some places, lying over bedrock of volcanic origin, as shown in Figure 8. The alluvial deposits originated from the beginning of the Quaternary, are formed by sediments transported by rivers and glacial movements. Generally, the gravel soil is composed of calcareous sediments, with occasional intercalations of clayey lenses (Mazzola, et al., 2013).

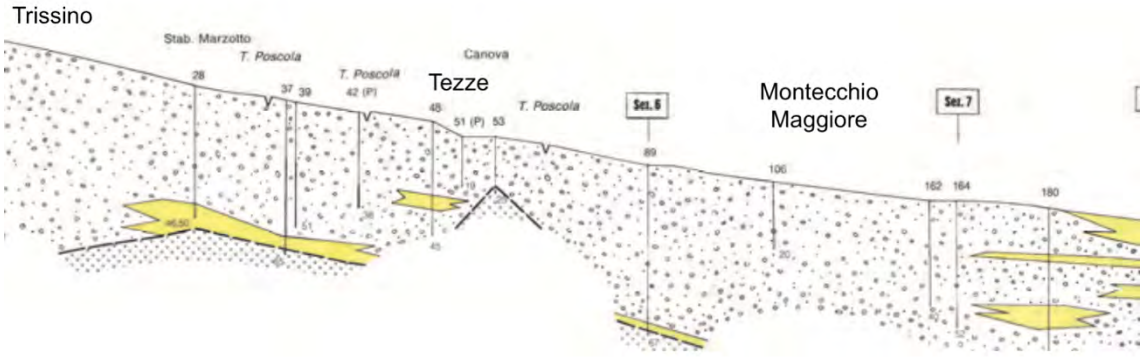

Figure 8. Stratigraphic section of the central portion of the Agno valley: in yellow silt-clayey deposits, the dotted wash represents gravelly soil (Mazzola, et al., 2013)

While the creek flowing through the valley exhibits an erratic behavior (Vezzil, et al., 2018), the unconfined aquifer system has always shown high productivity, with a groundwater flow direction that follows the one of the valley, as can be observed in Figure 9.

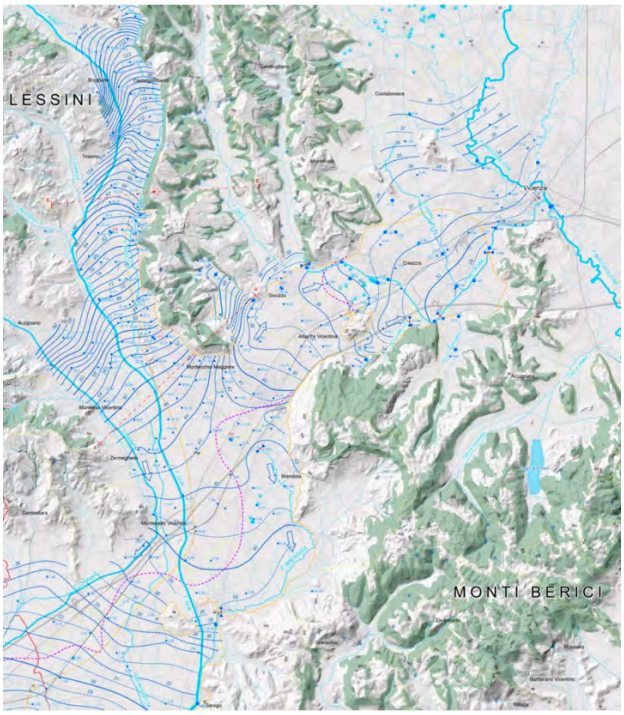

Figure 9. Iso-phreatic map (m above msl) in the Agno valley. The values refer to October 2017 (ARPAV, 2018).

Groundwater is extracted for potable, industrial and irrigation purposes, with numerous private wells in the area. It is important to note that the area is well known for its industrial activities, particularly by the numerous tanning factories, where a large amount of water is typically used in the production processes to cool machinery. The importance of industrial activities in the area is clearly recognizable in Figure 10, where the use of soil is represented. Even though the surface covered by industrial sites is not vast in absolute terms, it actually represents large portion of the urbanized surface.

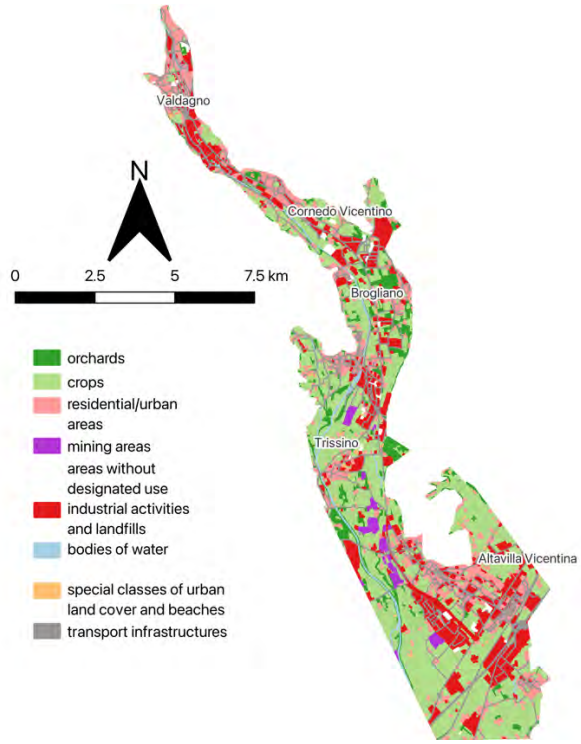

Figure 10. Land cover of the Agno valley (Geoportale Regione Veneto).

This fact, combined with the relatively high hydraulic conductivity of the soil in the area, with values ranging between 10^{-4} to 10^{-5} m/s and the large transmissivity from 10^{-3} to 10^{-2} m^2/s, poses a threat to groundwater quality.

As a matter of fact, the presence of industries and farms has led to increasing concentrations of salts, chlorinated solvents, and nitrates in the water. Additionally, the issue of PFAS contamination is significant, with this area having some of the highest levels in the European Union. While the phenomenon is under study, much remains unknown about the pathways of pollutants from their source to the water table. Once in the aquifer, PFAS spread throughout the underground water system due to hydrodynamic dispersion and their high mobility. Concentrations of 68.600 ng/l have been detected at the points of the aquifers closest to the source (Mazzola, et al., 2013).

3. ANALYZED POLLUTANTS

As previously mentioned, an important source of groundwater contamination is related to the productive sector, including both industries and farms. The concern about pollutants is not only an Italian issue but also a European one, with the EU responsible for defining guidelines that must then be implemented by member states.

Specifically, this began in the 1980s with Directive 80/68/EEC, aimed at safeguarding groundwater from dangerous pollutants (Socchera & Minutolo, 2022). Currently, the protection of water bodies is regulated by the "Water Framework Directive", the "Groundwater Directive" and the "Environmental Quality Standards Directive", which set maximum allowable concentrations, with stricter limits introduced in 2023 (Popp, 2023).

Based on the European framework, Italy has enacted Legislative Decree 30/2009 and Ministerial Decree 06.07.2016, which build upon the existing Legislative Decree 152/99. Both decrees define the maximum concentrations of certain pollutants in groundwater and the ideal values of other substances to ensure high potable water quality, emphasizing the importance of distinguishing between naturally occurring pollutants and those resulting from human activities. They have been recently updated with the decree 18/2023.

In Legislative Decree 152/99, the quality of a body of water is classified into five classes, ranging from 4 (low quality) to 1 (high quality), based on the values of at least 14 parameters. Water systems with high values due to natural processes are assigned to class 0.

The area of interest is in the Veneto Region, where in 2022, 292 wells were analyzed by ARPAV. Of these, 68% showed pollutant concentrations within legal limits and were classified as good quality, while the remaining wells had at least one parameter exceeding the limits, thus classified poor quality. These wells are shown in Figure 11.

Moreover, from the map in Figure 11, it can be observed that wells of poor quality are typically located in the Low plain area, while good quality groundwater is generally located in the High plain area (ARPAV, 2023).

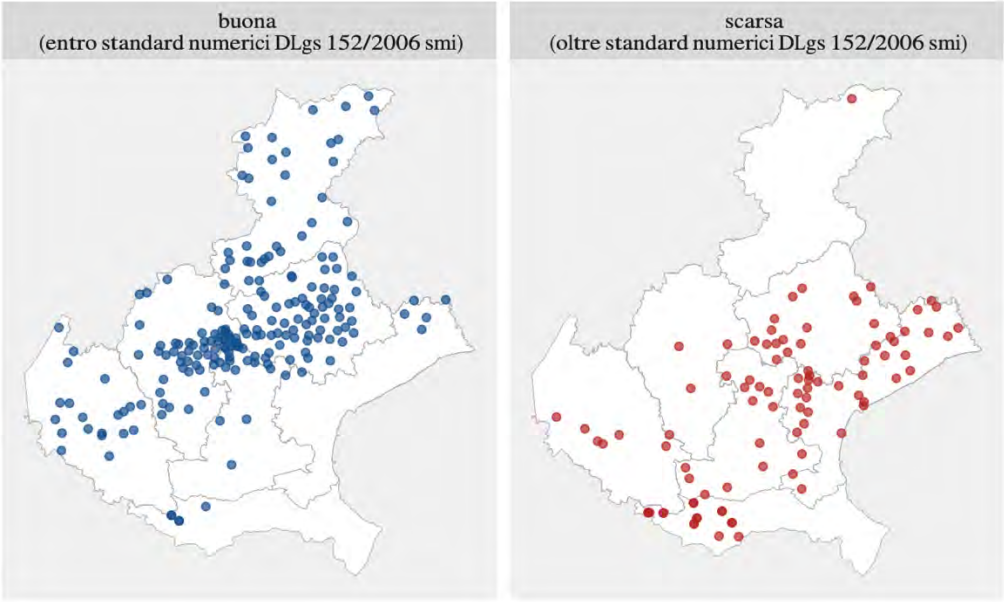

Figure 11. Wells with good and poor quality in 2022 (ARPAV, 2023).

When observing alarming concentrations of pollutants in groundwater, it is crucial to investigate the potential sources. For contaminants such as pesticides and total solvents, the source is often linked to anthropogenic activities. However, for molecules like nitrates, chlorides, and sulfates, which are naturally present in the environment, it is essential to consider the Natural Background Level (NBL).

The NBL represents the naturally occurring concentration of an element in the groundwater being analyzed. For instance, chloride concentrations can vary significantly between different aquifer systems. A study by Hinsby et al. (2008) highlighted that the NBL for chlorine in Finland is typically below 10 mg/l, while in Portugal, it can reach values as high as 200 mg/l.

Besides the values of contaminant concentrations in groundwater, it is ideal to first define the groundwater risk to pollution. This risk is determined by analyzing the vulnerability of the water and the pollution load. Firstly, to assess how prone groundwater is to pollution (Groundwater Vulnerability Assessment – GVA), the analysis should be conducted in two directions: considering intrinsic and specific vulnerability. Intrinsic vulnerability assesses the aquifer behavior in relation to pollutants, taking into account the hydrogeological, hydrological, and geological characteristics of the area. In contrast, specific vulnerability evaluates the groundwater response to the particular pollutant under consideration.

Furthermore, the approach can focus on either resource or source consideration. In the first case, the entire body of water is considered for protection, while in the second case, only a specific well needs safeguarding.

The most widely used method globally is the “DRASTIC”, which considers seven variables to assess the groundwater vulnerability: the depth to the water table, net recharge, aquifer media, soil media, topography of the area, impact of the vadose zone, and hydraulic conductivity of the aquifer (Taghavi, et al., 2022).

Secondly, the pollution load assesses the threat of contaminants to the groundwater resource. An index of the pressure can be obtained by considering the toxicity of the pollutant, the quantity dispersed by the source, the potential release, and the weights coefficient associated with the characteristics of the pollutant (Liu, et al., 2024).

By considering these values, a proper assessment of the risk of contamination to an aquifer can be achieved.

3.1. TOTAL SOLVENTS

Total solvents are a group of pollutants composed of chlorinated compounds, which can come from the chlorination of either ethane, methane, or ethenes.

In this thesis, the sum of two pollutants is considered. These are:

- PCE (tetrachloroethene): contains four chlorine atoms. It is used in industrial activities due to its properties as a metal degreaser, dry cleaner, and solvent, thanks to its ability to dissolve a wide range of chemicals.
- TCE (trichloroethene): contains three chlorine atoms bonded to the ethene chain. With a structure similar to PCE, it can be used as a solvent, particularly in wood manufacturing industry.

The study of PCE and TCE is driven by the changes in the use of them over the past decades. Since its formulation in 1821, PCE experienced its highest usage during the 1960s and 1970s. Authors assert that by the late 1980s, the use of PCE was widespread, appearing in 56% of dry-cleaning formulations in the US (Izzo, 1992).

These substances are colorless and non-flammable. They have an ether-like smell at high concentrations, while their odor is barely noticeable when diluted in water. Both

pollutants exhibit high vapor tension, making them volatile. Due to the presence of chlorine radicals, they are denser than water and therefore are classified as “dense non-aqueous phase liquids” (DNAPLs) (Minnesota Pollution Control Agency, 2024).

The high density of DNAPLs makes it challenging to predict the movement of the pollution plume once these reach the saturated porous medium (Matteucci, et al., 2015). This arises due to the low organic partitioning, viscosities, and interfacial tension combined with their high tendency to vaporize, related to high vapor pressures of the investigated solvents (Moran, et al., 2007). Furthermore, groundwater is more susceptible to this type of pollution as biodegradation and evaporation processes are significantly slower compared to surface waters (Mattioli & Bicchielli, 2018).

The fate of these pollutants once they reach the soil depends on various parameters, and the processes they undergo when approaching the aquifer include dispersion, dilution, volatilization, sorption, and biodegradation. The most impactful processes are sorption and biodegradation. The first one, sorption, consists in the attachment of the pollutants to the soil particles. The effect depends on geochemical conditions and the composition of the porous media, with factors such as grain-size distribution and organic content playing an effective role (Kret, et al., 2015). On the other hand, biodegradation plays the role of transforming molecules. In the presence of oxygen, ethene is the intermediate product (Aulenta, s.d.), whereas, under anoxic conditions the middle way compounds could include DCE (dichloroethane) or DCM (dichloromethane) (Pierri, 2021). Both anoxic and oxic conditions result in the final production of carbon dioxide, chloride and hydrogen, while only aerobic conditions produce water (Figures 12 and 13).

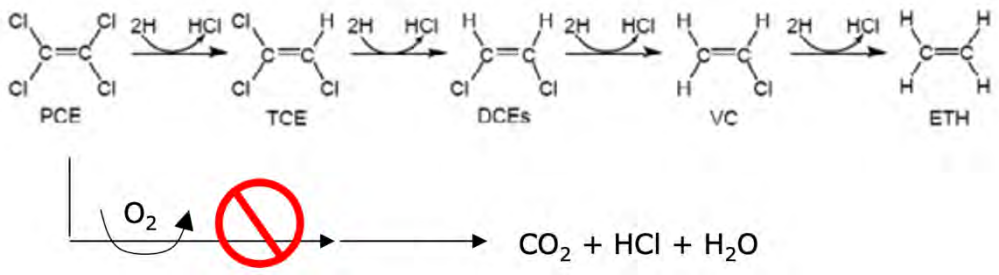

Figure 12. Reaction chain for PCE degradation in aerobic conditions (Aulenta).

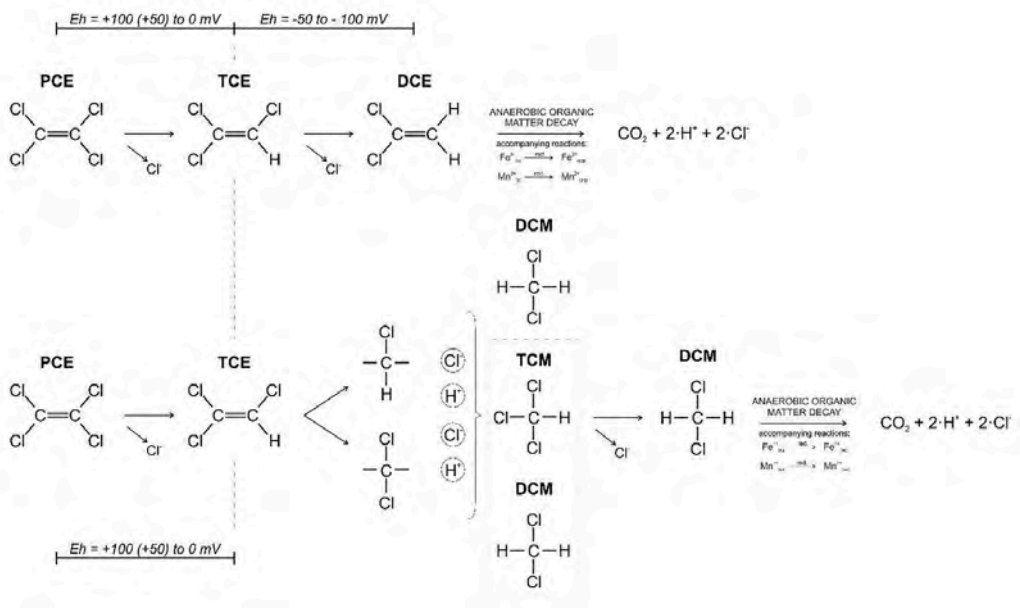

Figure 13. Chain of reactions underwent by PCE in anoxic conditions (Pierri, 2021).

The degradation rate of these molecules depends on site-specific variables. Literature reports first-order rate constants ranging from 1.1 to 3.7 $year^{-1}$ for PCE and 0.9 to 1.5 $year^{-1}$ for TCE (Kret, et al., 2015).

Chlorinated substances, particularly total solvents, are persistent contaminants and are classified as “hazardous waste” due to their well-documented toxicity. These substances, along with their metabolites, are likely to be carcinogenic to humans. The WHO suggests a guideline value for a 60 kg person drinking 2 liters of water per day, with a maximum concentration of 0.02 mg/l for TCE and 0.04 mg/l for PCE, which are conservative values. Based on these guidelines, Italian law has set the maximum concentration of the sum of the two pollutants at 10 μg/l (0.01 mg/l) according to Legislative Decree 31/2001, in alignment with Council Directive 98/83/EC.

3.2. NITRATES

Nitrates are naturally occurring molecules that take part into the nitrogen cycle.

According to the WHO the concentration of nitrates in surface water typically ranges from 0 to 18 mg/l due to oxidized conditions. In contrast, groundwater usually contains only a few milligrams per liter (World Health Organization, 1998).

Groundwater pollution by nitrates is generally associated with agricultural activities, due to the use of fertilizers and the production of manure.

Since 2003 ISTAT gathers information about the total mass of fertilizers used in each province of Italy. Figure 14 shows the data for the Veneto Region and Vicenza province. Notice the drastic decrease in the use of nitrated fertilizers between 2013 and 2014.

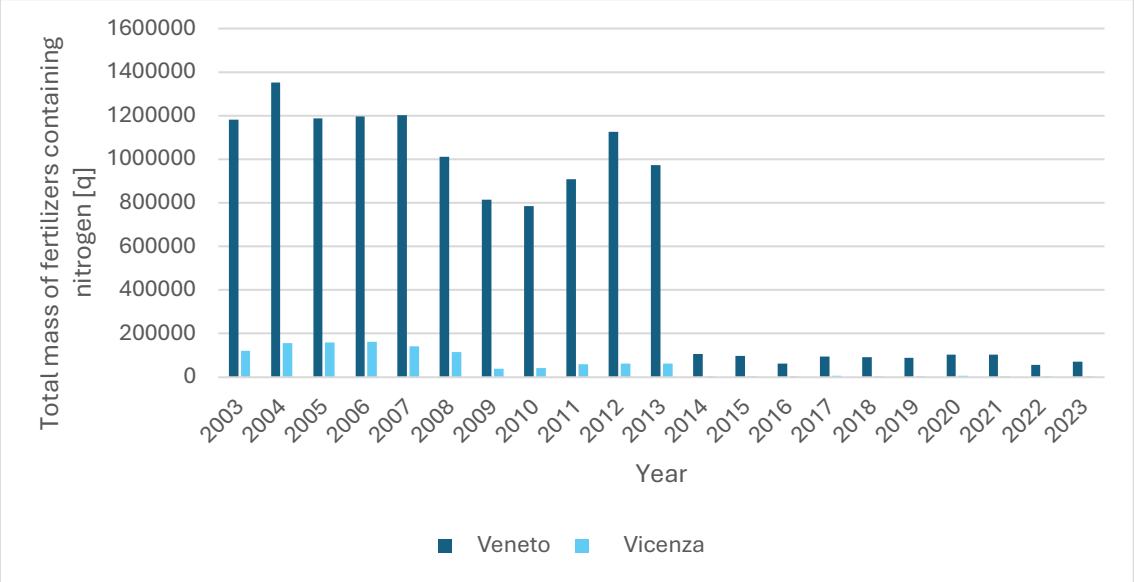

Figure 14. Total mass of fertilizers containing nitrogen used in Veneto Region and Vicenza province per year over the two decades between, i.e. 2003 and 2023 (ISTAT, 2024).

Another issue pertains to livestock farming, where manure, once produced, can follow different pathways. For instance, in 2018, livestock activities produced 125 million tons of nitrogen worldwide. Of this, 88 million tons were left on pasture, 34 million tons were treated to produce biogas, and 27 million tons were used as crop fertilizers, marking a 23% increase since 1990 (WHO, 2020).

Once ammonia is released into the soil, it undergoes nitrification, transforming first into nitrite and then into nitrate. This process can occur in one, or two steps:

- In the two-steps sequence, ammonia-oxidizing bacteria or ammonia-oxidizing archaea convert ammonia to nitrite, followed by nitrite-oxidizing bacteria converting nitrite to nitrate.
- In the single-step reaction, comammox bacteria carry out the entire transformation.

The conversion of ammonia to nitrates has multiple disadvantages. Firstly, ammonia is a more effective nutrient for plants. Secondly, and more relevant to this discussion, nitrate tends to leach away due to the presence of negatively charged soil particles, eventually reaching groundwater (Beeckman, et al., 2018). It has been estimated that no more than 50% of the nitrogen in fertilizers is absorbed by plant roots.

The presence of nitrates in groundwater is problematic both for human health and environmental quality. In water, nitrates cause eutrophication, a phenomenon that leads to hypoxia in the water body, making it unsuitable for living organisms. In humans, nitrates can cause methemoglobinemia.

Regulations about nitrates are found in the Veneto Region decree of 3rd April 2006 to comply with the Nitrates Directive 91/676/CEE by the European Union. This directive aims to mitigate water pollution due to farming activities – particularly coming from manure and fertilizers (Ministero dell'Ambiente e della Sicurezza Energetica, 2024). Nitrates Directive imposes to all the member States of the EU to periodically monitor the concentration of the considered pollutant. Moreover, regions with catchment areas that release water into bodies with elevated nitrate concentrations are designated as “Nitrate Vulnerability Zones” (NVZs), prompting farmers to implement initiatives aimed at enhancing water quality. Additionally, to reinforce these efforts, a Ministerial Decree was issued on February 25, 2016, outlining specific practical methodologies concerning the utilization of wastewater and manure generated within these areas (Ministero dell'Ambiente e della Sicurezza Energetica, 2024).

The directive sets a threshold of 50 mg/l of nitrate concentration in water bodies to classify them as polluted (Ministero dell'Ambiente e della Sicurezza Energetica, 2024).

Considering the hydrogeologic setting of the Po plain, it has been noted that vulnerable zones tend to be concentrated in the High plain areas, characterized by the presence of thick vulnerable phreatic aquifers, while a less critical situation characterizes the Low plain. As illustrated in Figure 15, the Treviso province stands out as the area mostly affected by this type of pollution in the Veneto Region (ARPAV, 2024).

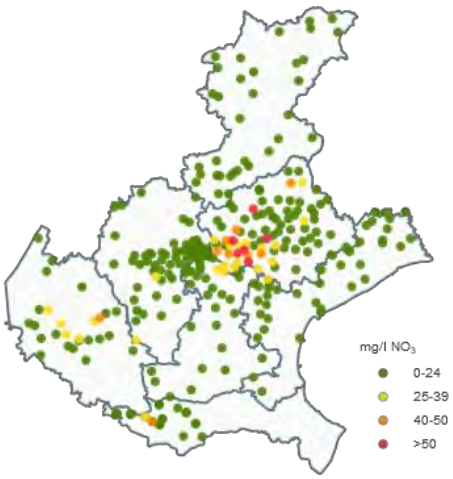

Figure 15. Nitrate concentration in wells of Veneto Region (ARPAV, 2024).

3.3. PESTICIDES

The word “pesticides” refers to a group of chemicals comprising over 1000 substances that can be either synthesized or natural (WHO, 2022). The most common definition refers to a group that includes herbicides, fungicides, insecticides, acaricides, plant growth regulators, and repellents. The most widespread classification for these molecules defines three classes based on chemical composition, function and mode of entry (Kaur, et al., 2019).

As well known, these pollutants are released into the environment through agricultural activities. Their intensive use started in the 1950s, particularly in monocultural agriculture (Hassaan & El Nemr, 2020). Concerns regarding them began in the 1960s due to their presence in surface water, becoming compelling in the 1970s and 1980s due to their detection in groundwater – and therefore in many sources of drinking water.

Pesticides are used by spraying them on crops and/or soil or can be in the form of seeds and thus applied directly into the soil. However, even when placed close to the crops, many studies claim that only 0.3% of the substance applied reaches the target, while 99.7% remains in the environment.

Thus, about the 99.7% of the applied substance can undergo different processes such as chemical and biological degradation, sorption, volatilization, root uptake, and dilution. Volatilization is the most effective process in environmental pollution, depending on

many variables such as the Henry's law constant of the substance, the moisture content of the soil, and the atmospheric conditions.

Concerning chemical and biological degradation, the effectiveness of these processes depends on environmental conditions. Nevertheless, it is generally observed that reaction rates increase in high temperature and high-moisture states (Hayo & van der Werf, 1996). Tables containing the half-life values of pesticides relative to the crops to which they are applied are available: in some cases, the values are lower than one day, while in others, the molecules can be observed on-site for more than hundreds of days. That is why a classification relative to their half-life exists:

- Non-persistent pesticides present a half-life lower than 16 days;
- Moderately persistent pesticides have a half-life between 16 and 59 days;
- Highly persistent pesticides show a half-life value higher than 60 days.

It is important to note that degradation of the pollutant does not necessarily resolve the problem, as it is essential to consider the metabolites that are formed (Hanson, et al., 2015).

Degraded or not, the pesticide tends to attach to soil particles: it has been observed that 20 to 70% of it is bound to soil grains. As with other processes, sorption is also related to working conditions, particularly affected by the quantity of organic matter present in the superficial layer of the soil. The higher the portion of organic carbon, the higher the sorption effect.

Once links are formed, the pollutant mobility is reduced, but water through wash-off and leaching still affects them. Before the 1980s, the potential pollution of groundwater by these molecules was always associated with their mobility, whereas in 1989, Gustafson proposed considering both mobility and persistence through the so-called "GUS" index (Gustafson, 1989).

Consequently, pesticides with a GUS index higher than 2.8 can be detected in groundwater, while if the value is lower than 1.8, the likelihood of finding these pollutants in groundwater is minimal (Hayo & van der Werf, 1996).

The root uptake of the analyzed substances leads to bioaccumulation, therefore entering the food chain. Many diseases are recognized as related to pesticides, and in developing countries 99% of yearly deaths are connected to them. They cause biochemical alterations

that exhibit through mild allergies, breathing difficulties, and more severe illnesses such as cancer (Tomer, 2013).

The environment is threatened due to both direct and indirect effects: through the impact on living beings and the aquatic habitat (Hassaan & El Nemr, 2020).

Knowing the serious impact of pesticides on the environment and living beings, proper regulation to protect them is essential. The Europe Union launched Directive 2006/118/EC, defining guidelines used in Italy in legislation 30/2009, which states that the maximum concentration of pesticides and their metabolites in groundwater must be 0.1μg/l for a single substance and 0.5 μg/l for the sum of them. Also, the use of pesticides is regulated at European level by the "Pesticide Directive", adopted in Italy through the legislative decree 150/2012. This decree called for a stricter supervision and the production of a plan every five years that defines the proper use of pesticides (Socchera & Minutolo, 2022).

In this thesis, the only pesticide analyzed is 2,4-diamino-6-chloro-s-triazine (DACT), a metabolite of atrazine (GUS = 3.2). The interest to this pollutant is related to its usage history and regulations. Atrazine is a chlorotriazine class used as selective systemic herbicides to control broadleaf and grassy weeds.

Once released onto the soil, atrazine is degraded with a half-life of 4 to 57 weeks (Hu, et al., 2023), after which it can be found in the form of deethylatrazine (DEA), deisopropylatrazine (DIA), and diaminochlorotriazine (DACT), as shown in Figure 16.

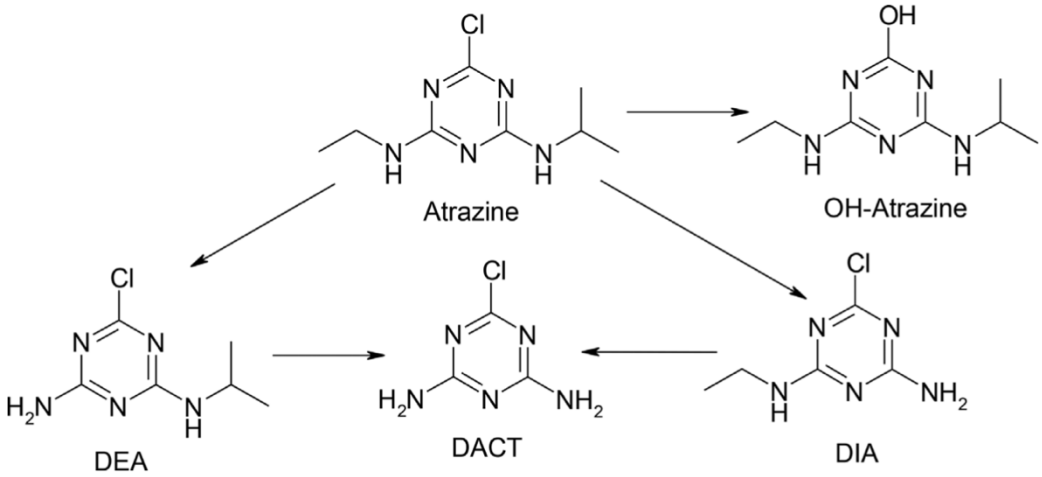

Figure 16. Scheme of atrazine degradation (Scialli, et al., 2014).

The metabolites are produced in different percentages. A study conducted by Scialli et al. (2014) on a group of workers exposed to atrazine showed that in their urine, 80% of the total pesticide traces were DACT, 10% DIA, and 8% DEA. It is therefore reasonable to think that the most present metabolite is DACT (Scialli, et al., 2014)

Since the commercialization of atrazine, it has been widely used in Italy until 1986, when its usage started decreasing. Then in 1992, the herbicide was banned by Italian law, although it still produces negative effects on soil and water quality (Ghirardelli , et al., 2020).

Therefore, since Vicenza is an intensively cropped province, and research by Ghirardelli et al.(2020) showed that 155 out of 785 wells sampled between 1987 and 2016 exceeded the Maximum Acceptable Concentration (MAC) fixed by law for the single pollutant. Consequently, this thesis aims to analyze the spatio-temporal behavior of DACT.

3.4. CHLORIDES

Chloride is an element that is normally present in groundwater, and its concentration can vary based on the hydrogeological conditions of the water body. It is primarily influenced by the contact time of water with soils rich in CaCl, $CaCl_2$ and KCl, but it can also depend on biological reactions. Although chloride pollution of groundwater is sometimes related to sewage water discharge, its main source in coastal regions is represented by seawater intrusion, which results from the effect of salty water with chloride concentrations that can reach 19 000 mg/l (ARPAV, 2019).

With reference to chloride concentration values, it is important to know the so-called “Natural Background Level” (NBL), which represents the natural level of the element in the analyzed groundwater. For this reason, chloride concentrations can vary significantly between different aquifer systems. A study conducted by Hinsby et al. (2008) has highlighted that, for instance, in Finland the NBL of chlorine is lower than 10 mg/l, while in Portugal it can approach values of 200 mg/l. Typically, waters not subjected to saline intrusion present chloride concentrations that rarely exceed 10 mg/l and can sometimes be even lower than 1 mg/l (WHO , 1996).

In the area of the study, no NBL has been specified, so it can be assumed to be 0 mg/l.

Regarding the presence of chloride due to the dissolution of KCl, NaCl and $CaCl_2$, it is important to consider that these salts have solubilities at 20°C equal to 34.4 g/100 ml, 35.7 g/100 ml, and 74.5 g/100ml, respectively (WHO , 1996). Considering that the underground water temperature of the considered area ranges between 10 and 14°C, the solubility of these salts should be lower than the values reported above. Despite the relatively high solubility of these salts, their presence in rocks is relatively limited. In fact, it has been reported that the chloride content in rocks is 100-200 mg/kg for igneous rocks, 660 mg/kg in dolomites, while in sedimentary rocks it decreases to 20-130 mg/kg (GTK, 2005).

Once in water, chlorine can be considered a conservative substance: thanks to its high mobility (Tariq Bashir, et al., 2012) it relocates at different compartments of the hydrosphere undergoing only physical transformations (GTK, 2005).

Short-term observations indicate that chloride has no toxicity on healthy individuals. The long-term impacts of high chlorine consumption have not been extensively studied. It is noted that a daily intake higher than the norm of 6 g is not harmful, provided there is an adequate intake of fresh water (WHO , 1996). Italian regulation defined the standard values for groundwater with Decree 30/2009, setting the limit concentration at 250 mg/l.

3.5. SULPHATES

Sulphate is an anion that could be found in water, mainly originating from natural sources, with the mostly significant contributors being minerals containing sulphate (e.g.,gypsum) or oxidized sulphide (e.g.,pyrite), precipitations and volcanic activity.

Anthropogenic pressures on this element in groundwater come from domestic and industrial wastewaters, particularly from soap and detergents, pesticides, glass, paper, wood and tanning industries (Moreno, et al., 2009). Furthermore, water withdrawal by wells can cause the increase of sulphate concentration into the ground due to the impact on geological stocks through overexploitation of the groundwater source (Wang & Zhang, 2019).

The sulphate ion can come from its saline forms, where it is bound to the ions of sodium potassium, magnesium, calcium and barium. Among these, the first three are highly soluble, while the latter two are sparingly soluble (WHO , 2004).

To better understand the sources of this pollution, it could be useful to consider the sulfur cycle in which it is places. As shown in Figure 17, sulphate is the most frequent form of sulfur in water and soil (Britannica , 2024).

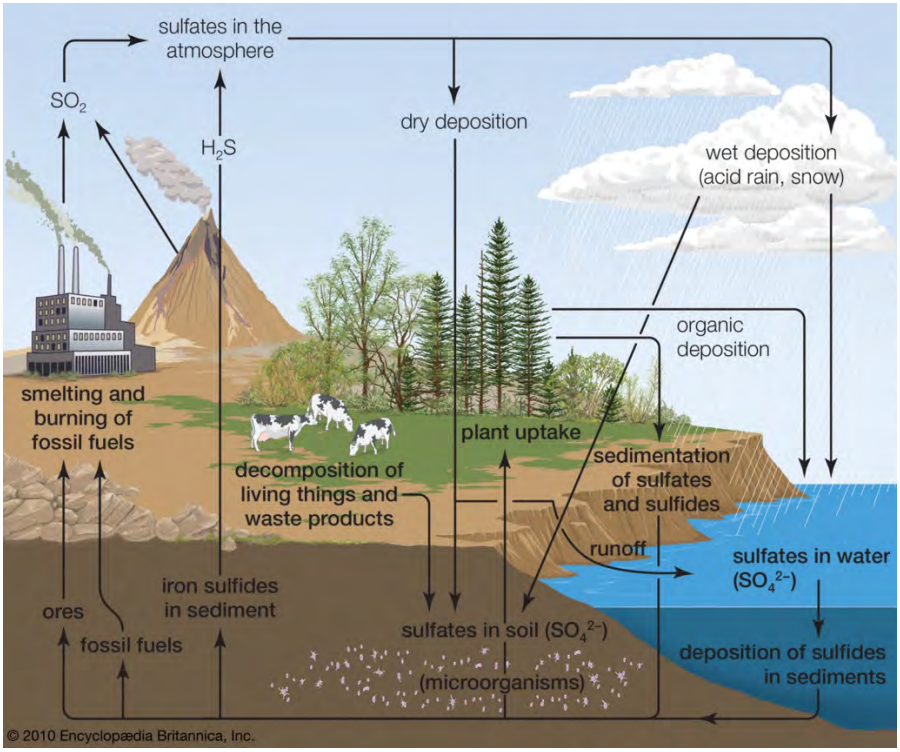

Figure 17. Sulfur cycle (Britannica, 2024).

When sulfur is released into the environment as hydrogen sulphide, it promptly converts to sulphate in aqueous conditions. Once sulphate is solubilized in water, it shows high stability, and it can both be transported and diluted or undergo chemical reactions due to the reducing environment that characterizes groundwater. Due to the low concentrations of oxygen in groundwater, anaerobic microorganisms use sulphate as an electron acceptor, thereby reducing it. In water rich in heavy metals, the increase in sulphite concentration causes the precipitation of metals as metal sulphites (Miao, et al., 2012). This, combined with the effect on carbonate weathering and the carbon cycle, represents an indirect impact of high sulphate concentrations in water (Wang & Zhang, 2019).

Impacts on human health have shown that even in high concentrations, the analyzed ion does not have any toxic effects, and in 28-day observations, it only causes diarrhea. However, it has been reported that humans can adapt to long-term exposure to relatively

high concentrations. Eventually, the prolonged consumption of high quantities of salts derived from sulphate paired with magnesium and sodium causes dehydration (WHO , 2004). Therefore, as no toxicity has been detected, the limit set by WHO, and adopted in Italy, is of 250 mg/l in groundwater.

4. MATERIALS AND METHODS

4.1. DATASET

The dataset employed in this study was compiled through various survey campaigns conducted by different authorities responsible for water quality monitoring in the Vicenza Province between 1981 and 2023. More precisely, the public bodies providing data are VIacqua SpA, Acegasaps, CIN (Centro Idrico Novoledo), ATO Bacchiglione, ULSS, SPV (Strada Pedemontana Veneta).

This extensive historical series was collected and released by VIacqua SpA, the company in charge of water supply to 68 municipalities within the Vicenza province, located in the upper portion of ATO (Ambito Territorriale Ottimale) Bacchiglione.

VIacqua, established in 2018 by merging Alto Vicentino Servizi and Acque Vicentine, it represents a relatively recent organization.

Due to the succession of various authorities governing the water management in the area, the resultant database exhibits considerable heterogeneity in terms of data sources, derived from a total of 914 wells (as depicted in Figure 18). These wells have undergone monitoring with at least one measurement.

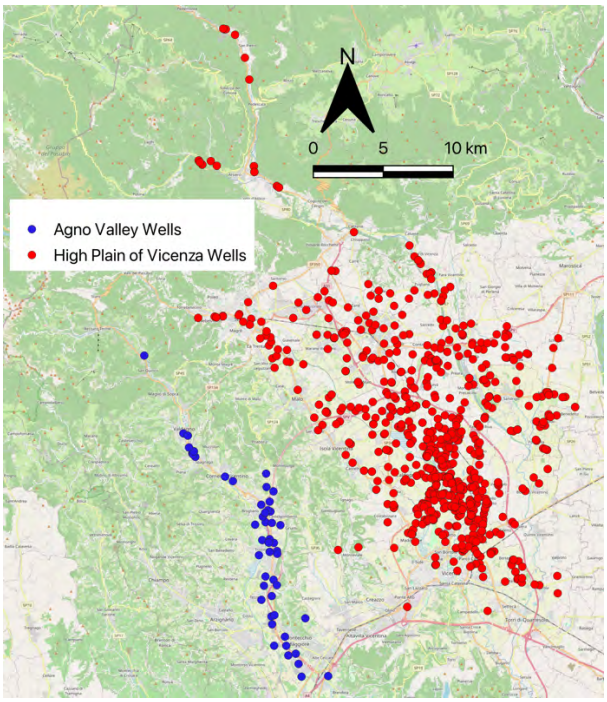

Figure 18. Location of wells with water quality measurements in the two sub-domains of the study area.

Figure 18 delineates the wells analyzed within the two sub-domains: the Agno Valley (denoted in blue) and the of Vicenza high plain (denoted in red). The sampled wells occasionally belong to private users and were not periodically inspected. Conversely, the wells managed by public organizations were subjected to systematic measurements, providing a more accurate representation of the temporal evolution of water quality in the region.

A significant number of wells have fewer than ten samples over the 43-year period of analysis, complicating the examination of the historical behavior of water intercepted by specific wells. In this context, the application of geostatistical methods is indispensable for interpolating these sparse data, thereby enabling a clearer understanding of their spatial distribution within the studied area.

Within the Vicenza high plain sub-domain, the database includes concentration values, georeferencing, and occasionally the aquifer layer intercepted by the well. Figure 19 illustrates that the wells with specification about the reference layers are predominantly situated in the southern portion of the domain. The majority of these wells tap into the fourth aquifer, corroborating the domain description regarding the productivity of the multi-aquifer system.

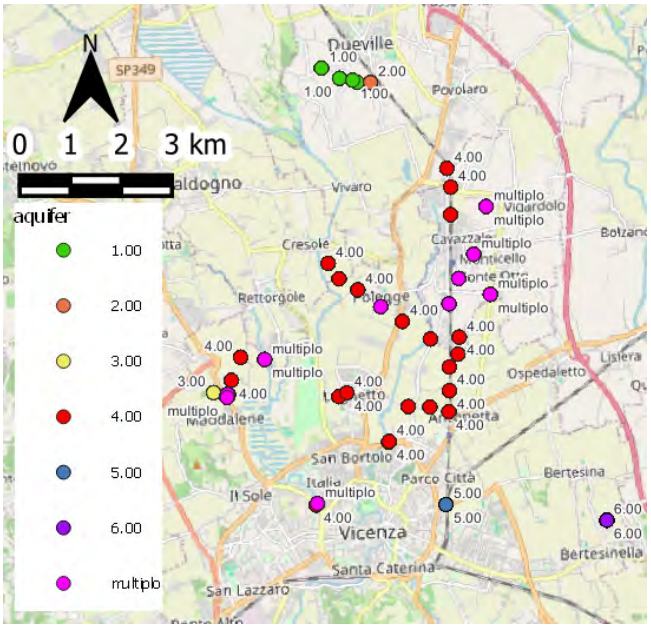

Figure 19. ID of the aquifer layer intercepted by wells in the multi-aquifer system.

As observed in Figure 18, the spatial distribution of the monitoring points is uneven yet adequate to facilitate reliable interpolation results. The influence of spatial distance on the precision of result will be further elucidated through the development of error maps.

To ensure accurate results, the domain must be meticulously defined. Consequently, two wells were excluded from the analysis due to their substantial distance from the other points: the P84001 well in Sovizzo, and the P67001 one, located 13 717,2 m and 21 644,2 m apart from the nearest point, respectively. In certain instances, data anomalies were observed, particularly null values in series where values were consistently non-null. These anomalous data were excluded from the analysis.

In the Agno valley, the area is characterized by an unconfined aquifer system, thus the intercepted hydrological system is well understood. Significant points, well-distributed and presented in Figure 20, were sampled exclusively between 2016 and 2020, thereby lacking the temporal distribution requisite for a comprehensive study.

Figure 20. Sampling years of wells in Agno valley.

4.2. SAMPLING CAMPAIGN

Samples were collected and analyzed by various authorities over the 38 years covered by the dataset. More likely each administration followed different procedures.

- from the direct participation to the VIacqua sampling campaigns carried out in P40003 on 29 May 2024, the procedure implemented by this company can be streamlined as follows: upon arriving at the well area, the water table depth is measured using a phreatimeter. This step is needed to determine the static water level;
- the water sample is taken form a depth of 30 meters below the static water table line defined by the measurement. This specific depth is chosen to ensure the water collected is at the level of the well filter;
- the low flow method is employed. This method involves a withdrawal flow rate of less than 500 ml/min to minimize the decrease in the water table level;
- a pipe connected to a pump is inserted into the well to begin water withdrawal. The pumped water is collected into a bucket, where temperature, pH, conductivity, and dissolved oxygen are measured using the multiparametric probe HQ2100 by HACH. These measurements are taken at 5-minute intervals until the values stabilize, indicating equilibrated conditions;
- once equilibrium is achieved, a sample is collected and transported to the laboratory for further analyses.

The monitoring setting and instrumentation are shown in Figure 21.

Figure 21. Setting and instrumentation used in water sampling procedure.

4.3. STATISTICAL ANALYSIS

When approaching the statistical analysis if a dataset, it is initially fundamental to observe if the series exhibit any significant distribution pattern, homogeneity, or the presence of outliers. An initial analysis of the data, independent of their spatial distribution, facilitates a more critical evaluation of the obtained results. Furthermore, understanding data trends and patterns ensures that program outputs can be interpreted and discussed more accurately, provided there are no errors.

In the specific of the dataset handled in this thesis, the available data are characterized by an asymmetric and typically exponential or Poisson distribution due to their inherently non-negative nature. The Kriging approach is the spatial interpolation method selected to obtain predictions at unsampled locations based on observed geostatistical data. The derivation of the Kriging equations to determine the coefficients in the kriging estimator does not depend on any distribution assumptions (Matheron, 1969; Chilès and Delfiner, 2012), except for stationarity. Before conducting any statistical or geostatistical analysis, a transformation of the data was performed to optimize Kriging.

Two transformation methods were tested: logarithmic and Box-Cox transformations. For the logarithmic transformation, values were first adjusted to be non-zero by adding one,

followed by the logarithm calculation. The Box-Cox transformation applied the following equation:

$$\begin{cases} \frac{y^{\lambda}-1}{\lambda} & if\ \lambda \neq 0 \\ \ln(y) & if\ \lambda = 0 \end{cases} . \quad (1)$$

After examining the transformed data, the logarithmic transformation was selected for further use because it produces more representative of the values.

For what concerns the statistical analysis, calculating the mean for the entire data series would not be sufficiently representative and would be reductive, as it would not highlight concerning values related to water contamination events, which is the focus of this thesis. Therefore, understanding other statistical values and their significance is necessary.

The mean is calculated by summing the observed values and dividing by their count, while the median represents the value above which 50% of the measured values lie. Together, the mean and the median provide a first idea about the shape of the distribution. The further the median is from the mean, the more asymmetric the histogram describing the data distribution will be.

The median can also be called “second quartile”. In a distribution, the first and the third quartiles can also be identified, indicating the value below which the first 25% and 75% of the data lie, respectively.

The mode represents the most frequently observed value. This is important in environmental contexts because it defines the state in which the measured class, such as subsurface water quality, is most often found.

Two values provide an itemized information about the distribution shape: variance and skewness. Variance is calculated as the sum of the squared difference between each value and the mean, divided by the number of observations. It indicates the dispersion of values around the mean. Since this parameter is dimensional, it can sometimes be difficult to interpret. Therefore, a more easily understandable parameter is the coefficient of variation, which is the standard deviation (obtained taking the square root of the variance) divided by the mean. Both formulas are shown below:

$$\sigma^2 = \frac{1}{n-1}\sum_{i=1}^{n}(x_i - \mu)^2 . \quad (2)$$

$$CV = \frac{\sqrt{\sigma^2}}{\mu}. \tag{3}$$

The second parameter of the distribution is skewness, defined by the following equation:

$$G = \frac{n}{(n-1)(n-2)} \sum_{i=1}^{n} \left(\frac{x_i - \mu}{\sigma}\right). \tag{4}$$

For a perfectly symmetrical, Gaussian distribution, the value of G is zero. As skewness deviates from zero, the distribution shows a tendency towards one side. The value can be positive or negative: positive values indicate a tendency of measures exceeding the mean, resulting in a right-skewed distribution, while negative values indicate a left-skewed distribution.

Figure 22 shows the three forms of unimodal distribution that can be encountered.

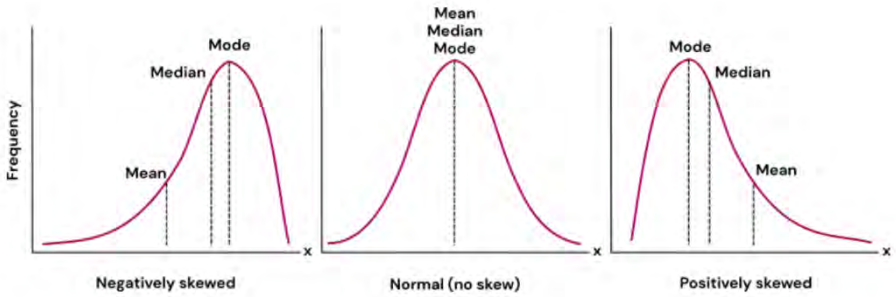

Figure 22. Mean, mode, median and asymmetries of distributions (Van Parys).

Outliers were not considered in the statistical analysis, as focusing on individual data points would obscure the perception of contamination evet peaks. Instead, each measure showing a particularly significant value was assessed in relation to its geographical position and historical data series. Isolated events were regarded as potential measurement errors and were excluded, while values consistent with adjacent data were retained and incorporated into the analysis. This approach ensures that the analysis remains robust, reflecting true patterns of contamination rather than anomalies.

4.4. GEOSTATISTICAL ANALYSIS

Geostatistical methods represent a specific branch of statistics focused on the modeling and prediction of spatial phenomena. These methods are extensively applied in environmental engineering due to their integration of spatial coordinates of data, which aids in the delineation of spatial trends. To minimize uncertainties, these methods employ probabilistic models and pattern recognition techniques.

Geostatistical techniques apply to both spatial extrapolation and interpolation, with interpolation generally producing more accurate results (Olea, 2018). Various methods exist and can be classified as either “deterministic” or “stochastic”. Deterministic methods yield unique values at specific locations within the domain, while stochastic methods do not, the output depends on the application of the method. Examples of deterministic techniques include nearest neighbor, inverse distance weighted, and spline interpolation. Among stochastic methods, Kriging is the most prevalently utilized and is the primary subject of this thesis. Kriging operates based on the minimization of error variance.

In the application of geostatistical models to analyze a regionalized variable, the following steps are typically undertaken:

1. Spatial association: Examining the spatial relationships between points within the domain.
2. Spatial interpolation: Predicting the values associated with each point in the domain.
3. Definition of the error: Quantifying the error associated with the predictions (Panagiotou, et al., 2022).

4.4.1. SPATIAL ASSOCIATION

Spatial association involves examining the relationship between the values of a variable at two proximate locations. This process, also known as “spatial autocorrelation”, operates on the premise that measurements taken at closer points will exhibit greater similarity. Autocorrelation can take on a value of zero, which indicates no relationship between the pairs of points regarding the variable under consideration.

After performing a logarithmic transformation of the data, the concentrations can be modeled as a Gaussian random field (GRF), signifying that the data points are random variables within a continuous domain, following a normal distribution. In a stationary process involving such variables, the distribution remains unchanged across different locations within the domain, and the second order stationarity ensures a constant mean. Mathematically, the bi-dimensional domain is defined as follows:

$$GRF = \{Z(x): x \in D \subset \mathbb{R}^2\}. \tag{5}$$

Second-order stationarity can be expressed as:

$$E[Z(x)] = \mu, \forall\, x \in D. \tag{6}$$

Under the assumption of weak stationarity, the covariance function is defined as:

$$Cov\big(Z(x), Z(x+h)\big) = C(h), \forall x \in D, \forall h \in \mathbb{R}^2. \tag{7}$$

Since the distribution remains unchanged across different points within the domain, the variance should also remain independent of position, it is therefore called intrinsically stationary, yielding:

$$Var\big[Z(x_i) - Z\big(x_j\big)\big] = 2\gamma\big(x_i - x_j\big), \forall x_i, x_j. \tag{8}$$

where γ is a function defined as "semivariogram". In Kriging analysis γ is primarily used to determine the weights in the interpolation process rather than the variogram. The semivariogram measures the structure, magnitude, and intensity of spatial patterns and is typically expressed as a function of the distance between two points (h):

$$2\hat{\gamma}(h) = \frac{1}{|N(h)|}\sum_{i=1}^{N(h)}\big[Z(x_i) - Z(x_i+h)\big)]^2. \tag{10}$$

where:

$\gamma(h)$ is the semivariance,

h is the distance between pairs of points (lag distance);

Z is the variable value (in this context, concentrations);

N(h) is the number of pairs of points at distance h;

x_i and x_i+h are the locations of the points.

By considering the constant mean, the semivariogram can also be defined as:

$$2\gamma(h) = Var\big(Z(s+h) - Z(s)\big) = E[(Z(s+h) - Z(s))^2]\,. \tag{9}$$

The semivariogram, as a continuous function, enables the estimation of values at any point within the domain, not just at discrete locations (Moraga , 2021).

When defining the formulation of the semivariogram, the lag distance is a critical parameter. It represents the distance between points used when constructing the function. Choosing the correct lag distance is crucial: if it is too small excessive noise would be introduced into the variogram, obscuring the function's shape; if it is too large, the variogram would be overly smoothed, eliminating important details. Therefore, it is essential to consider not only the average distance between the nearest neighboring points but also the variability of their values when selecting the lag distance (Deutsch , 2015). The significance of this parameter is illustrated in Figure 23. Once the lag distance is defined the shape of the variogram is obtained.

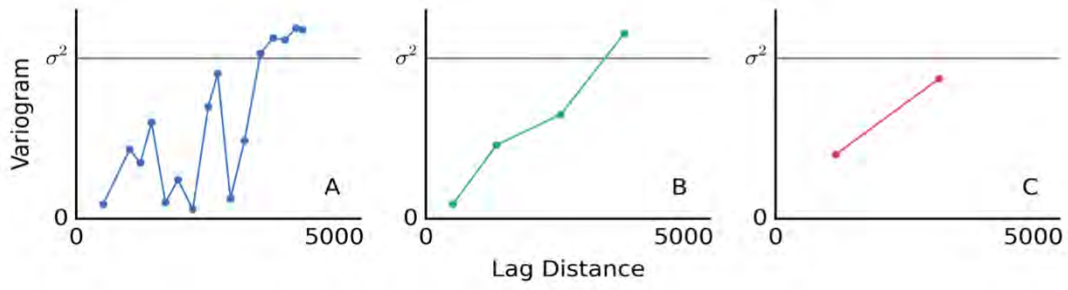

Figure 23. Dependency of the variogram on the lag distance chosen (Deutsch , 2015).

Figure 24 is reported a typical variogram, displaying features such of the nugget, range, and sill.

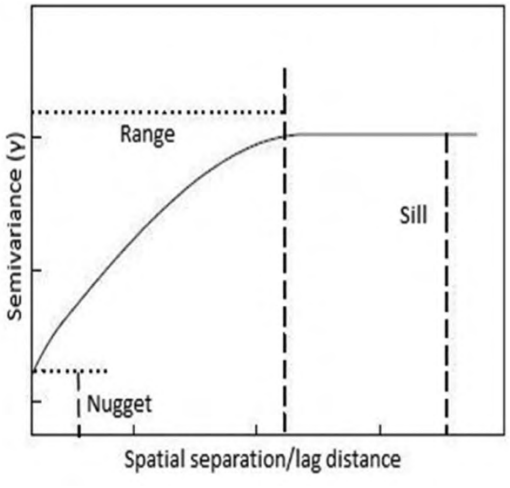

Figure 24. Parameters of variogram (Hilal, et al.).

The nugget represents the value of the semivariogram near zero lag distance. Theoretically, the variogram value at exactly zero distance is null, corresponding to the covariance of the same point with only one measure. The nugget value should be consistent in all directions. Interestingly, the presence of a nugget does not hinder process analysis; it can be attributed to the randomness of the event and differences in sampling processes. Generally, a higher number of observations results in a lower nugget value. Counterintuitively, a higher nugget effect leads to smoother estimations because the kriging method tends to minimize the impact of discontinuities observed at lower lag values, relying more on further distances.

The range in a variogram represents the distance at which points cease to be correlated with each other. It indicates the radius within which a point influences the values on the map. Specifically, the range is the distance from the origin of the variogram graph to the point where the function reaches the sill, which is where the variogram flattens out.

The sill represents the maximum variance of the values. Above this point, a negative correlation is observed, meaning that the values of point pairs tend to change in opposite directions. Below the sill, a positive correlation is present.

The variogram can exhibit different shapes, even when the same values of the above described parameters are assumed. Although there are many functions in the literature designed to better fit specific data distributions, the three most commonly used models

are the Gaussian, exponential, and spherical variograms. These will be further illustrated below.

In summary, spatial association and its underlying principles, particularly through the use of semivariograms, are critical for understanding and predicting spatial patterns within a given domain.

4.4.2. VARIOGRAM MODELS

In environmental process descriptions, the most recurring shapes of variograms are the exponential, Gaussian, and spherical, as shown in Figure 25.

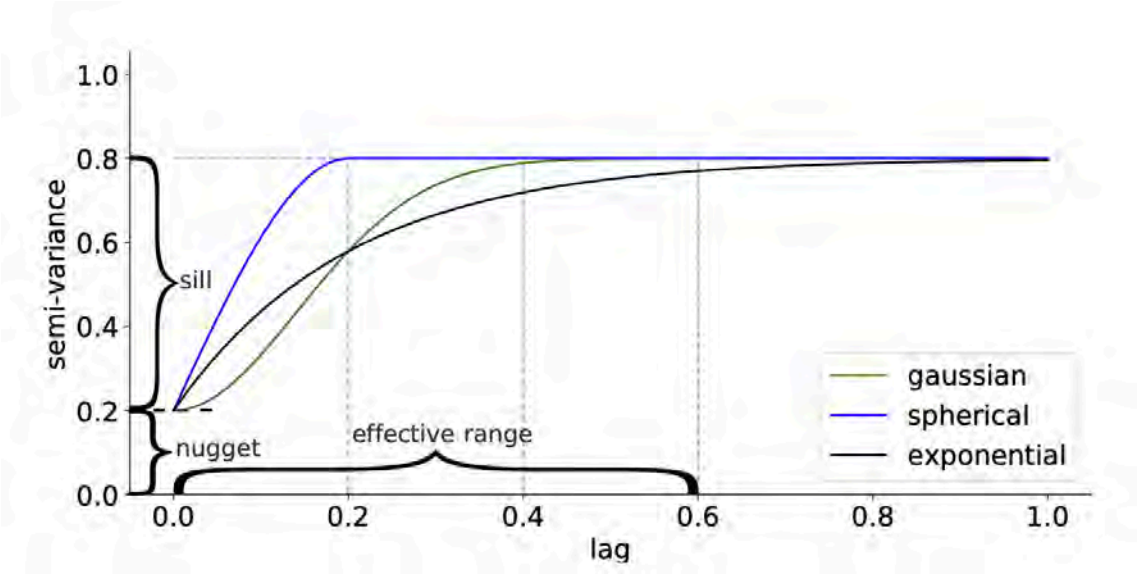

Figure 25. Gaussian, spherical and exponential variogram models (Mälicke , et al., 2018).

By observing these shapes, it becomes clear that even with the same values for the sill, nugget, and range the behaviors of the functions differ. As highlighted in Figure 24, the point where the function reaches – or almost reaches – the sill is labeled as the "effective range", which differs from the range. Specifically, the Gaussian and exponential functions take time to reach the sill; therefore, the effective sill is the point where 95% of the correlation is lost.

The mathematical formulations, of the three models are defined with the parameters of the nugget (c_0),, the partial sill ($c_1 = sill - c_0$), the norm of the distance from the center ($\|h\|$) and the range (r) as follows:

- Gaussian model

$$\gamma(h) = \begin{cases} 0 & h = 0 \\ c_0 + c_1 \left\{ 1 - \exp\left(-\frac{\|h\|^2}{r^2} \right) \right\} & h > 0 \end{cases} . \quad (11)$$

In this case, the effective range is defined as $\sqrt{3} \cdot range$. This model is suitable for describing values that are highly correlated at short distances and then decrease rapidly;

- Spherical model

$$\gamma(h) = \begin{cases} 0 & h = 0 \\ c_0 + c_1 \left[\frac{3}{2} \left(\frac{\|h\|}{r} \right) - \frac{1}{2} (\|h\|/r)^3 \right] & 0 < \|h\| \leq r \\ c_0 + c_1 & \|h\| \geq r \end{cases} . \quad (12)$$

In this case, the effective range corresponds to the range. The sharp transition to the sill makes it suitable for data distributions where the distance beyond which points stop being correlated is clearly defined;

- Exponential model

$$\gamma(h) = \begin{cases} 0 & h = 0 \\ c_0 + c_1 \left[1 - \exp\left(-\frac{\|h\|}{r} \right) \right] & h \neq 0 \end{cases} . \quad (13)$$

The effective range of the exponential model is a distance equal to 3·range. In this case, the sill is never fully reached, but the variogram approaches it asymptotically. This model is therefore useful when correlation decreases gradually with distance (National Research Council, 1991).

4.4.3. ANISOTROPIC VARIOGRAM

The descriptions above consider the condition of isotropy. Isotropy is observed when data are independent of the chosen direction. In contrast, anisotropy occurs when data vary with direction, which is more commonly observed in nature. Anisotropy often arises from heterogeneity in underground settings and can be classified into geometric and zonal anisotropy:

- in geometric anisotropy, the range of the variogram varies with direction, while the sill remains constant;
- in zonal anisotropy, both the range and the sill vary depending on the direction. Zonal anisotropy is less common and is not considered in this thesis.

Geometric anisotropy defines an ellipsoid (Figure 26) with a direction θ, where the maximum diagonal a_{max} is observed, and the minimum a_{min} is orthogonal to it. In variogram determination, a_{max} corresponds to the maximum range, and a_{min} to the minimum range.

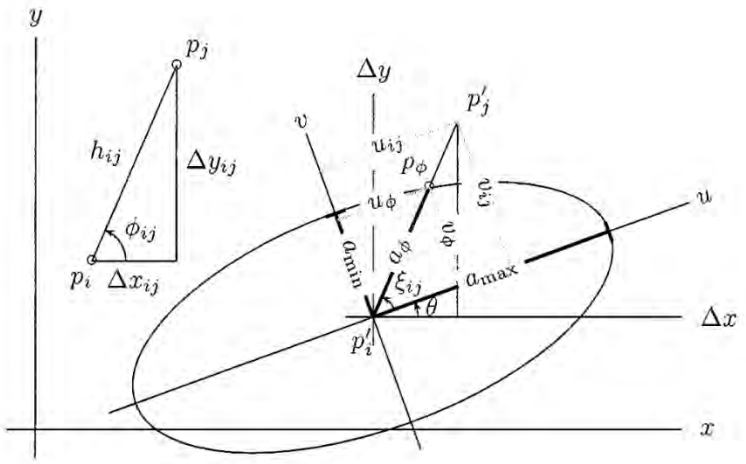

Figure 26. Ellipsoid of the geometrical anisotropy (Eriksson, et al., 1999).

When defining directional variation, it is essential to normalize distances based on scale and direction. This is done using the reduced distance, obtained through a mathematical transformation derived from the ellipse equation. The ellipse is defined as:

$$\left(\frac{u}{a_{max}}\right)^2 + \left(\frac{v}{a_{min}}\right)^2 = 1. \tag{14}$$

where u and v are rectangular coordinates. Defining the coordinate system ΔxΔy, and considering the points p_i and p_j, where p_i' is the center of the ellipse, and p_j' is obtained by rotating p_j, the equation is (Figure 26):

$$\begin{bmatrix} u_{ij} \\ v_{ij} \end{bmatrix} = \begin{bmatrix} cos\theta & sin\theta \\ -sin\theta & cos\theta \end{bmatrix} \begin{bmatrix} \Delta x_{ij} \\ \Delta y_{ij} \end{bmatrix}. \tag{15}$$

Substituting $v = \frac{v_{ij}}{u_{ij}} u$ into the ellipse equation yields:

$$\frac{u^2}{u_{ij}^2} \left(\frac{u_{ij}^2}{a_{max}^2} + \frac{v_{ij}^2}{a_{min}^2} \right) = 1 \, . \tag{16}$$

A point p located on the perimeter of the ellipse at an angle ϕ, in position *i,j* will have a distance from the center, and hence a range of the variogram of:

$$a_{\phi ij} = \frac{h_{ij} a_{max} a_{min}}{\sqrt{a_{min}^2 u_{ij}^2 + a_{max}^2 v_{ij}^2}}. \tag{17}$$

Thus, the reduced distance, which is the transformed distance, is defined as follows (Eriksson & Siska, 1999):

$$\begin{bmatrix} u'_{\phi ij} \\ v'_{\phi ij} \end{bmatrix} = \begin{bmatrix} 1/a_{max} & 0 \\ 0 & 1/a_{min} \end{bmatrix} \begin{bmatrix} cos\theta & sin\theta \\ -sin\theta & cos\theta \end{bmatrix} \begin{bmatrix} \Delta x_{ij} \\ \Delta y_{ij} \end{bmatrix}. \tag{18}$$

To properly define the variogram in the anisotropic case, the principal direction and the angle tolerance must be specified. The major direction should be chosen considering both the hydrogeologic setting and the spatial distribution of values. It is recognized as the direction along which there is maximum data continuity. The angle tolerance defines the range of angles within which points are considered to belong to the same directional bin. Typically, angle intervals of 45° are considered, with an angle tolerance of 22.5° (Deutsch , 2015).

4.5. SPATIAL INTERPOLATION: THE KRIGING METHOD

The Kriging method is one of the most common techniques used for spatial data interpolation. It is known as an optimal interpolar due to its advantageous properties:

- The interpolation results depend on nearby observations;
- The results include a quantifiable uncertainty, with the model focused on minimizing uncertainties;
- Predictions can be made about the probability of exceeding certain values;
- The resulting maps are smooth and do not exhibit discontinuities (Interstate Technology & Regulatory Council (ITRC), 2016).

In conclusion, the application of the kriging method yields a map of results expressed as mean values and a corresponding map of the errors of those values, hence its designation as an “unbiased interpolation method”. This method is flexible due to the numerous functions available to describe variogram shapes, which can be used to investigate both linear and non-linear processes. Additionally, it is highly useful for small datasets as it requires relatively few parameters (Li & Zheng, 2017).

4.5.1. TYPES OF KRIGING

Several types of Kriging exist:

- ordinary Kriging: assumes that the mean of the variable is constant but unknown;
- simple Kriging: assumes that the mean of the variable is constant and known;
- universal Kriging: assumes that the mean of the variable changes across the domain according to a specified function of location;
- indicator Kriging: provides the probability that the variable exceeds a certain threshold, resulting in binary outputs;
- probability Kriging: produces a map of the probability that the variable exceeds a certain value;

- Co-Kriging: considers two variables simultaneously based on their relationship and covariance (esri, 2021).

All Kriging methods rely on the same stationary function:

$$\hat{Z}(x) = m(x) + \varepsilon(x). \tag{19}$$

where:

- $\hat{Z}(x)$ is the mean value of the variable;
- $m(x)$ is the trend component;
- $\varepsilon(x)$ is the stochastic residual.

The value assumed by the variable Z at certain location x_0 using the Kriging method is computed as:

$$\hat{Z}(x_0) = \sum_{i=1}^{N} \lambda_i \, Z(x_i) \tag{20}$$

In this equation, $\hat{Z}(x_0)$ is expressed as weighted mean of N sampled points, where λ_i represents the weight associated with the i-th sampled point, determining is importance relative to the final value. These weights are determined using the semi-variogram, which describes how data similarity decreases with distance.

4.5.2. ORDINARY KRIGING

Ordinary kriging is particularly suitable for cases where the mean of the values changes across the domain, making it a non-stationary method. The requirements for its application are:

- the data trend should be approximated by the same function throughout the domain;
- the data should follow a normal distribution (Bostan, 2017).

Optimal results in Ordinary Kriging depend on the appropriate choice of weights, which is achieved by minimizing the error variance. This method is known as the best linear unbiased predictor, meaning the error is neither underestimated nor overestimated. Mathematically, this is expressed as the mean of the errors being equal to zero:

$$\begin{aligned} E\left[\hat{Z}(x_0)\right] - E[Z(x_0)] = E[\sum_{i=1}^{N} \lambda_i \, Z(x_i)] - E[Z(x_0)] = \\ = \sum_{i=1}^{N} \lambda_i \, E[Z(x_i)] - E[Z(x_0)] = \\ = \sum_{i=1}^{N} \lambda_i \, \mu - \mu = \\ = \mu \left(\sum_{i=1}^{N} \lambda_i - 1 \right). \end{aligned} \tag{21}$$

For the method to be unbiased, the following equation must hold true:

$$\mu \left(\sum_{i=1}^{N} \lambda_i - 1 \right) = 0. \tag{22}$$

Therefore:

$$\sum_{i=1}^{n} \lambda_i = 1. \tag{23}$$

To solve this minimization problem with constraints, the Lagrange multiplier (ν) is introduced:

$$
\begin{aligned}
F(\lambda_i, \nu) = E\left[\hat{Z}(x_0)\right] - E[Z(x_0)] + 2\nu\left(\sum_{i=1}^{N}\lambda_i - 1\right) = \\
= Var\left[\sum_{i=1}^{N}\lambda_i\, Z(x_i)\right] + Var[Z(x_0)] - 2Cov\left[\sum_{i=1}^{N}\lambda_i\, Z(x_i), Z(x_0)\right] \\
+ 2\nu\left(\sum_{i=1}^{N}\lambda_i - 1\right) = \\
= \sum_{i=1}^{N}\sum_{j=1}^{N}\lambda_i\lambda_j Cov[Z(x_i), Z(x_0)] + Var[Z(x_0)] \\
- 2\sum_{i=1}^{N}\lambda_i\, Cov[Z(x_i), Z(x_0)] + 2\nu\left(\sum_{i=1}^{N}\lambda_i - 1\right)
\end{aligned}
\tag{24}
$$

To minimize the error, the partial derivatives of the function with respect to λ_i and ν are set to zero (Franklin, 2014):

$$
\begin{aligned}
\frac{\partial F(\lambda_i, \nu)}{\partial \lambda_i} = 2\sum_{j=1}^{N}\lambda_j Cov[Z(x_i), Z(x_j)] - 2Cov[Z(x_i), Z(x_0)] + 2\nu = 0 \\
\sum_{j=1}^{N}\lambda_j Cov[Z(x_i), Z(x_j)] + \nu = Cov[Z(x_i), Z(x_0)]
\end{aligned}
\tag{25}
$$

$$
\frac{\partial F(\lambda_i, \nu)}{\partial \nu} = 2\sum_{i=1}^{N}\lambda_i - 2 = 0.
$$

This results in a system of n+1 equations for n observed values:

$$
\begin{aligned}
\sum_{i=1}^{n}\lambda_i C(x_1, x_i) + \nu = C(x_1, x_0) \\
\sum_{i=1}^{n}\lambda_i C(x_2, x_i) + \nu = C(x_2, x_0)
\end{aligned}
\tag{26}
$$

$$\vdots$$

$$\sum_{i=1}^{n} \lambda_i C(x_n, x_i) + \nu = C(x_n, x_0)$$

$$\sum_{i=1}^{n} \lambda_i = 1.$$

with C representing the covariances between the i-th and the j-th points or between the i-th point and the prediction point.
The matrix of the system results as:

$$\begin{bmatrix} C_{11} & C_{12} & \cdots & C_{1n} & 1 \\ C_{21} & C_{22} & \cdots & C_{2n} & 1 \\ \vdots & \vdots & \cdots & \vdots & \vdots \\ C_{n1} & C_{n2} & \cdots & C_{nn} & 1 \\ 1 & 1 & \cdots & 1 & 0 \end{bmatrix} \begin{bmatrix} \lambda_1 \\ \lambda_2 \\ \vdots \\ \lambda_n \\ \nu \end{bmatrix} = \begin{bmatrix} C_{10} \\ C_{20} \\ \vdots \\ C_{n0} \\ 1 \end{bmatrix}. \quad (27)$$

Using this system of equations, the weights and the Lagrange multiplier are obtained as follows (Ashtiani & Deutsch, 2024):

$$\begin{bmatrix} \lambda \\ \nu \end{bmatrix} = \begin{bmatrix} C & 1 \\ 1^T & 0 \end{bmatrix}^{-1} \begin{bmatrix} c_0 \\ 1 \end{bmatrix}. \quad (28)$$

Finally, the variance of the prediction can be derived starting from the Mean Squared Error (MSE) as follows:

$$MSE = \sum_{i=1}^{N} \sum_{j=1}^{N} \lambda_i \lambda_j Cov[Z(x_i), Z(x_j)] + Var[Z(x_0)] - 2Cov[\sum_{i=1}^{N} \lambda_i Z(x_i), Z(x_0)] \quad (29)$$

Simplifying, the result is:

$$\sum_{i=1}^{N}\sum_{j=1}^{N}\lambda_i\lambda_j Cov[Z(x_i),Z(x_j)] = \sum_{i=1}^{N}\lambda_i \sum_{j=1}^{N}\lambda_j\, Cov[Z(x_i),Z(x_j)] =$$

$$= \sum_{i=1}^{N}\lambda_i(\, Cov[Z(x_i),Z(x_0)] - \nu). \tag{30}$$

Thus, the final equation for the variance of the prediction method, which combines the variance of the sampled data with the variance of the predicted data, is given by (Franklin, 2014):

$$\sigma_{OK}^2 = \sigma^2 - \sum_{i=1}^{N}\lambda_i(\, Cov[Z(x_i),Z(x_0)] - \nu. \tag{31}$$

4.6. DEFINITION OF THE ERROR

The final step of the Kriging analysis involves assessing the reliability of the results by examining the associated error. In ArcGIS, as in many geostatistical software applications, cross-validation is used to evaluate the fit of the data.

Specifically, the "leave-one-out" method is employed. This technique involves systematically removing each known data point one at a time and comparing the predicted value from the model at that point with the actual known value. The residual error for each point is calculated as follows:

$$\varepsilon_{residual} = \hat{Z}(x_0) - Z(x_0). \tag{32}$$

This process produces a set of known errors equal to the number of observation points, providing an estimate of the overall error. This also enables the evaluation of errors in unsampled locations.

By analyzing the errors on residuals, the software calculates the following metrics:

- Mean error (ME): the average of the errors between predicted and actual values at each known point. Ideally, this value should approach zero.

$$\hat{\varepsilon} = \frac{1}{n}\sum_{i=1}^{n}\left(\hat{Z}(x_i) - Z(x_i)\right); \tag{33}$$

- Root-Mean-Square Error (RMSE): the square root of the mean of the squared differences between predicted and actual values. It indicates the reliability window of the predicted values and should be as low as possible.

$$RMSE = \sqrt{\frac{1}{n}\sum_{i=1}^{n}(\widehat{Z}(x_i) - Z(x_i))^2}; \tag{34}$$

- Mean Standardized Error (MSE): the mean of the standardized errors (error divided by the mean error). Also its value should be close to zero.

$$MSE = \frac{1}{n}\sum_{i=1}^{n}\left(\frac{\hat{Z}(x_i) - Z(x_i)}{\hat{\varepsilon}(x_i)}\right); \tag{35}$$

- Root-Mean-Square Standardized Error (RMSSE): the square root of the mean of the squared standardized errors. The optimal value is close to one.

$$RMSSE = \sqrt{\frac{1}{n}\sum_{i=1}^{n}\left(\frac{\hat{Z}(x_i) - Z(x_i)}{\hat{\varepsilon}(x_i)}\right)^2}; \tag{36}$$

- Average Standard Error (ASE): the average of the squared standard errors, providing information about the distribution of errors around the mean. Its value should be close to the RMSE.

$$ASE = \sqrt{\frac{1}{n}\sum_{i=1}^{n}\hat{\varepsilon}(x_i)^2}; \tag{37}$$

Additionally, various charts are produced to visualize the errors:

- predicted values vs measured values; it should follow the bisector (Figure 27a);

- error vs measured values; it should be flat (Figure 27b);
- standardized error vs measured values; it should be flat (Figure 27c);
- normal QQ plot, comparing standardized errors with a normal distribution; it should follow the reference line (Figure 27d);
- probability distribution plots of the errors, the measured and predicted values (esri, s.d.).

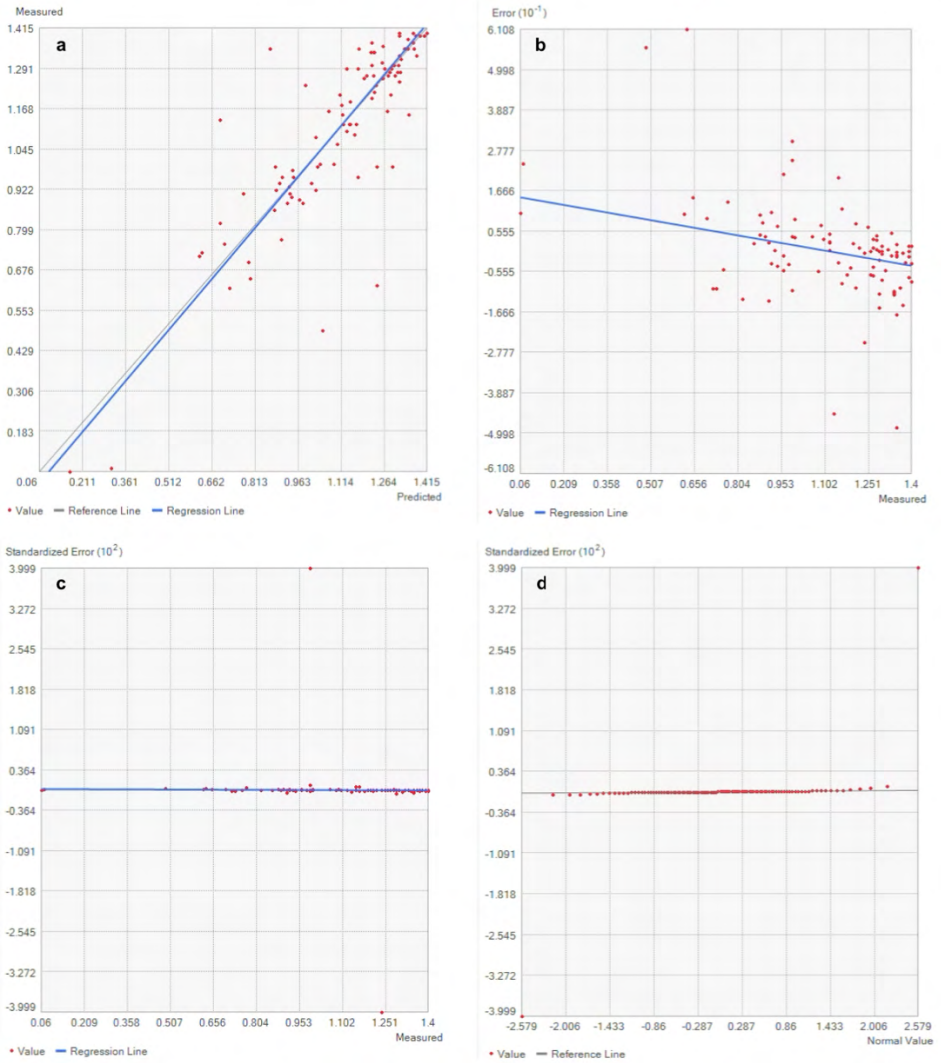

Figure 27. Plots describing errors obtained after Kriging implementation: (a) predicted values vs measured values, (b) error vs measured values, (c) standardized error vs measured values, and (d) standardized errors with versus a normal distribution.

5. RESULTS

This chapter summarizes the pollution measurements collected in the two sub-domains of interest and the outcomes of their statistical and geostatistical analyses.

Records and data processing are presented in this order. Each pollutant is analyzed according with the following list:

- total solvents;
- nitrates;
- pesticides – DACT;
- chlorides;
- sulphates;

and fore each of them the two sub-basins, i.e.:

- Vicenza high plain;
- Agno valley;

are addressed.

Irrespective of the pollutant considered, the methodological approach adopted to present the measurements, and their statistical and geostatistical analyses is the following:

- Both the sub-basins: the numerosity of the sample gathered each year (from 1981 to 2023 in the Vicenza high plain and from 1998 to 2023 in the Agno valley) is presented, followed by a basic statistical analysis with the value distribution and boxplot representations, and the computation of statistical parameters characterizing the concentration distribution in the investigated years;
- Vicenza high-plain: a geostatistical analysis through isotropic and/or anisotropic variogram and ordinary Kriging has been carried out for each pollutant with a 3-year interval starting from 1985. The data collected between 1981 and 1984 have not been processed due to the limited size of the samples. Notice that the color scale adopted in the map obtained by the Kriging interpolation is composed of two portion, from green to red and from red to black to emphasize the values below and above the maximum concentration by law, respectively. Since Kriging provides an estimation of error, error maps related to the interpolation are included;

- Agno valley: due to the narrow and elongated shape of the valley and the clustered distribution of the monitoring well (Figure 18) the geostatistical analysis cannot be developed. Therefore, the geographical distribution of the pollutant concentration has been provided through simple “post-maps” showing the spatial distribution of the original data. This graphical representation has been carried out for a few significant years only using the same color scale as adopted in the maps for the Vicenza high plain. The maps have been developed for total solvents and nitrates, that are characterized by some alarming values.

Finally, it is important to emphasize that all data were transformed using a logarithmic scale to better align with the optimal conditions for Kriging analysis. This transformation should be kept in mind, particularly when reviewing tables that present the parameter values used in interpolation and the associated errors. While the values can be compared relative to one another, they should not be interpreted in a practical sense. Moreover, the analyses have been carried out considering unique dataset for all the data available each year, irrespective of the well depth and, consequently, the aquifer from which the water has been sampled. Obviously this introduces a certain degree of uncertainty.

5.1. TOTAL SOLVENTS

5.1.1. VICENZA HIGH PLAIN

Total solvents are the first class of pollutants analyzed. The total sample size amounts to 7713. In Figure 28, the distribution of sample data over the years is depicted. The year with the fewest samples is 1982, when 8 wells were sampled, resulting in a total of 9 measurements for that year. Conversely, the year with the highest number of sampled wells is 2015, with 201 wells sampled. However, 2018 stands out as the year with the highest number of measurements, totaling 412 samples. This variation in sample density over the years provides an important context for understanding trends in solvent pollution over time.

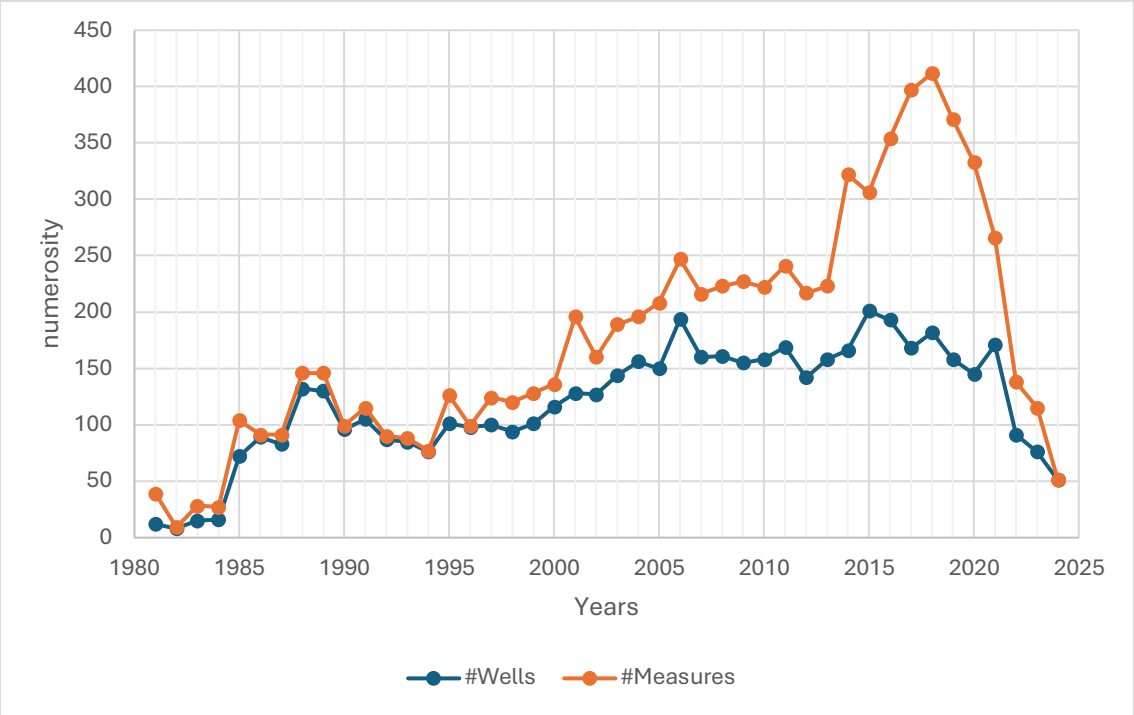

Figure 28. Total solvents, Vicenza high plain: yearly number of sampled wells and measurements between 1981 and 2023.

The concentrations of PCE and TCE recorded during the analyzed years tend to assume low values, with about 69% of the values falling below 5 µg/l. However, 18.34% of the measurements exceeded the legal limit. The numbers are confirmed by the histogram reported in Figure 29 and the boxplot in Figure 30, which reveal the highly skewed distribution of data over the 43 years period covered by the dataset.

In the boxplot, the whiskers are close to the box, and the mean does not coincide with the median, being located at the limit of the box. This effect discrepancy is due to the presence of some unusually high values.

One notable example of variability occurred in 1985, when a total solvent concentration of 382 µg/l was recorded. This value is significantly higher than the nearly null values observed in many other years.

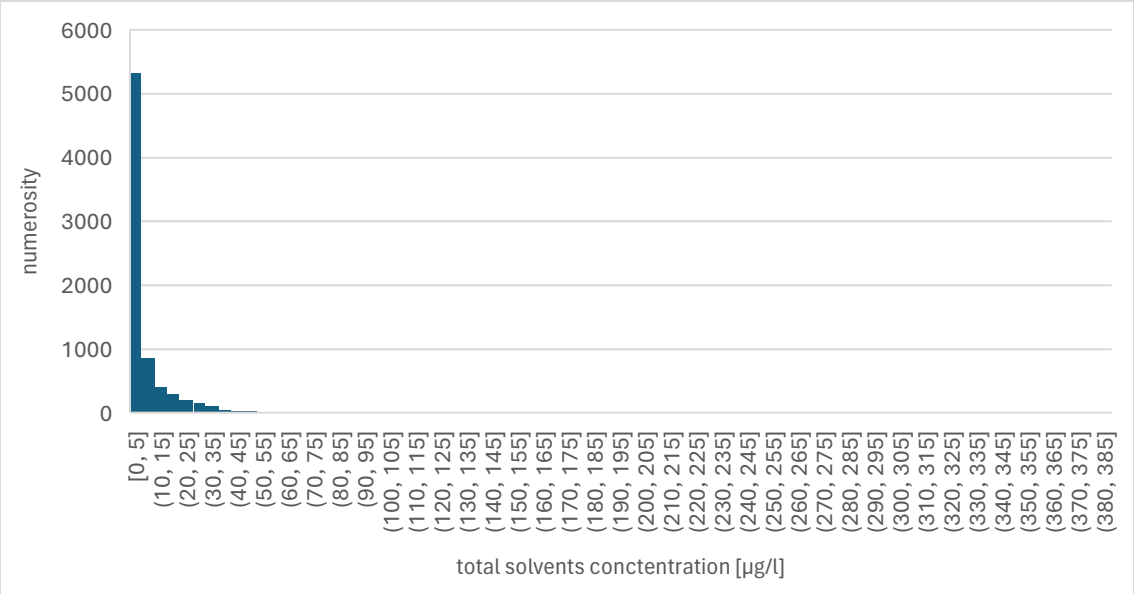

Figure 29. Total solvents, Vicenza high plain: histogram of concentration between 1981 and 2023.

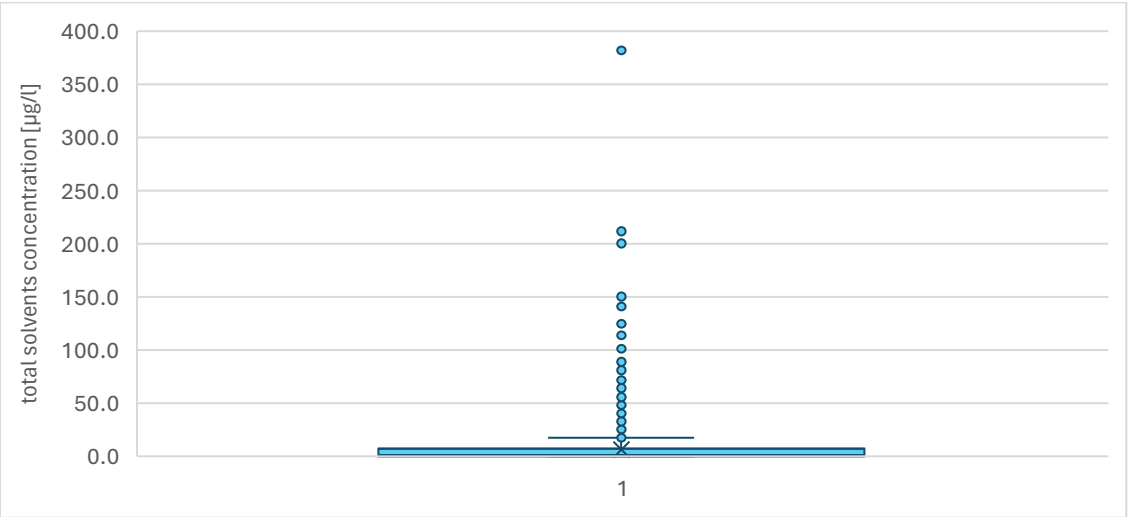

Figure 30. Total solvents, Vicenza high plain: boxplot of the concentration between 1981 and 2023.

It is crucial to understand how water quality changes over time. this has been obtained by computing descriptive statistics for each single year. This allows for a clearer understanding of the temporal evolution of contaminants in the area.

Table 1 presents the descriptive statistics calculated for the same years that are further analyzed using the Kriging method in the following.

The table underscores the table importance of distinguishing values recorded in different years, particularly with respect to the maximum values. Both the maximum and the mean values show a decreasing trend over time.

Table 1. Total solvents, Vicenza high plain: descriptive statistics of the data recorded in the selected years. the meaning of the parameters is the following:μ= mean, Q1=first quartile, Q3= third quartile, G=skewness, CV=Coefficient of Variation.

Year	μ [µg/l]	Mode [µg/l]	Q1 [µg/l]	Median [µg/l]	Q3 [µg/l]	σ^2 $[(\mu g/l)^2]$	CV [-]	G [-]	Min [µg/l]	Max [µg/l]
1985	27.69	0.00	1.86	8.03	27.14	56.75	0.27	4.30	0.00	382.00
1988	19.37	0.00	0.78	6.43	21.88	30.15	0.28	2.13	0.00	141.10
1991	13.87	0.00	0.30	3.80	26.70	18.42	0.31	1.64	0.00	101.10
1994	10.36	0.00	0.40	2.35	15.35	16.68	0.39	2.52	0.00	87.70
1997	7.62	0.00	0.00	3.00	13.13	9.45	0.40	1.30	0.00	40.50
2000	6.81	0.00	0.00	1.95	10.33	9.63	0.46	1.88	0.00	46.00
2003	6.57	0.00	0.00	1.60	9.71	9.93	0.48	1.72	0.00	44.90
2006	8.62	0.00	0.00	3.75	14.89	10.47	0.38	1.16	0.00	49.00
2009	5.40	0.00	0.00	1.00	7.00	8.14	0.53	1.74	0.00	34.20
2012	3.69	0.00	0.00	1.00	5.83	5.30	0.62	1.71	0.00	22.00
2015	2.92	0.00	0.00	0.57	4.00	4.80	0.75	2.28	0.00	25.00
2018	1.15	0.00	0.00	0.00	1.44	2.35	1.33	3.26	0.00	15.93
2021	2.29	0.00	0.25	1.09	3.38	5.46	1.02	10.52	0.00	68.25
2022	1.86	0.00	0.00	0.93	2.89	2.57	0.86	2.09	0.00	11.08
2023	1.09	0.00	0.00	0.59	1.61	1.39	1.08	1.50	0.00	5.71

Once the values assumed by the parameters have been considered, it is crucial to evaluate the quality of the data for the application of Kriging interpolation. This involves assessing the distribution and reliability of the data, as well as the consistency of the dataset, to ensure that the Kriging method will yield accurate and meaningful spatial predictions.

Inspection of Table 1 reveals that the dataset is characterized by a high skewness coefficient, which always exceeds 1, even reaching 10.52 in 2021. Also, mean, mode and median are always different with quite values, with the variation coefficient increasing over time.

Because of that, it is crucial to convert data with a logarithmic transformation and assess the impact of the distribution shape. The impact of the values transformation is pointed out by the summary statistics in Table 2. It can be observed that in many years the log-

transformation produces a positive effect, particularly on skewness. For example, a value of G of 0.13 is computed for the year 2006.

Table 2. Total solvents, Vicenza high plain: descriptive statistics of the log-transformed data in the selective years.

Year	μ [μg/l]	Mode [μg/l]	Q1 [μg/l]	Median [μg/l]	Q3 [μg/l]	σ^2 $[(\mu g/l)^2]$	CV [-]	G [-]	Min [μg/l]	Max [μg/l]
1985	0.99	0.00	0.46	0.96	1.45	0.63	0.80	0.28	0.00	2.58
1988	0.86	0.00	0.25	0.87	1.36	0.65	0.94	0.27	0.00	2.15
1991	0.77	0.00	0.11	0.68	1.44	0.64	1.04	0.21	0.00	2.01
1994	0.67	0.00	0.15	0.52	1.21	0.58	1.15	0.48	0.00	1.95
1997	0.64	0.00	0.00	0.60	1.15	0.54	1.15	0.14	0.00	1.62
2000	0.58	0.00	0.00	0.47	1.05	0.52	1.24	0.39	0.00	1.67
2003	0.54	0.00	0.00	0.41	1.03	0.54	1.37	0.52	0.00	1.66
2006	0.67	0.00	0.00	0.68	1.20	0.56	1.11	0.13	0.00	1.70
2009	0.50	0.00	0.00	0.30	0.90	0.51	1.44	0.56	0.00	1.55
2012	0.43	0.00	0.00	0.30	0.83	0.80	0.21	0.43	0.00	1.36
2015	0.36	0.00	0.00	0.19	0.70	0.42	1.79	0.79	0.00	1.41
2018	0.20	0.00	0.00	0.00	0.39	0.30	2.72	1.43	0.00	1.23
2021	0.37	0.00	0.10	0.32	0.64	0.31	1.48	0.80	0.00	1.84
2022	0.33	0.00	0.00	0.29	0.59	0.32	1.71	0.64	0.00	1.08
2023	0.24	0.00	0.00	0.20	0.42	0.25	2.05	0.68	0.00	0.83

The boxplot of the log-transformed values is shown in Figure 31. Comparison with Figure 30 highlights the effectiveness of the log-transformation, with only two values falling out the whiskers. The boxplot reveals a wider distribution, indicating greater variability in the dataset. However, the distribution remains right-skewed, although the asymmetry is less pronounced.

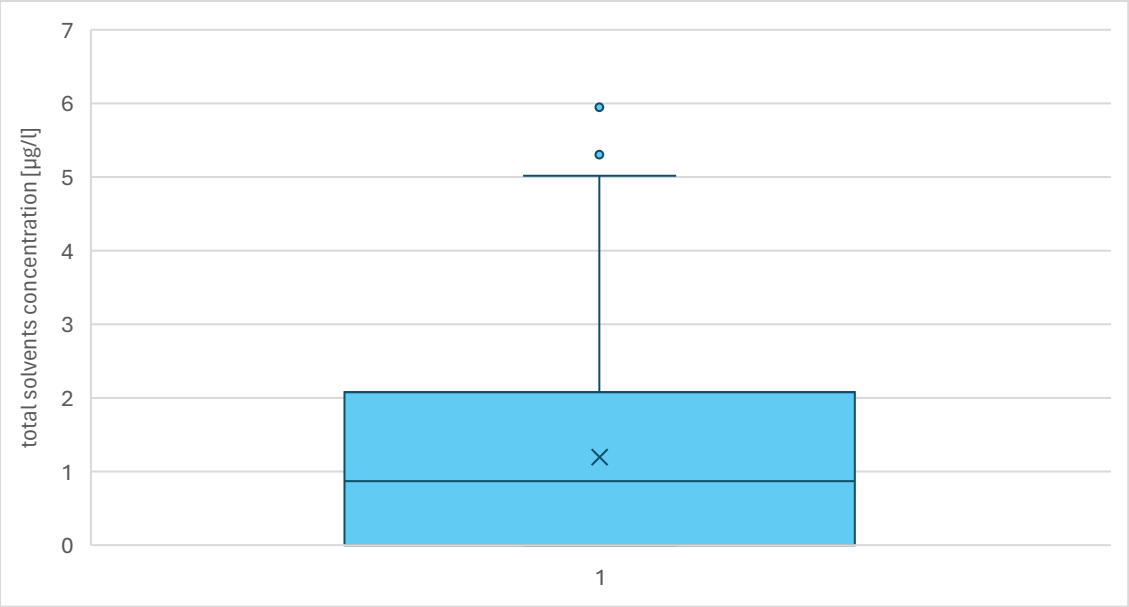

Figure 31. Total solvents, Vicenza high plain: boxplot of the log-transformed concentration between 1981 and 2023.

As observed, the logarithmic transformation yields satisfactory results in shaping the distribution closer to a normal distribution. This ensures that Kriging is the best predictor among all unbiased predictors, with the possibility of quantifying quantile and error maps in ordinary and universal Kriging application. Therefore, log-transformed data have been used in the geostatistical analysis.

In the case of the sum of tri- and tetrachloroethenes records, it may be challenging to identify measurement errors due to the relatively high number of null values. However, data points largely above legal limits and null values are significant numbers confirmed by the time series and by values recorded at nearby points. Therefore, null values have been shift to the value 1 before the log-transformation to keep properly into account the low value of these measurements.

The only discarded value refers to the measure recorded on May 4th, 2006, at the VIMC-11 well (in Figure 32), where a reading of 0 µg/l was detected. However, Figure 33, shows that this value does not align with the historical series for this well and, consequently, has been excluded from the analysis.

Figure 32 highlights the wells that will undergo further inspection.

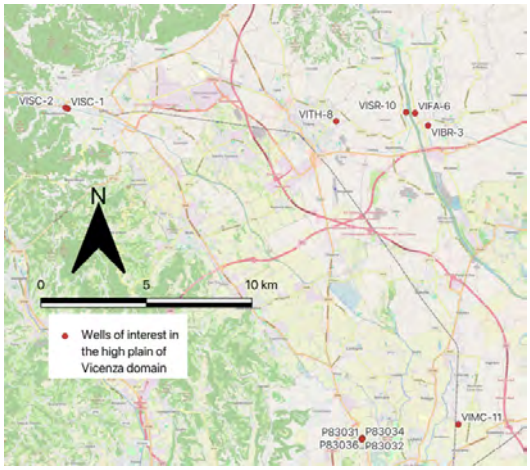

Figure 32. Vicenza high plain: wells to be inspected in the analysis.

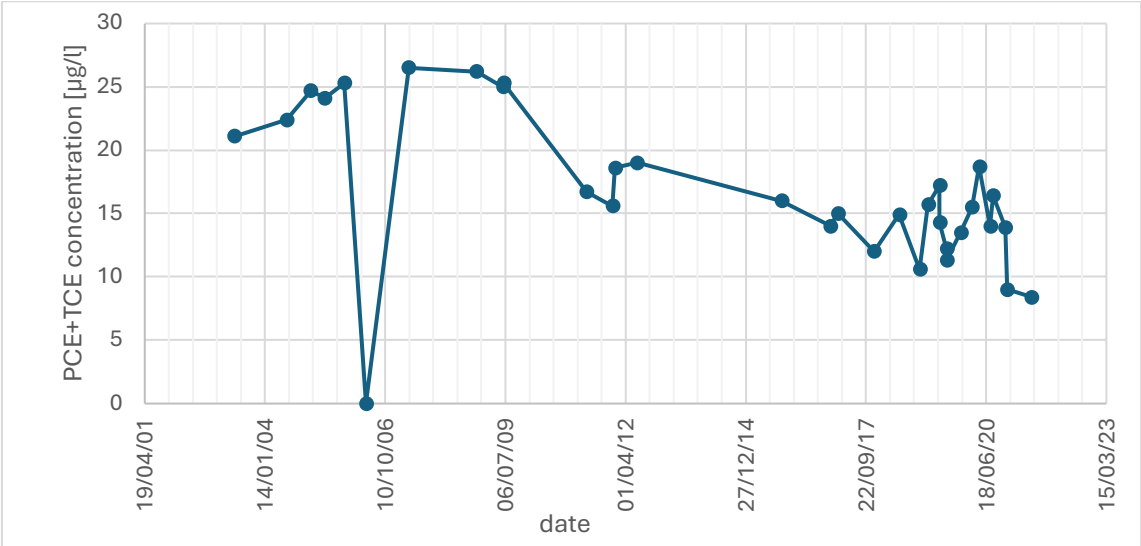

Figure 33. time series of total solvents recorded in the VIMC-11 well. The well location is provided in Figure 30.

The information of specific aquifer layer intercepted by the various wells allows to compare the contaminant trends in the various units of the aquifer system. The results are presented in Figure 34 where the average value of the total solvents concentration in each aquifer is plotted versus time. Notice the general decrease of the concentration over time, in agreement with the dataset provided in Table 1. Moreover, there is a gap in the records from the multi-aquifer system between 1990 and 1994, an the least well documented aquifers are the fist, the second and the fifth ones. The fourth and the undifferentiated aquifers typically show the highest concentrations, while the deepest, the sixth, along with the second aquifer are the least polluted.

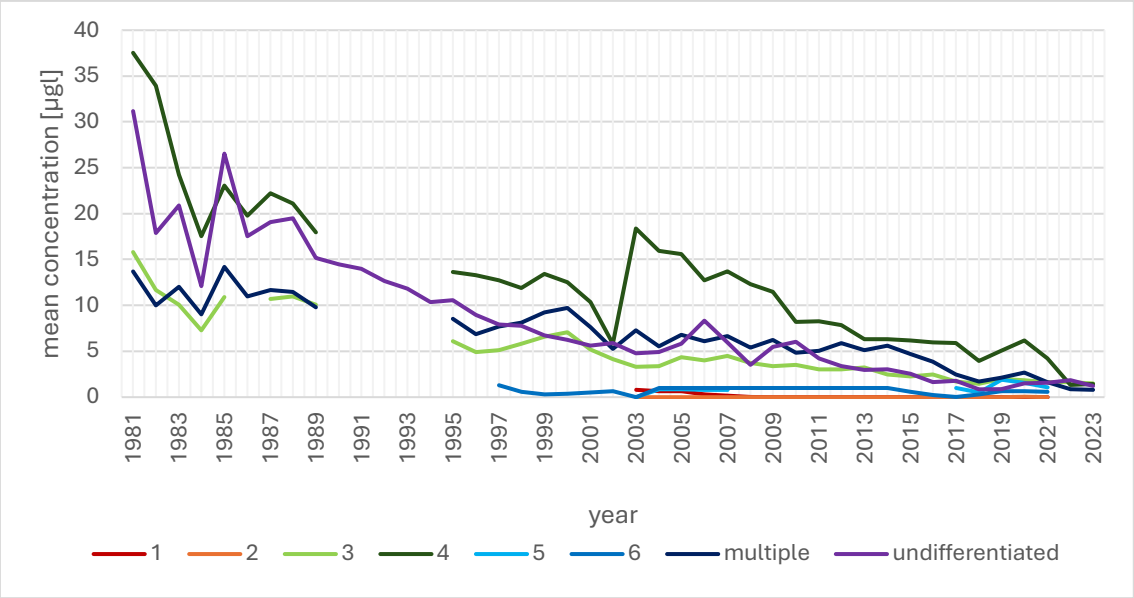

Figure 34. Total solvents, Vicenza high plain: concentration trend in each aquifer layer. The numbers 1 to 6 refer to the aquifers composing the multi-aquifer system, from the shallower to the deeper one; "undifferentiated" refers to the phreatic aquifer in the high plain to the north of the spring line; "multiple" refers to wells where the intakes tap different aquifers. The number of wells in each aquifer is the following: confined aquifer 1: 4 wells; confined aquifer 2: 1 well; confined aquifer 3: 3 wells; confined aquifer 4: 24 wells; confined aquifer 5: 1 well; confined aquifer 6: 1 well; multiple confined aquifers: 15 wells, undifferentiated aquifer:853 wells.

Table 3 provides the variogram model built up from the log-transformed data assuming an isotropic distribution.

Table 3. Total solvents, Vicenza high plain: variogram model for each of the selcted year with the assumption of isotropic distribution.

Isotropic analysis							
Year	**Mean dist [m]**	**Model**	**Lag [m]**	**Nugget**	**Partial Sill**	**Range [m]**	**RMSE**
1985	728.31	Spherical	1163.2	0.0360	0.42	5638.09	0.50
1988	695.83	Spherical	1017.9	0.1500	0.30	5564.15	0.50
1991	722.84	Spherical	1200.0	0.1260	0.30	5439.43	0.49
1994	875.98	Exponential	1688.8	0.0000	0.17	20265.80	0.49
1997	847.99	Spherical	1000.0	0.0020	0.27	3550.34	0.41
2000	760.00	Spherical	1200.0	0.0130	0.27	4378.61	0.37
2003	783.19	Spherical	1200.0	0.0003	0.31	38866.26	0.30
2006	568.28	Exponential	1000.0	0.0060	0.35	8875.00	0.30
2009	620.48	Spherical	1000.0	0.0130	0.25	5128.72	0.26

2012	651.20	Spherical	1000.0	0.0100	0.19	3445.84	0.25
2015	489.51	Spherical	800.0	0.0100	0.14	2615.70	0.21
2018	605.34	Spherical	1000.0	0.0085	0.09	4883.21	0.17
2021	391.20	Spherical	700.0	0.0050	0.09	5149.75	0.13
2022	1050.44	Spherical	1500.0	0.0300	0.08	8653.14	0.18
2023	1129.97	Spherical	1800.0	0.0130	0.07	18778.26	0.12

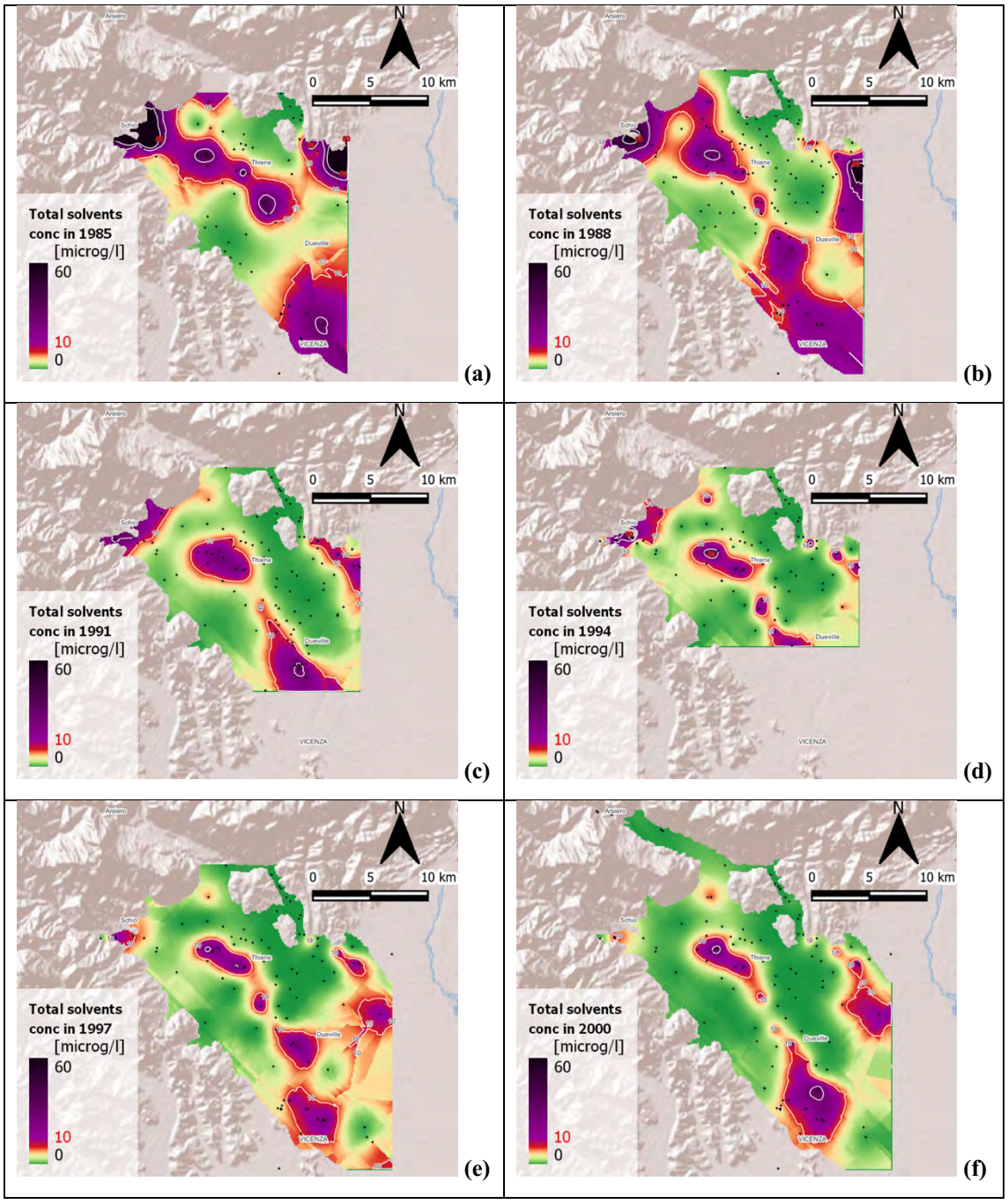

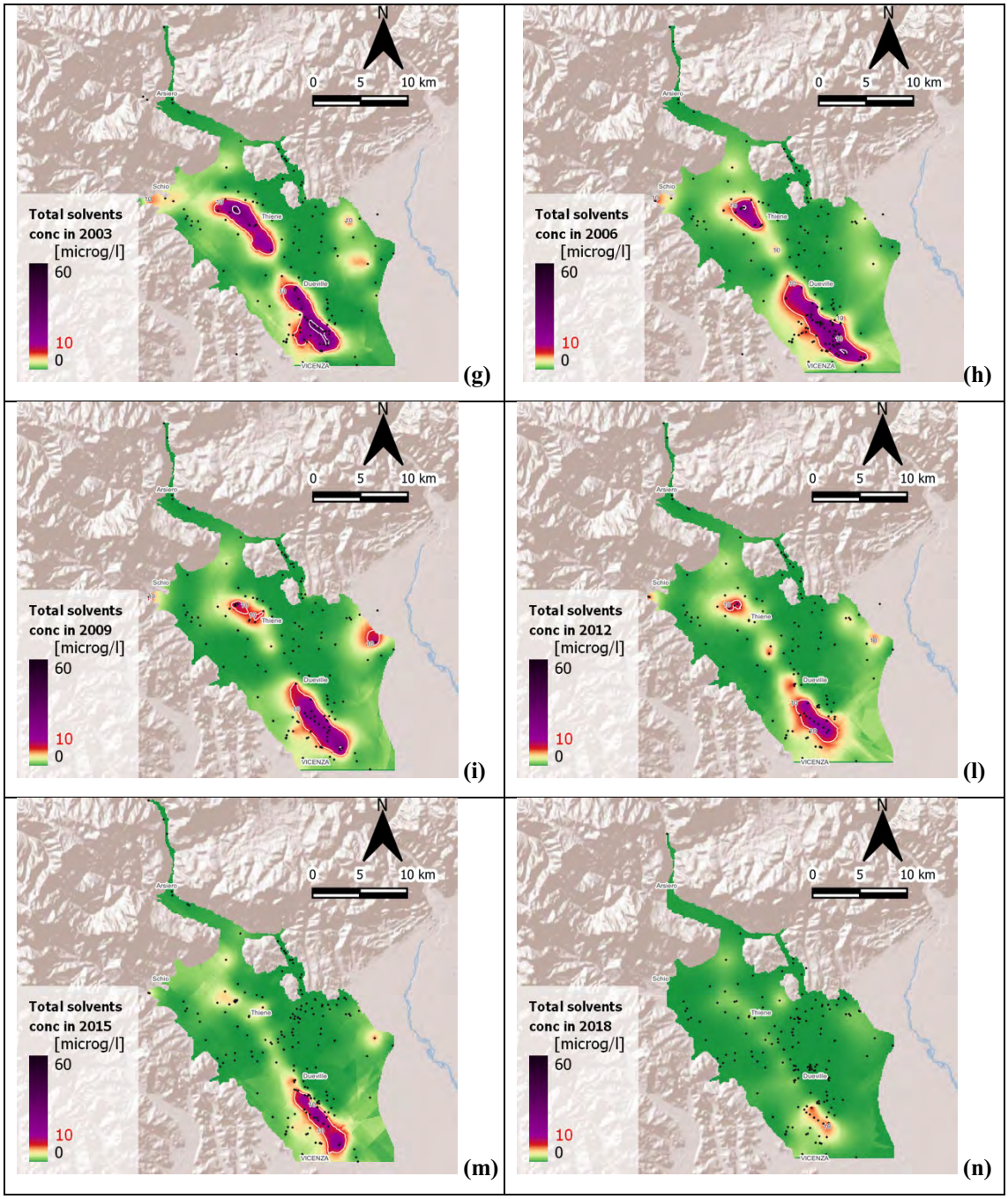
N
0 5 10 km
Total solvents conc in 2003 [microg/l]
60
10
0
(g)
Total solvents conc in 2006 [microg/l]
60
10
0
(h)
Total solvents conc in 2009 [microg/l]
60
10
0
(i)
Total solvents conc in 2012 [microg/l]
60
10
0
(l)
Total solvents conc in 2015 [microg/l]
60
10
0
(m)
Total solvents conc in 2018 [microg/l]
60
10
0
(n)

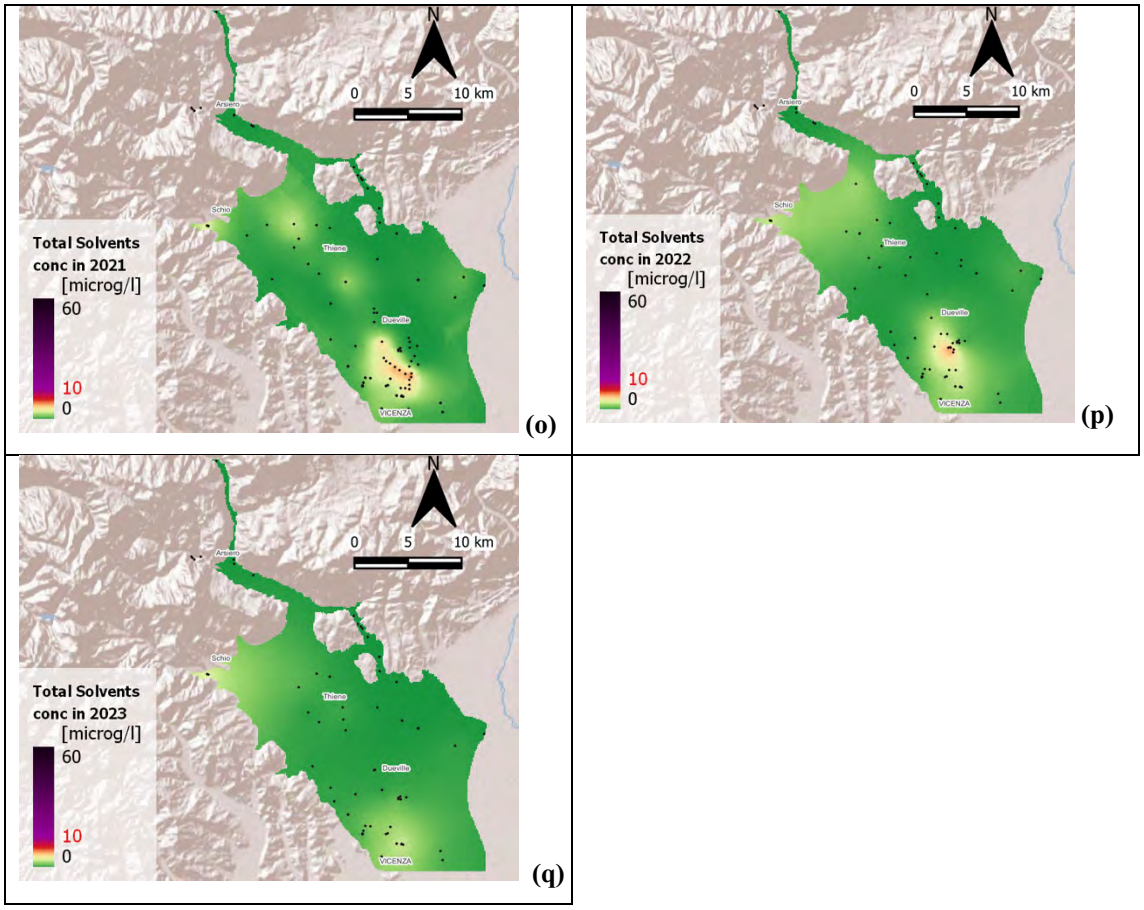

Figure 35. Total solvents, Vicenza high plain: maps of the expected values resulting from Kriging interpolation with isotropic variogram for the years (a) 1985, (b) 1988, (c) 1991, (d) 1994, (e) 1997, (f) 2000, (g) 2003, (h) 2006, (i) 2009, (l) 2012, (m) 2015, (n), (o) 2021, (p) 2022, and (q) 2023. Map extension can vary depending on well availability. The black dots represent the locations of the wells used to build-up the map. The red number in the legend represents the max concentration admissible by law.

Figure 35 provides the map of the expected value of total solvents as generated by Kriging for the 15 selected years. For the years 1988, 2000, 2012 and 2023 the maps of the standard deviation are provided in Figure 36. Notice that the maps cover different areal extension in relation to the wells with available information. It should be noted that, especially in 1997 and 2000, the concentration distribution in the southeastern part of the domain is characterized by a non-physical pattern due to the lack of measurements associated with large concentration gradient in the surrounding wells. Notice also in Figure 36(d) how the map of the standard deviation associated to the expected concentration for the year 2023 is characterized by a uniform pattern with values much smaller than in the other cases. Since the number of monitoring wells remain unchanged since the 2010s, this is due to the uniformly small concertation recorded in all the wells in 2023.

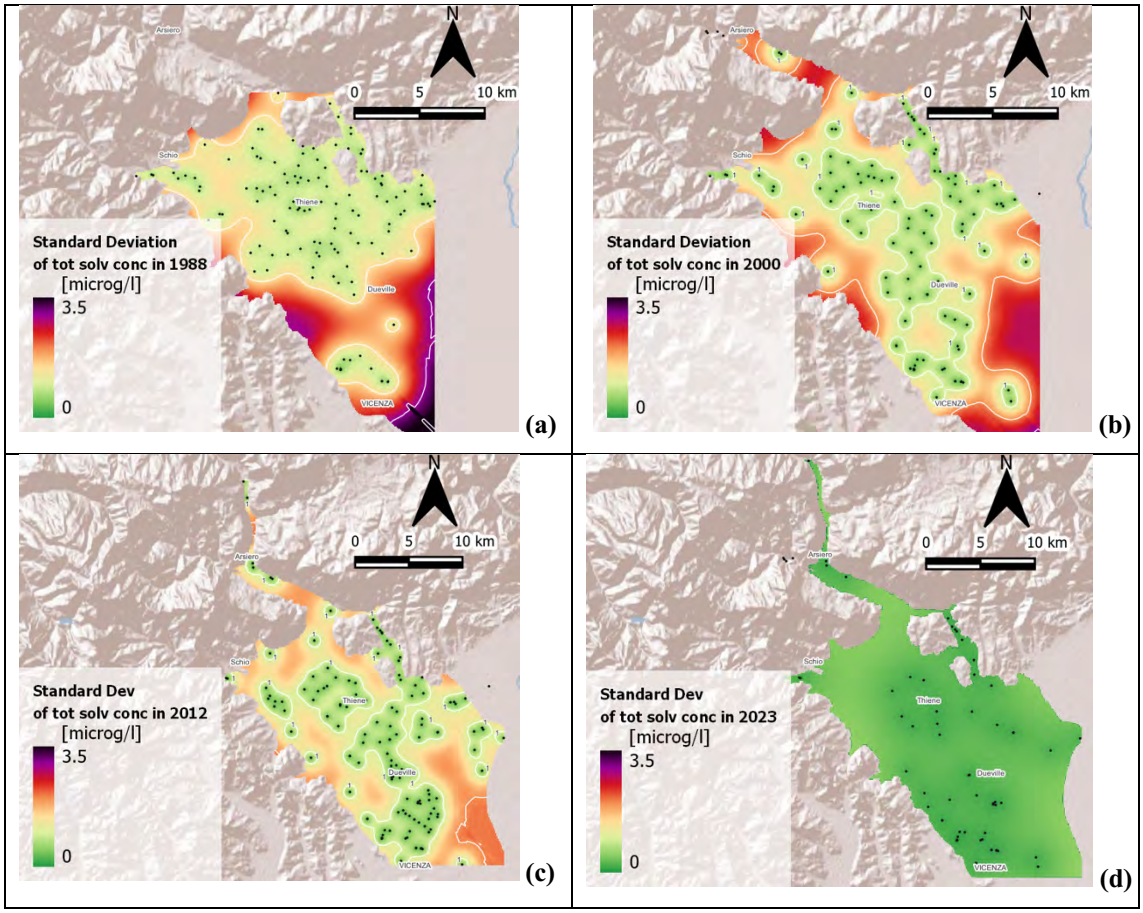

Figure 36. Total solvents, Vicenza high plain: maps of the standard deviation resulting from Kriging interpolation with isotropic variogram for the years (a) 1988, (b) 2000, (c) 2012, and (d) 2023. Map extension can vary depending on well availability. The black dots represent the locations of the wells used to build-up the map.

A second analysis has been carried out with the option of an anisotropic variogram, as suggested by the dataset. This condition seems also physically acceptable as the ground water flow in this sub-basin is mainly oriented along the north-west to south-east direction (Figure 4), and consequently this would be the main direction of pollutant fate as well. The parameters of the anisotropic variogram for each of the investigated year are provided in Table 4.

Table 4. Total solvents, Vicenza high plain: variogram model for each of the selected year with the assumption of anisotropic distribution.

Anisotropic analysis								
Year	**Model**	**Lag [m]**	**Preferential angle [°]**	**Nugget**	**Sill**	**Major range [m]**	**Minor range [m]**	**RMSE**
1985	Spherical	1163.2	135.0	0.0450	0.42	8008.03	4639.47	0.48
1988	Spherical	1017.9	152.8	0.1500	0.31	12215.18	4268.60	0.49
1991	Exponential	1000.0	149.2	0.0700	0.35	12000.00	2725.80	0.49
1994	Exponential	1688.8	135.0	0.1200	0.25	12000.00	5281.00	0.48
1997	Spherical	1000.0	150.0	0	0.31	13000.00	3500.00	0.38
2000	Exponential	1000.0	145.0	0	0.28	10000.00	2908.83	0.33
2003	Spherical	1200.0	143.3	0	0.31	9110.54	3053.62	0.28
2006	Exponential	1000.0	132.0	0.0020	0.33	12000.00	4809.20	0.29
2009	Spherical	1000.0	138.0	0.0040	0.27	10276.4	3441.20	0.25
2012	Spherical	1000.0	138.0	0.0040	0.21	8000.00	2700.00	0.24
2015	Spherical	800.0	136.4	0.0170	0.14	6500.00	2200.00	0.19
2018	Spherical	1000.0	130.0	0.0100	0.08	11000.00	3600.00	0.17
2021	Spherical	700.0	136.0	0.0036	0.09	8400.00	3000.00	0.11
2022	Spherical	1500.0	147.0	0.0100	0.10	11000.00	3700.00	0.17
2023	Spherical	1800.0	135.0	0.0100	0.07	18000.00	13000.00	0.12

Figure 37 provides the map of the expected value of total solvents as generate by Kriging for the 15 selected years using the anisotropic variogram models provided in Table 4. For the years 1988, 2000, 2012 and 2023 the maps of the standard deviation are provided in Figure 38. Notice that, conversely from the cases with isotropic variogram model, here the concentration distribution in the southeastern part of the domain is not characterized by an unphysical pattern.

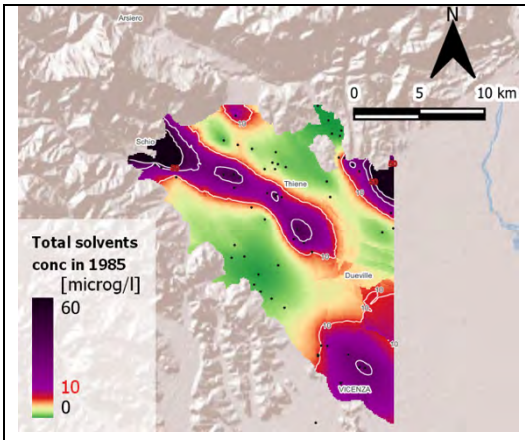
Arsiero
N
0 5 10 km
Schio
Thiene
Dueville
VICENZA
Total solvents
conc in 1985
[microg/l]
60
10
0

(a)

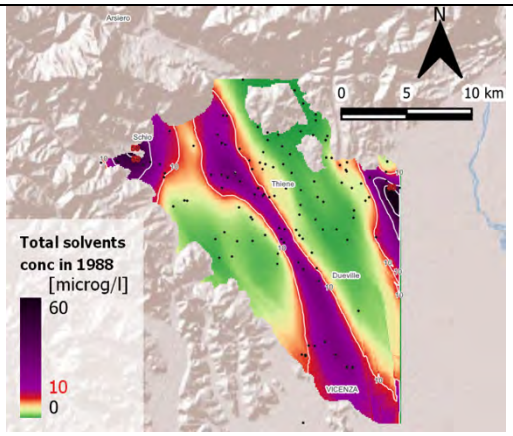
Arsiero
N
0 5 10 km
Schio
Thiene
Dueville
VICENZA
Total solvents
conc in 1988
[microg/l]
60
10
0

(b)

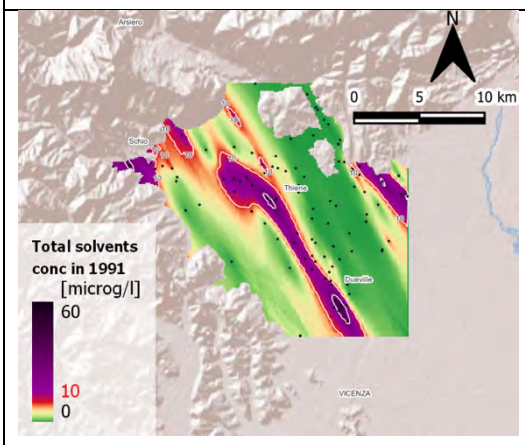
Arsiero
N
0 5 10 km
Schio
Thiene
Dueville
VICENZA
Total solvents
conc in 1991
[microg/l]
60
10
0

(c)

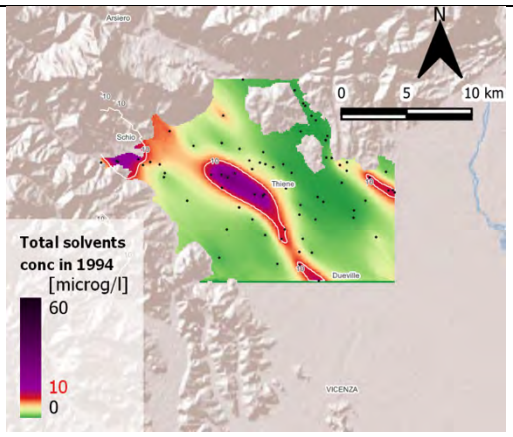
Arsiero
N
0 5 10 km
Schio
Thiene
Dueville
VICENZA
Total solvents
conc in 1994
[microg/l]
60
10
0

(d)

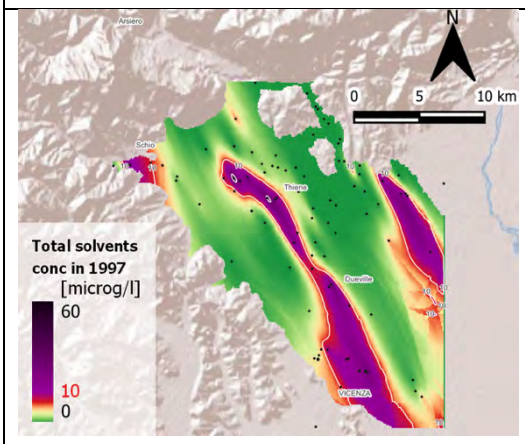
Arsiero
N
0 5 10 km
Schio
Thiene
Dueville
VICENZA
Total solvents
conc in 1997
[microg/l]
60
10
0

(e)

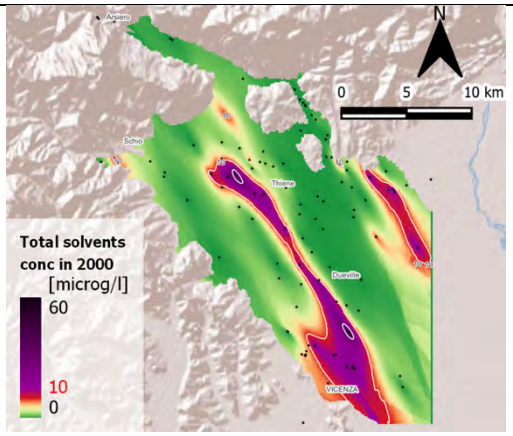
Arsiero
N
0 5 10 km
Schio
Thiene
Dueville
VICENZA
Total solvents
conc in 2000
[microg/l]
60
10
0

(f)

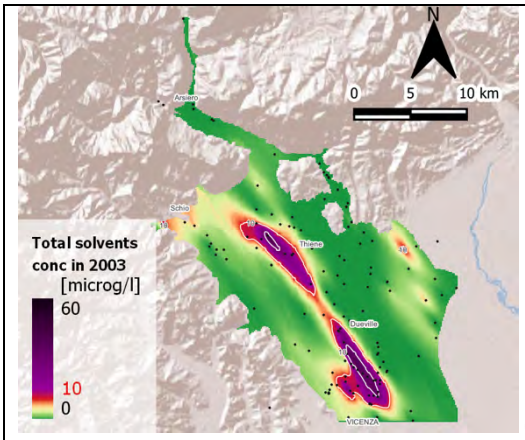
N
0 5 10 km
Total solvents conc in 2003 [microg/l]
60
10
0
Arsiero
Schio
Thiene
Dueville
VICENZA

(g)

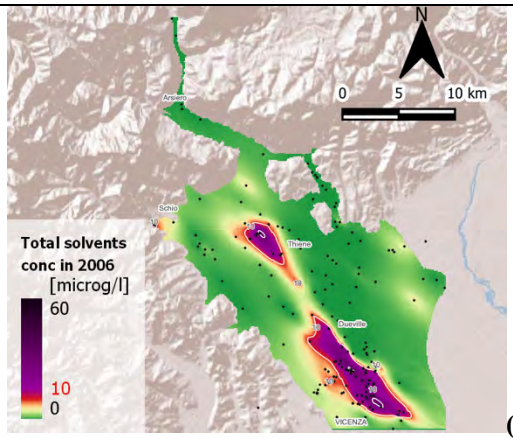
N
0 5 10 km
Total solvents conc in 2006 [microg/l]
60
10
0
Arsiero
Schio
Thiene
Dueville
VICENZA

(h)

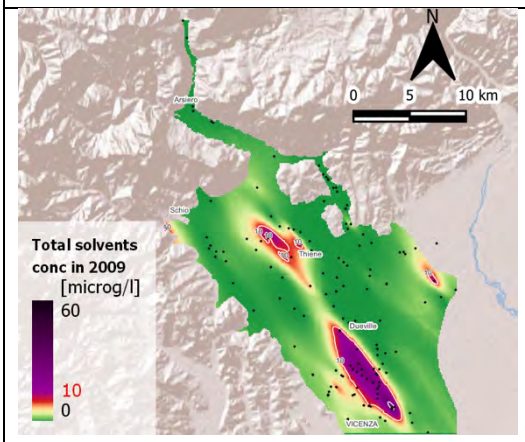
N
0 5 10 km
Total solvents conc in 2009 [microg/l]
60
10
0
Arsiero
Schio
Thiene
Dueville
VICENZA

(i)

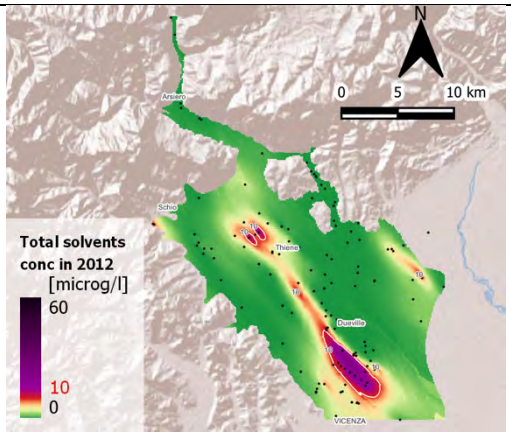
N
0 5 10 km
Total solvents conc in 2012 [microg/l]
60
10
0
Arsiero
Schio
Thiene
Dueville
VICENZA

(l)

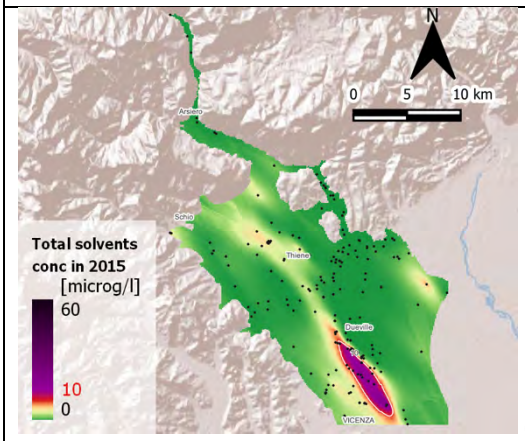
N
0 5 10 km
Total solvents conc in 2015 [microg/l]
60
10
0
Arsiero
Schio
Thiene
Dueville
VICENZA

(m)

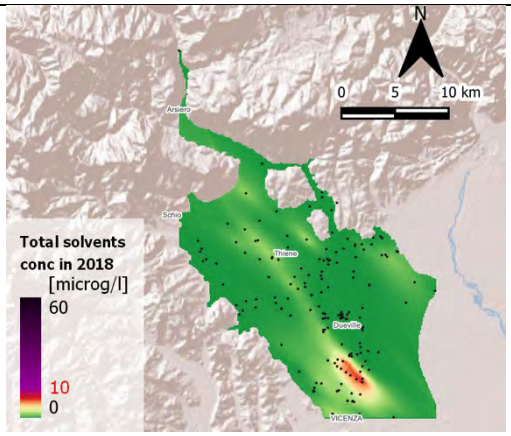
N
0 5 10 km
Total solvents conc in 2018 [microg/l]
60
10
0
Arsiero
Schio
Thiene
Dueville
VICENZA

(n)

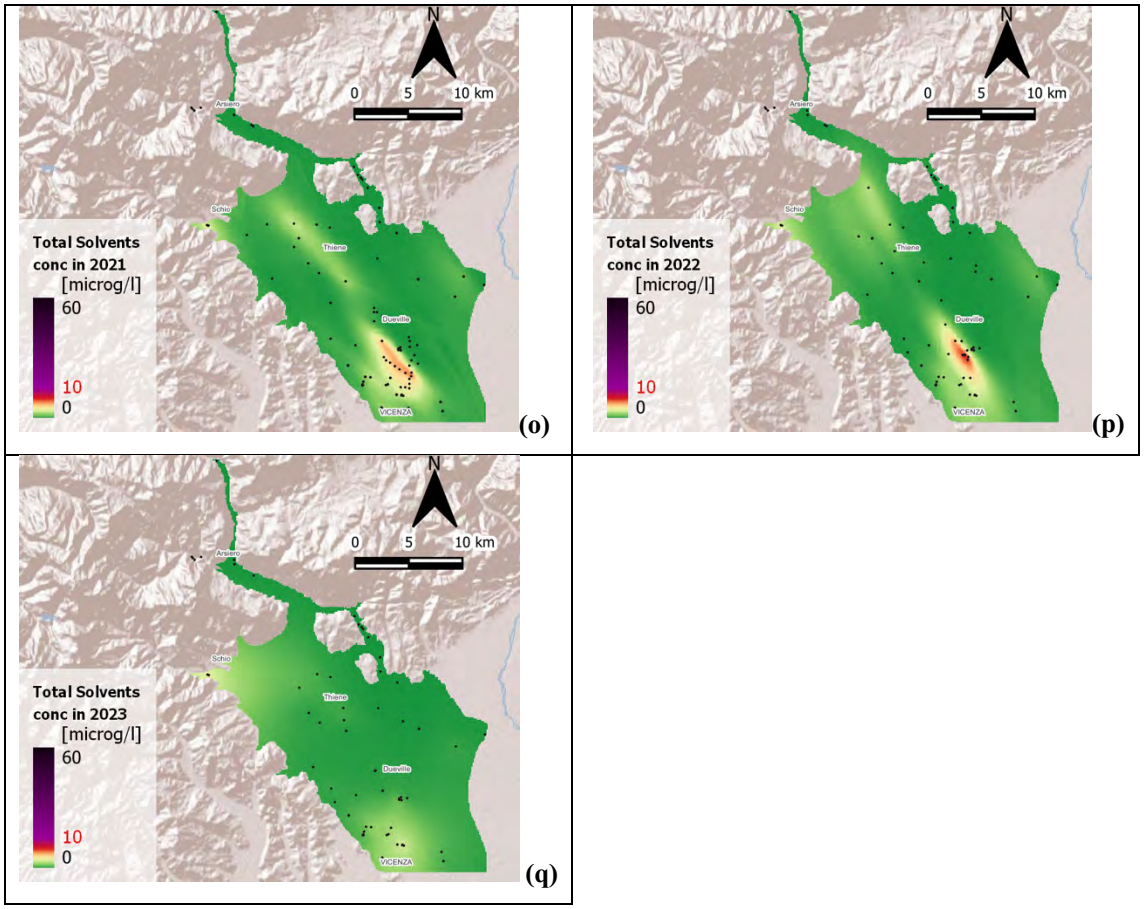

Figure 37. Total solvents, Vicenza high plain: maps of the expected values resulting from Kriging interpolation with anisotropic variogram for the years (a) 1985, (b) 1988, (c) 1991, (d) 1994, (e) 1997, (f) 2000, (g) 2003, (h) 2006, (i) 2009, (l) 2012, (m) 2015, (n) 2018, (o) 2021, (p) 2022, and (q) 2023. Map extension can vary depending on well availability. The black dots represent the locations of the wells used to build-up the maximum concentration admissible by law.

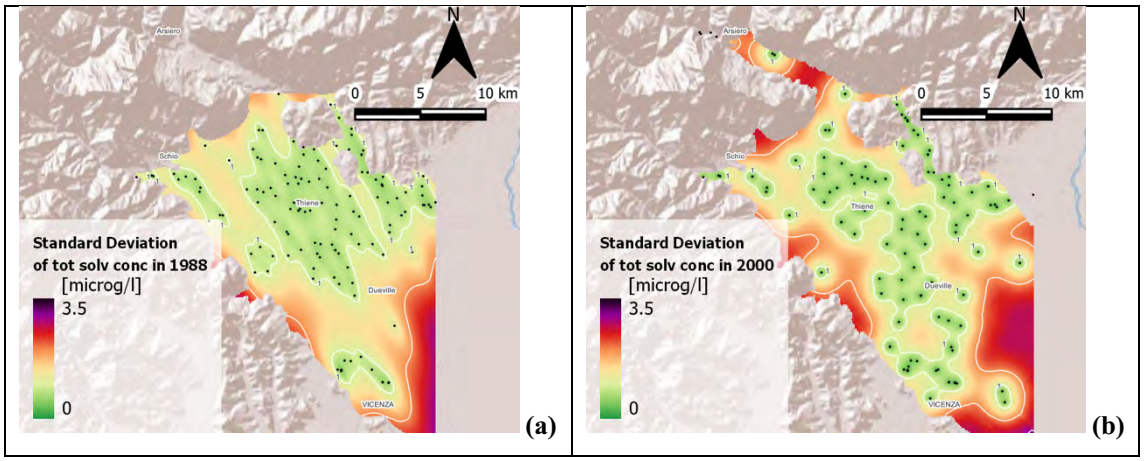

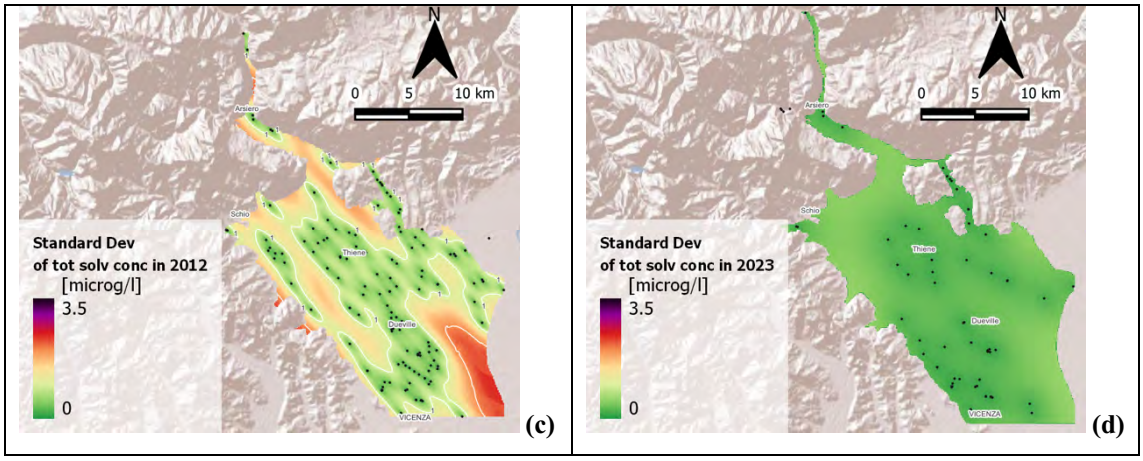

Figure 38. Total solvents, Vicenza high plain: maps of the standard deviation resulting from Kriging anisotropic variogram for the years (a) 1988, (b) 2000, (c) 2012, and (d) 2023. Map extension can vary depending on well availability. The black dots represent the locations of the wells used to build-up the map.

5.1.2. AGNO VALLEY

As reported in the introductive part of the chapter, in the second sub-domain the datasets have been characterized from the statistical point of view only.

Figure 39 compares the behavior over time of the number of measurements with the number of sampled wells.

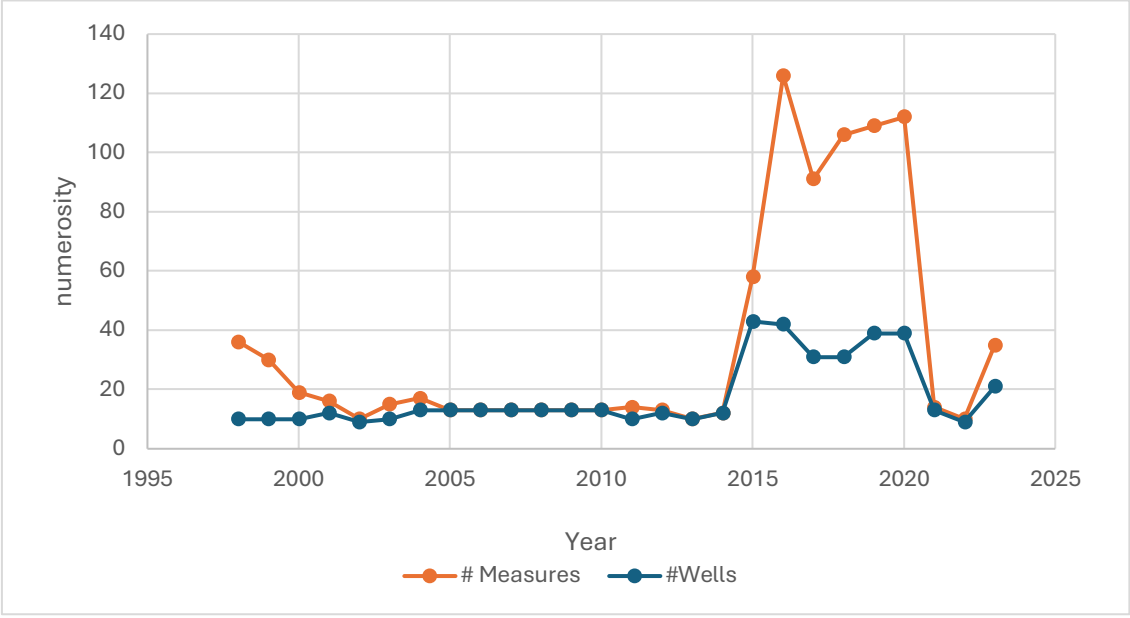

Figure 39. Total solvents, Agno valley: yearly number of sampled wells and measurements between 1998 and 2023.

The figure shows that the number of measurements and sampled wells remained scares until 2014, with less than 14 location. The number of samples/well increased significantly to more than 80 form 2016 to 2020 to decrease again in the range of 20-30 over the last three years (2021-2023).The increase is due to a five-year investigation conducted by the Strada Pedemontana Veneta organization to monitor water quality during the construction of the highway infrastructure. The total sample size amounts to 908. Although the valley is relatively narrow the number of sampling points is relatively small poorly distributed across the domain (Figure 18), the sample size is considered sufficient to provide a reliable indication of water quality.

The distribution of all values recorded from 1998 to 2023 is reported in the histogram of Figure 40 and Figure 41.

As noted in the Vicenza high plain, the values tend to be close to zero; however non exceeds the law limit. Unsurprisingly, the box in the boxplot is narrow and positioned well below 1 µg/l. Additionally, the plot highlights the discrepancy between the position of the mean and of the median, despite both are relatively small.

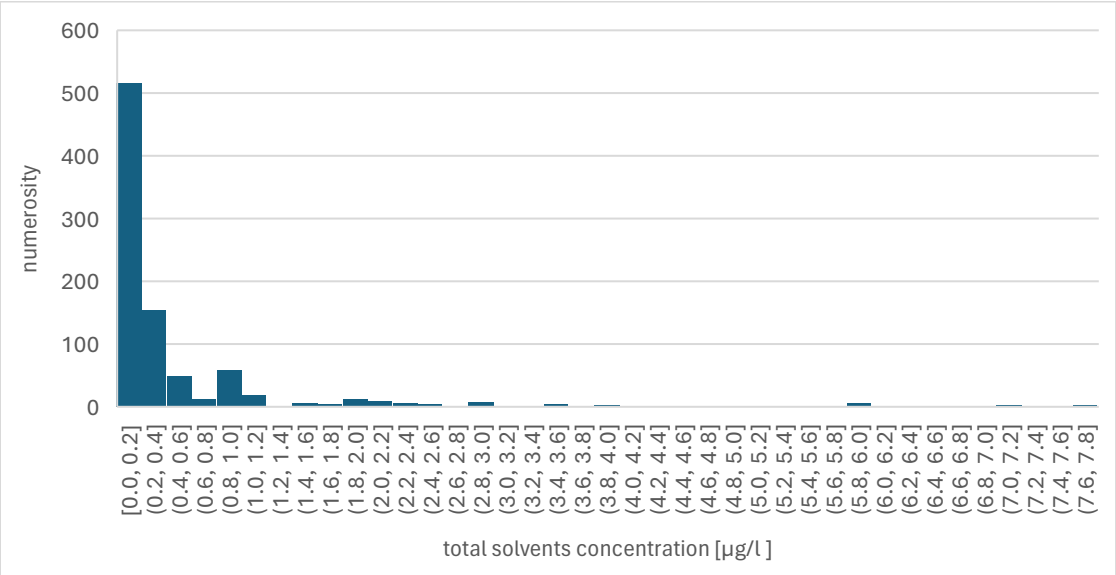

Figure 40. Total solvents, Agno valley: histogram of concentration data between 1998 and 2023.

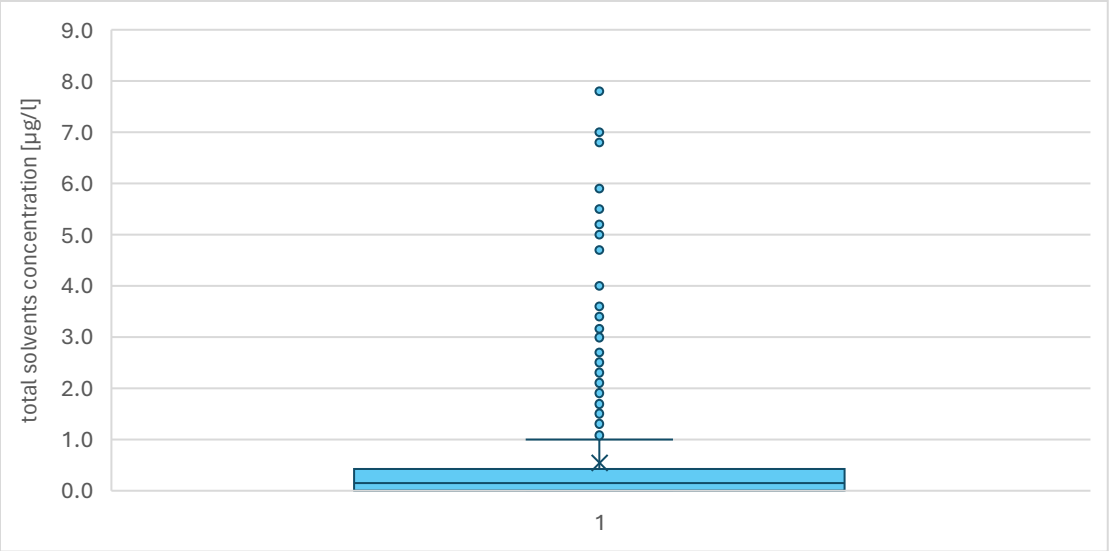

Figure 41. Total solvents, Agno valley: boxplot of the concentration between 1998 and 2023.

Table 5 shows the descriptive statistics calculated for the selected years (every 3 years).

Table 5. Total solvents, Agno valley: descriptive statistics of data recorded in the selected years.

Year	μ [µg/l]	Mode [µg/l]	Q1 [µg/l]	Median [µg/l]	Q3 [µg/l]	σ^2 $[(\mu g/l)^2]$	CV [-]	G [-]	Min [µg/l]	Max [µg/l]
1998	2.08	0.00	0.56	1.40	2.19	2.42	0.75	1.57	0.00	7.45
2001	1.26	0.00	0.00	0.93	1.90	1.46	0.96	1.33	0.00	4.70
2003	1.47	0.00	0.15	1.08	1.35	1.86	0.93	1.83	0.00	5.90
2006	1.00	0.00	0.00	0.00	1.00	1.73	1.32	2.39	0.00	6.00
2009	0.92	0.00	0.00	0.00	1.00	1.66	1.39	2.74	0.00	6.00
2012	0.75	0.00	0.00	0.00	1.00	1.22	1.47	2.03	0.00	4.00
2015	0.27	0.00	0.00	0.07	0.27	0.58	2.86	3.67	0.00	3.00
2017	0.25	0.00	0.01	0.25	0.35	0.25	1.98	1.64	0.00	1.14
2020	0.33	0.00	0.02	0.21	0.40	0.61	2.39	4.80	0.00	3.74
2023	0.66	0.00	0.00	0.31	0.63	1.19	1.65	2.83	0.00	4.86

Notice the significant gap between the mean and the median, as well as the high skewness, values, particularly in recent years when the number of samples increased.

Finally, Figure 42 provides the map of the recorded values for year 2018. If more than one sample is available in a single well, the value shown in the figure correspond to the average.

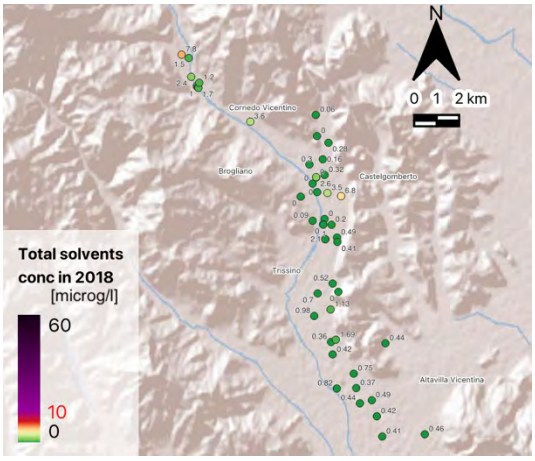

Figure 42. Total solvents, Agno valley: distribution of the measured concentration in the year 2018. Notice that the color legend used to represent the measurements is consistent with that used for the Vicenza high plain (Figure 35 and 37).

5.2. NITRATES

5.2.1. VICENZA HIGH PLAIN

Figure 43 shows the number of sampled points and the number of measurements, confirming the earlier observation of data scarcity prior 1985. The year with the highest number of measurements was 2018, with 388 records, while 2015 was characterized by the greatest number of sampled wells (191), providing the most widespread distribution. The total sample size amounts to 7366.

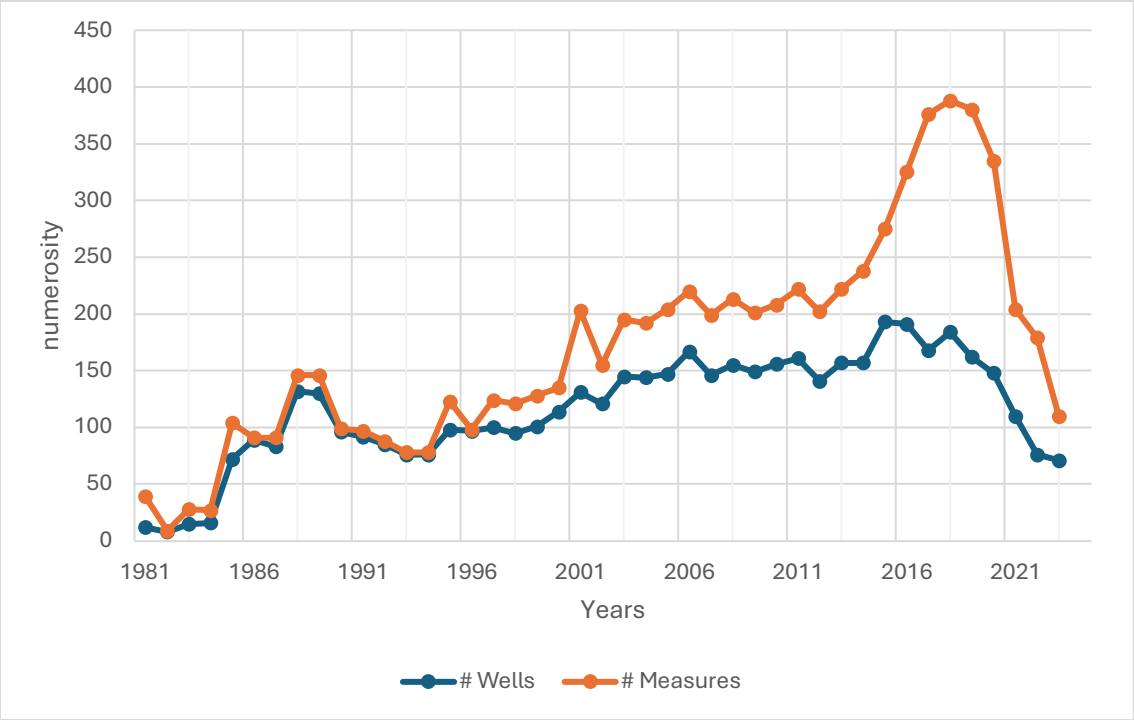

Figure 43. Nitrates, Vicenza high plain: yearly number of sampled wells and measurements between 1981 and 2023.

The data distribution shown in Figure 44 is not perfectly symmetric, displaying a right skewed tendency. Approximately 72% of the values are fall between 10 mg/l and 40 mg/l. This is further evidenced the boxplot in Figure 45, where the box limits indicating the first and third quartile are relatively symmetric around the median.

Additionally, the mean is close to the median, but the whiskers are of different lengths, and there are several outliers with high concentration.

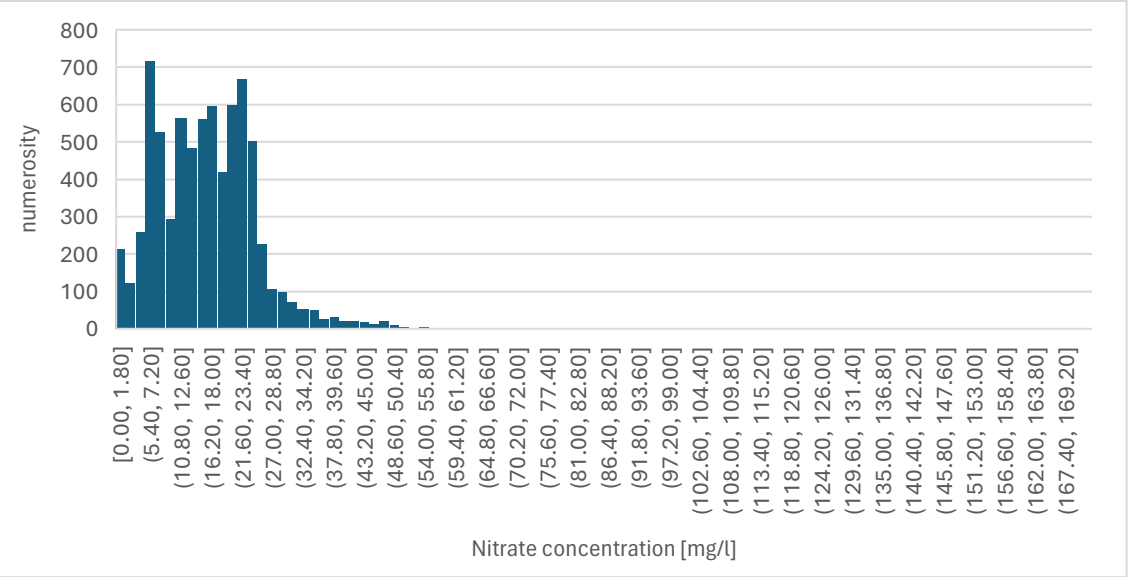

Figure 44. Nitrates, Vicenza high plain: histogram of nitrate concentration data between 1981 and 2023.

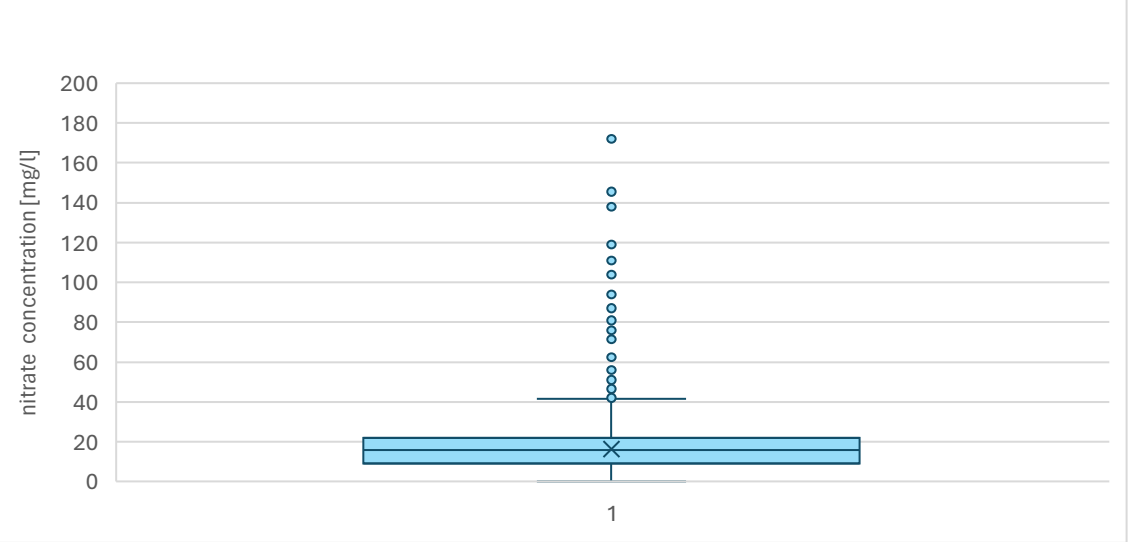

Figure 45. Nitrates, Vicenza high plain: boxplot of the concentration between 1981 and 2023.

The parameters characterizing the statistical distribution of the measurements in the selected years are provided in Table 7.

While the table points out a decreasing trend in average and maximum concentrations from 1988 to 2022, the maximum value in 2023 increased to 44 mg/l. However, the values of mean and median tend to remain low, consistent with the patterns observed in the other years of the 21st century.

Table 6. Nitrates, Vicenza high plain: descriptive statistics in the analyzed years.

Year	μ [mg/l]	Mode [mg/l]	Q1 [mg/l]	Median [mg/l]	Q3 [mg/l]	σ^2 $[(mg/l)^2]$	CV [-]	G [-]	Min [mg/l]	Max [mg/l]
1985	17.85	11.50	11.50	15.88	23.50	8.98	0.17	0.84	0.00	43.00
1988	23.72	19.50	11.50	19.50	30.63	20.58	0.19	2.97	0.00	145.50
1991	21.17	24.00	12.25	19.75	25.13	12.08	0.16	1.68	0.00	77.00
1994	20.57	22.00	11.38	20.00	25.13	13.35	0.18	2.74	0.00	97.00
1997	18.03	7.00	10.75	15.75	23.25	11.10	0.18	1.76	0.00	76.00
2000	15.86	7.50	8.13	15.00	19.69	10.97	0.21	2.76	0.00	87.00
2003	15.54	17.00	7.00	17.00	22.50	9.03	0.19	0.37	0.00	45.00
2006	17.63	7.00	10.00	18.00	23.00	8.71	0.17	0.29	0.00	46.00
2009	17.50	6.00	7.00	17.50	24.00	10.30	0.18	0.46	0.00	48.00
2012	15.99	19.00	8.00	17.00	22.00	8.30	0.18	0.13	0.00	36.00
2015	14.97	5.00	7.00	14.00	22.00	8.36	0.19	0.14	0.00	36.25
2018	14.40	7.00	8.50	14.00	20.00	6.74	0.18	0.00	0.00	28.33
2021	13.77	23.8	7.84	14.57	18.98	6.82	0.19	-0.25	0.00	24.40
2022	12.13	6.70	6.23	12.09	17.68	6.63	0.21	0.05	0.00	25.80
2023	11.68	10.70	6.51	10.80	16.68	6.61	0.22	1.14	0.00	44.00

Before 2003, the skewness coefficient exhibits high values, likely due to the elevated concentration recorded in well VITH-8 (Figure 32). This well was sampled annually from 1986 to 2000, consistently showing high values, similarly to well VISR-1 (Figure 32), located 927 m apart in the same area. Well VISR-1 was monitored every year from 1986 to 1998, as shown in Figure 46.

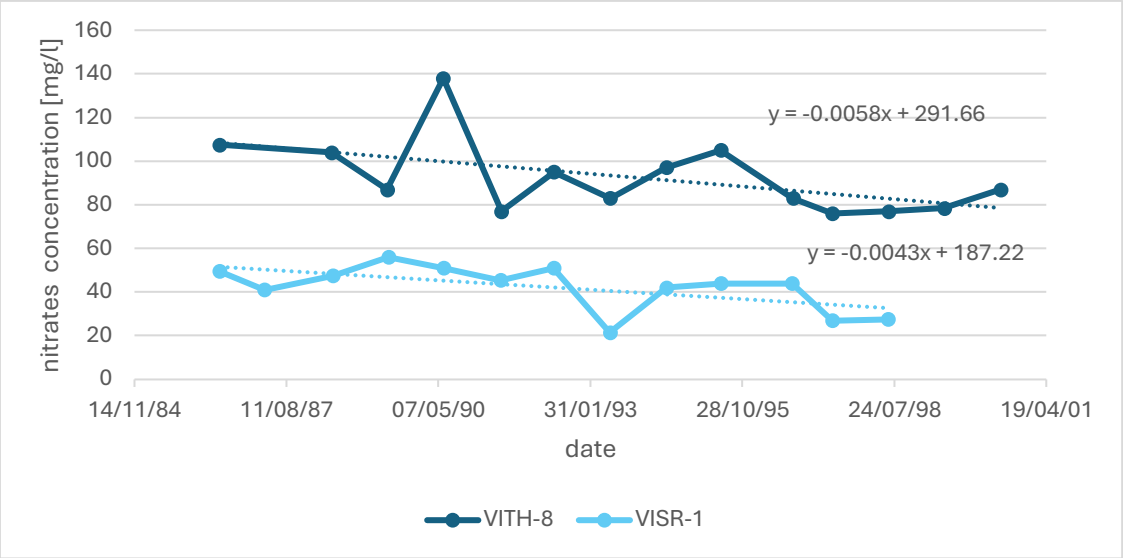

Figure 46. Trends Nitrates concentration versus time observed in wells VITH-8 and VISR-1 in the Vicenza high plain. The equation of the linear regression (dotted lines) of the measurements are provided.

The lack of data for well VISR-1 in 2000 poses a challenge for the definition of the variogram model required for the Kriging interpolation. To overcome this issue the correlation between the two well datasets was analyzed and, being the two trends sufficiently similar, a fictitious concentration for the year 2000 was introduced in the VISR-1 dataset using. The value was determined through a linear regression, resulting in an estimated concentration of 39.9 mg/l, as depicted in Figure 47.

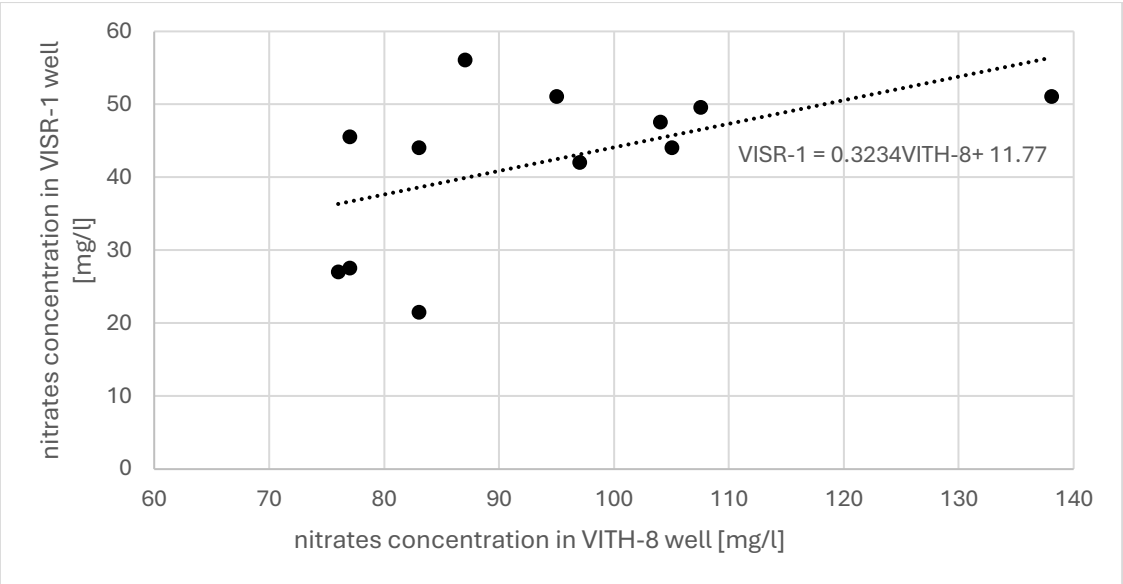

Figure 47. Relation between nitrates concentration observed in the wells VITH-8 and VISR-1.

In the analysis of year 2021, four values from wells P83031, P83032, P83034, and P83035 (Figure 32) were excluded. These records available from the VIacqua database and related to the same area, provide a value equal to 0, which is unrealistic. In fact, both the time series of records from the same wells as well as that available from other two wells in the nearby point out a steady concentration of nitrates in the range 17-25 mg/l (Figure 48).

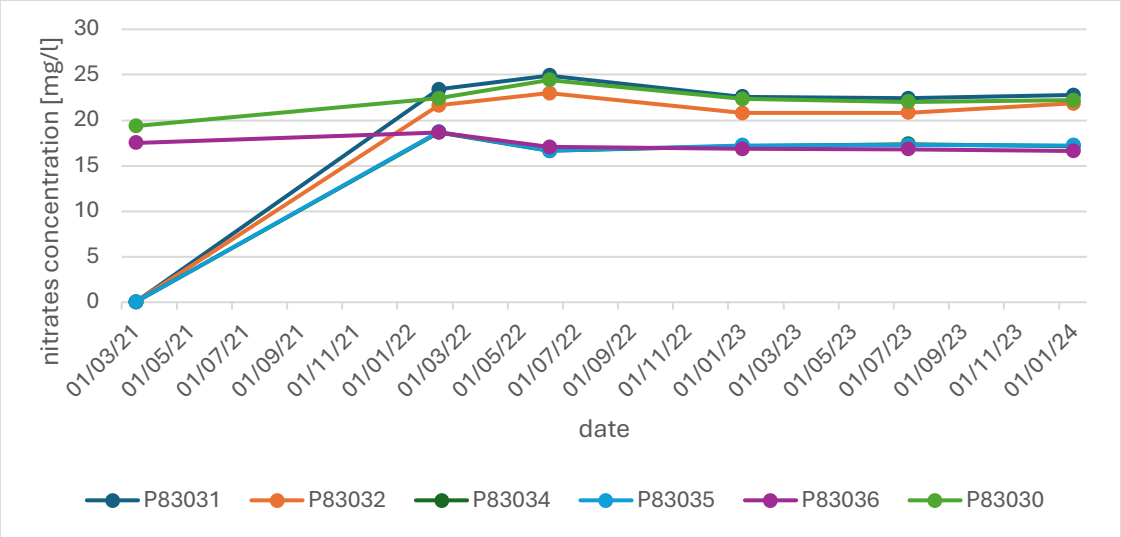

Figure 48. Comparison of the time series of nitrate concentration registered in wells P83031, P83032, P83034, P83035, P83036, and P83030 from January 2021 to January 2024.

In the case of study of nitrates, which have a diffuse source of pollution, a possible relationship with precipitation is specifically investigated. Daily precipitation data from 1994 to 2023 are collected from the ARPAV pluviometric stations located in the study area. The monthly averages have been calculated and plotted in Figure 49. The highest values of precipitation are typically registered in November, with a monthly mean of 150.94 mm, while the driest month is February with a monthly mean precipitation of 71.5 mm.

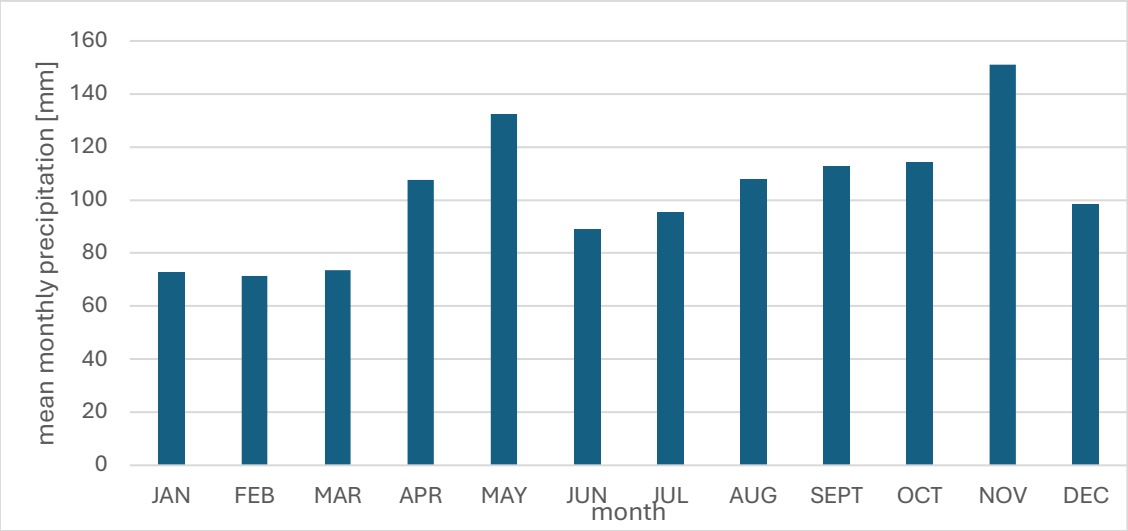

Figure 49. Monthly precipitation in the Vicenza High plain as obtained by averaging the records between 1994 and 2023. The list of the pluviometric station used: Breganze, Isola Vicentina, Malo, Montecchio Precalcino, Quinto Vicentino, Vicenza (Sant'Agostino).

The monthly probability density function and cumulative probability distribution of the recorded nitrate concentration have been computed and are reported in Figure 50 and 51, respectively. The cumulative probability distribution of the monthly-averaged concentration are very similar with the exception of January and June, generally presenting higher nitrates concentrations.

This is confirmed by Figure 50, where the distribution of values recorded in January has a wider base and similarly, although less evident, in June. This relates to farming activities regulated by a prohibition on spreading manure between November 1st and March 1st. As a result, rainfall observed during November and May months washes manure previously spread on the soil together with the use of fertilizers in spring, leading to increased nitrate concentrations in groundwater by of January and June.

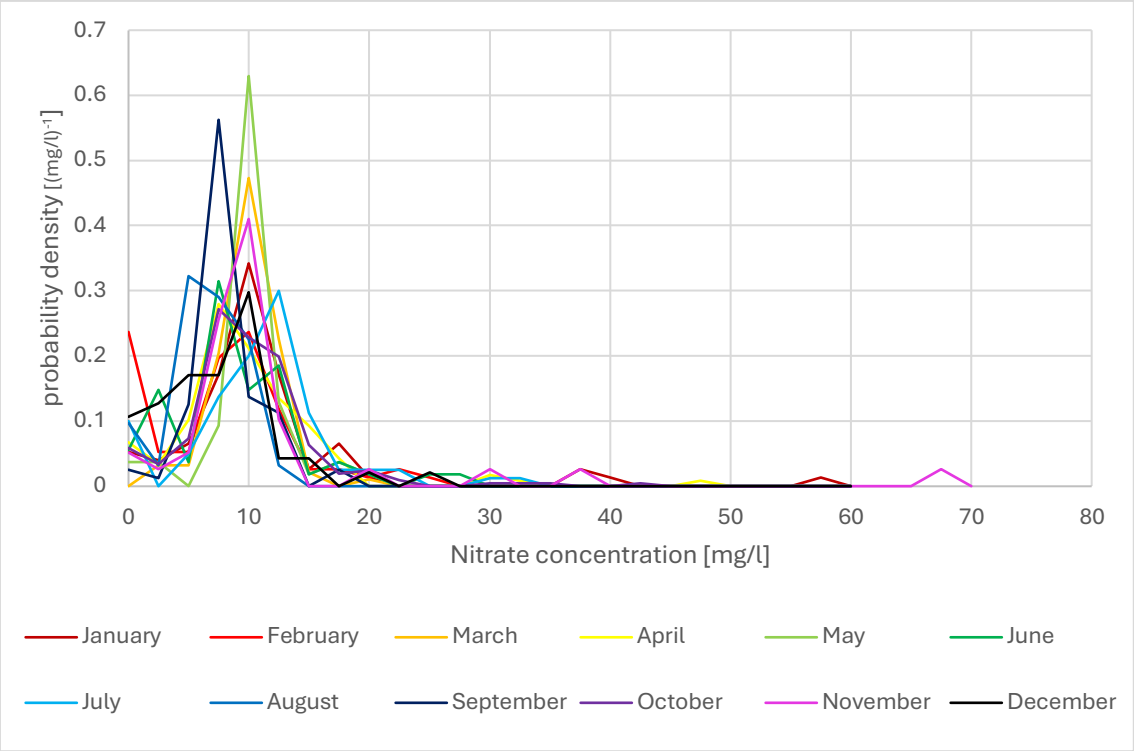

Figure 50. Nitrates, Vicenza high plain: probability density function of concentration values.

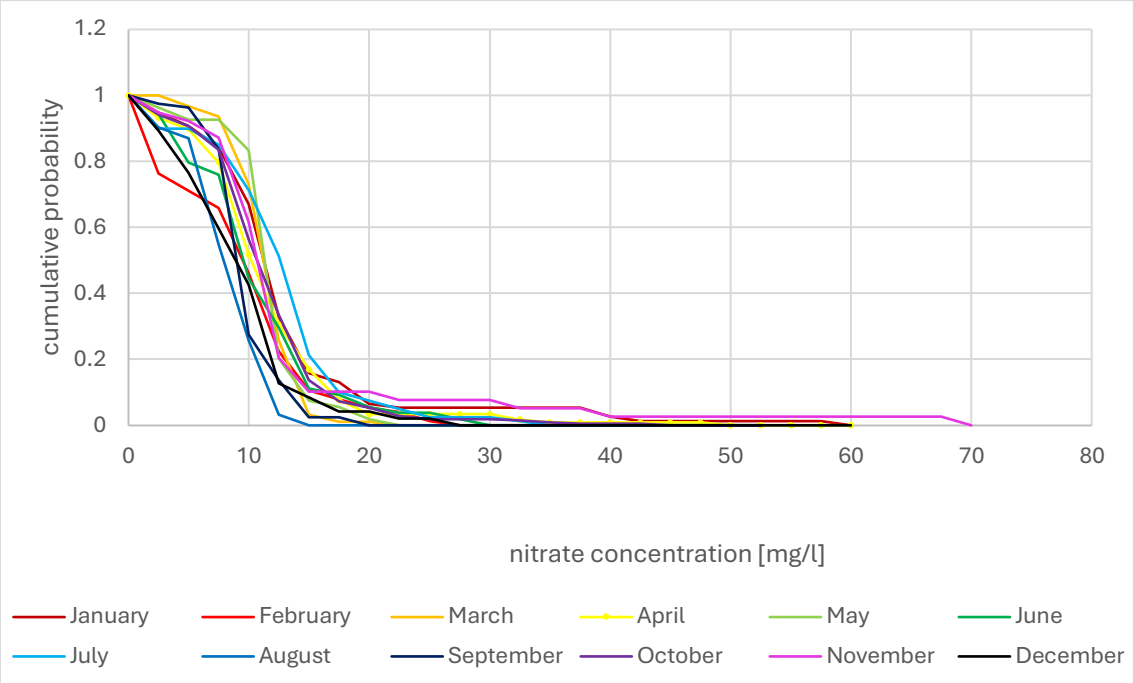

Figure 51. Nitrates, Vicenza high plain: cumulative probability distribution of monthly-averaged concentration values.

In relation to the geospatial analysis, Table 8 reports the parameters of the isotropic variogram models as derived from the log-transformed data.

Table 7. Nitrates, Vicenza high plain: isotropic variogram model for each selected year.

Isotropic analysis							
Year	**Mean dist [m]**	**Model**	**Lag [m]**	**Nugget**	**Partial Sill**	**Range [m]**	**RMSE**
1985	728.30	Spherical	1276.1	0.0007	0.05	6266.28	0.19
1988	695.83	Spherical	1200.	0.0400	0.08	4143.50	0.3
1991	820.30	Spherical	1400.0	0.0100	0.04	5487.40	0.18
1994	876.00	Spherical	1400.0	0	0.06	5313.70	0.16
1997	848.00	Spherical	1348.0	0	0.10	10120.60	0.17
2000	766.14	Spherical	1000.0	0	0.09	5500.00	0.24
2003	771.63	Spherical	1000.0	0	0.12	6500.00	0.29
2006	655.30	Spherical	1000.0	0.0030	0.07	7000.00	0.20
2009	638.45	Spherical	1000.0	0.0040	0.10	7500.00	0.20
2012	664.30	Spherical	1000.0	0.0040	0.08	8080.82	0.22
2015	509.90	Spherical	950.5	0.0090	0.09	8879.60	0.20
2018	601.88	Spherical	1000.0	0.0250	0.04	7800.00	0.20
2021	664.62	Spherical	1000.0	0	0.09	9543.15	0.14
2022	734.66	Spherical	1485.5	0.0020	0.08	9236.26	0.16
2023	642.97	Spherical	1130.2	0.0190	0.07	10867.4	0.18

Figure 52 shows the map of the expected value for the nitrates concentration as obtained by isotropic Kriging for the selected 15 years. Figure 53 provides the associated standard deviation for the years of 1988, 2000, 2012 and 2024.

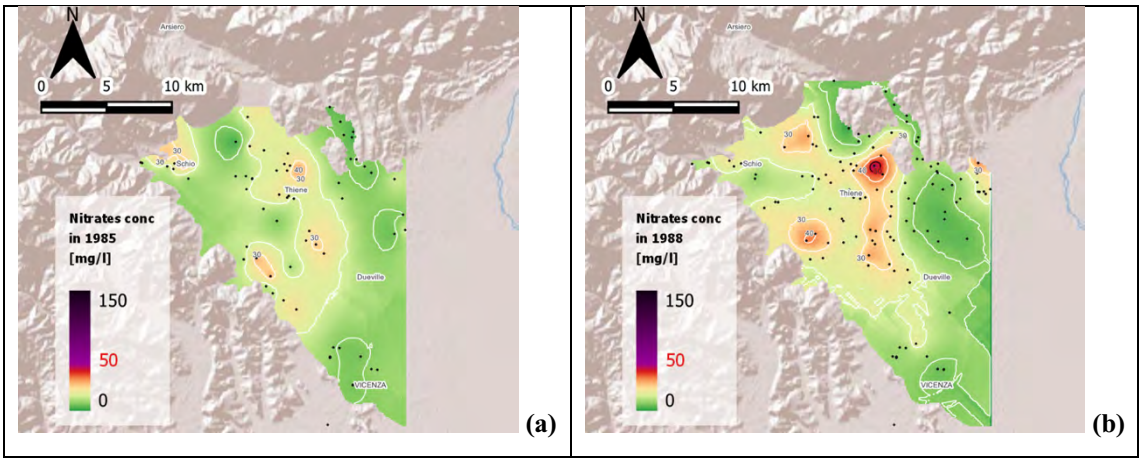

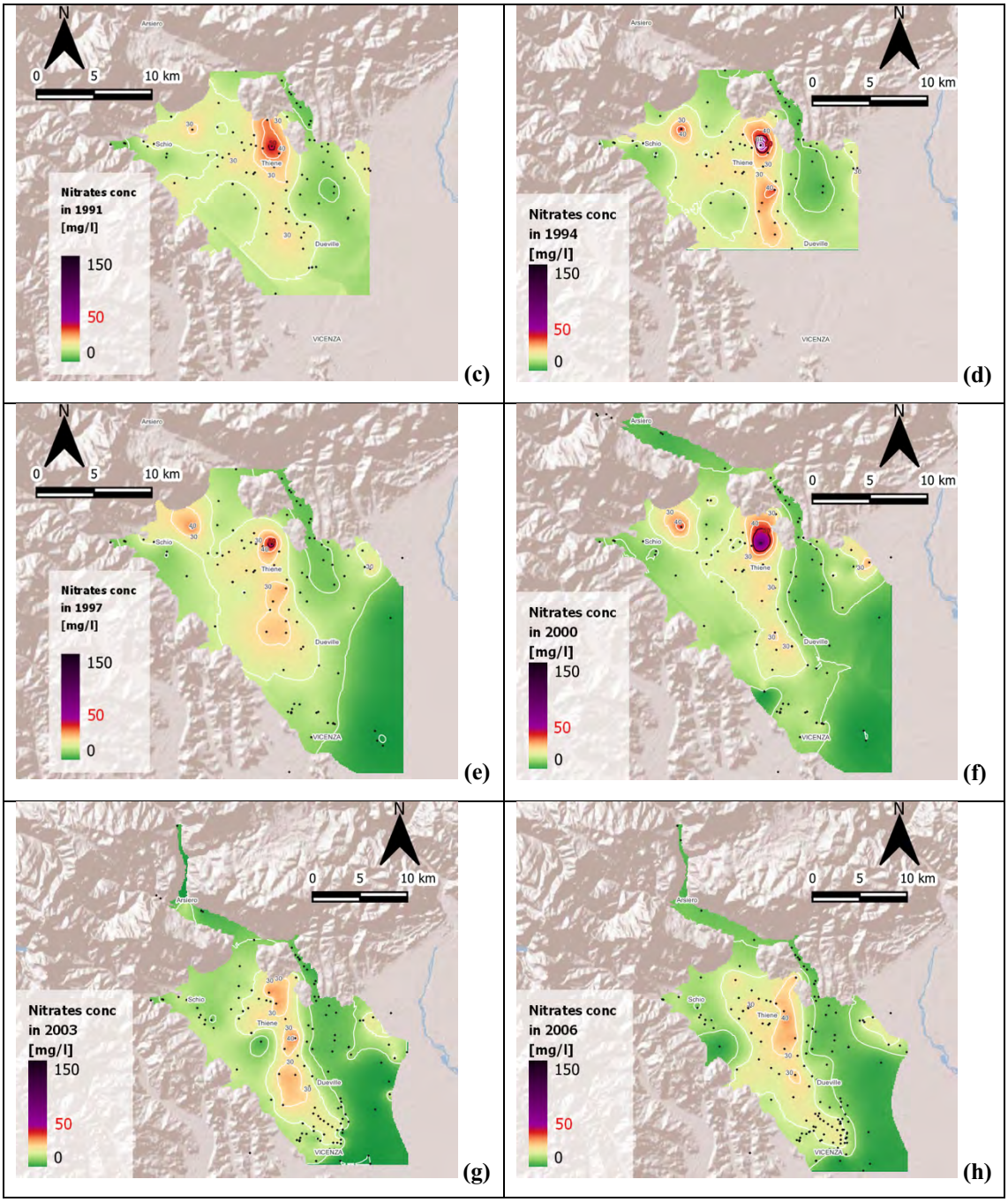
N
0 5 10 km
Nitrates conc in 1991 [mg/l]
150
50
0
(c)
Nitrates conc in 1994 [mg/l]
(d)
Nitrates conc in 1997 [mg/l]
(e)
Nitrates conc in 2000 [mg/l]
(f)
Nitrates conc in 2003 [mg/l]
(g)
Nitrates conc in 2006 [mg/l]
(h)
Arsiero
Schio
Thiene
Dueville
VICENZA

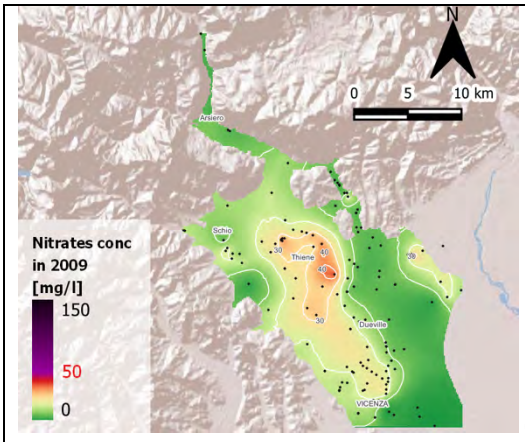
N
0 5 10 km
Nitrates conc
in 2009
[mg/l]
150
50
0
Arsiero
Schio
Thiene
Dueville
VICENZA

(i)

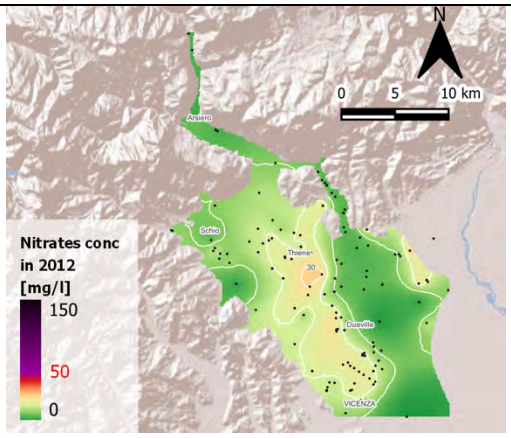
N
0 5 10 km
Nitrates conc
in 2012
[mg/l]
150
50
0
Arsiero
Schio
Thiene
Dueville
VICENZA

(l)

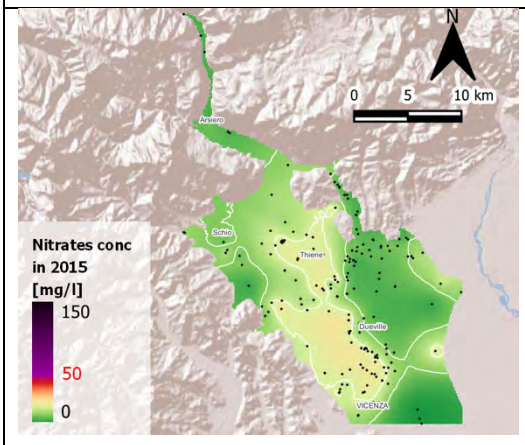
N
0 5 10 km
Nitrates conc
in 2015
[mg/l]
150
50
0
Arsiero
Schio
Thiene
Dueville
VICENZA

(m)

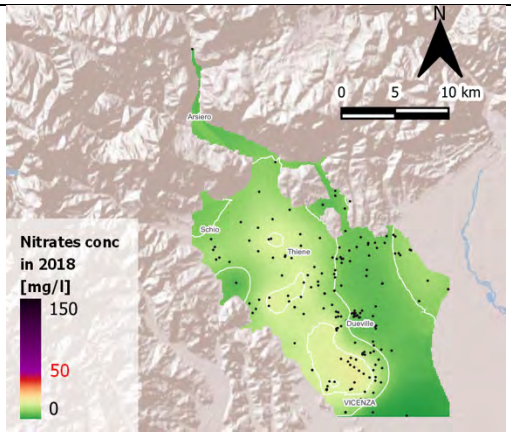
N
0 5 10 km
Nitrates conc
in 2018
[mg/l]
150
50
0
Arsiero
Schio
Thiene
Dueville
VICENZA

(n)

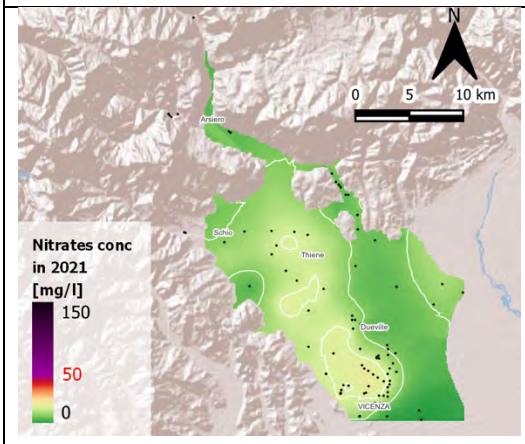
N
0 5 10 km
Nitrates conc
in 2021
[mg/l]
150
50
0
Arsiero
Schio
Thiene
Dueville
VICENZA

(o)

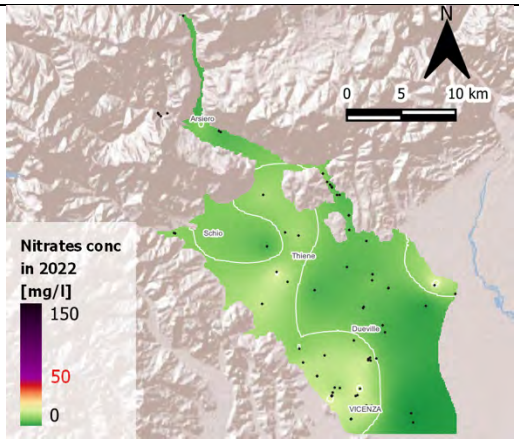
N
0 5 10 km
Nitrates conc
in 2022
[mg/l]
150
50
0
Arsiero
Schio
Thiene
Dueville
VICENZA

(p)

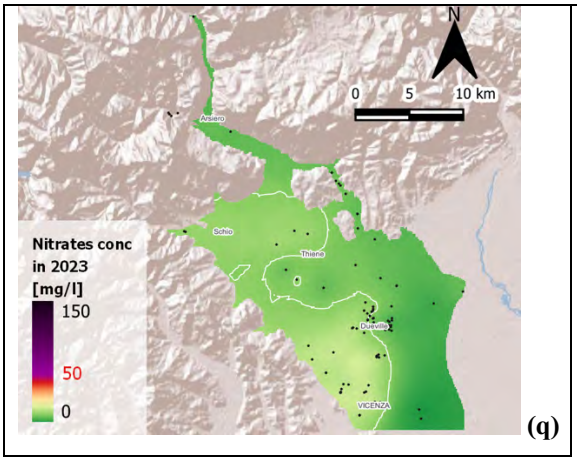

Figure 52. Nitrates, Vicenza high plain: maps of the expected values resulting from Kriging interpolation with isotropic variogram for the years (a) 1985, (b) 1988, (c) 1991, (d) 1994, (e) 1997, (f) 2000, (g) 2003, (h) 2006, (i) 2009, (l) 2012, (m) 2015, (n) 2018, (o) 2021, (p) 2022, and (q) 2023. Map extension can vary depending on well availability. The black dots represent the locations of the wells used to build-up the map. The red number in the legend represents the max concentration admissible by law.

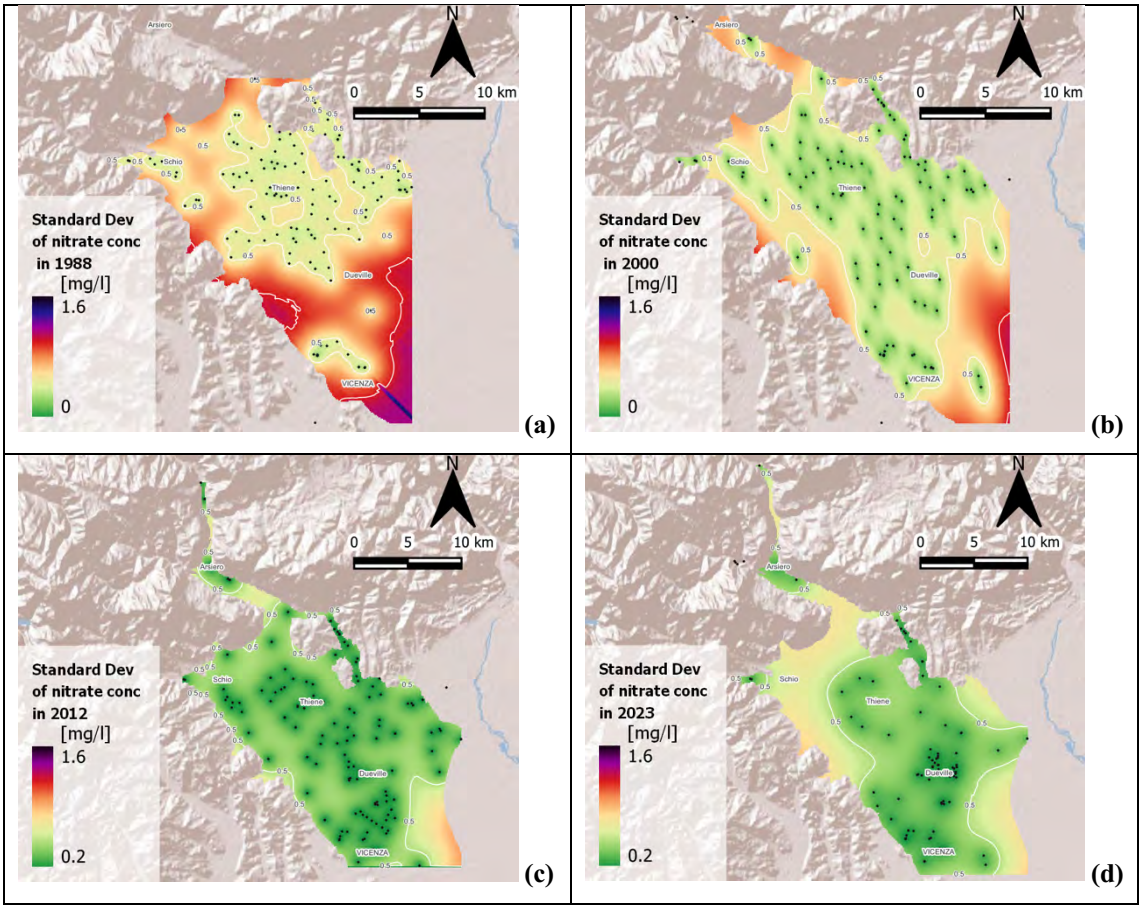

Figure 53. Nitrates, Vicenza high plain: maps of the standard deviation resulting from Kriging interpolation with isotropic variogram for the years (a) 1988, (b) 2000, (c) 2012 and (d) 2023. Map extension can vary depending on the well availability. The black dots represent the locations of the wells used to build-up the map.

The parameters of the anisotropic variogram model for each selected year analysis are reported in Table 8.

Table 8. Nitrates, Vicenza high plain: parameters of the anisotropic variogram models.

Anisotropic analysis								
Year	**Model**	**Lag [m]**	**Preferential Angle [°]**	**Nugget**	**Partial sill**	**Major range [m]**	**Minor range [m]**	**RMSE**
1985	Spherical	1276.11	145.0	0.0030	0.05	15000.00	7000.00	0.17
1988	Spherical	1000.00	145.0	0.0500	0.07	8000.00	3000.00	0.29
1991	Spherical	1500.00	156.8	0.0100	0.04	14436.50	4819.50	0.18
1994	Spherical	1500.00	145.0	0	0.07	14460.40	4842.80	0.18
1997	Spherical	1347.95	155.0	0.0040	0.09	16175.40	6642.56	0.17
2000	Spherical	1000.00	165.0	0	0.10	12000.00	5500.00	0.23
2003	Spherical	1200.00	167.0	0.0140	0.12	14400.00	7000.00	0.27
2006	Spherical	1000.00	157.0	0.0040	0.07	8000.00	4000.00	0.20
2009	Spherical	1000.00	165.0	0.0080	0.10	10000.00	7367.13	0.19
2012	Spherical	1000.00	156.0	0.0040	0.08	15000.00	5425.68	0.21
2015	Spherical	950.50	158.0	0.0080	0.09	11406.43	8000.00	0.20
2018	Spherical	1000.00	163.0	0.0270	0.04	10000.00	6500.00	0.21
2021	Spherical	1000.00	165.0	0	0.08	12000.00	6000.00	0.15
2022	Spherical	1500.00	160.0	0.0010	0.08	10000.00	4000.00	0.18
2023	Spherical	1000.00	160.0	0.0200	0.07	12000.00	8000.00	0.18

Figure 54 provides the maps of the expected value of nitrates as generated by Kriging for the 15 selected years using the anisotropic variogram models provided in Table 8. Additionally, Figure 55 provides the maps of the associated standard deviation for the years 1988, 2000, 2012, and 2023.

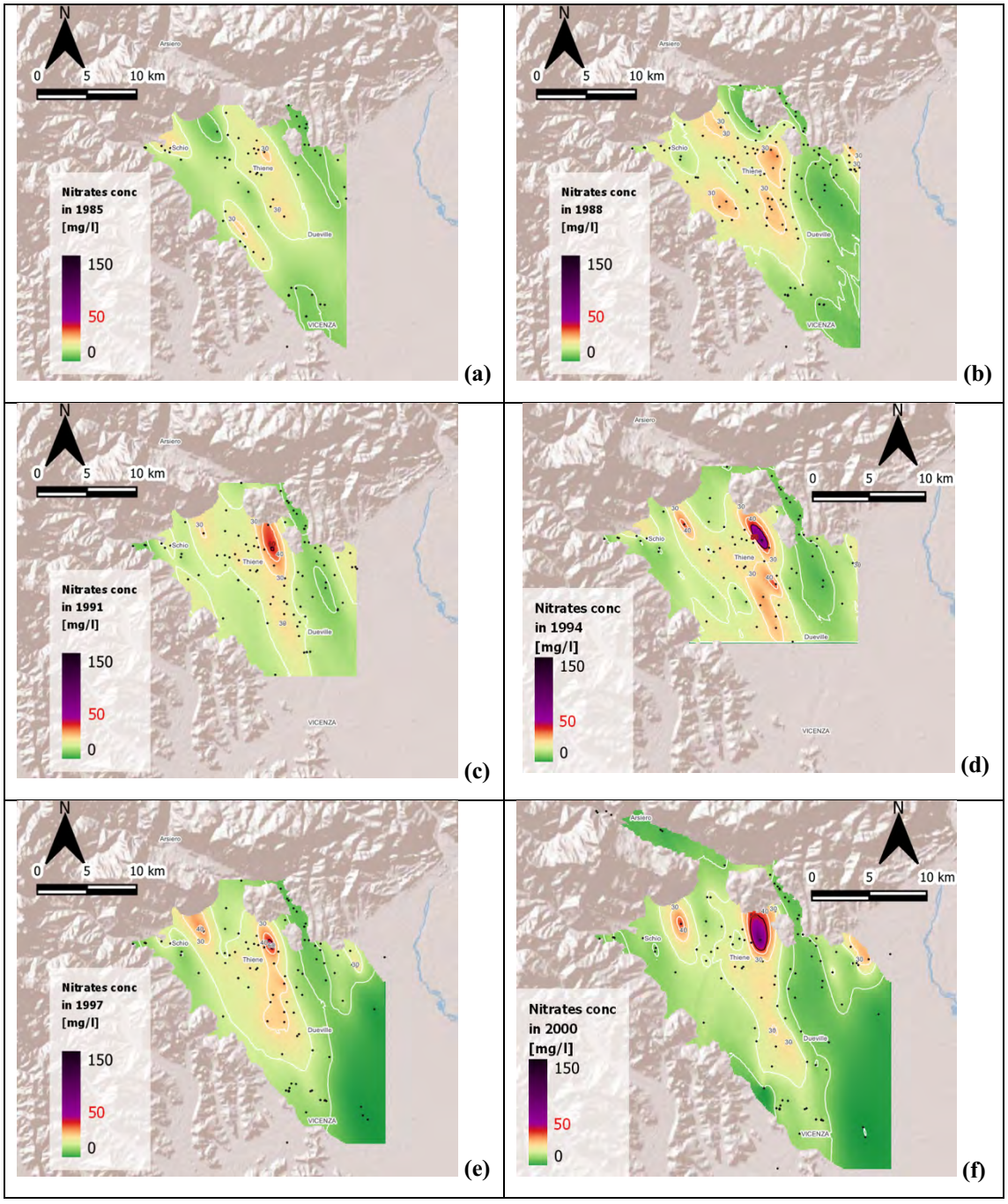
N
0 5 10 km
Nitrates conc in 1985 [mg/l]
150
50
0
(a)
Nitrates conc in 1988 [mg/l]
(b)
Nitrates conc in 1991 [mg/l]
(c)
Nitrates conc in 1994 [mg/l]
(d)
Nitrates conc in 1997 [mg/l]
(e)
Nitrates conc in 2000 [mg/l]
(f)
Arsiero
Schio
Thiene
Dueville
VICENZA

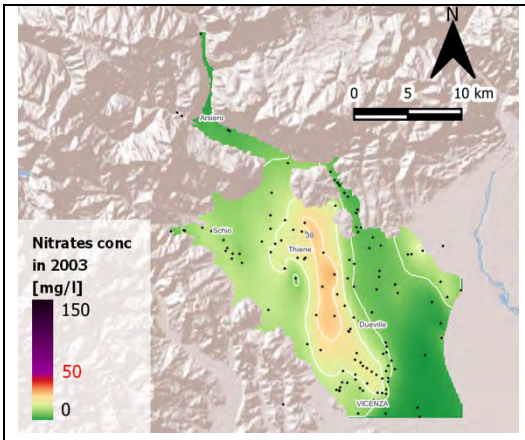
N
0 5 10 km
Nitrates conc
in 2003
[mg/l]
150
50
0
Schio
Thiene
Dueville
VICENZA

(g)

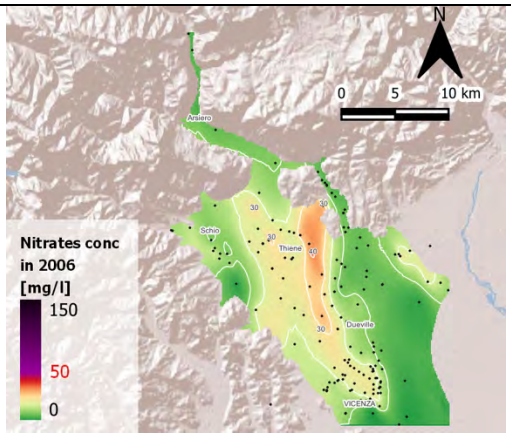
N
0 5 10 km
Nitrates conc
in 2006
[mg/l]
150
50
0
Schio
Thiene
Dueville
VICENZA

(h)

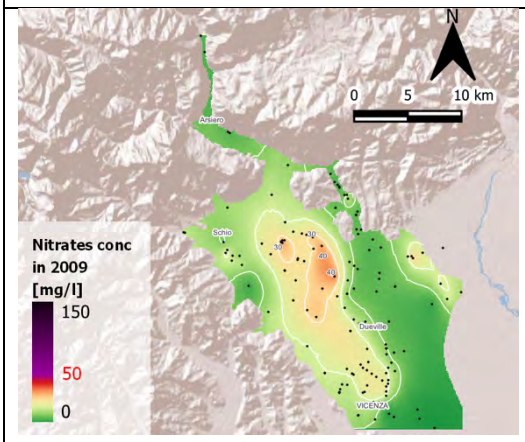
N
0 5 10 km
Nitrates conc
in 2009
[mg/l]
150
50
0
Schio
Dueville
VICENZA

(i)

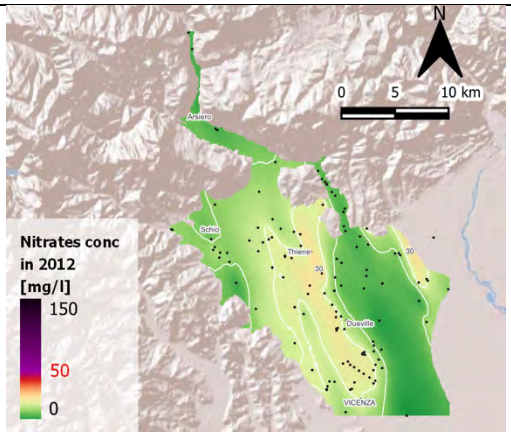
N
0 5 10 km
Nitrates conc
in 2012
[mg/l]
150
50
0
Schio
Thiene
Dueville
VICENZA

(l)

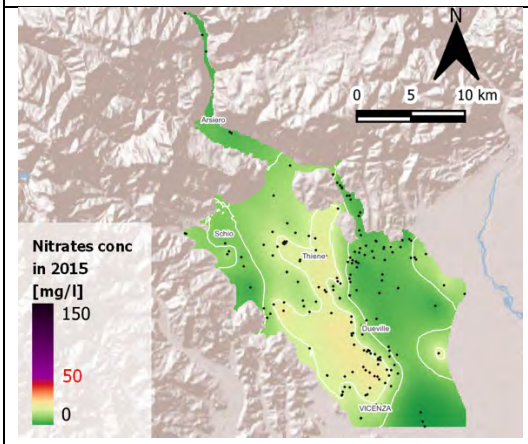
N
0 5 10 km
Nitrates conc
in 2015
[mg/l]
150
50
0
Schio
Thiene
Dueville
VICENZA

(m)

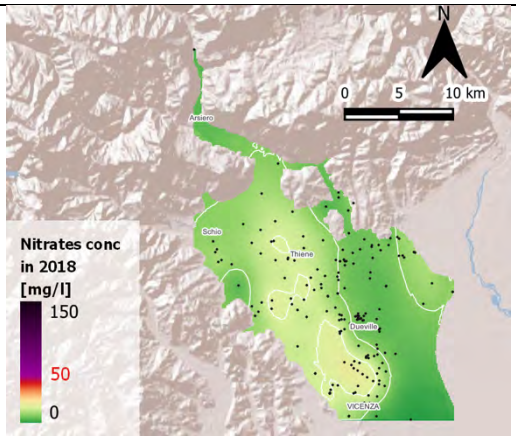
N
0 5 10 km
Nitrates conc
in 2018
[mg/l]
150
50
0
Schio
Thiene
Dueville
VICENZA

(n)

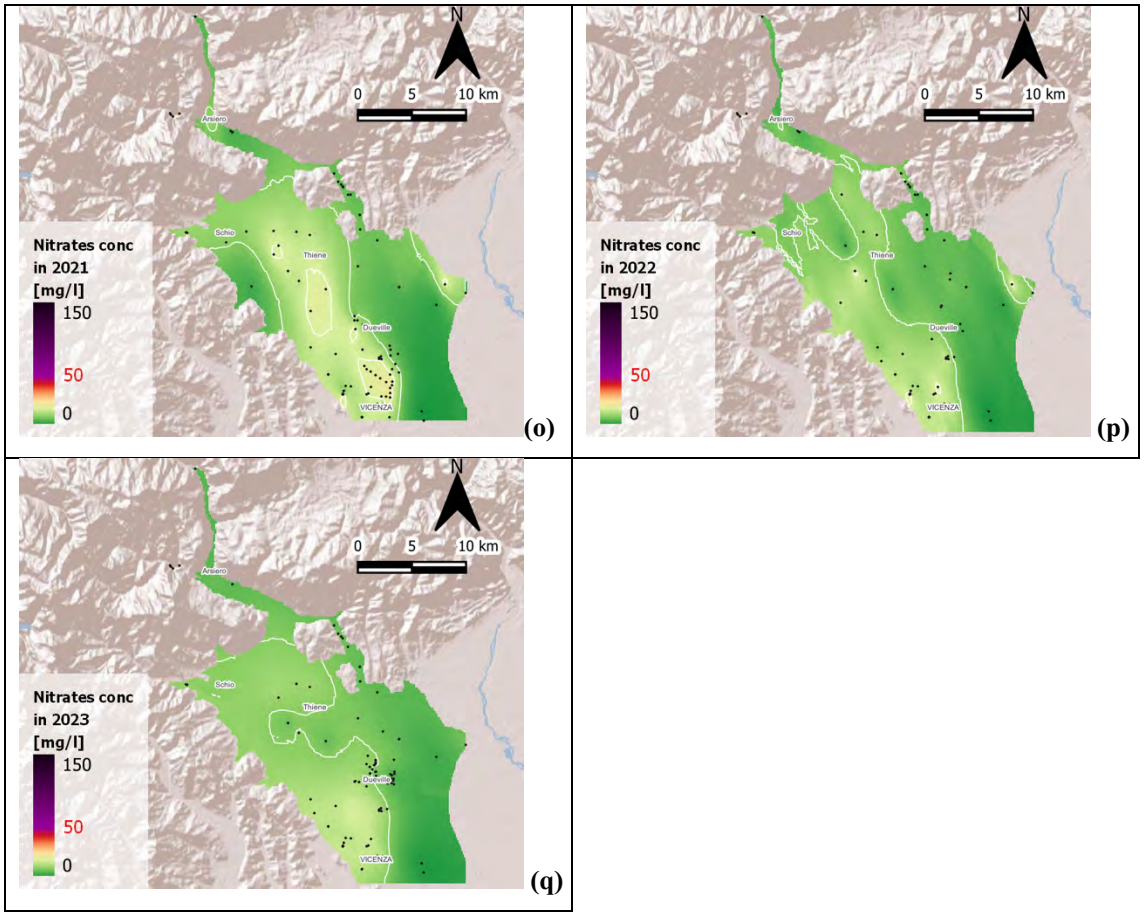

Figure 54. Nitrates, Vicenza high plain: maps of the expected values resulting from Kriging interpolation with anisotropic variogram for the years (a) 1985, (b) 1988, (c) 1991, (d) 1994, (e) 1997, (f) 2000, (g) 2003, (h) 2006, (i) 2009, (l) 2012, (m) 2015, (n) 2018 (o) 2021, (p) 2022 and (q) 2023. Map extension can vary depending on well availability. The black dots represent the location of the wells used to build-up the map. The red number in the legend represents the max concentration admissible by law.

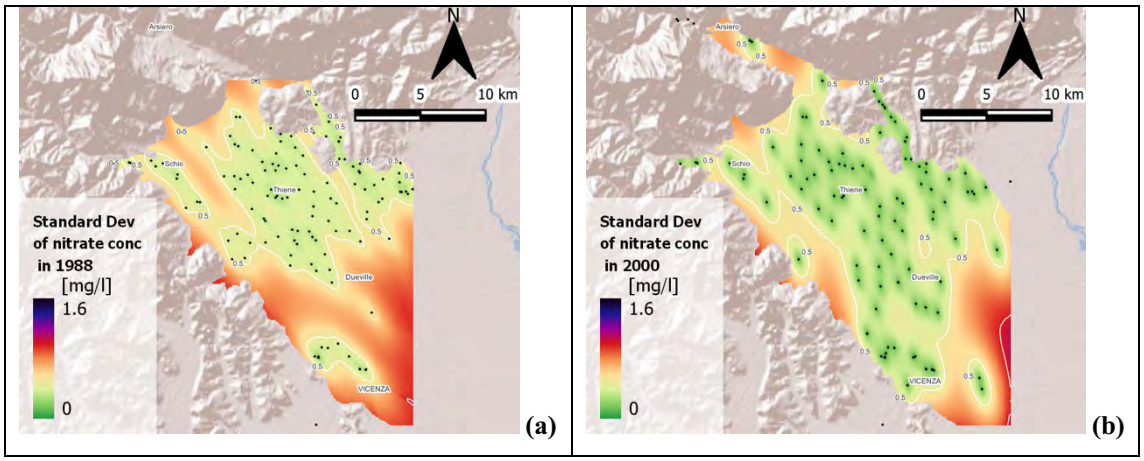

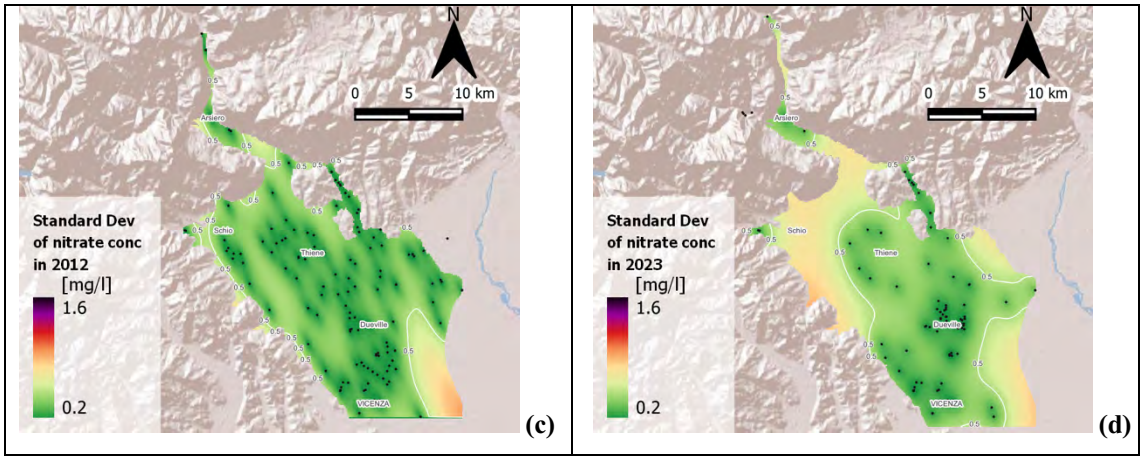

Figure 55. Nitrates, Vicenza high plain: maps of the standard deviation resulting from Kriging interpolation with anisotropic variogram for the years (a) 1988, (b) 2000, (c) 2012, and (d) 2023. Map extension can vary depending on well availability. The black dots represent the locations of the wells used to build-up the map.

5.2.2. AGNO VALLEY

For the analysis of nitrates in the Agno valley, records are available since 1998. Although the number of wells rarely exceeds 30 units, as shown in Figure 56, this can be considered sufficient given the relatively small size of the area.

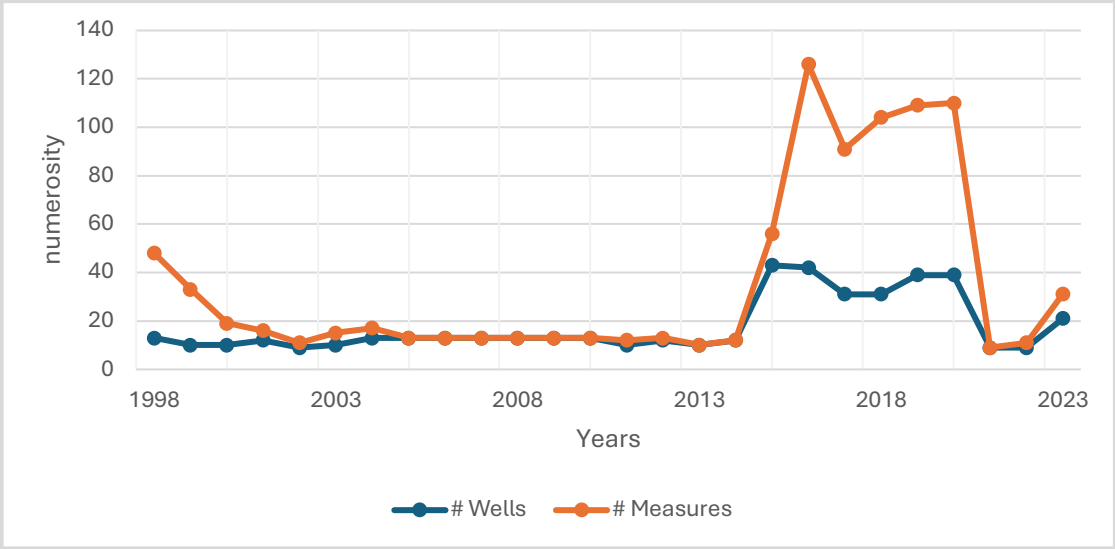

Figure 56. Nitrates, Agno valley: yearly number of sampled wells and measurements between 1998 and 2023.

The statistical analysis starts from a check on the distribution of values of the entire dataset. By observing the histogram and the boxplot (Figure 57 and 58, respectively) the distribution appears almost normally distributed, with the main represented class the interval of between 10 and 12 mg/l. Data only in two cases exceed the law limit of 50 mg/l (Figure 58). In the boxplot the whiskers are almost symmetrical as the box, with the number of outliers above the major whisker suggesting a right skewed distribution.

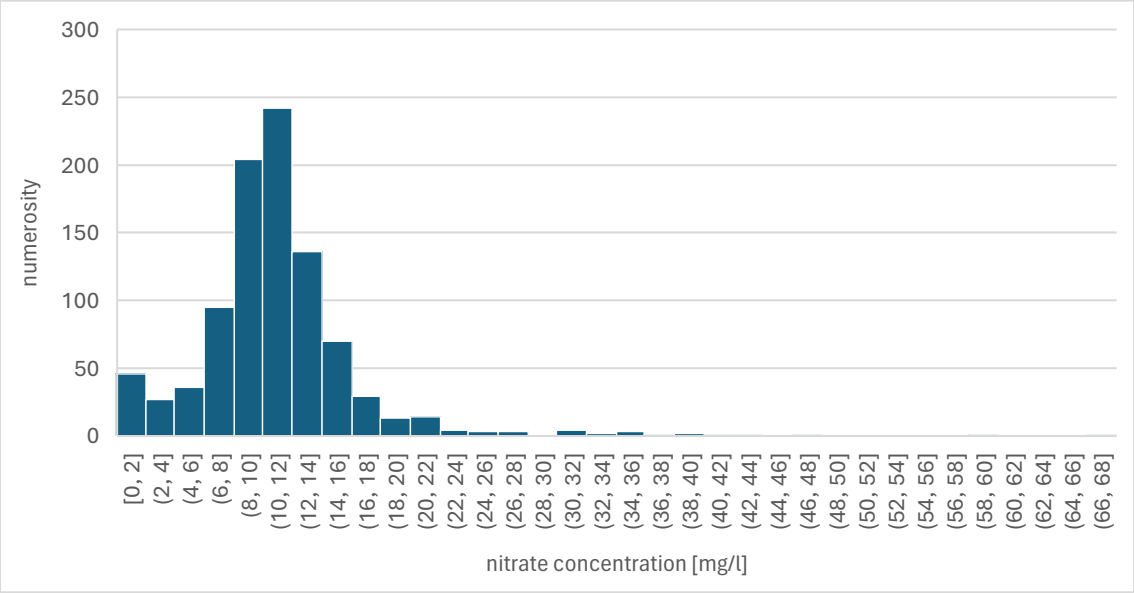

Figure 57. Nitrates, Agno valley: histogram of concentration between 1998 and 2023.

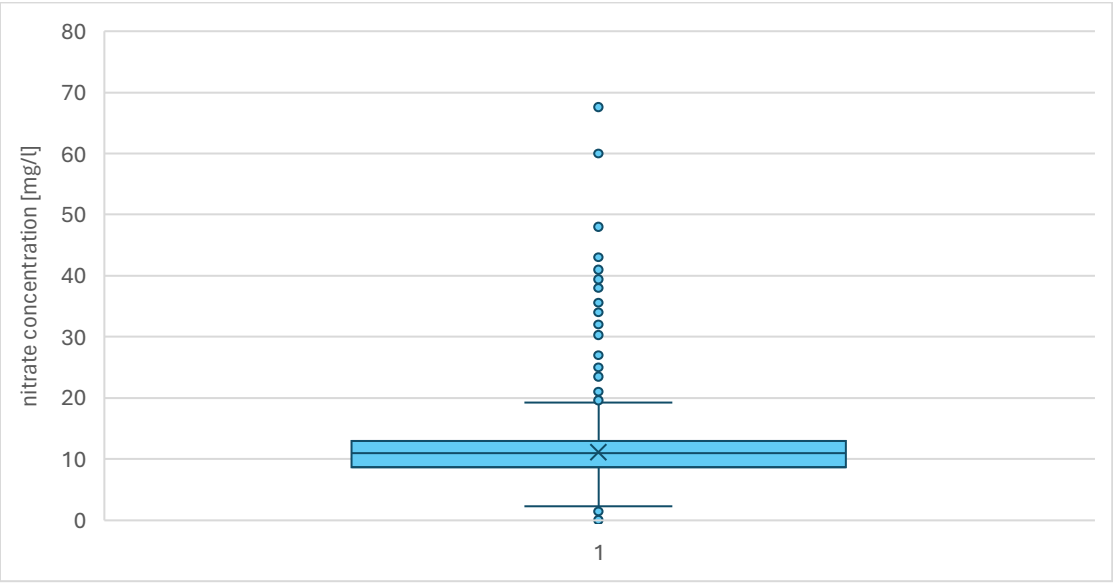

Figure 58. Nitrates, Agno Valley: boxplot of the concentration between 1998 and 2023.

The statistical analysis of the data for the years under analysis are shown in Table 9. Nitrate concentrations consistently remained below the legal limit of 50 mg/l in each of the considered years. However, the scarcity of data often makes it impossible to determine the mode.

Despite the almost normal distribution of data, skewness values are relatively high, which can be attribute to the small dataset size. The range of values remains relatively narrow in most years, with the exception of 2018 and 2023.

Table 9. Nitrates, Agno valley: descriptive statistics of the data recorded in the analyzed years.

Years	**μ [mg/l]**	**Mode [mg/l]**	**Q1 [mg/l]**	**Median [mg/l]**	**Q3 [mg/l]**	**σ^2 $[(mg/l)^2]$**	**CV [-]**	**G [-]**	**Min [mg/l]**	**Max [mg/l]**
1998	11.24	11.40	10.00	10.75	11.50	1.92	0.12	1.33	9.00	15.25
2000	11.13	11.25	9.81	11.13	11.63	2.45	0.14	1.47	8.00	17.00
2003	12.25	11.00	10.13	11.00	11.00	4.94	0.18	2.91	9.00	26.00
2006	12.00	11.00	11.00	12.00	13.00	1.35	0.10	0.71	10.00	15.00
2009	10.85	9.00	9.00	11.00	12.00	1.68	0.12	0.41	9.00	14.00
2012	8.63	8.00	8.00	8.00	9.13	1.40	0.14	1.27	7.00	12.00
2015	9.40	7.00	7.00	8.00	11.45	5.50	0.25	2.62	0.90	35.60
2018	11.97	13.00	7.75	11.00	14.00	8.61	0.25	2.91	0.00	60.00
2021	10.38	-	9.45	10.22	11.58	1.67	0.12	0.38	8.13	13.05
2022	9.14	-	8.59	8.89	9.69	0.95	0.11	0.69	7.74	10.93
2023	13.55	-	8.71	10.13	13.13	12.50	0.26	3.21	0.35	67.60

A graphical analysis has been carried out to check if a certain trend in the nitrates concentration can be observed at the municipality level moving from upstream to downstream. The following municipalities are located in sequence: Valdagno, Cornedo, Brogliano, Castelgomberto, Trissino and Montecchio Maggiore (Figure 59). However, no significant relationship was found. A plot displaying the mean values over time recorded by the wells located in the various municipalities is shown in Figure 60.

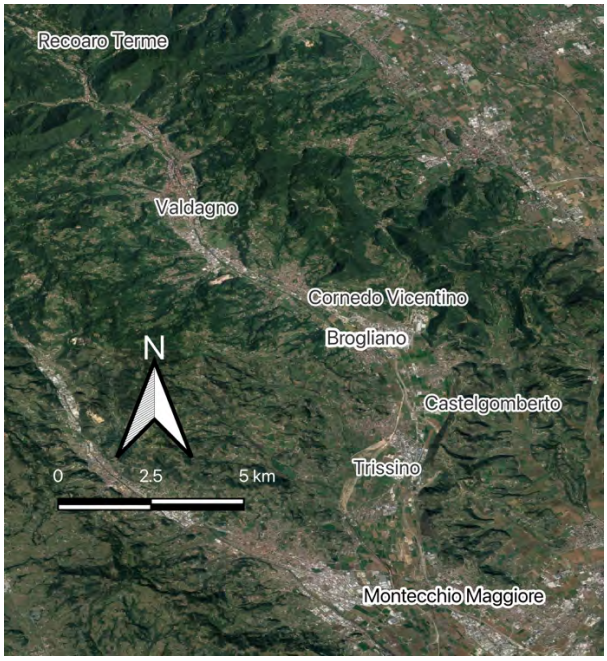

Figure 59. Position of the municipalities inspected in the Agno valley sub-domain.

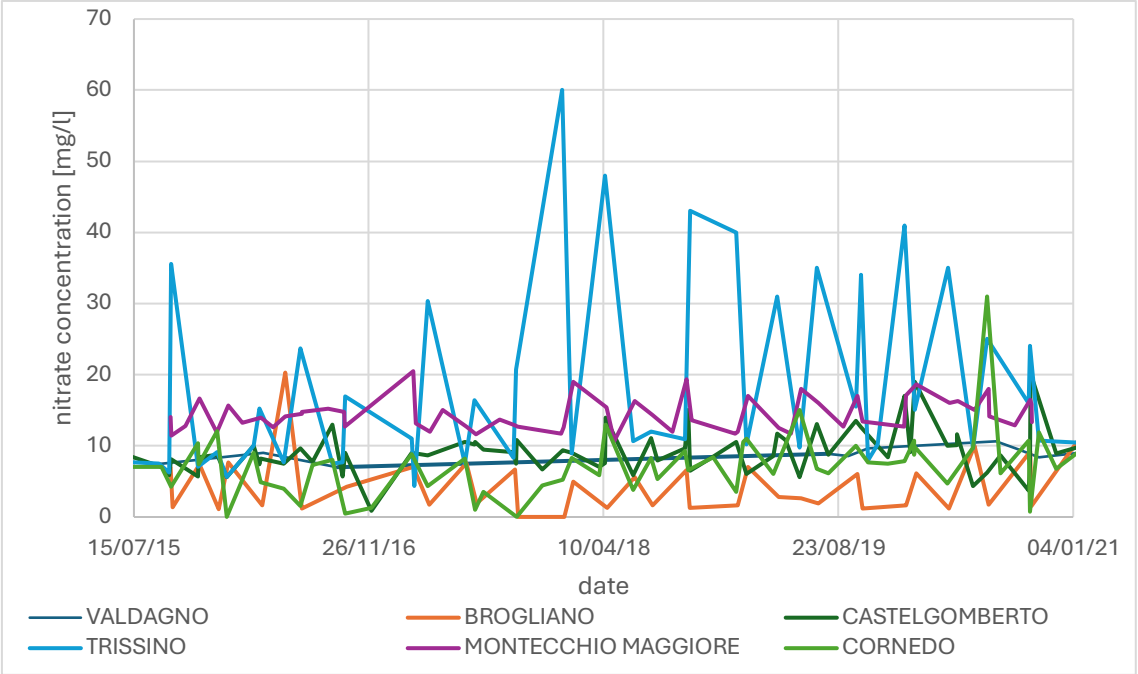

Figure 60. Nitrates, Agno valley: data series of concentration collected between 2015 and 2021 for the verious municipalities located in the sub-domain.

Similar to the analysis carried out in the Vicenza high plain, the possible relationship between rainfall and nitrate concentration in groundwater has been investigated. Figure 61 shows the average monthly rainfall, based on data from ARPAV collected between

1993 and 2023. As the expected, also here February is characterized by the smallest cumulative precipitation, with a value of 96.6 mm, while November results the one with the largest precipitation amounting to 217.7 mm.

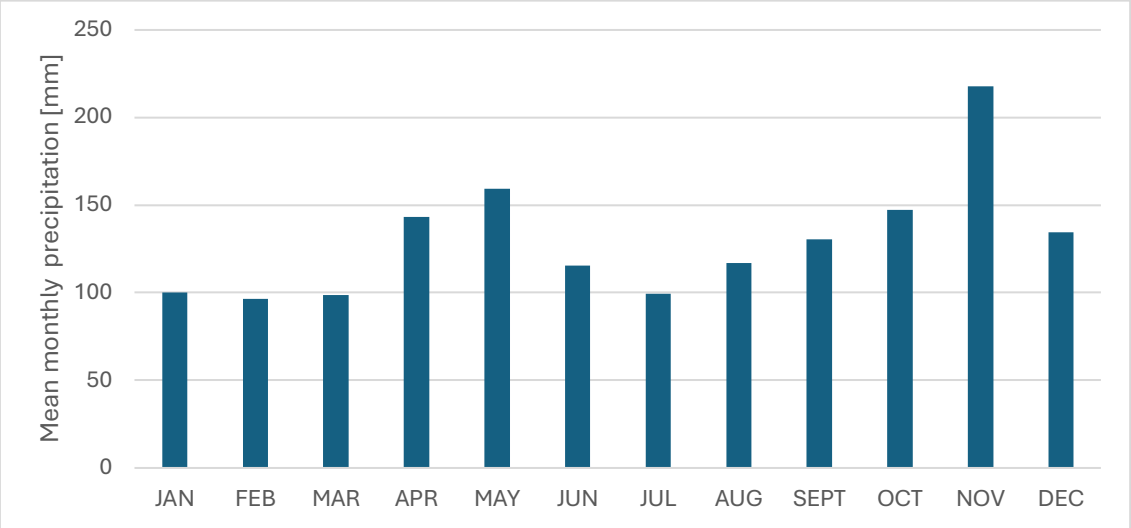

Figure 61. Monthly precipitation in the Agno valley as obtained by averaging the records between 1993 and 2023. The list of the used pluviometric stations are the following:Trissino, Valdagno, Recoaro 1000.

The monthly probability density function and cumulative probability distribution of nitrate concentrations in groundwater recorded in the Agno Valley between 1998 and 2024 are provided in Figure 62 and 63 respectively.

By analyzing the cumulative probability graph in Figure 63, it can be observed that the month of January shows relatively high concentrations, similarly to November, whereas the months of August and September are characterized by lower values, never registering a concentration of more than 20 mg/l.

Furthermore, the probability density function of each month (Figure 62) show that during the January, March, May, November and December a concentrations of 10 mg/l is more likely to be measured. In contrast, April, June, and October show a peak of probability (about 7.5 mg/l), though presenting a broader range of recorded values.

As with Vicenza high plain sub-domain, this can be explained by the impact of livestock activities, where manure spreading is followed by intense rainfall, causing it to be washed away.

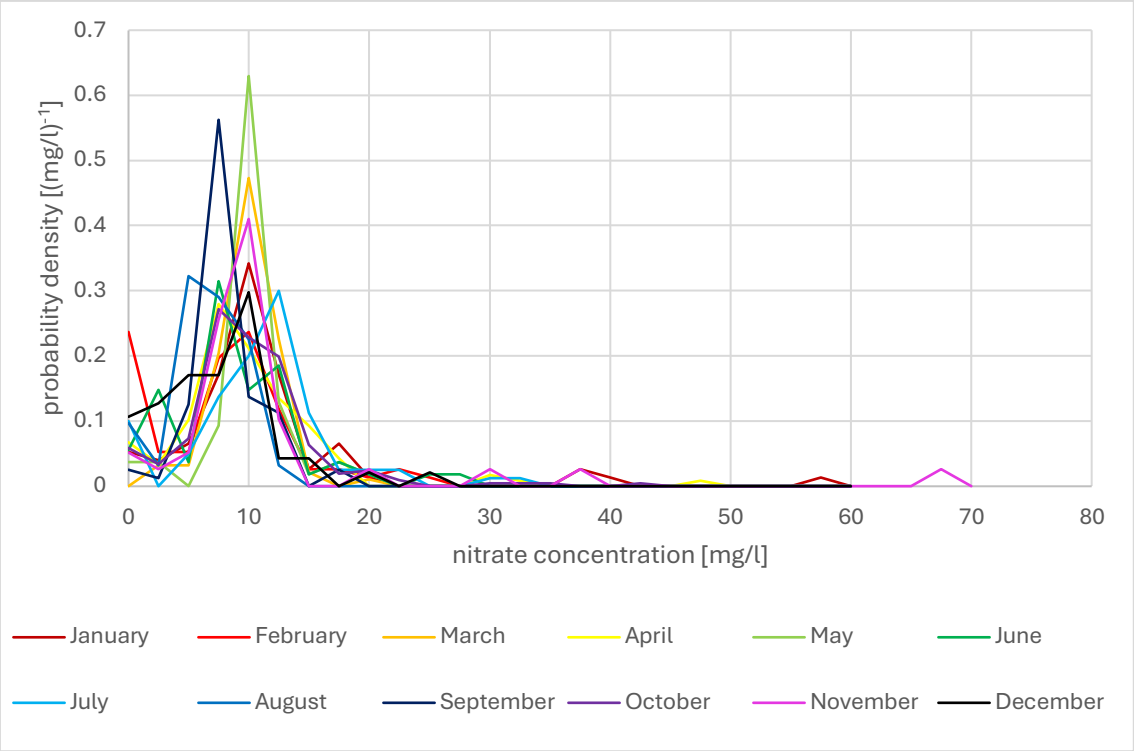

Figure 62. Nitrates, Agno valley: probability density function of concentration between 1988 and 2023.

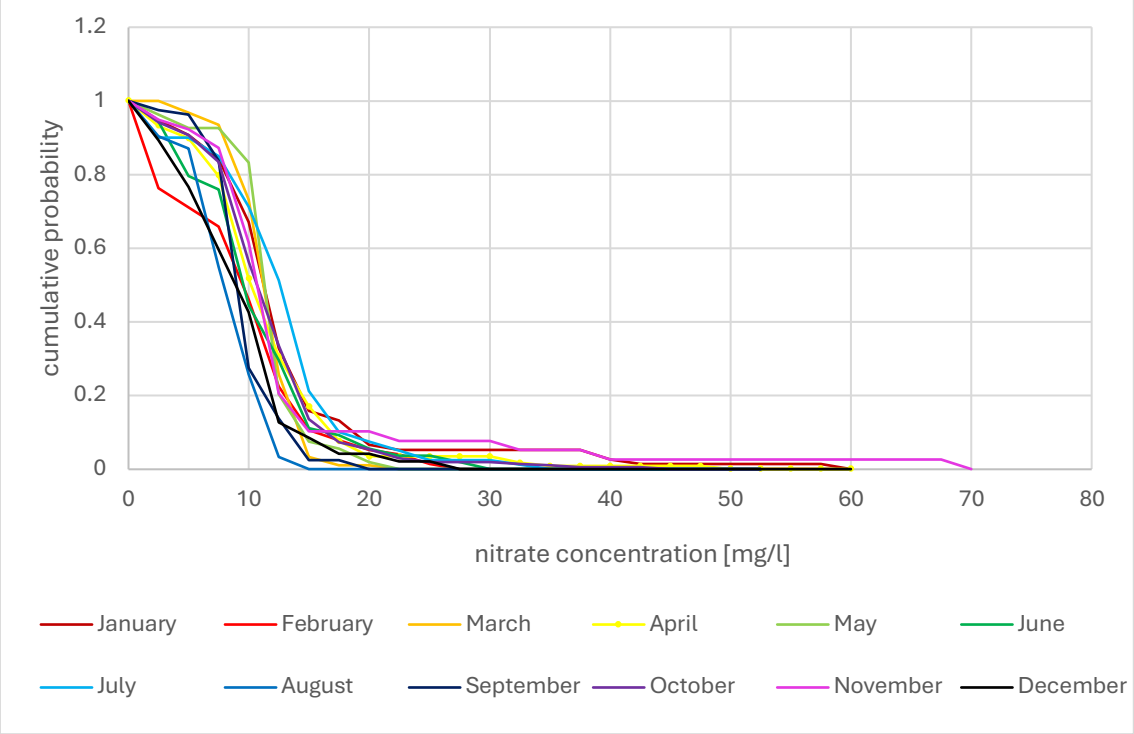

Figure 63. Nitrates, Agno valley: cumulative probability distribution of monthly-averaged concentration values.

Finally, Figure 64 provides the map of the recorded values for year 2018. When more than one sample is available in a single well per year, the value shown in the figure correspond to the average.

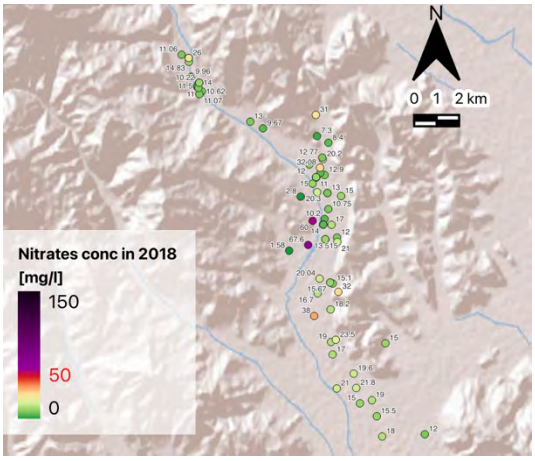

Figure 64. Nitrates, Agno valley: distribution of the measured concentration in the year 2018. Notice that the color legend used to represent the measurements is consistent with that used for the Vicenza high plain (Figure 52 and Figure 54).

5.3. PESTICIDES – DACT

5.3.1. VICENZA HIGH PLAIN

The third pollutant analyzed is a specific chemical coming from pesticides, the diaminochloramide (DACT). In this case the data series cover a period much shorter than those of total solvents and nitrates, starting only in 2019 (Figure 65).

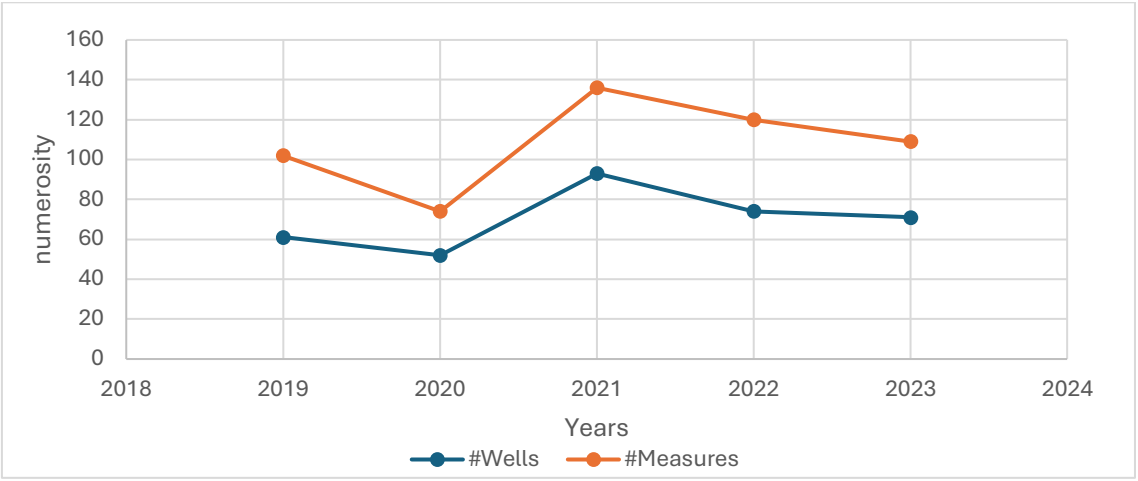

Figure 65. DACT, Vicenza high plain: yearly number of sampled wells between 2019 and 2023.

Despite the limited number of years in the historical dataset, the Kriging method can still be applied thanks to the large number of sampled wells. Consequently, an initial statistical analysis is required. Figure 66 and Figure 67 display the histogram and boxplot for the entire dataset of DACT concentrations.

By analyzing the histogram and boxplot, it is evident that the distribution closely resembles a Gaussian distribution. However, the high frequency of null values skews the graph significantly to the left. Generally, the values remain within legal limits, with only a few sporadic instances of excessively high concentrations.

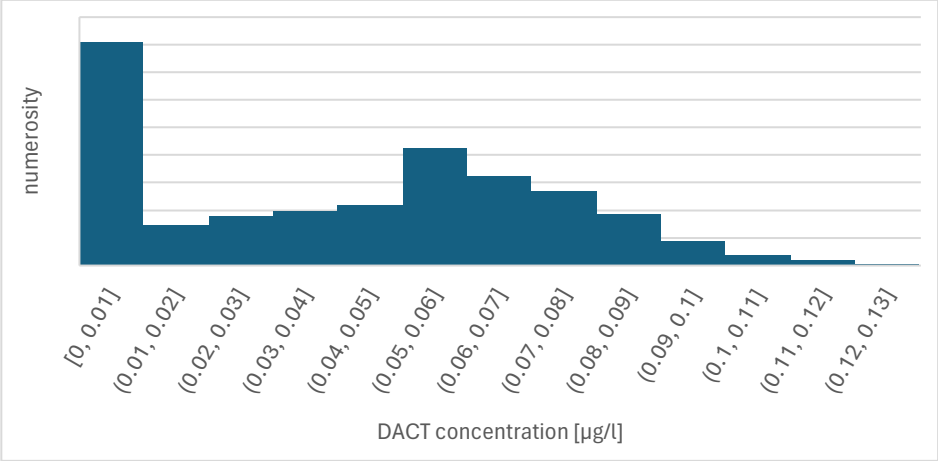

Figure 66. DACT, Vicenza high plain: histogram of concentration between 2019 and 2023.

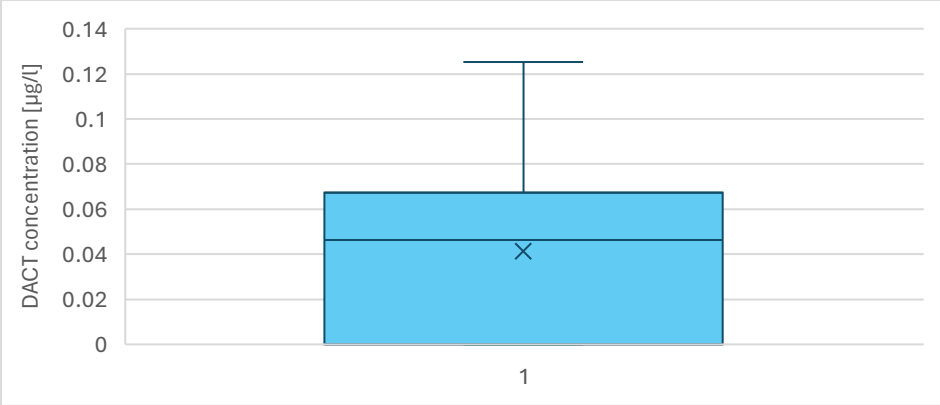

Figure 67. DACT, Vicenza high plain: boxplot of the concentration between 2019 and 2023.

This observation is further supported by the year statistics presented in Table 10. Data distributions are similar for each year.

Table 10. DACT, Vicenza high plain: descriptive statistics of concentration values for the monitored years.

Year	μ [μg/l]	Mode [μg/l]	Q1 [μg/l]	Median [μg/l]	Q3 [μg/l]	σ^2 $[(\mu g/l)^2]$	CV [-]	G [-]	Min [μg/l]	Max [μg/l]
2019	0.04	0.00	0.00	0.05	0.06	0.03	4.44	0.05	0.00	0.10
2020	0.04	0.00	0.00	0.04	0.08	0.04	4.77	0.30	0.00	0.13
2021	0.04	0.00	0.00	0.04	0.07	0.03	4.81	0.24	0.00	0.12
2022	0.03	0.00	0.00	0.03	0.06	0.03	5.52	0.38	0.00	0.10
2023	0.03	0.00	0.00	0.03	0.06	0.03	5.36	0.29	0.00	0.10

The skewness coefficient is not high, with median and mode quite similar. Although data show an almost optimal distribution for the application of Kriging method, the log-normal transformation is applied, producing the descriptive statistics reported in Table 11.

Table 11. DACT, Vicenza high plain: descriptive statistics of log-transformed data.

Year	μ [μg/l]	Mode [μg/l]	Q1 [μg/l]	Median [μg/l]	Q3 [μg/l]	σ^2 $[(\mu g/l)^2]$	CV [-]	G [-]	Min [μg/l]	Max [μg/l]
2019	0.02	0.00	0.00	0.02	0.03	0.01	6.82	0.02	0.00	0.04
2020	0.02	0.00	0.00	0.02	0.03	0.02	7.34	0.27	0.00	0.05
2021	0.02	0.00	0.00	0.02	0.03	0.01	7.40	0.21	0.00	0.05
2022	0.01	0.00	0.00	0.01	0.02	0.01	8.47	0.35	0.00	0.04
2023	0.01	0.00	0.00	0.01	0.03	0.01	8.23	0.27	0.00	0.04

Although the distribution shape is satisfactory even without data normalization, applying a logarithmic transformation brings it closer to the ideal distribution. Therefore, the modified data have been used in the geostatistical analysis. The parameters of the isotropic variogram models are summarized in Table 12.

Table 12. DACT, Vicenza high plain: isotropic variogram model for each year.

Isotropic analysis							
Year	**Mean Dist [m]**	**Model**	**Lag [m]**	**Nugget**	**Partial Sill**	**Range [m]**	**RMSE**
2019	714.13	Gaussian	1200	5.49E-05	0.0003	24000	0.0069
2020	940.84	Gaussian	1500	5.04E-05	0.0004	18000	0.0067
2021	887.11	Gaussian	1400	3.06E-05	0.0003	24000	0.0059
2022	760.51	Gaussian	1200	3.21E-05	0.0002	17394	0.0065
2023	775.16	Gaussian	1200	3.15E-05	0.0002	18000	0.0058

The maps of the expected value and associated standard deviation obtained by Kriging are shown in Figure 68 and 69, respectively.

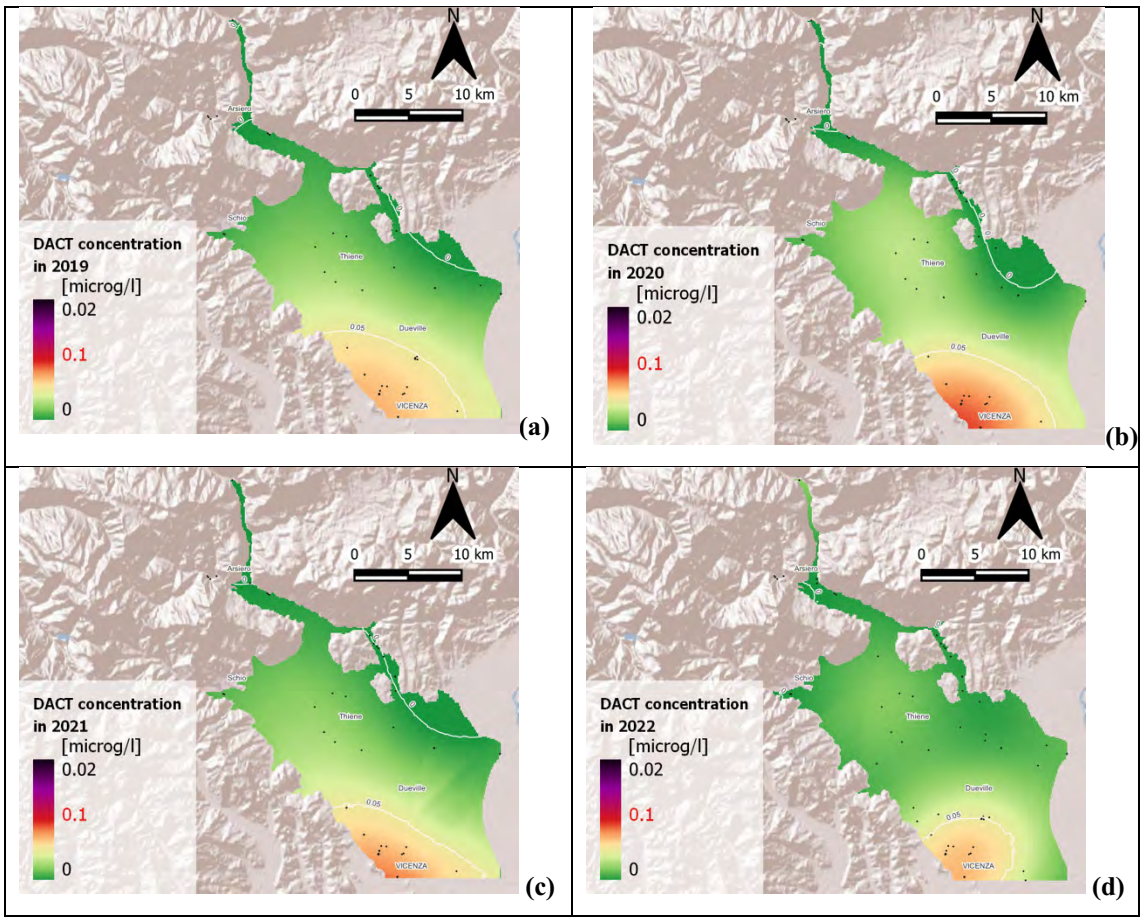

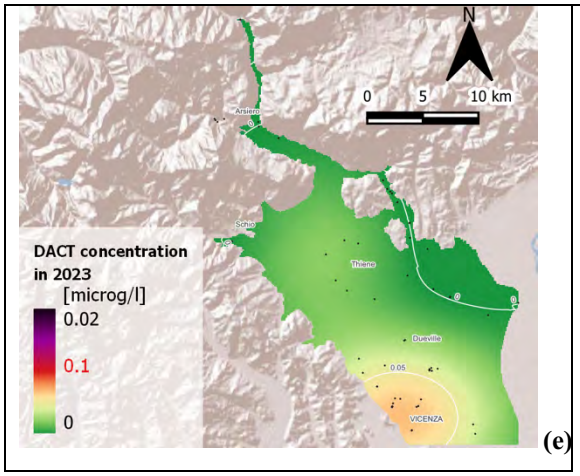

Figure 68. DACT, Vicenza high plain: maps of the expected values resulting from Kriging interpolation with isotropic variogram for the years (a) 2019, (b) 2020, (c) 2021, (d) 2021, and (3) 2023. The black dots represent the locations of the wells used to build-up the map. The red number in the legend represents the max concentration admissible by law.

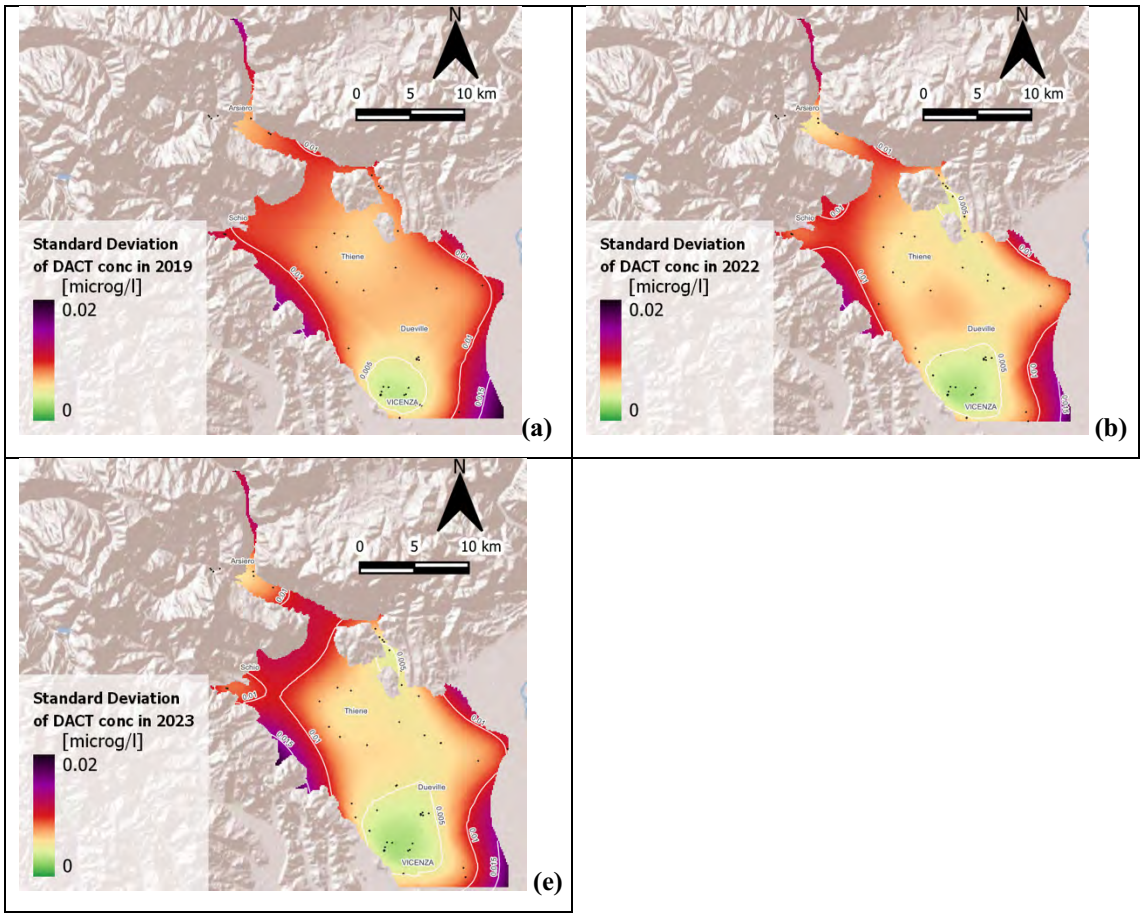

Figure 69. DACT, Vicenza high plain: maps of the standard deviation resulting from Kriging interpolation with isotropic variogram for the years (a) 2019, (b) 2022, and (d) 2023. The black dots represent the locations of the wells used to build-up the map.

The same analysis has been developed using anisotropic variograms. The parameters of the variogram models fitted on the data are provided in Table 13 and the results of the

Kriging interpolation in terms of expected values and associated standard deviation are mapped in Figure 70 and Figure 71, respectively.

Table 13. DACT, Vicenza high plain: parameters of the anisotropic variogram models.

Ansotropic analysis								
Year	**Model**	**Lag [m]**	**Preferential angle [°]**	**Nugget**	**Partial Sill**	**Major Range [m]**	**Minor range [m]**	**RMSE**
2019	Gaussian	1200.0	125.0	6.14E-05	0.00014	19000.00	14435.00	0.0068
2020	Gaussian	1500.0	119.0	5.46E-05	0.0002	18000.00	11000.00	0.0065
2021	Gaussian	1400.0	118.0	2.54E-05	0.00028	25000.00	18000.00	0.0061
2022	Gaussian	1200.0	110.0	3.36E-05	0.00016	20000.00	10000.00	0.0066
2023	Gaussian	1200.0	118.0	3.06E-05	0.0002	24000.00	13300.00	0.0063

The comparison between Figure 70 and Figure 71 points out how anisotropy plays a negligible for DACT.

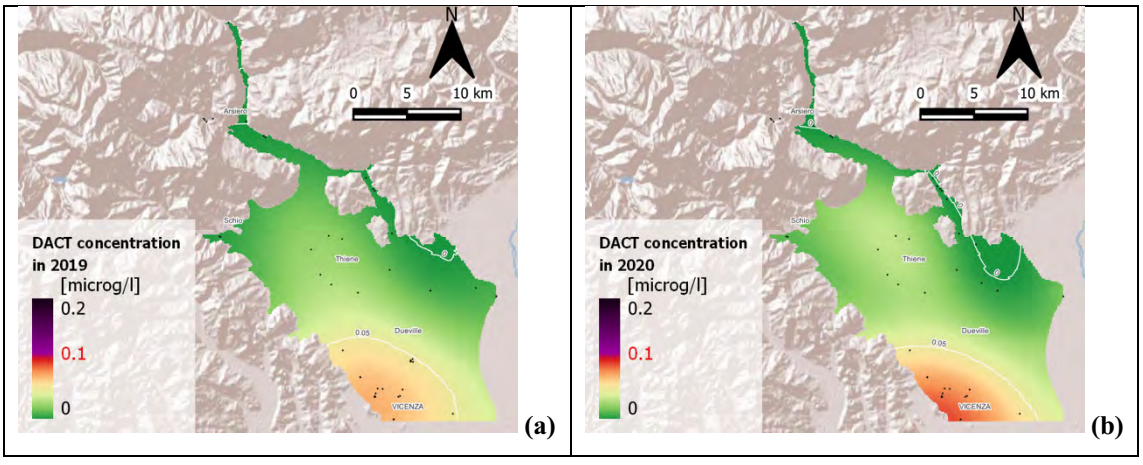

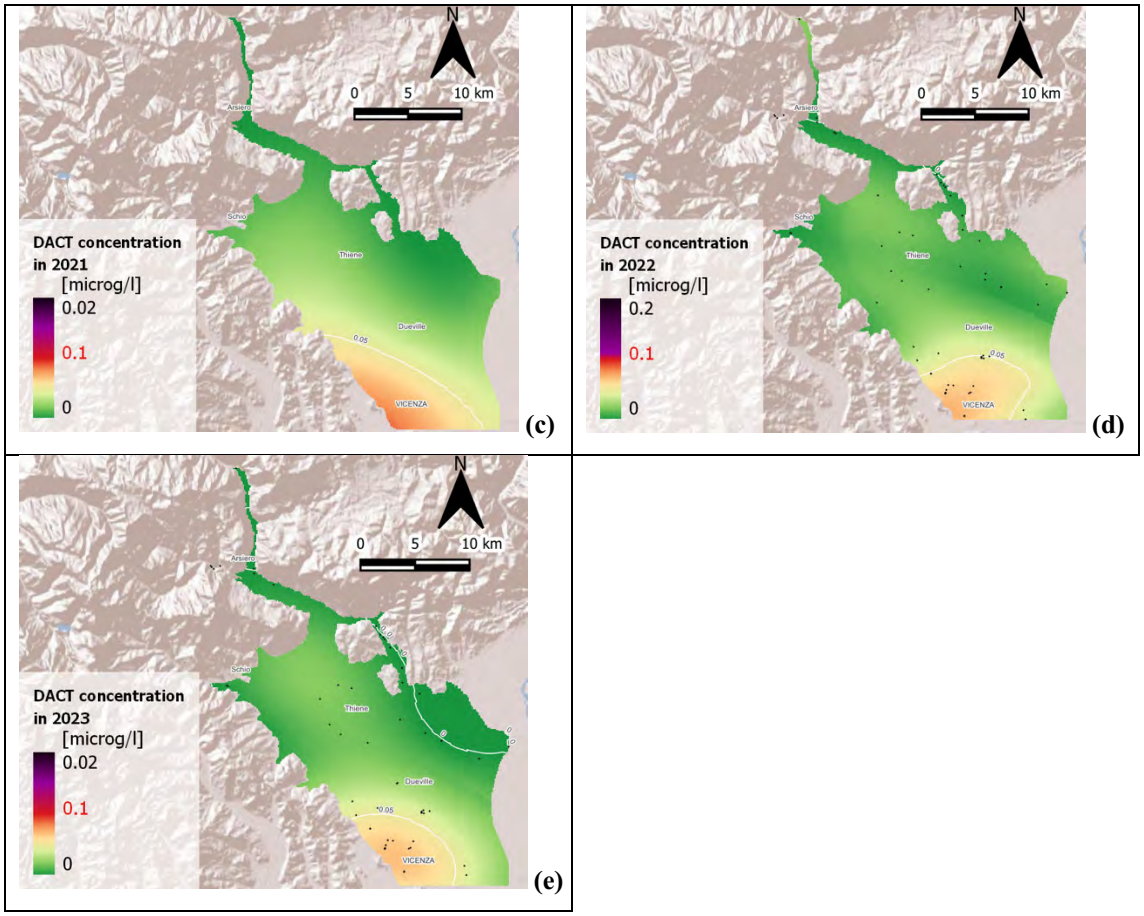

Figure 70. DACT, Vicenza high plain: maps of the expected values resulting from Kriging interpolation with anisotropic variogram for the years (a) 2019, (b) 2020, (c) 2021, (d) 2021, and (3) 2023. The black dots represent the locations of the wells used to build-up the map. The red number in the legend represents the max concentration admissible by law.

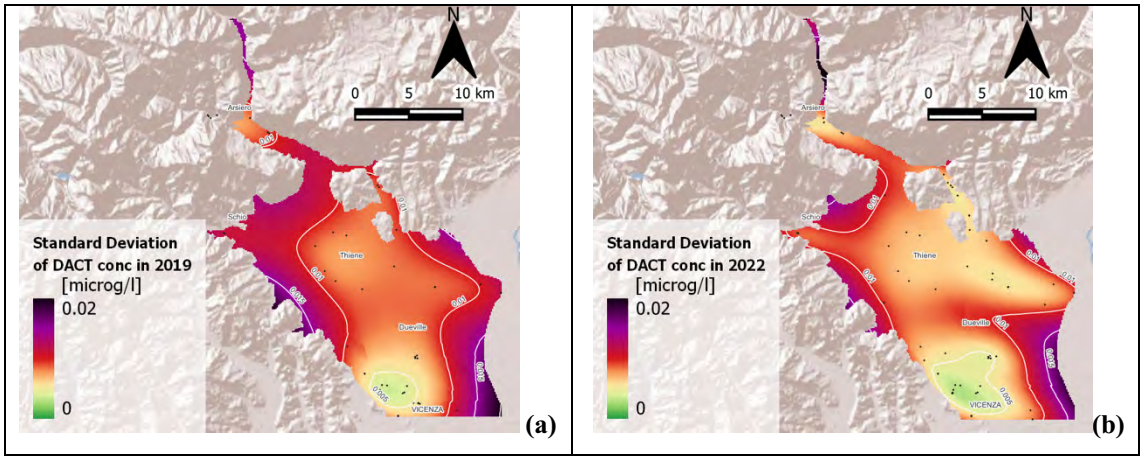

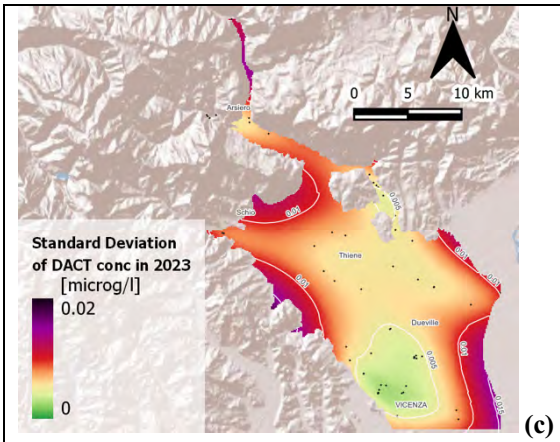

Figure 71. DACT, Vicenza high plain: maps of the standard deviation resulting from Kriging interpolation with anisotropic variogram for the years (a) 2019, (b) 2022, and (c) 2023. The black dots represent the locations of the wells used to build-up the map.

5.3.2. AGNO VALLEY

Regarding the Agno Valley, there are limited data to draw any meaningful conclusions. As shown in Figure 72, the dataset is insufficient for a reliable statistical analysis. The number of samples collected each year never exceeds 10, reaching 20 only in 2023.Only 48 samples were gathered over the four years between 2019 and 2023.

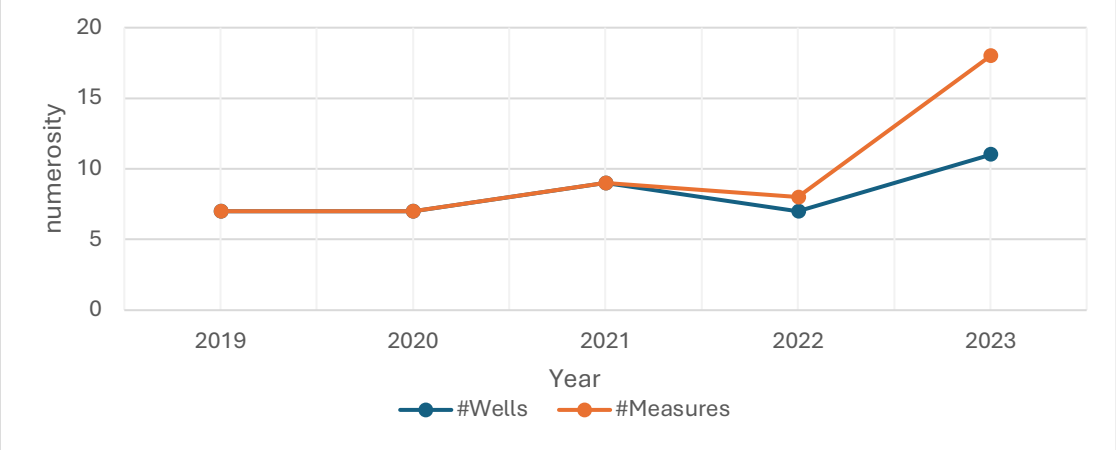

Figure 72. DACT, Agno valley: number of sampled wells and measurements between 2019 and 2023.

The recorded values consistently remain below the legal limits and are generally equal to zero, with only two exceptions. These two cases occurred at different locations (Figure 32):

- in well P03006, a concentration of 0.02183 µg/l was recorded on October 17th, 2023. However, a subsequent sample taken on October 30th, 2023, showed a null DACT concentration of zero.
- in well P06001, the same pollutants was measured with a concentration of 0.07085 µg/l on November 14th, 2023. No further inspections have been conducted to confirm or reassess the water quality at this location, so no definitive conclusions can be made. Additionally, there is no historical data for this well, so, nothing can be said about the water quality in that point with that isolated measure.

5.4. CHLORIDES

5.4.1. VICENZA HIGH PLAIN

An initial check on the number of sampled wells is conducted by comparing the number of measurements available each year with the number of sampled wells. The results are displayed in Figure 73. The peak of collected measures was in 2018 with 453 samples, while the minimum inspected year is 1982. The number of data sufficient for the statistical and geostatistical analyses was reached since 1985. The total sample size amounts to 7178.

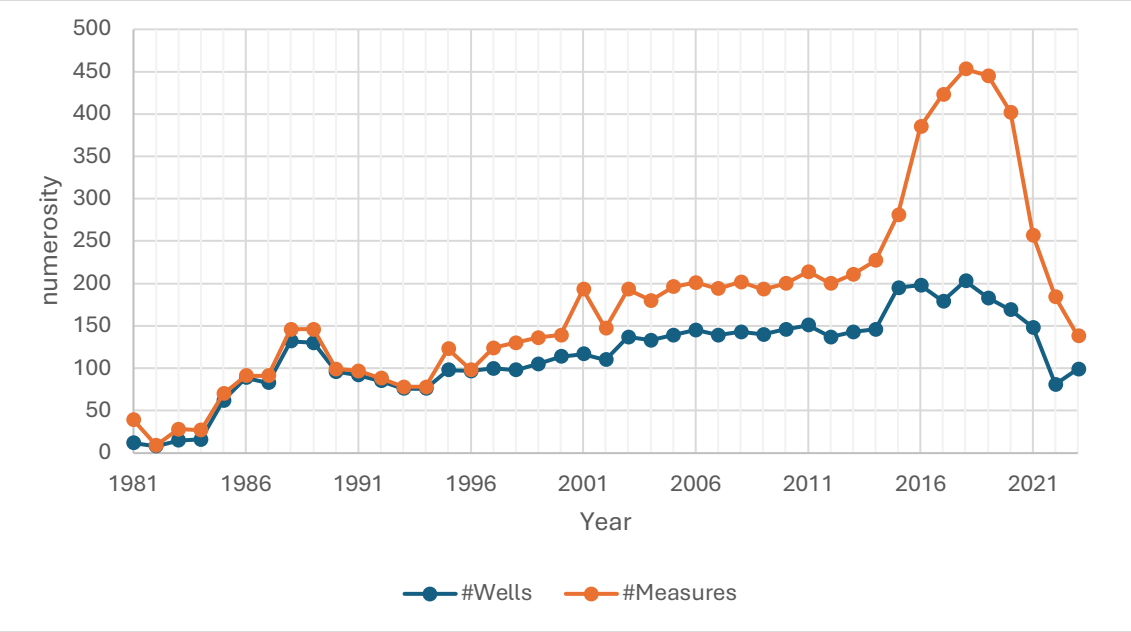

Figure 73. Chlorides, Vicenza high plain: yearly number of sampled wells and measurements between 1981 and 2023.

A preliminary analysis of the contaminant concentration values is conducted by examining the distribution of the entire dataset. This provides an initial understanding of the most commonly occurring values and the overall distribution, which is visualized using a histogram and a boxplot in Figure 74 and 75. The law limit is never exceeded, with the highest recorded value equal to 134.5 mg/l. Most of the values are placed in the classes (6,8] and (8,10] mg/l.

The histogram is characterized by a pronounced right tail, and the boxplot evidences it by the position of the third quartile and of the mean.

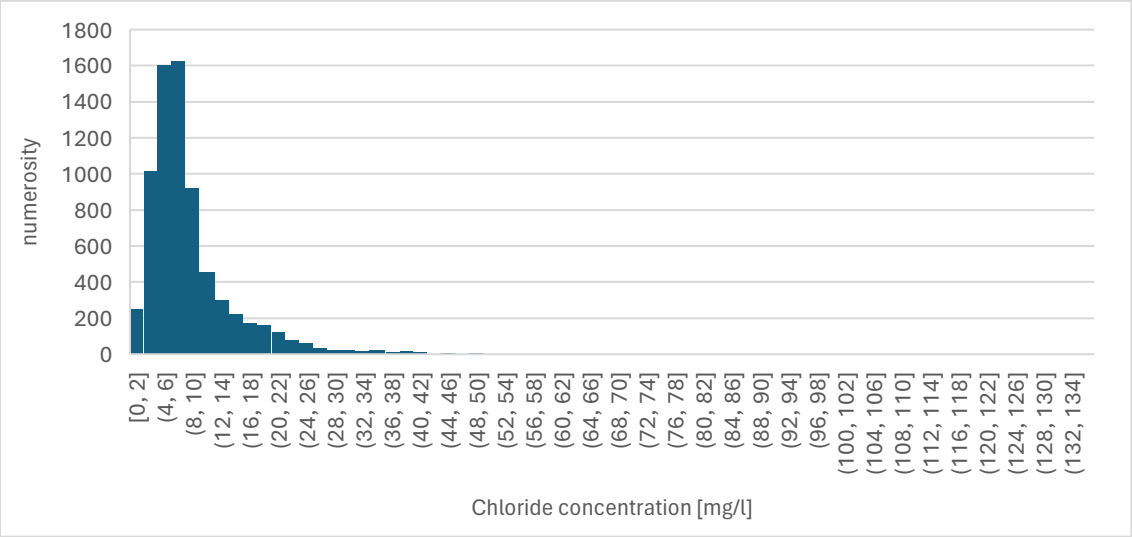

Figure 74. Chlorides, Vicenza high plain: histogram of concentrations data between 1981 and 2023.

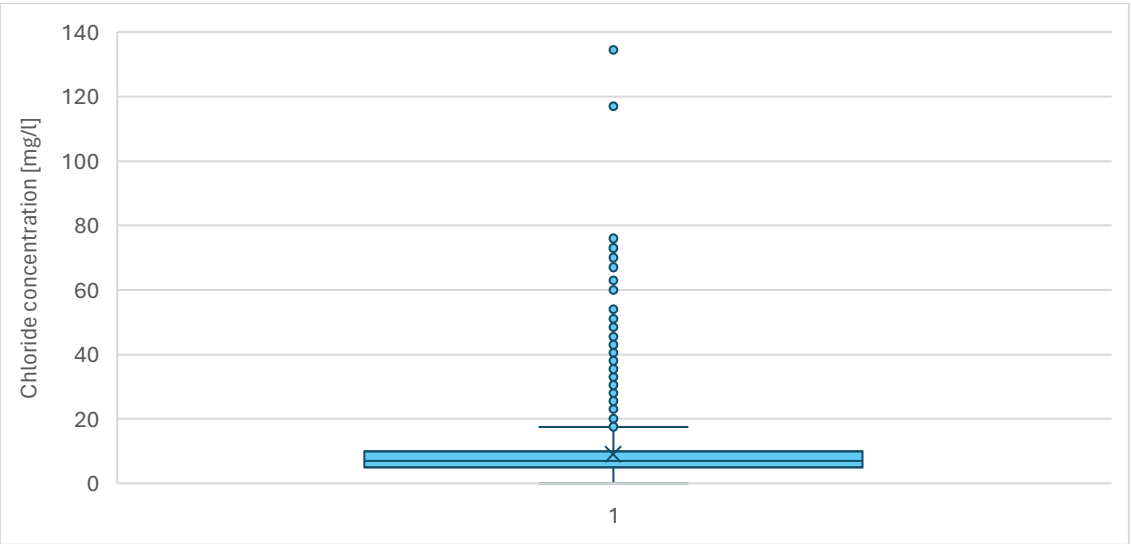

Figure 75. Chlorides, Vicenza high plain: boxplot of the concentration between 1981 and 2023.

Many of the values that exceeded the whiskers of the boxplot originate from the well VIFA-6 (Figure 32). This well is located in the nearby of a dry-cleaning facility, whose activity likely impacts water quality through the use of detergents. However, this elevated value remains below the maximum concentration permitted by law of 250 mg/l. Additionally, the historical data for well VIFA-6 shows significant decline in chloride concentrations over time, as evident in Figure 76.

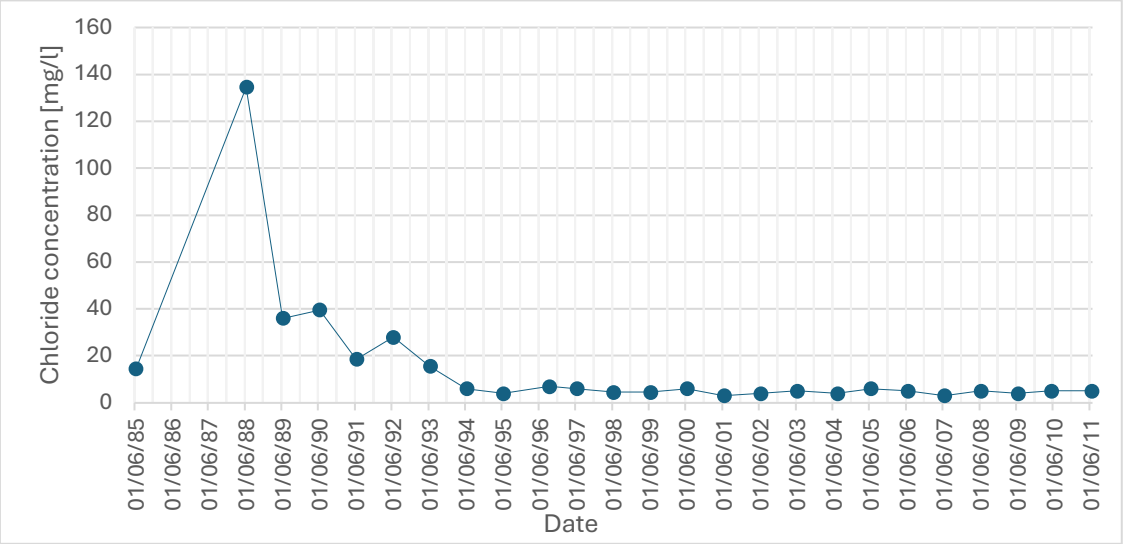

Figure 76. Chlorides concentration versus time measured at well VIFA-6.

The descriptive statistics for each analyzed year are reported in the Table 14.

Table 14. Summary of descriptive statistics of data collected in the analyzed years in the domain.

Year	μ [mg/l]	Mode [mg/l]	Q1 [mg/l]	Median [mg/l]	Q3 [mg/l]	σ^2 $[(mg/l)^2]$	CV [-]	G [-]	Min [mg/l]	Max [mg/l]
1985	7.56	6.50	6.00	7.00	8.50	3.34	0.24	1.98	1.00	23.50
1988	11.07	6.00	4.69	7.50	13.50	13.53	0.33	6.21	2.00	134.50
1991	13.35	7.00	7.00	10.00	14.63	10.98	0.25	2.00	1.50	51.50
1994	10.07	3.00	5.50	8.75	11.25	6.55	0.25	1.29	2.50	30.50
1997	9.04	3.50	5.50	7.63	11.31	5.16	0.25	1.40	3.00	26.50
2000	9.64	7.50	4.63	7.38	11.00	8.19	0.30	2.32	1.00	47.50
2003	9.37	4.00	5.00	7.00	11.00	8.12	0.30	3.07	1.00	61.50
2006	8.32	3.00	3.00	6.00	10.00	7.60	0.33	2.28	0.00	41.67

2009	8.81	8.00	4.69	7.67	10.00	6.68	0.29	2.44	1.00	49.00
2012	8.32	4.00	5.00	6.00	9.00	5.61	0.28	1.61	1.00	29.00
2015	7.12	3.00	4.00	6.00	8.00	4.81	0.31	2.50	1.00	38.00
2018	8.16	6.00	5.06	6.46	9.00	4.85	0.27	2.29	1.00	34.00
2021	7.35	4.70	4.70	6.77	8.25	4.26	0.28	1.27	0.90	21.60
2022	6.31	3.40	3.66	5.92	7.78	4.23	0.33	2.49	0.88	29.84
2023	6.52	3.70	3.82	5.47	7.22	5.62	0.36	4.29	1.29	45.35

The mean concentration values consistently range between 6 and 10, and the coefficient of variation supports the observation. The distributions show a high skewness, with a tail always oriented to the right part of the graph. This is not surprising as the values of the mean, mode, first, second and third quartiles are relatively close each other, while the maximum value is much higher.

The outcome of the data logarithmic transformation is shown in Table 15.

Table 15. Summary of descriptive statistics of the long transformed data collected in the analyzed years in the domain.

Year	**μ [mg/l]**	**Mode [mg/l]**	**Q1 [mg/l]**	**Median [mg/l]**	**Q3 [mg/l]**	**σ^2 $[(mg/l)^2]$**	**CV [-]**	**G [-]**	**Min [mg/l]**	**Max [mg/l]**
1985	0.90	0.88	0.85	0.90	0.98	0.16	0.45	-0.53	0.30	1.39
1988	0.97	0.85	0.75	0.93	1.16	0.29	0.56	0.80	0.48	2.13
1991	1.06	0.90	0.90	1.04	1.19	0.29	0.50	0.20	0.40	1.72
1994	0.98	0.60	0.81	0.99	1.09	0.24	0.50	0.19	0.54	1.50
1997	0.95	0.65	0.81	0.94	1.09	0.20	0.47	0.42	0.60	1.44
2000	0.93	0.93	0.75	0.92	1.08	0.28	0.56	0.32	0.30	1.69
2003	0.93	0.70	0.78	0.90	1.08	0.25	0.54	0.66	0.30	1.80
2006	0.86	0.60	0.60	0.85	1.04	0.31	0.64	0.06	0.00	1.63
2009	0.92	0.95	0.75	0.94	1.04	0.25	0.55	0.25	0.30	1.70
2012	0.91	0.70	0.78	0.85	1.00	0.23	0.53	0.27	0.30	1.48
2015	0.85	0.60	0.70	0.85	0.95	0.21	0.54	0.40	0.30	1.59
2018	0.92	0.85	0.78	0.87	1.00	0.18	0.47	0.80	0.30	1.54
2021	0.87	0.76	0.76	0.89	0.97	0.22	0.55	-0.37	0.28	1.35
2022	0.80	0.64	0.67	0.84	0.94	0.23	0.60	-0.17	0.27	1.49
2023	0.81	0.67	0.68	0.81	0.91	0.22	0.58	0.66	0.36	1.67

Thanks to the logarithmic transformation, the values of mode, mean and median become closer, while the maximum value decreases too. This leads to an enhancement in symmetry, which in some cases even assumes negative values.
Variogram models have been defined using the log-transformed data Table 16 provides the parameters of the isotropic variogram models.

Table 16. Chlorides, Vicenza high plain: isotropic variogram model for each selected year.

Isotropic analysis							
Year	**Mean distance [m]**	**Model**	**Lag [m]**	**Nugget**	**Partial sill**	**Range [m]**	**RMSE**
1985	724.73	Exponential	1000.0	0.0030	0.03	5000.00	0.17
1988	695.83	Exponential	1000.0	0.0200	0.06	3000.00	0.27
1991	832.88	Exponential	1300.0	0.0100	0.09	9800.00	0.23
1994	876.00	Exponential	1300.0	0	0.08	11000.00	0.14
1997	848.00	Exponential	1300.0	0.0040	0.04	6000.00	0.15
2000	737.88	Exponential	1200.0	0	0.07	10000.00	0.15
2003	744.66	Exponential	1300.0	0	0.05	10000.00	0.14
2006	686.00	Exponential	1000.0	0.0050	0.08	8000.00	0.19
2009	632.70	Exponential	1000.0	0	0.067	10000.00	0.15
2012	648.17	Exponential	1000.0	0	0.05	7000.00	0.14
2015	504.6	Exponential	1000.0	0.0070	0.05	16000.00	0.14
2018	601.88	Exponential	1000.0	0	0.035	10000.00	0.16
2021	669.00	Exponential	1200.0	0	0.04	9066.00	0.10
2022	734.66	Exponential	1200.0	0.0010	0.04	16000.00	0.13
2023	635.40	Exponential	1000.0	0.001	0.04	17000	0.17

The maps of the expected value of chloride concentration resulting from the Kriging interpolation are presented in Figure 77. The associated standard deviation for the years 1988, 2006, and 2022 are illustrated in Figure 78.

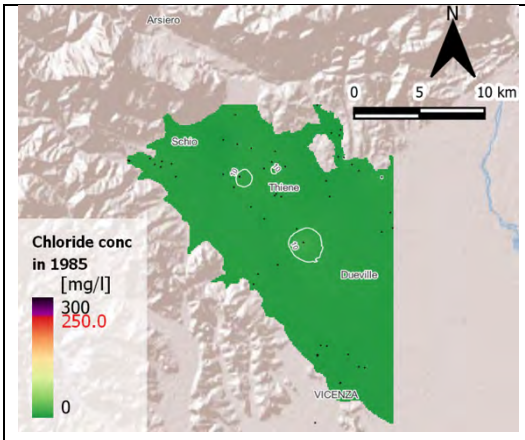
Arsiero
N
0 5 10 km
Schio
Thiene
Dueville
VICENZA
Chloride conc
in 1985
[mg/l]
300
250.0
0

(a)

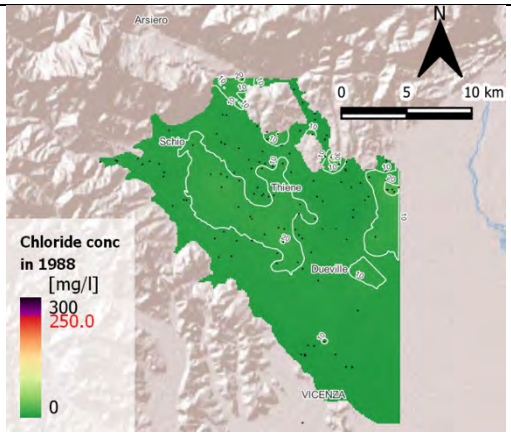
Arsiero
N
0 5 10 km
Schio
Thiene
Dueville
VICENZA
Chloride conc
in 1988
[mg/l]
300
250.0
0

(b)

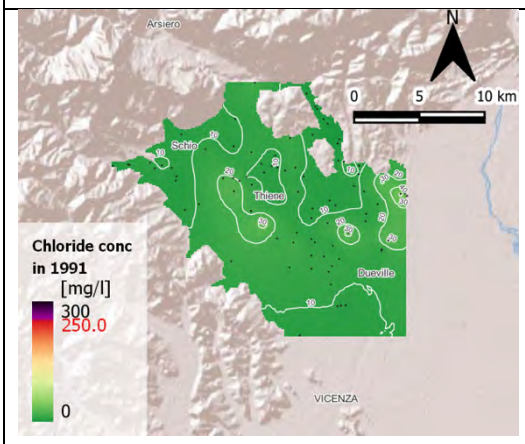
Arsiero
N
0 5 10 km
Schio
Thiene
Dueville
VICENZA
Chloride conc
in 1991
[mg/l]
300
250.0
0

(c)

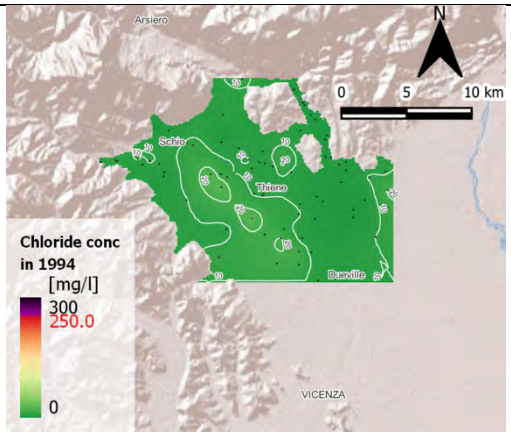
Arsiero
N
0 5 10 km
Schio
Thiene
Dueville
VICENZA
Chloride conc
in 1994
[mg/l]
300
250.0
0

(d)

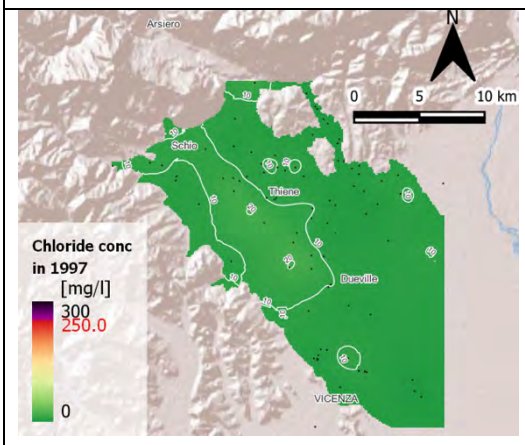
Arsiero
N
0 5 10 km
Schio
Thiene
Dueville
VICENZA
Chloride conc
in 1997
[mg/l]
300
250.0
0

(e)

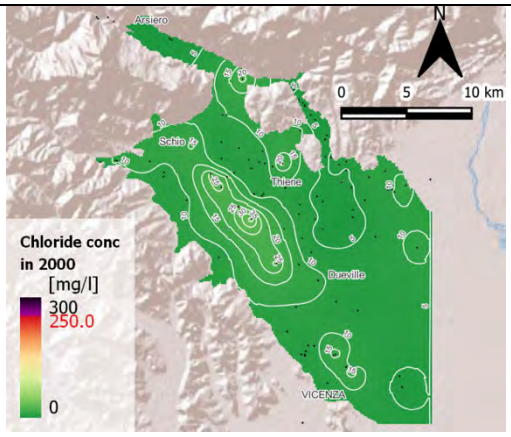
Arsiero
N
0 5 10 km
Schio
Thiene
Dueville
VICENZA
Chloride conc
in 2000
[mg/l]
300
250.0
0

(f)

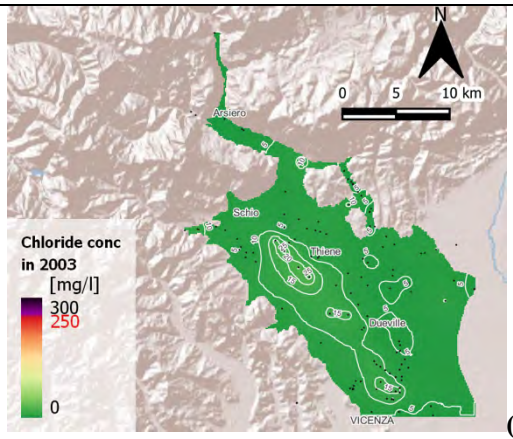
N
0 5 10 km
Arsiero
Schio
Thiene
Dueville
VICENZA
Chloride conc
in 2003
[mg/l]
300
250
0
(g)

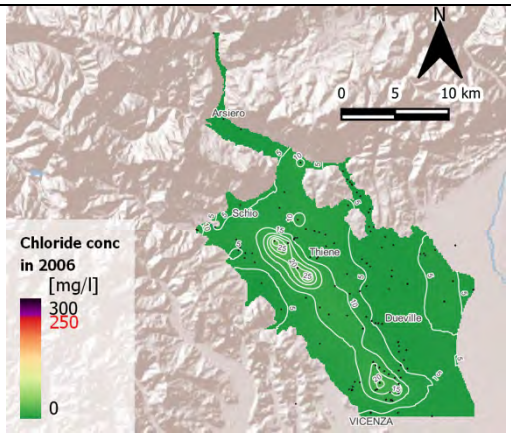
N
0 5 10 km
Arsiero
Schio
Thiene
Dueville
VICENZA
Chloride conc
in 2006
[mg/l]
300
250
0
(h)

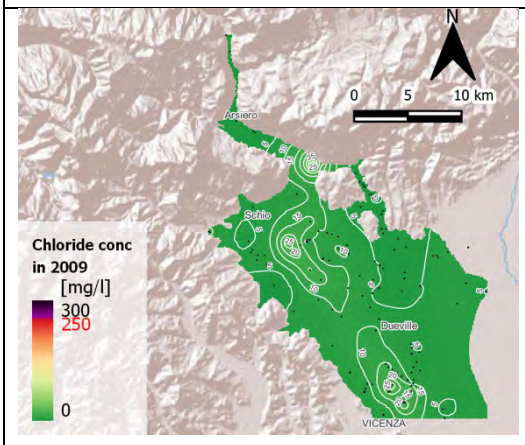
N
0 5 10 km
Arsiero
Schio
Thiene
Dueville
VICENZA
Chloride conc
in 2009
[mg/l]
300
250
0
(i)

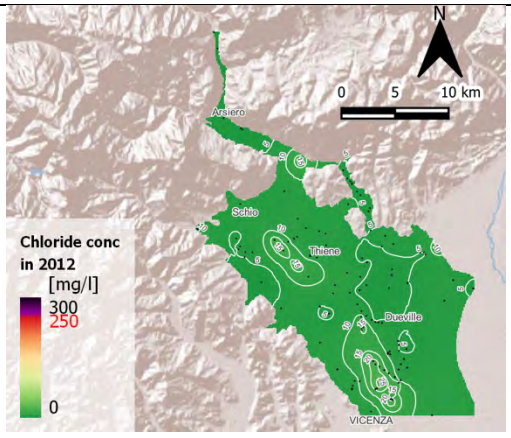
N
0 5 10 km
Arsiero
Schio
Thiene
Dueville
VICENZA
Chloride conc
in 2012
[mg/l]
300
250
0
(l)

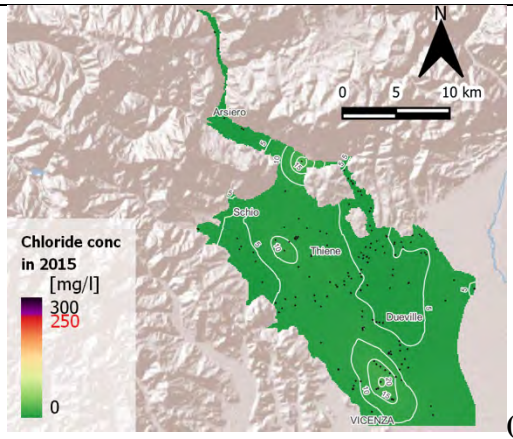
N
0 5 10 km
Arsiero
Schio
Thiene
Dueville
VICENZA
Chloride conc
in 2015
[mg/l]
300
250
0
(m)

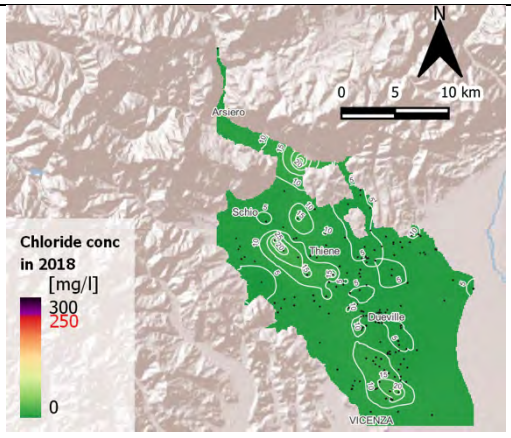
N
0 5 10 km
Arsiero
Schio
Thiene
Dueville
VICENZA
Chloride conc
in 2018
[mg/l]
300
250
0
(n)

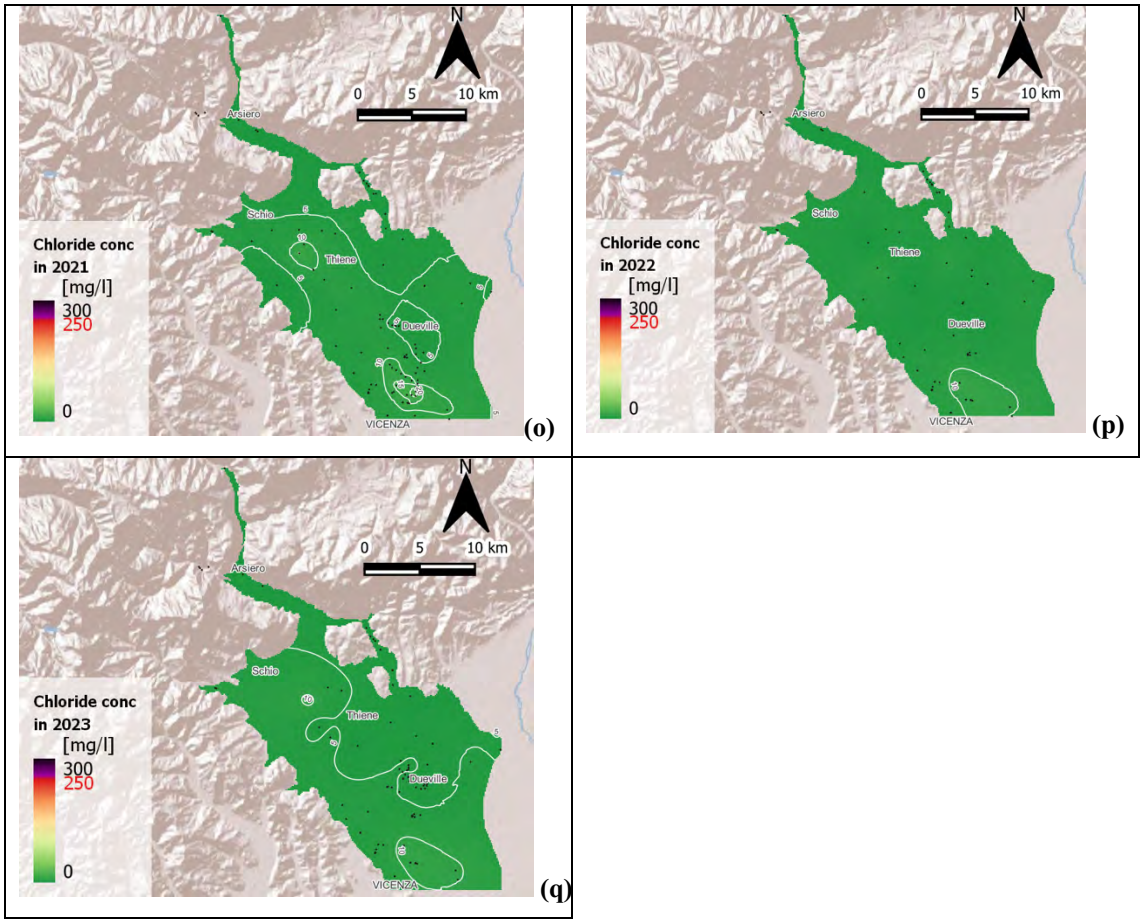

Figure 77. Chlorides, Vicenza high plain: maps of the expected values resulting from Kriging interpolation with anisotropic variogram for the years (a) 1985, (b) 1988, (c) 1991, (d) 1994, (e) 1997, (f) 2000, (g) 2003, (h) 2006, (i) 2009, (l) 2012, (m) 2015, (n) 2018, (o) 2021, (p) 2022, and (q) 2023. Map extension can vary depending on well availability. The black dots represent the locations of the wells used to build-up the map. The red number in the legend represents the max concentration admissible by law.

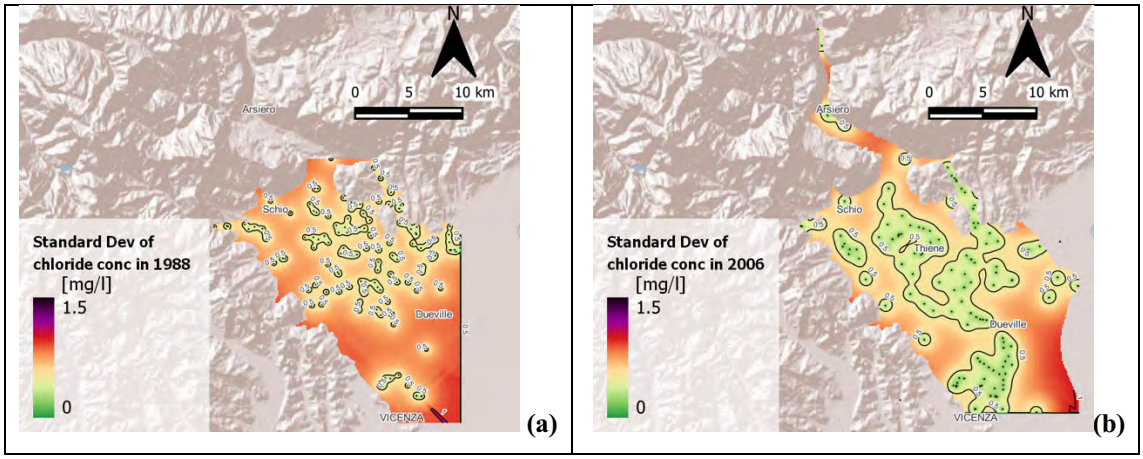

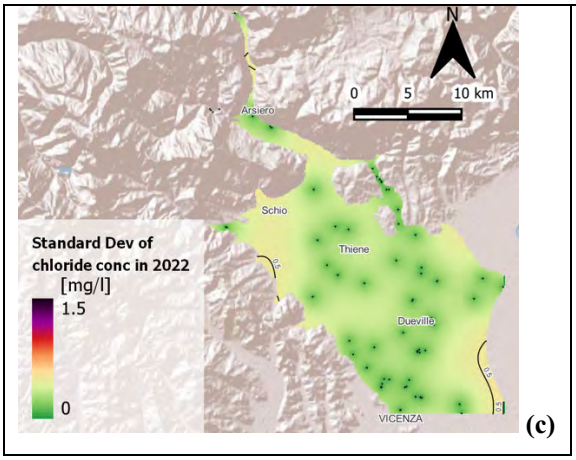

Figure 78. Chlorides, Vicenza high plain: maps of the standard deviation resulting from Kriging interpolation with anisotropic variogram for the years (a) 1988, (b) 2006, and (c) 2022. Map extension can vary depending on well availability. The black dots represent the locations of the wells used to build-up the map.

For what concerns the anisotropic analysis, the resulting interpolation parameters are reported in Table 17, followed by the maps of the expected value of the concentration (Figure 79) and the associated standard deviation for the years 1988, 2006 and 2022 (Figure 80).

Table 17. Chlorides, Vicenza high plain: parameters of the anisotropic variogram models.

Ansotropic analysis								
Year	**Model**	**Lag [m]**	**Pref Angle [°]**	**Nugget**	**Partial sill**	**Major range [m]**	**Minor range [m]**	**RMSE**
1985	Exponential	1000.0	123.0	0	0.04	10000.00	4000.00	0.17
1988	Exponential	1300.0	142.0	0.0400	0.05	13000.00	3000.00	0.25
1991	Exponential	1300.0	130.0	0	0.10	13000.00	6862.00	0.23
1994	Exponential	1300.0	155.0	0	0.07	12000.00	5000.00	0.13
1997	Exponential	1300.0	151.0	0.0030	0.04	13226.00	5000.00	0.13
2000	Exponential	1200.0	152.0	0	0.07	16500.00	4500.00	0.14
2003	Exponential	1300.0	147.0	0	0.05	15000.00	4000.00	0.13
2006	Exponential	1000.0	145.0	0	0.09	16000.00	4000.00	0.18
2009	Exponential	1000.0	150.0	0.0020	0.06	18000.00	6040.00	0.15
2012	Exponential	1000.0	144.0	0	0.05	17000.00	6000.00	0.13

2015	Exponential	1000.0	143.0	0.0020	0.05	18000.00	7700.00	0.13
2018	Exponential	1000.0	146.0	0	0.04	15000.00	5600.00	0.16
2021	Exponential	1000.0	136.0	0	0.04	15600.00	5208.00	0.09
2022	Exponential	1200.0	133.0	0	0.04	17000.00	8000.00	0.12
2023	Gaussian	1000.0	144.0	0.018	0.03	14500.00	10000.00	0.17

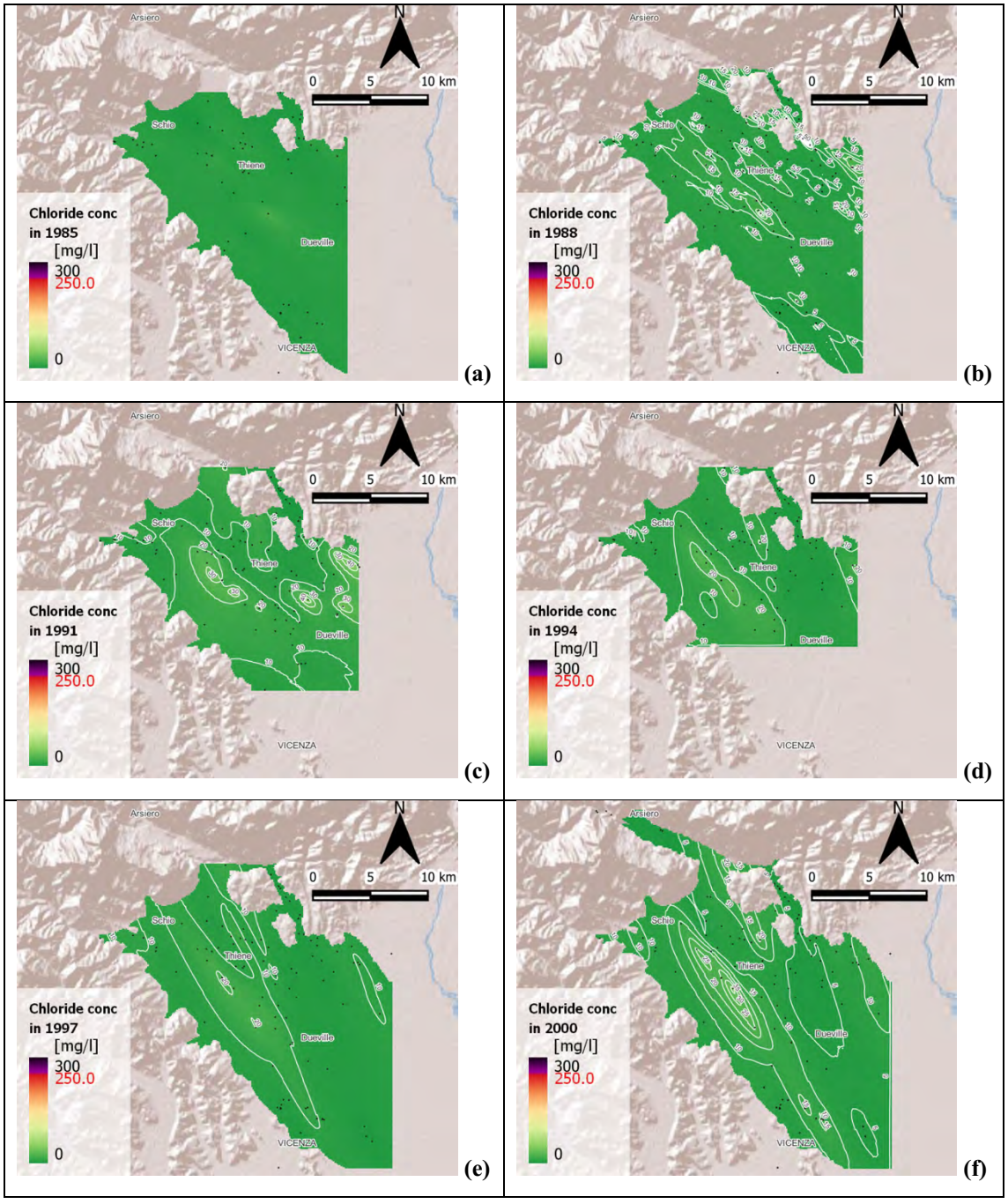

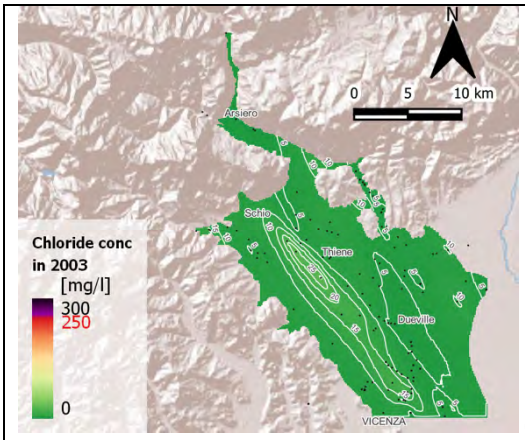
N
0 5 10 km
Arsiero
Schio
Thiene
Dueville
VICENZA
Chloride conc
in 2003
[mg/l]
300
250
0
(g)

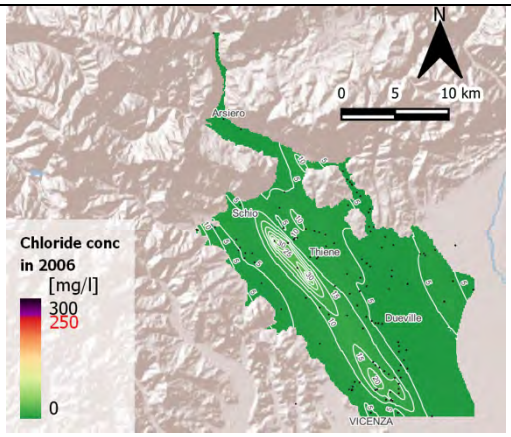
N
0 5 10 km
Arsiero
Schio
Thiene
Dueville
VICENZA
Chloride conc
in 2006
[mg/l]
300
250
0
(h)

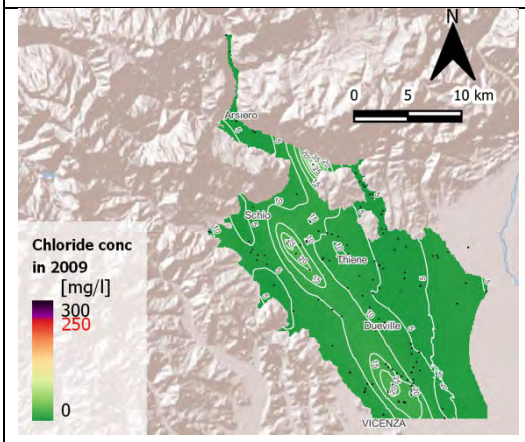
N
0 5 10 km
Arsiero
Schio
Thiene
Dueville
VICENZA
Chloride conc
in 2009
[mg/l]
300
250
0
(i)

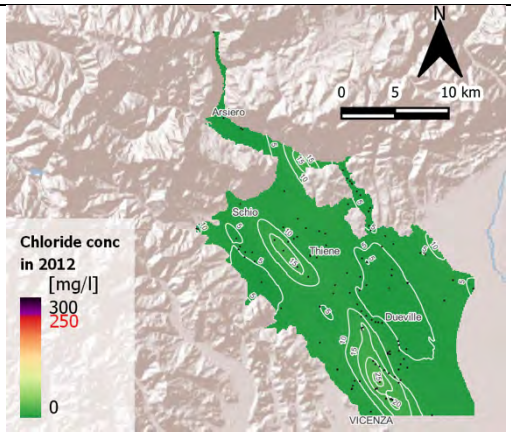
N
0 5 10 km
Arsiero
Schio
Thiene
Dueville
VICENZA
Chloride conc
in 2012
[mg/l]
300
250
0
(l)

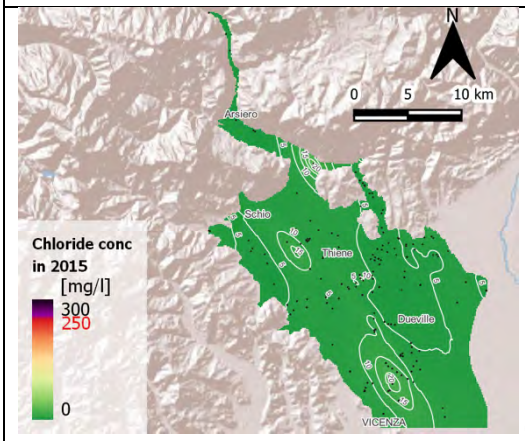
N
0 5 10 km
Arsiero
Schio
Thiene
Dueville
VICENZA
Chloride conc
in 2015
[mg/l]
300
250
0
(m)

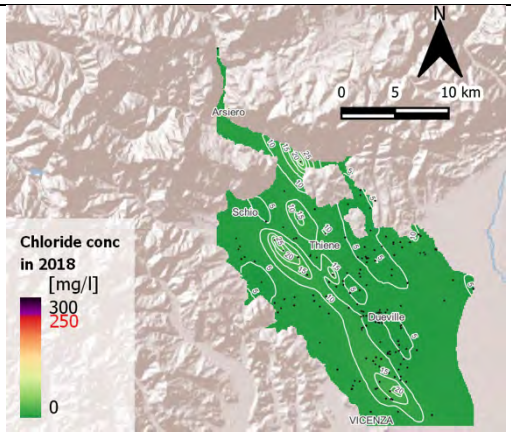
N
0 5 10 km
Arsiero
Schio
Thiene
Dueville
VICENZA
Chloride conc
in 2018
[mg/l]
300
250
0
(n)

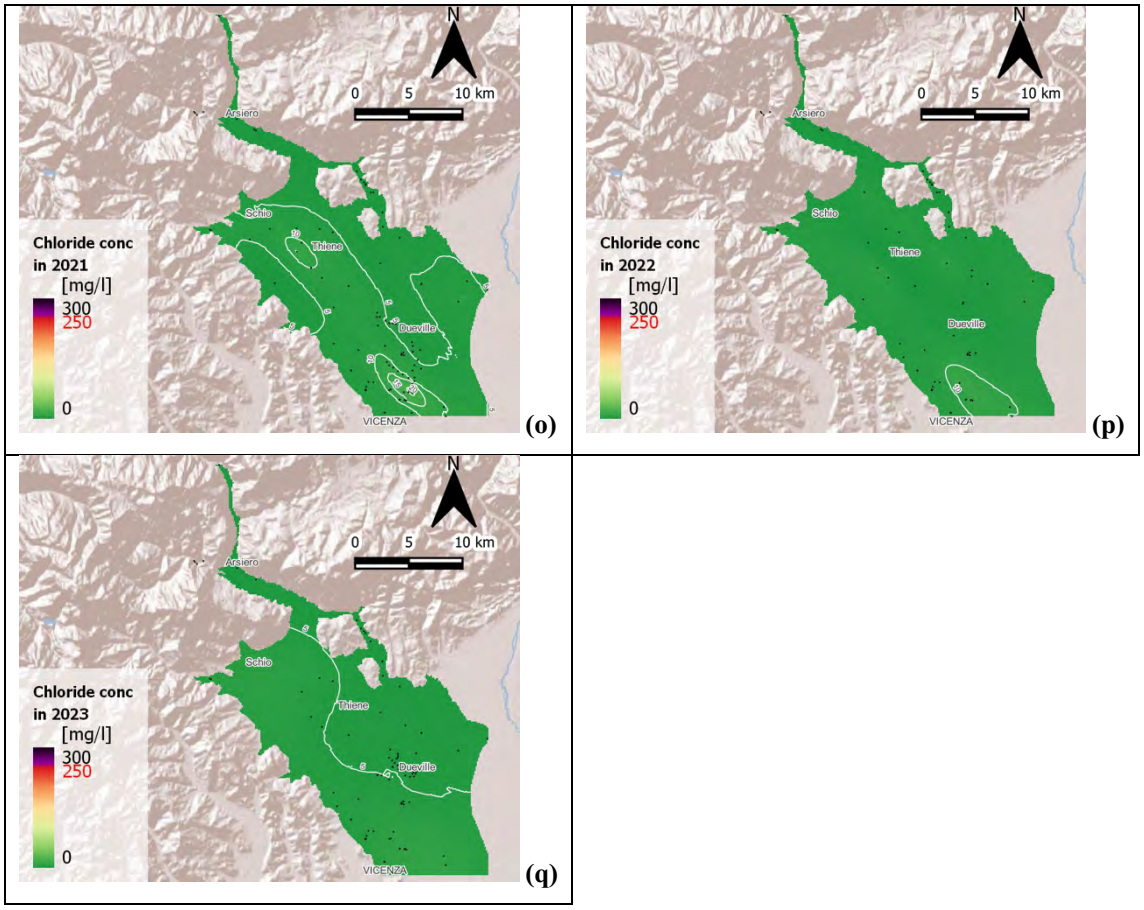

Figure 79. Chlorides, Vicenza high plain: maps of the expected values resulting from Kriging interpolation with anisotropic variogram for the years (a) 1985, (b) 1988, (c) 1991, (d) 1994, (e) 1997, (f) 2000, (g) 2003, (h) 2006, (i) 2009, (l) 2012, (m) 2015, (n) 2018, (o) 2021, (p) 2022, and (q) 2023. Map extension can vary depending on well availability. The black dots represent the location of the wells used to build-up the map. The red number in the legend represents the max concentration admissible by law.

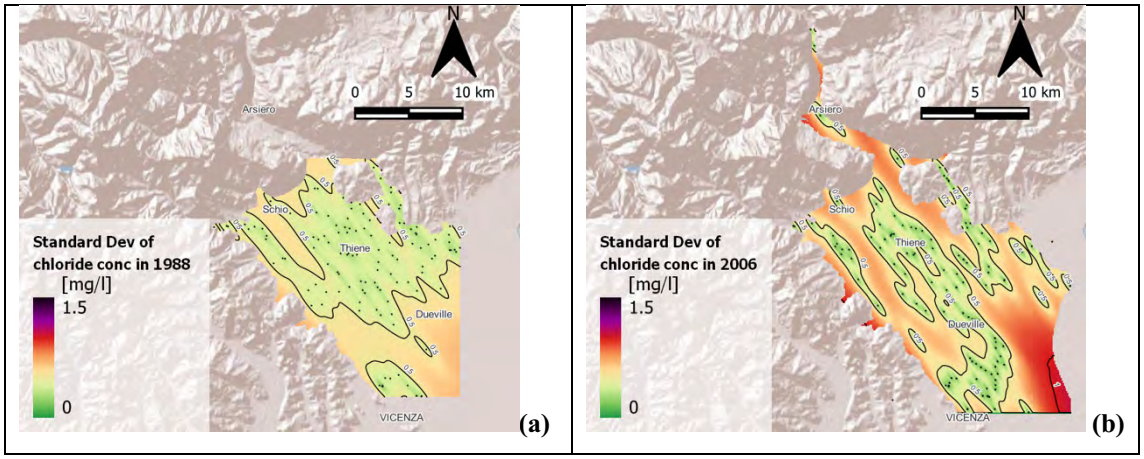

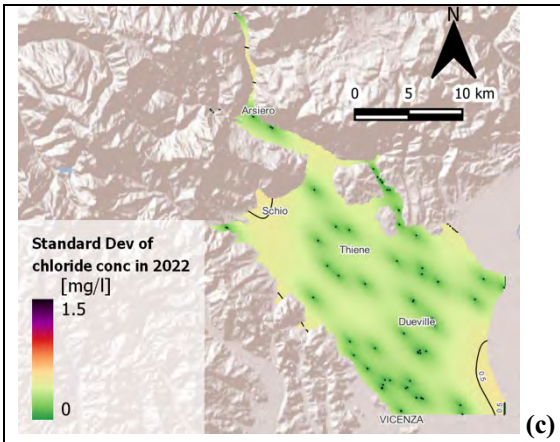

Figure 80. Chlorides, Vicenza high plain: maps of the standard deviation resulting from Kriging interpolation with anisotropic variogram for the years (a) 1988, (b) 2006, and (c) 2022. Map extension can vary depending on well availability. The black dots represent the locations of the wells used to build-up the map.

5.4.2. AGNO VALLEY

As noted before, the Agno Valley area has a limited number of sampled wells. This small sample size could impact the robustness of the analysis, making it more challenging to draw definitive conclusions about the pollutant distribution in this region. For chlorides the number of measurements is small until 2014. This is confirmed in Figure 81: until 2014 the number of wells amounted to 4 with a maximum of 8 measures. For that reason, the statistical analyses are carried out only in years between 2015 and 2020, plus 2023. The results are presented in Table 18.

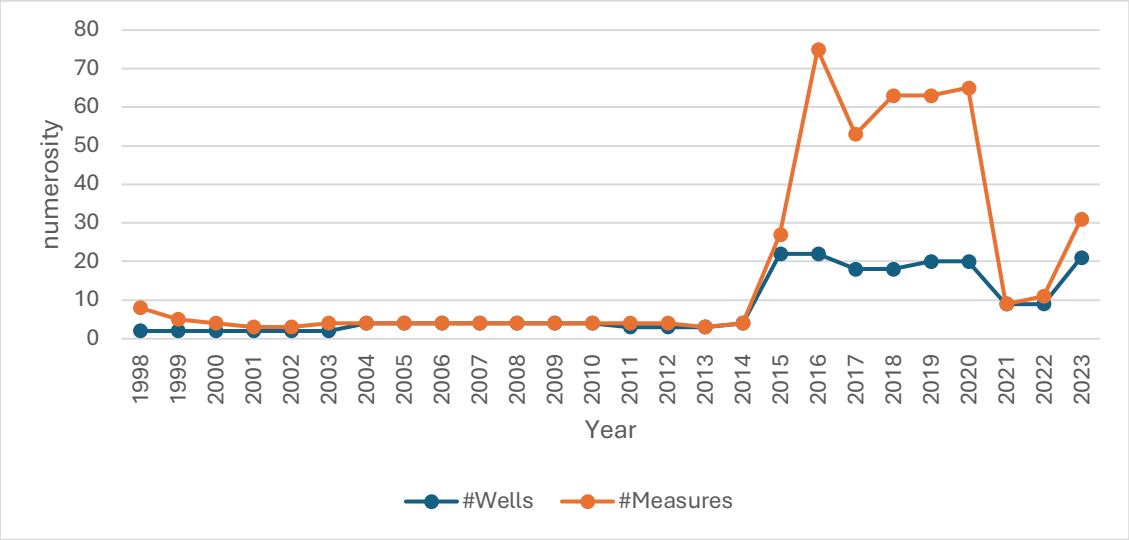

Figure 81. Chlorides, Agno valley: yearly number of sampled wells and measurements between 1998 and 2023.

The histogram and the boxplot of the entire dataset are presented in Figure 82 and 83, respectively. The limited dataset is primarily concentrated in the third and fourth classes of the histogram, with other present values less represented. The maximum concentration recorded is 70.8 mg/l, and the distribution is highly skewed to the right. Many values fall out of the whiskers, being statistically read as outliers. The discrepancy between the mean and the median, underlined by the boxplot is clearly related to high values that have an impact on the computation of the mean, increasing its value.

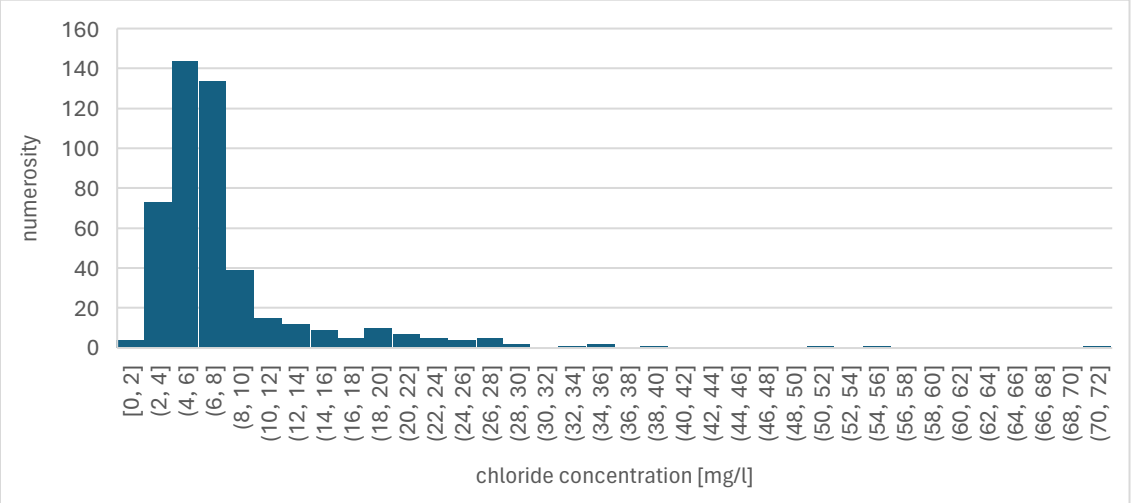

Figure 82. Chlorides, Agno valley: histogram of concentration between 1998 and 2023.

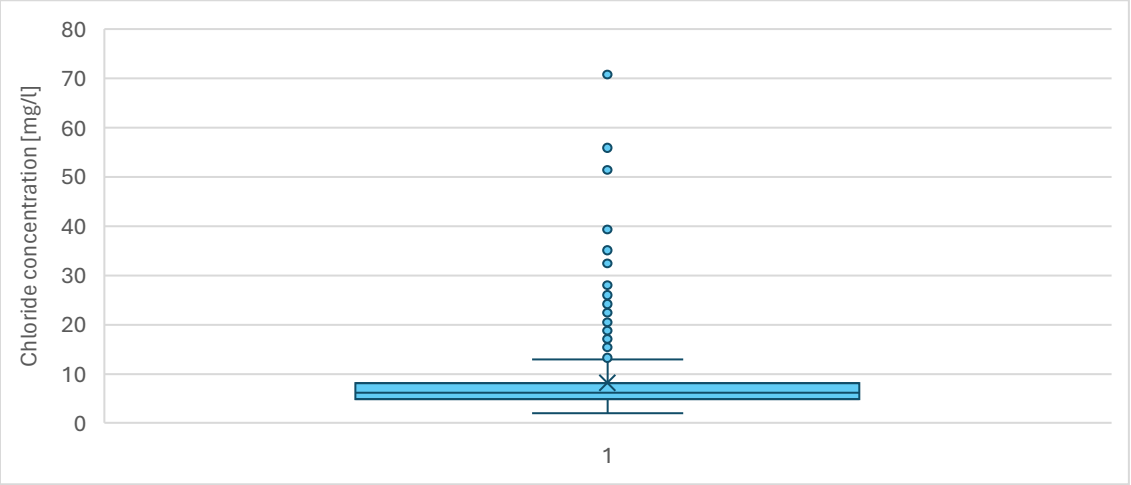

Figure 83. Chlorides, Agno valley boxplot of the concentration between 1998 and 2023.

In Table 18 the descriptive statistics of the data recorded in the representative years are presented.

Table 18. Chlorides, Agno vallye: descriptive statistics of the data collected in the analyzed years.

Year	μ [mg/l]	Mode [mg/l]	Q1 [mg/l]	Median [mg/l]	Q3 [mg/l]	σ^2 $[(mg/l)^2]$	CV [-]	G [-]	Min [mg/l]	Max [mg/l]
2015	6.03	4.00	4.19	5.17	7.24	2.93	0.28	2.64	3.00	17.90
2016	6.34	4.00	4.80	5.58	7.04	2.65	0.26	2.83	3.05	18.70
2017	6.94	5.26	4.76	5.63	8.19	3.23	0.26	1.64	3.72	18.50
2018	10.35	20.50	6.04	7.46	12.60	6.99	0.26	1.90	4.17	35.10
2019	12.23	14.30	6.23	7.13	16.70	9.67	0.25	1.94	3.33	51.40
2020	12.23	7.53	6.49	7.57	16.00	11.28	0.27	3.30	3.44	70.80
2023	6.66	-	5.75	6.27	6.98	2.06	0.22	2.68	3.62	14.37

The variability of values within individual years is relatively low. However, comparing the maximum value across different years reveals a significant variation, ranging from 70.80 mg/l to 14.37 mg/l. The mode and the median are often close to the minimum observed value, indicating that many values are concentrated on the left side of the data distribution.

5.5. SULPHATES

5.5.1. VICENZA HIGH PLAIN

A comparison of the number of samples and sampling wells is shown in Figure 84. Available measurements started in 1981 but, unlike for the other pollutants, the statistical and geostatistical analysis begins in 1988, as the number of measures before that year is insufficient to be considered representative. As with other substances, the year 2018 is characterized by the highest number of samples collected, with 493 measurements. The total number of samples amounts to 7908.

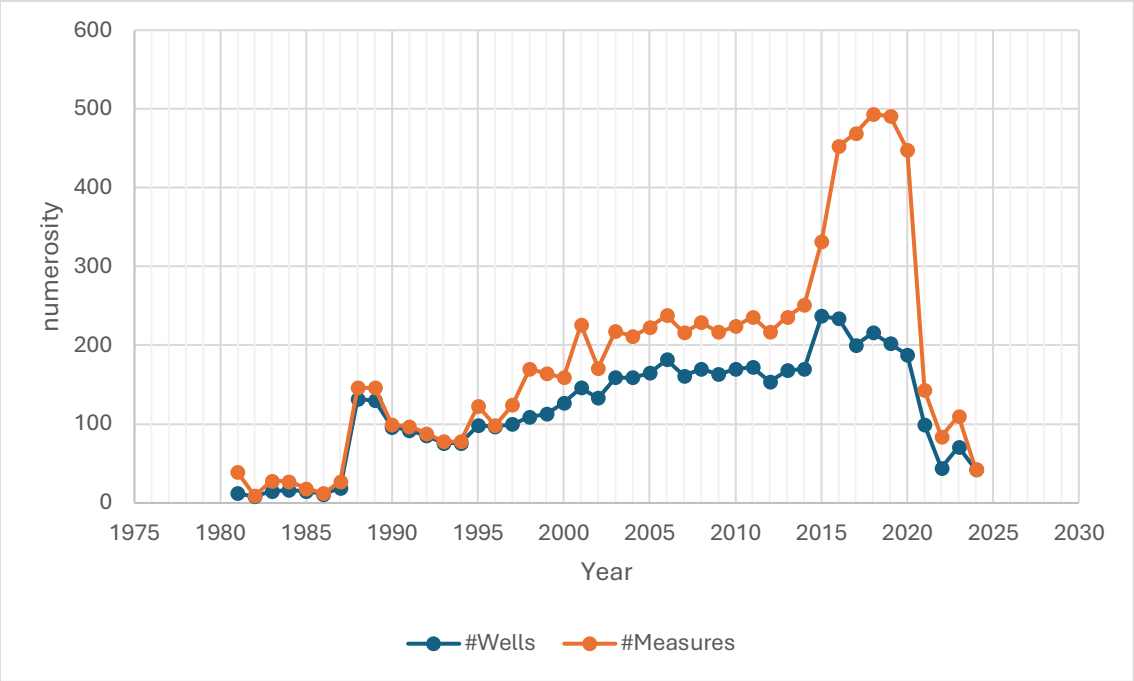

Figure 84. Sulphates, Vicenza high plain: yearly number of sampled wells and measurements between 1981 and 2023.

The histogram of the distribution of sulphate concentrations and the boxplot illustrating the main descriptive parameters are shown in Figure 85 and Figure 86, respectively. The data reveal a peak in the number of measured concentrations within the classes (8.00,12.00] and (12.00,16.00] mg/l. Values from 16.00 mg/l to 44.00 mg/l are relatively evenly distributed. However, there is a discernible rightward skew in the distribution, with the upper whisker extending to 69.00 mg/l.

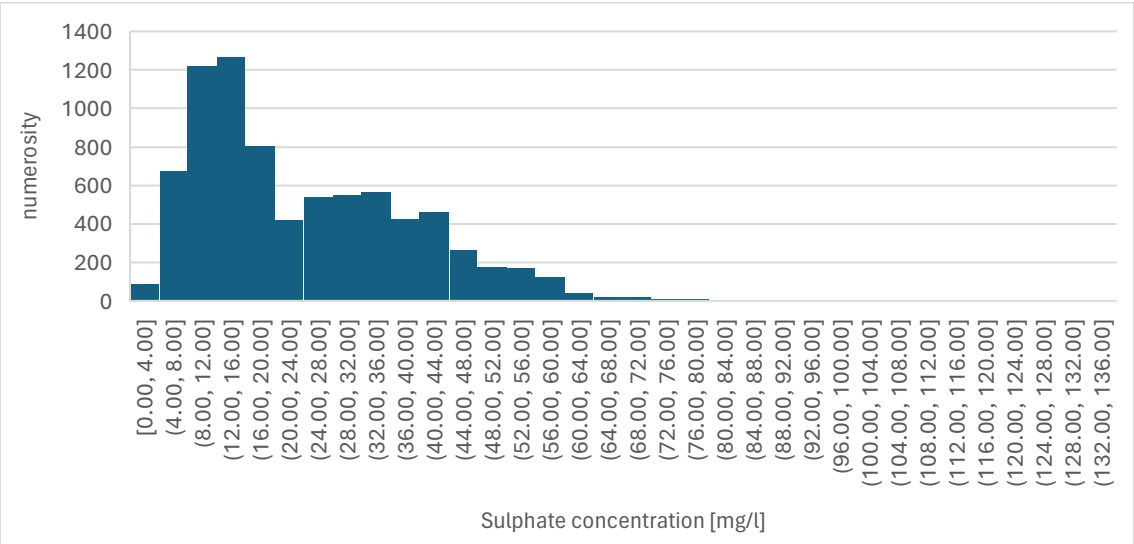

Figure 85. Sulphates, Vicenza high plain: histogram of concentration data between 1981 and 2023.

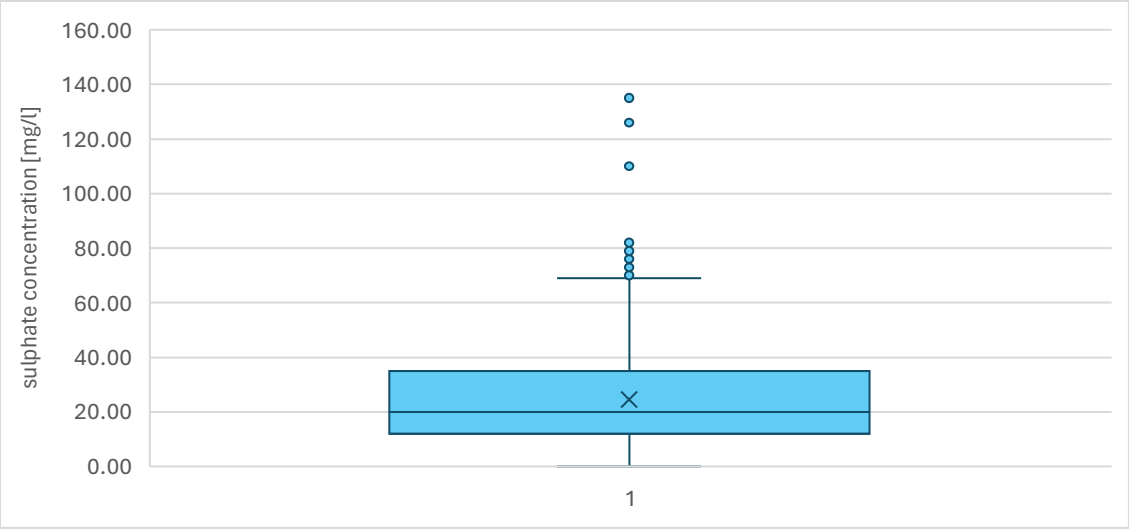

Figure 86. Sulphates, Vicenza high plain: boxplot of the concentration observed between 1981 and 2023.

The descriptive statistics for the years taken in consideration in geostatistical analysis is reported in Table 19.

Table 19. Sulphates, Vicenza high plain: descriptive statistics of data collected in the analyzed years.

Year	μ [mg/l]	Mode [mg/l]	Q1 [mg/l]	Median [mg/l]	Q3 [mg/l]	σ^2 $[(mg/l)^2]$	CV [-]	G [-]	Min [mg/l]	Max [mg/l]
1988	23.32	10.00	12.00	18.00	31.25	15.96	0.17	2.68	6.00	126.00
1991	25.86	18.00	17.00	20.50	33.00	13.13	0.14	1.14	6.00	63.00
1994	24.84	12.00	14.00	18.25	39.00	14.59	0.15	1.11	8.00	71.00
1997	24.00	11.00	15.00	19.00	31.00	13.09	0.15	1.48	8.00	75.00
2000	25.08	11.00	12.75	18.00	35.50	16.63	0.16	1.07	4.00	78.00
2003	25.61	11.00	13.00	20.00	36.00	16.34	0.16	1.20	6.00	81.00
2006	25.11	9.00	13.00	20.00	36.00	15.01	0.15	0.76	3.50	71.00
2009	24.30	14.00	11.50	19.00	35.67	15.66	0.16	0.77	3.00	72.00
2012	23.40	8.00	10.50	17.75	33.00	16.48	0.17	1.24	4.00	79.00
2015	19.29	7.00	8.00	14.30	28.00	13.49	0.19	1.17	2.30	68.10
2018	20.65	8.00	9.00	14.75	31.75	14.53	0.18	0.96	3.97	59.00
2021	23.97	11.00	10.69	21.00	36.43	14.92	0.16	0.47	0.00	64.29
2022	27.97	-	16.47	31.29	35.39	12.11	0.12	0.29	7.27	65.36
2023	22.34	-	10.19	15.33	32.39	14.32	0.17	0.79	2.07	66.24

The mean concentration of sulphates generally ranges between 20 mg/l and 28 mg/l across most of the years, with only one exception.

Although the coefficient of variation remains relatively low, consistently below 0.20, the skewness is notably high in some cases. The maximum values of each year consistently stay below the legal limits.

After applying logarithmic transformation, the parameters of the distributions for each year analyzed are described in Table 20.

Table 20. Sulphates, Vicenza high plain: descriptive statistics of log-transformed data in the analyzed years.

Year	μ [mg/l]	Mode [mg/l]	Q1 [mg/l]	Median [mg/l]	Q3 [mg/l]	σ^2 $[(mg/l)^2]$	CV [-]	G [-]	Min [mg/l]	Max [mg/l]
1988	1.39	1.04	1.11	1.28	1.51	0.24	0.35	0.50	0.85	2.10
1991	1.43	1.28	1.26	1.33	1.53	0.20	0.31	0.33	0.85	1.81
1994	1.41	1.11	1.18	1.28	1.60	0.22	0.33	0.60	0.95	1.86
1997	1.40	1.08	1.20	1.30	1.51	0.20	0.32	0.50	0.95	1.88
2000	1.42	1.08	1.14	1.28	1.56	0.26	0.36	0.30	0.70	1.90
2003	1.43	1.08	1.15	1.32	1.57	0.25	0.35	0.26	0.85	1.91
2006	1.42	1.00	1.15	1.32	1.57	0.26	0.36	-0.12	0.65	1.86
2009	1.40	1.18	1.10	1.30	1.56	0.29	0.38	-0.15	0.60	1.86
2012	1.39	0.95	1.06	1.27	1.53	0.28	0.38	0.18	0.70	1.90
2015	1.31	0.90	0.95	1.18	1.46	0.28	0.40	0.23	0.52	1.84
2018	1.34	0.95	1.00	1.20	1.52	0.28	0.40	0.33	0.70	1.78
2021	1.40	1.08	1.07	1.34	1.57	0.32	0.41	-0.86	0.00	1.81
2022	1.46	-	1.24	1.51	1.56	0.21	0.31	-0.79	0.92	1.82
2023	1.37	-	1.05	1.21	1.52	0.29	0.39	-0.25	0.49	1.83

The logarithmic transformation improves the shape of the distributions, though it is not identical to the Gaussian.

The parameters characterizing the isotropic variogram model and the root mean square error produced in each interpolation are summed in Table 21.

Table 21. Sulphates, Vicenza high plain: isotropic variogram model for each selected year.

Isotropic analysis							
Year	**Mean Dist [m]**	**Model**	**Lag [m]**	**Nugget**	**Partial sill**	**Range [m]**	**RMSE**
1988	695.80	Exponential	1000.0	0.0035	0.05	2798.00	0.19
1991	832.25	Gaussian	1200.0	0.0190	0.05	21600.00	0.15
1994	876.00	Gaussian	1200.0	0.0200	0.08	19200.00	0.15
1997	848.00	Exponential	1200.0	0	0.06	24000.00	0.1
2000	770.35	Gaussian	1200.0	0.0200	0.07	18000.00	0.15
2003	768.50	Exponential	1200.0	0	0.07	18000.00	0.11
2006	636.21	Exponential	1000.0	0	0.07	12211.00	0.12
2009	622.77	Gaussian	1000.0	0.0095	0.07	10000.00	0.13
2012	654.05	Exponential	1000.0	0.0200	0.07	14000.00	0.11
2015	513.03	Exponential	800.0	0.0200	0.06	11200.00	0.13
2018	610.71	Exponential	1000.0	0	0.08	15000.00	0.14
2021	554.57	Gaussian	1000.0	0.0060	0.09	9400.00	0.12
2022	1049.07	Gaussian	1700.0	0.0024	0.09	10284.00	0.11
2023	900.24	Gaussian	1500.0	0.0580	0.10	10000.00	0.18

The maps of the results from Kriging interpolation are shown in Figure 87 (expected value) and Figure 88 (standard deviation).

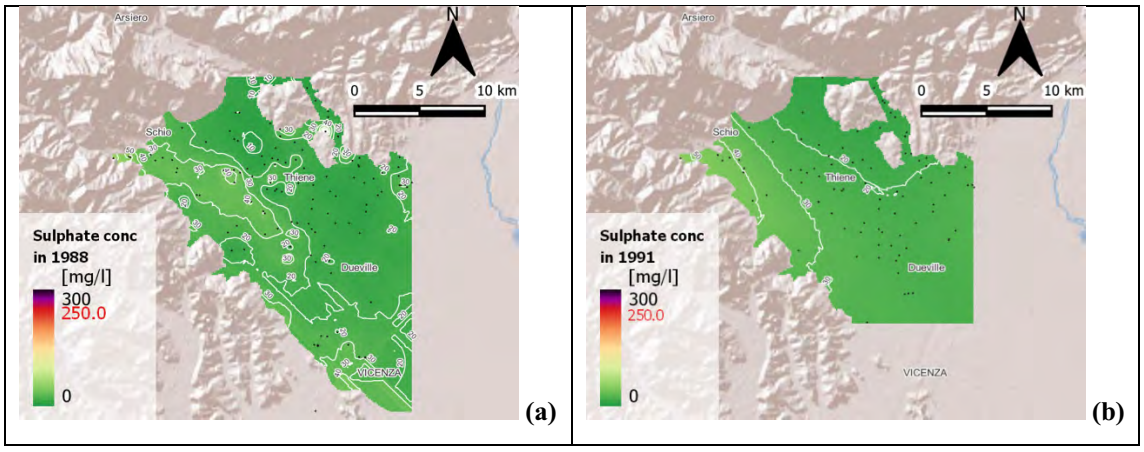

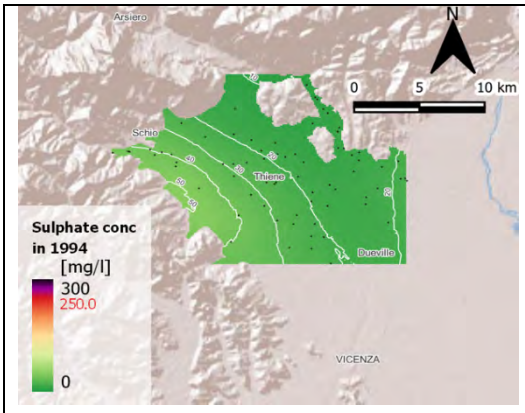
Arsiero
N
0 5 10 km
Schio
Thiene
Dueville
VICENZA
Sulphate conc
in 1994
[mg/l]
300
250.0
0

(c)

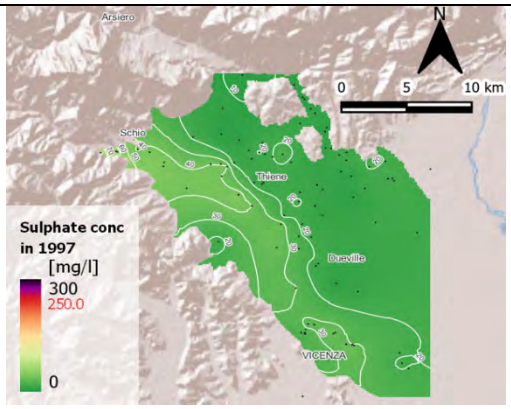
Arsiero
N
0 5 10 km
Schio
Thiene
Dueville
VICENZA
Sulphate conc
in 1997
[mg/l]
300
250.0
0

(d)

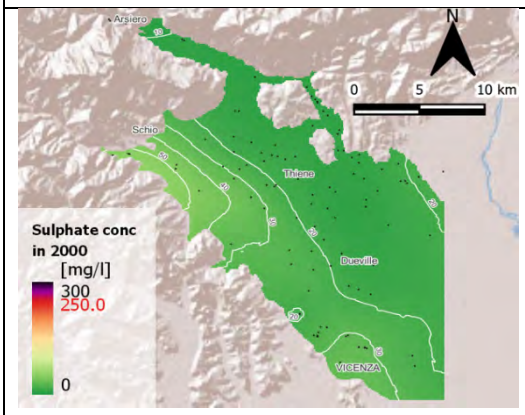
Arsiero
N
0 5 10 km
Schio
Thiene
Dueville
VICENZA
Sulphate conc
in 2000
[mg/l]
300
250.0
0

(e)

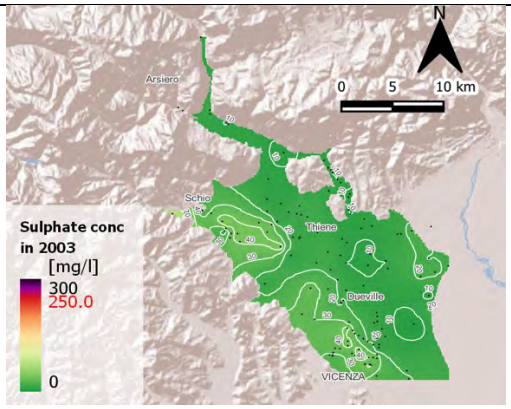
Arsiero
N
0 5 10 km
Schio
Thiene
Dueville
VICENZA
Sulphate conc
in 2003
[mg/l]
300
250.0
0

(f)

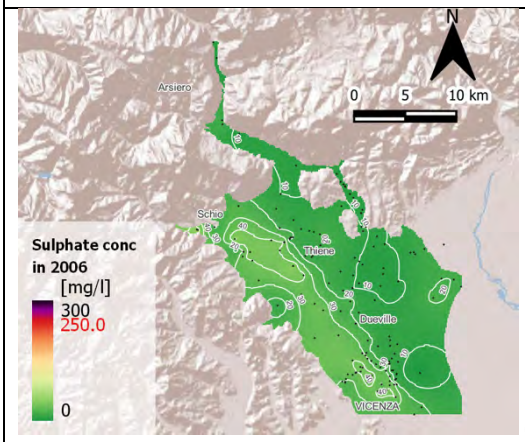
Arsiero
N
0 5 10 km
Schio
Thiene
Dueville
VICENZA
Sulphate conc
in 2006
[mg/l]
300
250.0
0

(g)

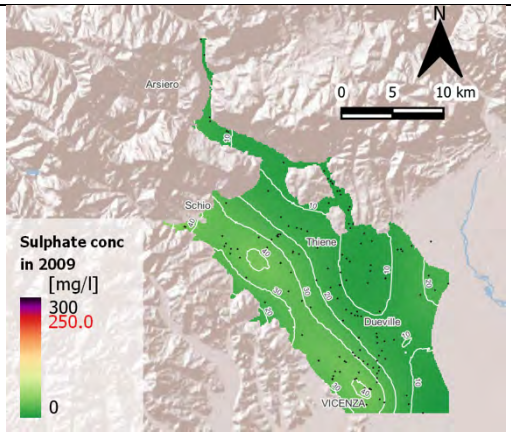
Arsiero
N
0 5 10 km
Schio
Thiene
Dueville
VICENZA
Sulphate conc
in 2009
[mg/l]
300
250.0
0

(h)

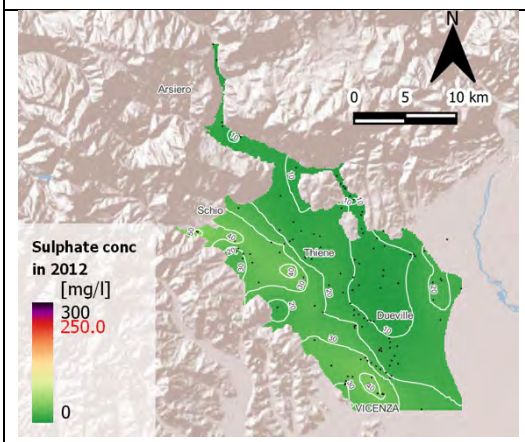
Arsiero
N
0 5 10 km
Schio
Thiene
Dueville
VICENZA
Sulphate conc
in 2012
[mg/l]
300
250.0
0

(i)

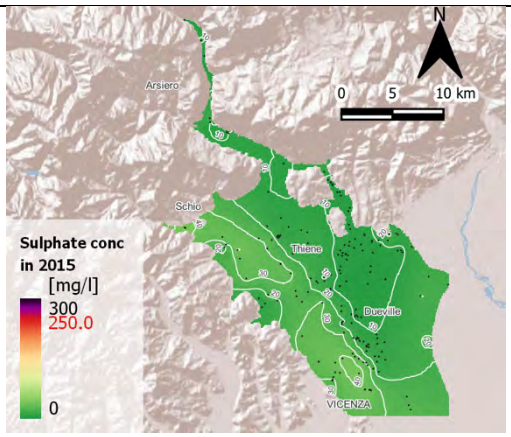
Arsiero
N
0 5 10 km
Schio
Thiene
Dueville
VICENZA
Sulphate conc
in 2015
[mg/l]
300
250.0
0

(l)

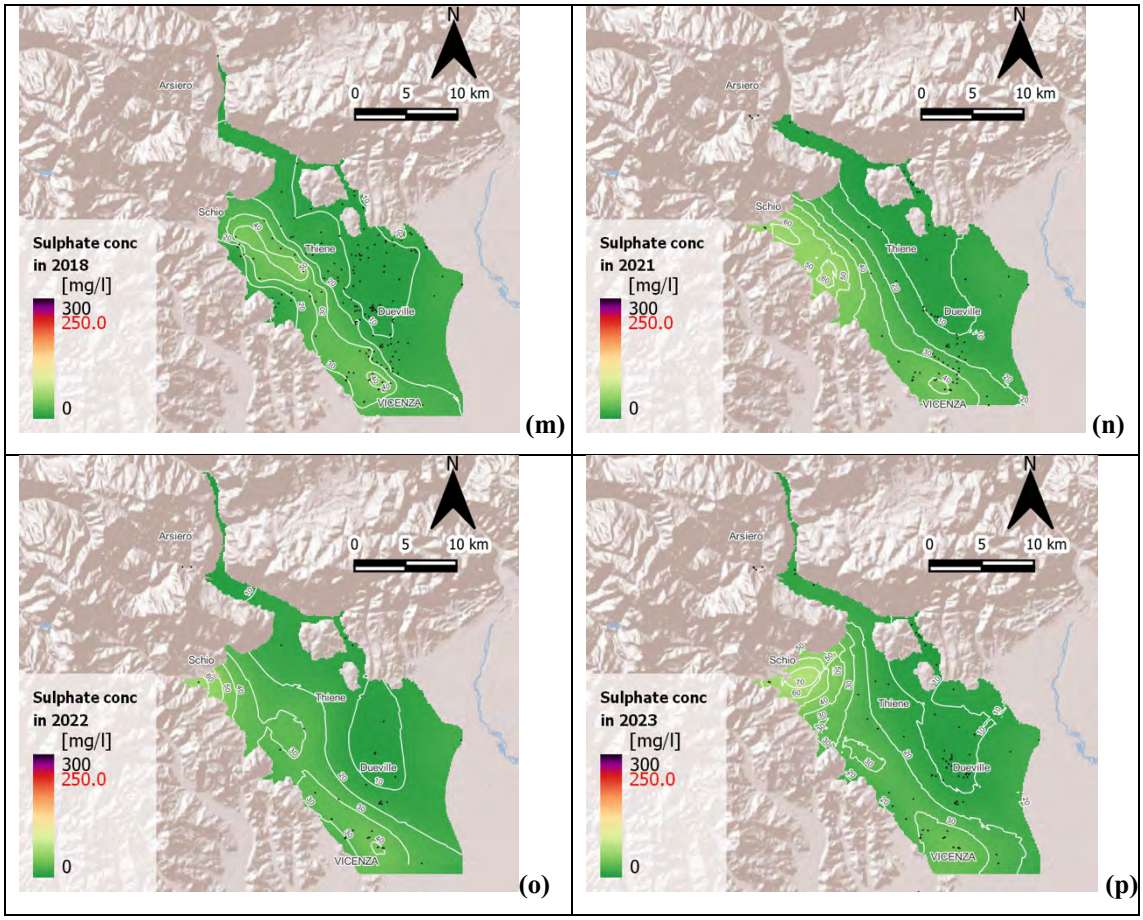

Figure 87. Sulphates, Vicenza high plain: maps of the expected values resulting from Kriging interpolation with isotropic variogram for the years (a) 1988, (b) 1991, (c) 1994, (d) 1997, (e) 2000, (f) 2003, (g) 2006, (h) 2009, (i) 2012, (l) 2015, (m) 2018, (n) 2021, (o) 2022, and (p) 2023. Map extension can vary depending on well availability. The black dots represent the locations of the wells used to build-up the map. The red number in the legend represents the max concentration admissible by law.

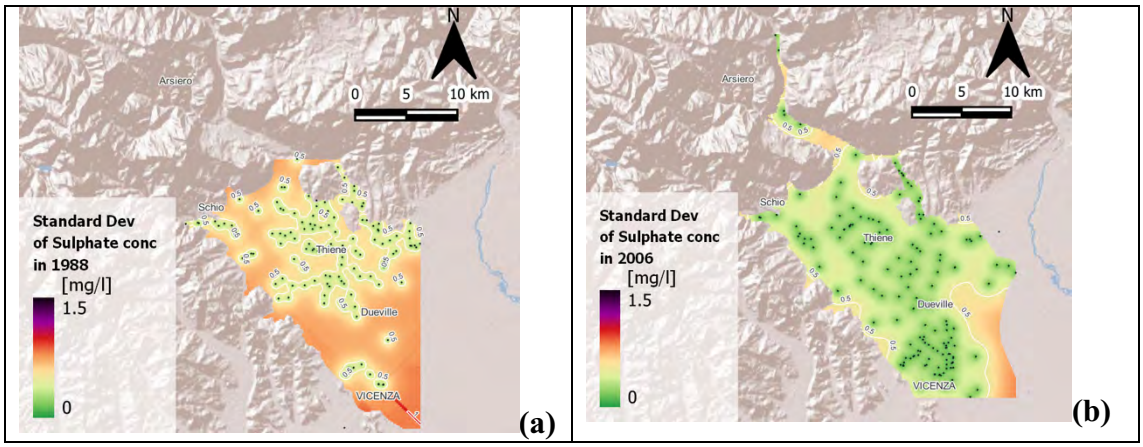

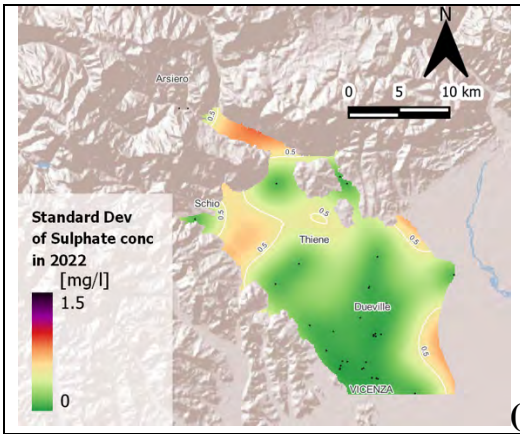

(c)

Figure 88. Sulphates, Vicenza high plain: maps of the standard deviation resulting from Kriging interpolation with isotropic variogram for the years (a) 1988, (b) 2006, and (c) 2022. Map extension can vary depending on well availability. The black dots represent the locations of the wells used to build-up the map.

The anisotropic Kriging interpolation is described by the parameters summarized in Table 22.

Table 22. Sulphates, Vicenza high plain: anisotropic variogram model for each selected year.

Anisotropic analysis								
Year	**Model**	**Lag [m]**	**Preferential Angle [°]**	**Nugget**	**Partial sill**	**Major Range [m]**	**Minor Range [m]**	**RMSE**
1988	Exponential	1000.0	137.5	0.0230	0.04	15000.00	5000.00	0.19
1991	Gaussian	1200.0	137.0	0.0160	0.04	20400.00	1000.00	0.14
1994	Gaussian	1200.0	139.7	0.0100	0.06	18000.00	6000.00	0.13
1997	Exponential	1200.0	146.6	0	0.05	24000.00	12000.00	0.09
2000	Gaussian	1200.0	142.9	0.0100	0.07	21000.00	9000.00	0.12
2003	Exponential	1200.0	142.2	0	0.06	16800.00	9000.00	0.11
2006	Gaussian	1000.0	144.0	0.0110	0.06	17000.00	7000.00	0.12
2009	Gaussian	1000.0	146.3	0.0070	0.07	17000.00	6000.00	0.12
2012	Exponential	1000.0	141.2	0	0.07	14000.00	7000.00	0.11
2015	Exponential	800.0	135.9	0.0020	0.05	11200.00	5500.00	0.13
2018	Exponential	1000.0	138.7	0	0.07	16000.00	7500.00	0.14
2021	Gaussian	1000.0	109.0	0.0060	0.07	17000.00	6000.00	0.11
2022	Gaussian	1700.0	135.0	0.0290	0.10	25500.00	8500.00	0.12
2023	Gaussian	1500.0	137.0	0.0060	0.11	18000.00	9000.00	0.18

Figure 89 provides the maps of the expected value of sulphates as generated by Kriging for the 14 selected years using the anisotropic variogram models provided in Table 24 Additionally, Figure 90 provides the maps of the associated standard deviation for the years 1988, 2006, and 2022.

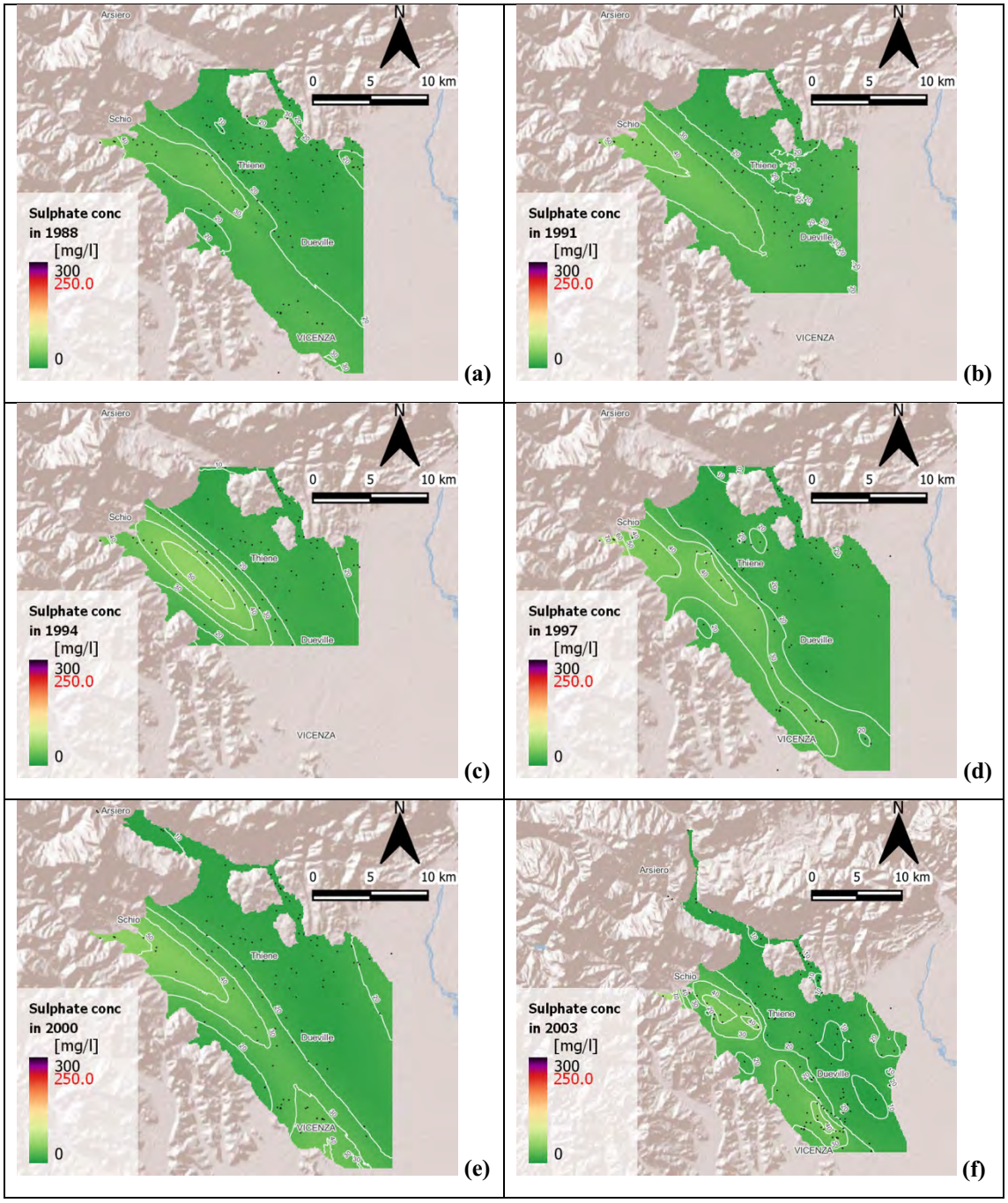

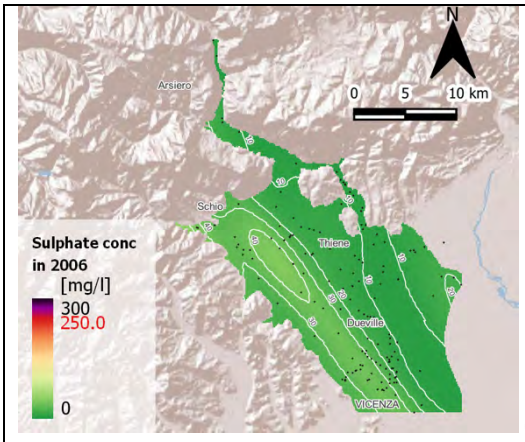
N
0 5 10 km
Arsiero
Schio
Thiene
Dueville
VICENZA
Sulphate conc
in 2006
[mg/l]
300
250.0
0

(g)

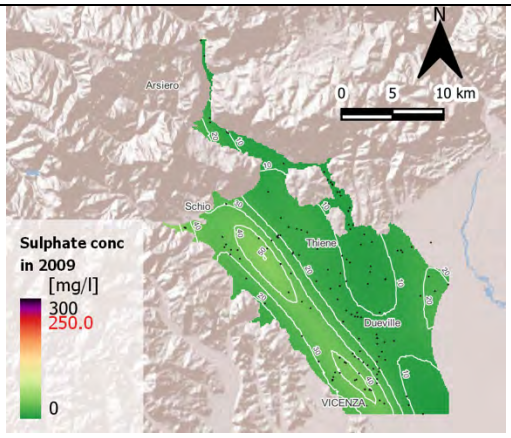
N
0 5 10 km
Arsiero
Schio
Thiene
Dueville
VICENZA
Sulphate conc
in 2009
[mg/l]
300
250.0
0

(h)

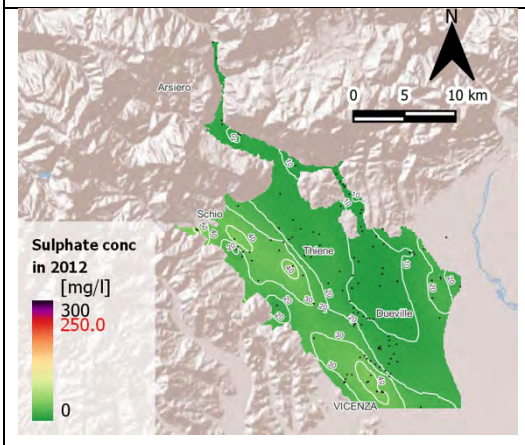
N
0 5 10 km
Arsiero
Schio
Thiene
Dueville
VICENZA
Sulphate conc
in 2012
[mg/l]
300
250.0
0

(i)

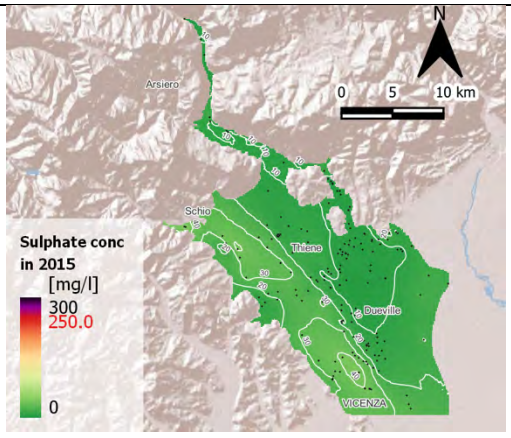
N
0 5 10 km
Arsiero
Schio
Thiene
Dueville
VICENZA
Sulphate conc
in 2015
[mg/l]
300
250.0
0

(l)

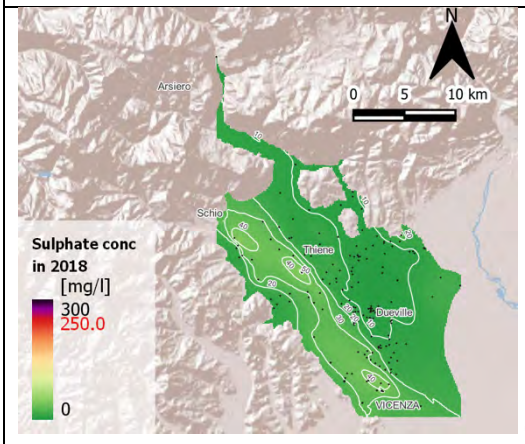
N
0 5 10 km
Arsiero
Schio
Thiene
Dueville
VICENZA
Sulphate conc
in 2018
[mg/l]
300
250.0
0

(m)

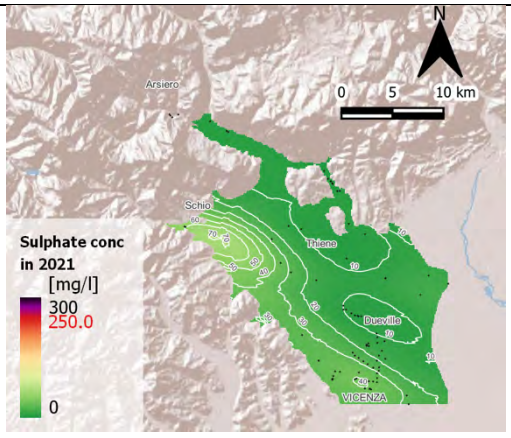
N
0 5 10 km
Arsiero
Schio
Thiene
Dueville
VICENZA
Sulphate conc
in 2021
[mg/l]
300
250.0
0

(n)

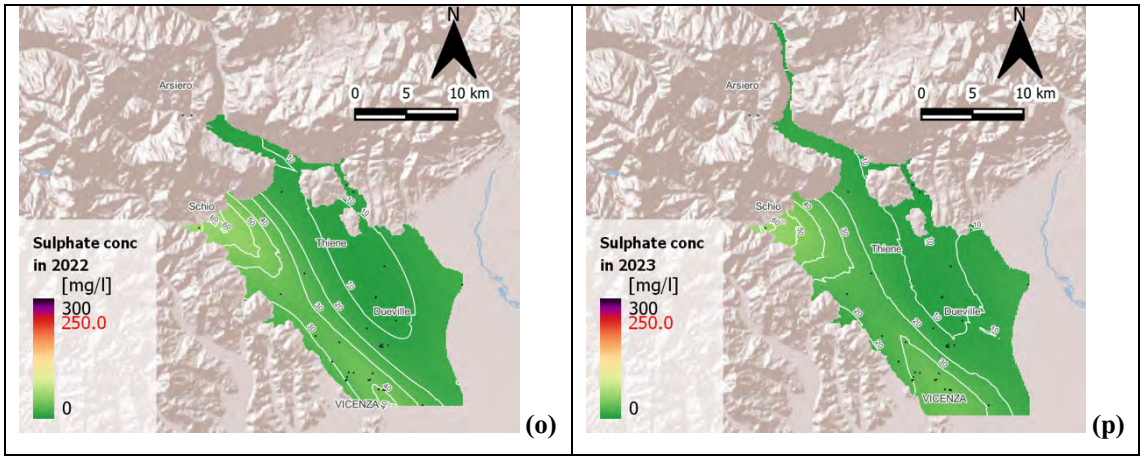

Figure 89. Sulphates, Vicenza high plain: maps of the expected values resulting from Kriging interpolation with isotropic variogram for the years (a) 1988, (b) 1991, (c) 1994, (d) 1997, (e) 2000, (f) 2003, (g) 2006, (h) 2009, (i) 2012, (l) 2015, (m) 2018, (n) 2021, (o) 2022, and (p) 2023. Map extension can vary depending on well availability. The black dots represent the locations of the wells used to build-up the map. The red number in the legend represents the max concentration admissible by law.

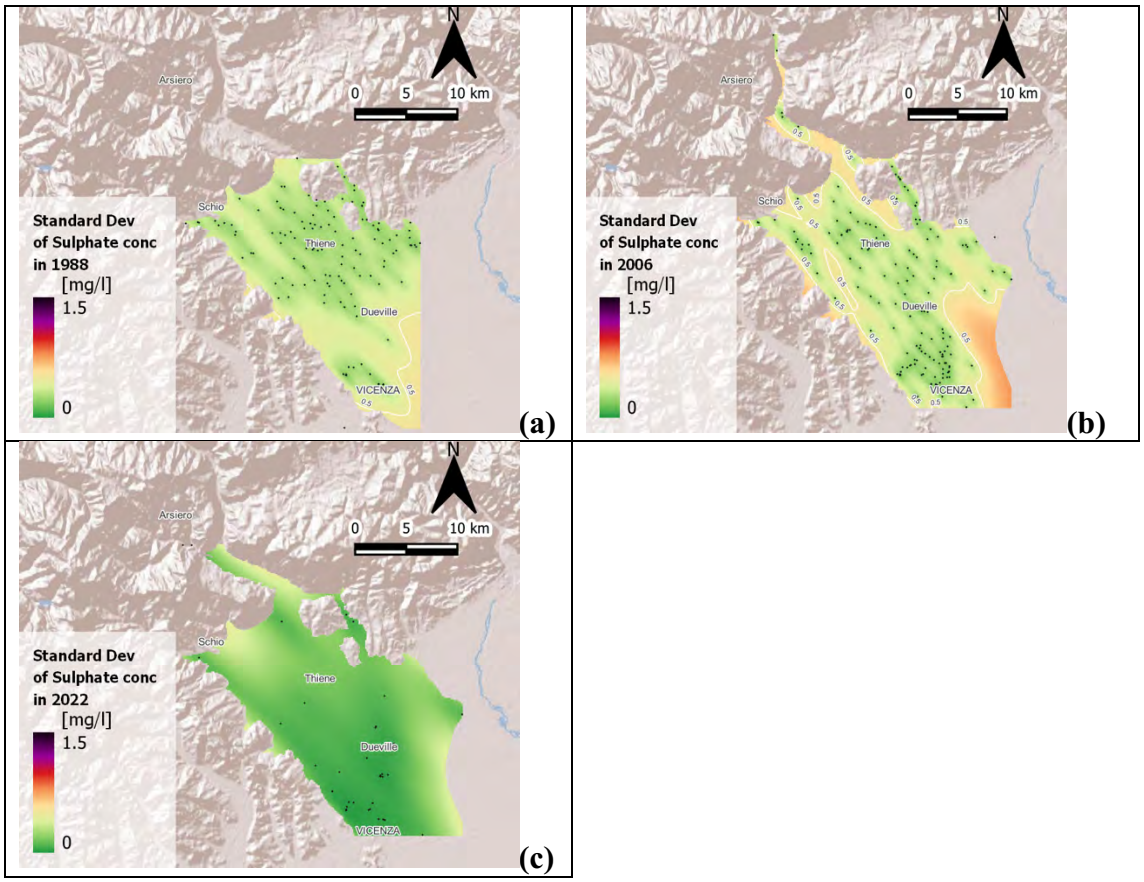

Figure 90. Sulphates, Vicenza high plain: maps of the standard deviation resulting from Kriging interpolation with anisotropic variogram for the years (a) 1988, (b) 2006, and (c) 2022. Map extension can vary depending on well availability. The black dots represent the location of the wells used to build-up the map.

5.5.2. AGNO VALLEY

In the case of sulphates, the numerosity of data (Figure 91) is characterized by a trend over time similar to those already detected for nitrates and chlorides. It is representative for the domain characterization, with the exception of years 2021 and 2022, when the number of measurements lowered to 5 only, equal to the number of sampled wells.

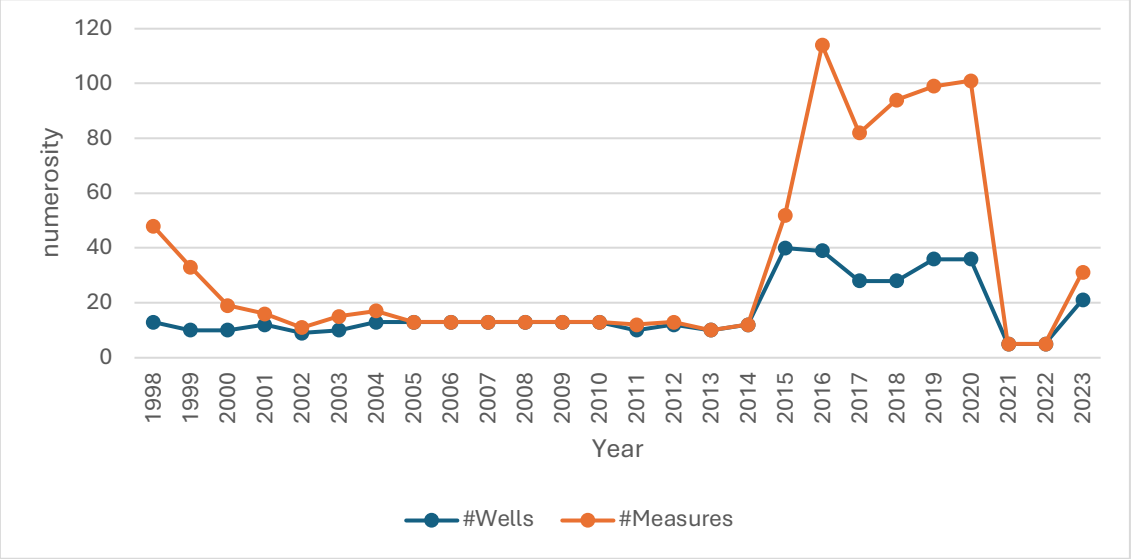

Figure 91. Sulphates, Agno valley: yearly number of sampled wells and measurements between 1998 and 2023.

The distribution of the entire dataset is illustrated with a histogram in Figure 92 and a boxplot in Figure 93. Unlike previous distributions, this one exhibits a nearly symmetrical behavior with a leftward skew. The most frequently observed values fall within the class of (49.5, 55] mg/l, and the maximum concentration recorded is 84.75 mg/l. The mean and median are relatively close to each other, and there are surprisingly more outliers on the left side of the distribution compared to the right side.

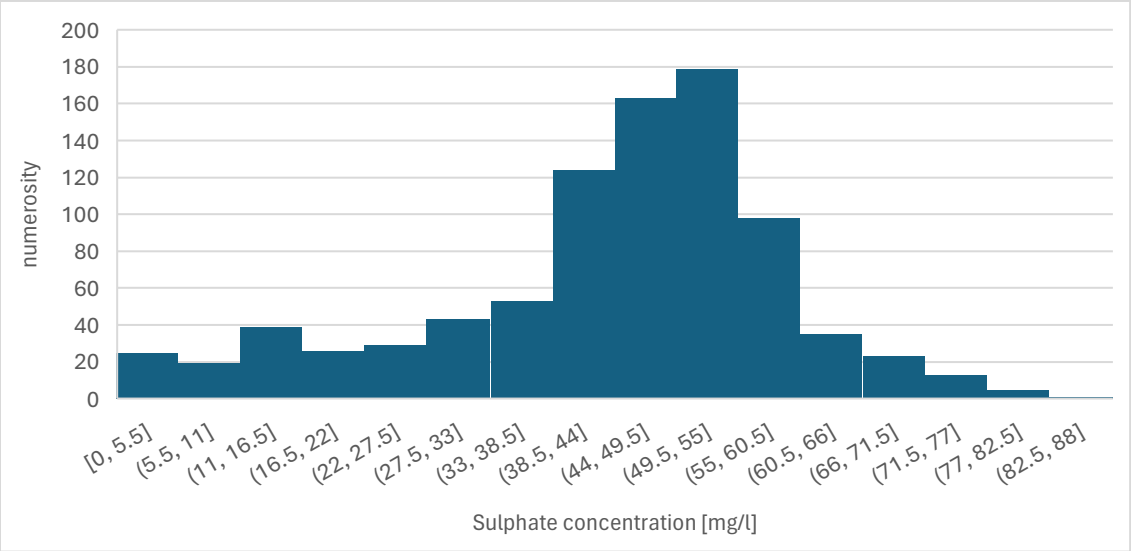

Figure 92. Sulphates, Agno valley: histogram of concentrations between 1998 and 2023.

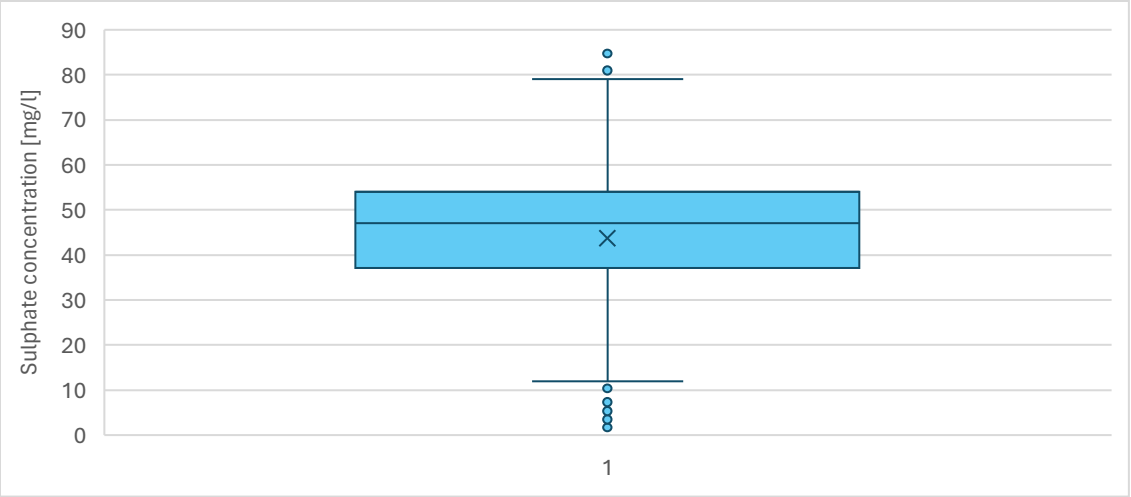

Figure 93. Sulphates, Agno valley: boxplot of the concentration between 1998 and 2023.

The descriptive statistics of data collected in different years are reported in Table 23.

Table 23. Sulphates, Agno valley: decriptive statistics of the data collected in the analyzed years.

Year	μ [mg/l]	Mode [mg/l]	Q1 [mg/l]	Median [mg/l]	Q3 [mg/l]	σ^2 $[(mg/l)^2]$	CV [-]	G [-]	Min [mg/l]	Max [mg/l]
1998	53.38	57.00	49.00	53.00	59.25	11.95	0.06	-0.62	21.00	75.00
2000	56.11	54.00	53.50	55.00	61.00	12.76	0.06	-0.76	20.00	81.00

2003	56.80	54.00	53.50	54.00	60.00	8.30	0.05	1.20	42.00	79.00
2006	54.77	54.00	53.00	54.00	60.00	12.05	0.06	-1.79	21.00	71.00
2009	50.85	49.00	48.00	52.00	56.00	12.23	0.07	-1.15	20.00	69.00
2012	60.46	58.00	53.00	58.00	70.00	10.96	0.05	0.58	44.00	79.00
2015	35.24	46.00	25.98	41.05	44.98	15.63	0.11	-0.39	2.30	68.10
2018	40.07	43.00	36.00	43.00	48.00	14.62	0.10	-0.95	3.70	66.00
2020	41.97	48.00	39.00	47.00	50.00	16.55	0.10	-0.81	4.10	84.75
2023	45.00	-	35.85	49.86	57.89	17.82	0.09	-0.82	6.50	68.83

The analysis of the entire dataset reveals that sulphate concentrations tend to be high, as evidenced by the mean, mode, median and minimum values. The minimum concentration is often above 20.00 mg/l until 2015, after which it drops significantly to just a few milligrams per liter. Despite this decrease in the minimum value, the average concentration remains relatively high.

A similar shift is observed in the range between the first and third quartiles, which remains narrow until 2012, after which it broadens, resulting in a distribution with a wider base. Except for two years, the distribution shows a leftward skew, as indicated by the negative skewness values. The coefficient of variation, never exceeding 0.11, reflecting a low variation in values.

6. DISCUSSION

6.1. TOTAL SOLVENTS

In the Vicenza high plain, concentrations of the total solvents have exceeded the legal limits on numerous occasions until 2022. Despite these exceedances, the average concentration has consistently remained below the admissible threshold.

In 2009, 75% of the sampled wells have reported concentration values below 7.00 μg/l (Figure 32). Since that year, the values of the third quartile have consistently remained below this threshold, indicating a general improvement in water quality. This trend is further confirmed by the decreasing sill values observed over the years, indicating reduced variability and a significant shift of the pollutant concentration towards lower values.

The highest levels of contamination are observed in the third and fourth, while the first, second, fifth, and sixth aquifers show no significant pollution. This pattern is logical, as the third and fourth aquifers are the most productive in the region, leading to higher water fluxes and recharge rates.

Until the end 1990s, only the northern part of the study should be considered for detailed analyses, as the southern portion has too few and poorly distributed wells. This limitation is evidenced by the standard deviation map for the year 1988 (Figure 36a), the non-physical concentration distribution in 1997 (Figures 35e and 37e), and the decreasing RMSE as sampling points became more evenly distributed across the domain (Tables 3 and 4).

Anisotropy models have a positive effect on interpolation, with lower root mean square error observed in each analyzed year. The direction of anisotropy varies between 130° and 152°, in agreement with the main regional flow direction. Both exponential and spherical models are used, suggesting that wells in close proximity do not exhibit high correlation.

Pollution events have been recorded in the areas of Schio, Zanè, and Breganze since 1985. Groundwater contamination in Schio appears to be connected to that of the Zanè-Thiene area, consistent with the distribution of industrial activities, which resembles a similar pattern to the pollution plume (compare Figure 6 with Figures 35 a and 35 b). The

persistence of contaminants is evident in the following years, with the pollution plume gradually moving southward, following the direction of groundwater flow.

The effects of pollution releases since the beginning of the 20th century are evident until 2022, due to the persistent nature of the chemicals involved. In the northern part of the domain, contaminant levels become less alarming (dropping below 10 μg/l) by 2012. However, in the southern part, high concentrations of total solvents in groundwater persisted until 2022. This trend is consistent with the soil stratigraphy (in Figure 3). Most likely, the contamination spread through the undifferentiated aquifer sowthward, reaching the Thiene area where the middle plain (multi-aquifer) system begins to take shape. The pollution plume is eventually blocked in the Vicenza area, where the decline of concentrations can be attributed to degradation and dilution processes.

In the Agno Valley, the issue of total solvent contamination has never arisen, as recorded values have consistently remained below legal limits (Table 5). Additionally, concentrations have always been low, with averages below 1 μg/l. Isolated instances of higher concentrations have occurred but have not spread to nearby areas.

In general, by 2023, the issue of total solvents contamination in the area can be considered resolved.

6.2. NITRATES

In the Vicenza high plain, nitrates concentrations have shown a non-monotonous trend, with values significantly exceeding 50 mg/l until the year 2000 (Table 6). This trend is evident in the data, which exhibits a strong right-skewed asymmetry (Figure 44), indicating a substantial number of high-concentration observations.

Monthly analyses indicate that the highest nitrate concentrations are typically recorded in January and June, likely in response to rainfall event that occur in November and May, respectively. In June, the elevated nitrate levels are associated with fertilizer application usually distributed in spring, while in January, they result from the spreading of manure by farmers after the harvest. The response time is likely longer during winter months due to climatic conditions: lower soil temperatures, slow water infiltration, solute transport, and rate of reaction of the nitrification. December and July follow similar patterns, which is not surprising.

The maps obtained by Kriging identify the peaks of nitrate contamination linked to the well VITH-8 (Figures 52 b, c, d, e, f and 54 b, c, d, e, f). Far from of this source, concentrations in the region never reach the legal limit. The pollution event has been recorded from 1988 and 2000, but it is clear that the entire pollution plume is not solely related to this source. The widespread "yellow" areas (i.e., with a nitrates concentration from 20 mg/l to 30 mg/l) on the maps in Figures 52 a, b, c, d, e, f, g, h, i, l, m, n, suggest that nitrate pollution is diffuse, originating from the most intensively farmed areas of the Vicenza Province.

Considering the diffuse nature of the pollution, the monthly analyses underline a clear link between agricultural activities and nitrate levels. It can therefore be concluded that, most likely, farming is the primary contributor to nitrate contamination in groundwater.

The isotropic Kriging analysis for the year 1988 produced unsatisfactory results (Figure 52 b), as reflected by the associated standard deviation map (Figure 53 a). However, the anisotropic analysis shows significantly smaller errors. Overall, though, the errors, expressed as RMSE, are comparable between the two methods. The preferential angles of contamination anisotropy show an average value of 157.5°, along the NW to SE direction, although not easily distinguishable due to the widespread nature of the pollution plume.

In the Agno valley, instances of nitrate concentrations exceeding legal limits are rare and isolated, with few occurrences of values surpassing the permissible ranges. As shown in Figure 64, which is representative of the entire dataset, there is no discernible relationship between the upstream and downstream areas of the sub-domain. Significant differences are observed even between nearby wells, making it impossible to identify a continuous pollution plume.

Additionally, Figure 60 demonstrates that the nitrate concentration patterns among wells in different municipalities do not align. For instance, the well in Trissino has recorded the highest concentrations compared to the others, but the downstream well in Montecchio Maggiore has shown much lower and non-comparable values, with differing trends in the behavior versus time.

Monthly nitrate concentration analysis indicates that the highest values occur in January, June and November. This pattern can be attributed to the combined effects of rainfall and human activities. Furthermore, it is important to note that the unconfined aquifer layer in

this valley is thinner compared to that of the Vicenza high plain, resulting in a shorter response time for pollutants to be detected.

In both analyzed domains, the nitrate concentration does not currently pose any danger. However, it is important to keep in mind the strong correlation observed between the nitrate concentration and farming activities.

6.3. DACT

The DACT concentration levels in the western part of the Vicenza high plain have been particularly concerning, especially in 2020 (Figures 68 b and 70 b). Outside of this area, the entire domain has reported concentrations below the legal limit. Additionally, a yellowish area can be observed to the north of Thiene, with notable concerns also emerging in 2020.

The elevated DACT concentrations are attributed to atrazine. The peak in DACT concentrations observed in 2020 likely reflects the time required for the pollutant to be metabolized, indicating that the contamination originated from pollution that occurred over 30 years ago.

Due to the lack of historical data on atrazine pollution and data series, it is difficult to draw definitive conclusions about the current situation. However, the well-known persistence of atrazine in groundwater for nearly 30 years (Ghirardelli , et al., 2020) demonstrates its long-lasting impact. The contamination is widespread across the entire domain, exhibiting low anisotropy with preferential directions between 110° and 125°. In fact, only in three out of five cases, the RMSEs are significantly smaller in the anisotropic analysis than in the isotropic one. The lack of the importance of anisotropic effect, generally associated to the movement of the pollutant with the groundwater flow. This suggests that the pollution may be trapped within the aquifer system, with little movement, implying that degradation is the primary mechanism for eliminating the contamination. This is supported by the fact that pesticide molecules have a strong tendency to bind with soil grains (Hayo & van der Werf, 1996).

In the Agno Valley, where DACT concentrations consistently remain equal to zero, suggesting that atrazine pollution in the past was less severe compared to the Vicenza

high plain. Consequently, the time required for atrazine to degrade into DACT and further mineralize has been shorter.

6.4. CHLORIDES

Chloride concentrations have consistently remained relatively low in the high plain of Vicenza (Figure ...). However, similar to nitrates, in 1988 and 1991 analyses are impacted by the presence of a well with unusually high values, although lower than the law prescription, which affects of the overall analysis. This site is located in the proximity of the Astico creek (Figure 94). Specifically, one well (VIFA-6) located on the eastern side of the water body registered high concentrations, while another (VISR-10) on the western side recorded significantly lower values. A third well (VIBR-3), situated in the direction of the anisotropy respect well VIFA-6, further confirms the elevated concentrations observed in this latter. Clearly, the presence of the Astico river has impacted the hydrology of the system at depth, recharging the phreatic aquifer, but Kriging method cannot account for it, thus proposing anisotropy as the only solution.

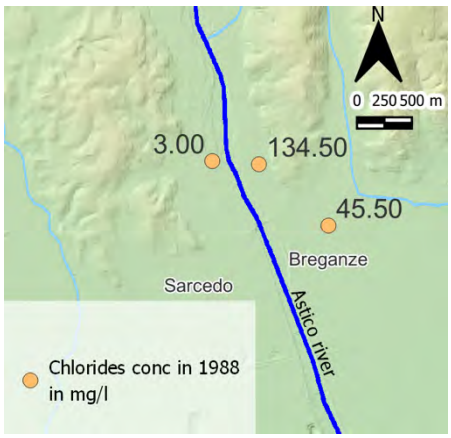

Figure 94. Position of wells with the relative chloride concentration in 1988: VISR-10 with 3.00 mg/l, VIFA-6 with 134.50 mg/l and VIBR-3 with 45.50 mg/l.

The anisotropic interpolation map based on the 1988 data show that, in the eastern area of the domain where the well VIFA-6 is located, the isolines are tightly clustered, resulting in irregularly shaped clouds around the wells. The error map for the isotropic case in 1988 displays higher values compared to the anisotropic one. However, both the isotropic and

anisotropic results should be interpreted with caution, as their RMSE values are the highest of the entire series.

Moreover, since 2000, a pollution source can be identified in the area around Thiene (Figures 77 f and79 f), with the movement of the plume resembling that of the other pollutants discussed above, but spreading more quickly. This rapid movement is attributed to the high mobility of the chloride ion in water, which also leads to a faster dissipation of the plume, making it undetectable by 2018 (Figures 77 n and 79 n). The swift progression of the contamination confirms the direction of the anisotropy, which follows a NW to SE orientation, characterized by a pronounced elongated shape.

Overall, the anisotropic model provides more accurate results with lower RMSE values.

In the Agno Valley, chloride concentrations are even lower, with a maximum of 70.80 mg/l recorded in 2020 (Table 18) following an upward trend in 2018 and 2019. However, the maximum concentration of 14.37 mg/l measured in 2023 suggests that the possibility of an emerging pollution issue has been ruled out.

In conclusion, chloride contamination is not a concern in either of the domains.

6.5. SULPHATES

In the Vicenza high plain sulphate concentrations consistently remain well below legal limits. In 1988, a single site in Zugliano recorded a concentration of 126 mg/l, which affected the interpolation map by generating irregular contours and introducing significant errors. Additionally, sparse well distribution in the southern part of the domain led to a concentration pattern that lacked physical relevance.

Overall, sulphate values have remained low throughout the observation period, as indicated by the predominant “green” color on all the maps. However, an exception occurs in 2023 when a yellow plume appears in the Schio area, signaling a localized increase in sulfate levels. This anomaly is linked to two wells in the area, VISC-1 and VISC-2. To investigate whether increased water withdrawal could be related to the rise in sulphate concentrations, the productivity of these wells is analyzed and shown in Figure 106. The analysis supports this hypothesis: in one of the wells, the volume of groundwater extraction sharply increased in 2022, suggesting a potential link between the increased withdrawal and the elevated sulphate levels.

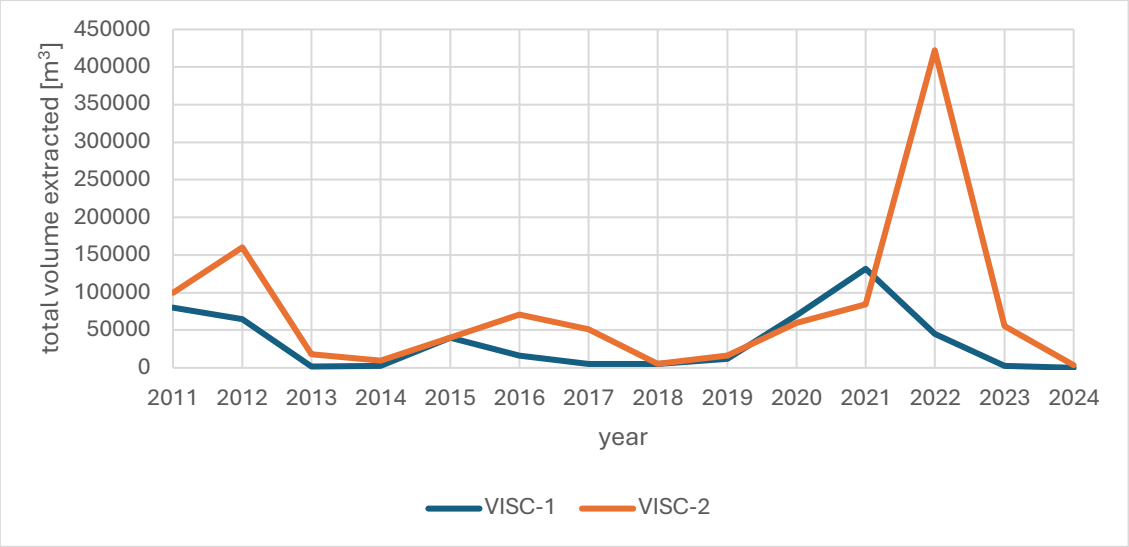

Figure 95. Yearly volume of groundwater withdrawn from wells VISC-1 and VISC-2.

In this case, as well as in the chloride one, the anisotropy seems exaggerated, which aligns with the high mobility of sulphate ions. Furthermore, both isotropic and anisotropic maps show that the west side of the domain has consistently exhibited higher concentrations across all years of the analysis. This patter is likely connected to the geological composition of the rock in that area.

In the Agno valley, until 2012 sulphate concentrations are slightly higher than those in the Vicenza domain. After that year, the minimum value drops from 44.00 mg/l to 2.30 mg/l in 2015. This decrease suggests that the previously higher minimum values are not due to an elevated Natural Background Level (NBL). The discovery of lower sulphate concentration could be attributed to the increase in the number of monitored wells from year 2014 to 2015.

However, as shown in the land-use map in Figure 10, the domain contains many mining areas rich in sulphate-containing minerals. Therefore, changes in mineral extraction processes should also be considered as a factor.

In conclusion, while the situation in both the Agno valley and the of Vicenza high plain is not alarming, the elevated sulphate concentrations observed in the Schio area should be carefully monitored.

7. CONCLUSION

In conclusion, the Kriging method has proven to be an effective interpolation technique for the Vicenza high plain, where the maps are consistent with the hydrogeologic characteristics of the area. The influence of the Astico and Leogra-Timonchio creeks is evident, strongly affecting the underground flow. This is reflected in the preferential direction of anisotropy, oriented from northwest to southeast.

However, challenges arise when isolated high values are surrounded by significantly different measurements, complicating the definition of the variogram. In such cases, the resulting maps should be interpreted with caution and contextualized appropriately.

In contrast, the Agno valley presents a more complex scenario. Here, the significant variability of concertation values over short distances indicates that interpolation using variograms and Kriging may not be the most suitable approach. Alternative methods, such as Inverse Distance Weighting (IDW), Spline, or mixed methods, could potentially yield better results.

Despite these “mathematical” challenges, water quality across both the studied areas has shown a general improvement over time.

To further explore the findings obtained in the Vicenza high plain, the following ideas are recommended:

- compare the maps of total solvent concentration with those of vinyl chloride, its metabolite, to investigate any potential correlations;
- continue monitoring nitrate concentration in well VITH-8, if permitted by authorities, to track long-term trends;
- compare the maps of atrazine with those of DACT, its breakdown product, and attempt to obtain a longer historical time series for these substances;
- monitor chloride and sulphate concentrations in wells VISC-1 and VISC-2, and explore other areas for additional sulphate data

In the Agno Valley, it could be an idea to monitor chloride and sulphate concentrations, possibly identifying their source.

Overall, the Agno valley, further studies are essential to deepen the understanding of its water quality dynamics. Since 2015, there has been an increase in data collection, but

consistent and ongoing sampling campaigns are crucial for building a reliable dataset that can support concrete water quality assessments.

References

AATO Bacchiglione, 2003. Relazione di inquadramento generale (Piano d'Ambito). In: s.l.:A.T.O. Bacchiglione.

Abascal, E., Gómez-Coma, L., Ortiz, I. & Ortiz , A., 2021. *Global diagnosis of nitrate pollution in groundwater and review of removal technologies.* Available at: http://dx.doi.org/10.1016/j.scitotenv.2021.152233

Altissimo, L., Bertoldo, S., Schiavo , A. & Sottani , A., 2010. *Rapporto Conclusivo del Progetto GIADA - Fase 2,* Arziagnano (VI): s.n.

ARPAV, 2018. *Studio, tutela e monitoraggio qualitativo e quantitativo delle risorse idriche dell'alta e media pianura vicentina.*

ARPAV, 2019. *Stato delle acque sotterranee della provincia di Padova ,* Padova : Dipartimento Provinciale di Padova .

ARPAV, 2019. *Studio, tutela e monitoraggio qualitativo e quantitativo delle risorse idriche dell'alta e media pianura vicentina,* Vicenza: s.n.

ARPAV, 2023. *QUALITÀ ACQUE SOTTERRANEE 2022,* Padova: Dipartimento Regionale Qualità dell'Ambiente.

ARPAV, 2024. *ACQUE SOTTERRANEE: concentrazione di nitrati.* Available at: https://www.arpa.veneto.it/arpavinforma/indicatori-ambientali/indicatori_ambientali/idrosfera/qualita-dei-corpi-idrici/acque-sotterranee-concentrazione-di-nitrati/2023

Ashtiani, Z. & Deutsch, C., 2024. *Kriging with Constraints.* Available at: https://geostatisticslessons.com/pdfs/krigingconstraints.pdf

Aulenta, F., s.d. *ISPRA.* Available at: https://www.isprambiente.gov.it/contentfiles/00000200/235-tc-aulenta2.pdf

Beeckman, F., Motte, H. & Beeckman, T., 2018. *Nitrification in agricultural soils: impact, actors and mitigation.* Available at: https://doi.org/10.1016/j.copbio.2018.01.014

Bijay-Singh & Craswell, E., 2021. *Fertilizers and nitrate pollution of surface and groundwater: an increasingly pervasive global problem..* Available at: https://doi.org/10.1007/s42452-021-04521-8

Bondesan, A. et al., 2004. *GEOMOFOLOGIA DELLA PROVINCIA DI VENEZIA, note illustrative della cart geomorfologica della provincia di Venezia.* Padova: Esedra editrice s.r.l..

Bonollo s.r.l., Idroesse Studio di Ingegneria, Studio Galli s.r.l. & Net Engineering S.p.A., 2003. Relazione di inquadramento generale (Piano d'Ambito). In: s.l.:A.A.T.O. Bacchiglione.

Boscolo , C., Mion, F., Vazzoler, P. & Camilla, S., 2008. *Le acque sotterranee della pianura veneta,* Padova: Servizio Acque Interne.

Bostan, P., 2017. *Basic Kriging Methods in Geostatistics.*

Britannica , 2024. *"food chain".* Available at: https://www.britannica.com/science/food-chain

Centro di Idrologia "Dino Tonini", Università degli Studi di Padova, 2021. *MODELLI MATEMATICI PER LA TUTELA E LA GESTIONE DELLE RISORSE IDRICHE SOTTERRANEE NELL'AMBITO DEL CONSIGLIO DI BACINO BACCHIGLIONE.* s.l.:Consiglio di Bacino AATO BACCHIGLIONE.

Chilès, J. & Delfiner, P., 2012. *Geostatistics: Modeling Spatial Uncertainty*.

Dalla Rosa, A. & Obber, S., 2018. *Carta dei suoli della provincia di Vicenza,* Treviso: La Grafica Faggian - Campodarsego (PD).

Deutsch , J., 2015. *Experimental Variogram Tolerance Parameters.* Available at: http://geostatisticslessons.com/lessons/variogramparameters

Eriksson, M. & Siska, P., 1999. Understanding Anisotropy Computations. In: *Mathematical Geology.* s.l.:s.n.

esri, 2021. *Kriging in Geostatistical Analyst.* Available at: https://desktop.arcgis.com/en/arcmap/latest/extensions/geostatistical-analyst/kriging-in-geostatistical-analyst.htm

esri, s.d. *Using cross validation to assess interpolation results.* Available at: https://pro.arcgis.com/en/pro-app/3.0/help/analysis/geostatistical-analyst/performing-cross-validation-and-validation.htm

Franklin, M., 2014. *Solution to Ordinary and Universal Kriging Equations.* Available at: https://www.researchgate.net/profile/Mohamed_El_Amine_Slimani/post/what_are_the_advantages_of_universal_Kriging_compared_with_ordinary_Kriging/attachment/59d63

d7d79197b807799a4b1/AS:419949395890176@1477135146143/download/Ordinary+and+Universal+Kriging.pdf

Geoportale Regione Veneto, s.d. *il geoportale dei dati territoriali.* Available at: https://idt2.regione.veneto.it/idt/downloader/download

Ghirardelli , A. et al., 2020. *Thirty-year monitoring of s-triazine herbicide contamination in the aquifer north of Vicenza (north-east Italy).* Available at: https://doi.org/10.1016/j.scitotenv.2020.141647

GTK, 2005. *Cl - Chlorine.* Available at: http://weppi.gtk.fi/publ/foregsatlas/text/Cl.pdf

Gustafson, D., 1989. *Groundwater ubiquity score: a simple method for assessing pesticide leachibility..* [Online].

Hanson, B., Bond , C., Buhl, K. & Stone, D., 2015. *Pesticide Half-life Sheet.* Available at: http://npic.orst.edu/factsheets/half-life.html#:~:text=Pesticide%20half%2Dlives%20can%20be,to%20persist%20in%20the%20environment.

Hassaan, M. & El Nemr, A., 2020. *Pesticides pollution: classifications, human health impact, extraction and treatment rechniques.* Available at: https://doi.org/10.1016/j.ejar.2020.08.007

Hayo, M. & van der Werf, 1996. *Assessing the impact of pesticides on the environment,* Colmar, France: ELSEVIER.

Hilal, A. et al., 2019. Geostatistical modeling - a tool for predictive soil mapping. In: *Remote Sensing in Precision Agriculture.* s.l.:Springer .

Hinsby, K., Condesso de Melo, M. & Dahl, M., 2008. *European case studies supporting the derivation of natural background levels and groundwater threshold values for the protection of dependent ecosystems and human health.* Available at: https://www.sciencedirect.com/science/article/pii/S0048969708002775?via%3Dihub

Hu, Y. et al., 2023. *Impact of atrazine on soil microbial properties: a meta-anlysis.* [Online]

Available at: https://doi.org/10.1016/j.envpol.2023.121337

Interstate Technology & Regulatory Council (ITRC), 2016. *Geospatial Analysis for Optimization at Environmental Sites,* Washington,DC : s.n.

ISTAT, 2024. *I.Stat.*
Available at: http://dati.istat.it/index.aspx?queryid=23961#
Izzo, V., 1992. *Dry cleaners - a major source of PCE in groundwater,* s.l.: California Regional Water Quality Control Board.
Kaur, R., Kaur Mavi, G. & Raghav, S., 2019. *Pesticides Classification and its Impact on Environment.*
Available at: https://www.ijcmas.com/8-3-2019/Rajveer%20Kaur,%20et%20al.pdf
Kret, E. et al., 2015. *Identification of TCE and PCE sorption and biodegradation parameters in a sandy aquifer for fate and transport modelling: batch and column studies.* [Online]
Available at: https://doi.org/10.1007/s11356-015-4156-9
Liu, M. et al., 2024. *Quantitative Assessment and Validation of Groundwater Pollution Risk in Southwest Karst Area.*
Available at: https://doi.org/10.1007/s12403-024-00647-3
Li, Z. & Zheng, X., 2017. *Review of design optimization methods for turbomachinery aerodynamics.*
Available at: http://dx.doi.org/10.1016/j.paerosci.2017.05.003
Mälicke, M. et al., 2018. *Exploring hydrological similarity during soil moisture recession periods using time dependent variograms.*
Available at: https://doi.org/10.5194/hess-2018-396
Matheron, G., 1969. Le Krigeage universel (Universal Kriging). In: *Le krigeage universel (Universal Kriging).* Fontainebleau: Cahiers du Centre de Morphologie Mathematique, Ecole des Mines de Paris.
Matteucci, F., Ercole, C. & Del Gallo , M., 2015. *Frontiers in Microbiology.* Available at: https://www.frontiersin.org/journals/microbiology/articles/10.3389/fmicb.2015.00924/full
Mattioli , A. & Bicchielli, U., 2018. *Valutazione di impatto sulla salute da uso irriguo di acqua contaminata da Percloroetilene e Tricloroetilene a Foligno.*
Mazzola, M., Saccardo, I. & Cappellin, R., 2013. *Stato dell'inquinamento da sostanze perfluoroalchiliche (PFAS) in provincia di Vicenza, Padova e Verona. - Aspetti geologici*

e idrogeologici, la rete idrografica, il sito potenzialmente inquinato e prima delimitazione dell'inquinamento al 30.09.2013 .

Miao, Z. et al., 2012. *SULFATE REDUCTION IN GROUNDWATER: CHARACTERIZATION AND APPLICATIONS FOR REMEDIATION.* Available at: https://www.researchgate.net/publication/51674776_Sulfate_reduction_in_groundwater_Characterization_and_applications_for_remediation

Ministero dell'Ambiente e della Sicurezza Energetica, 2024. *Governo Italiano.* Available at: https://www.mase.gov.it/pagina/linquinamento-delle-acque-di-origine-agricola-la- direttiva-nitrati-91676cee

Minnesota Pollution Control Agency, 2024. *Perchloroethylene/tetrachloroethylene (PCE or Perc).* Available at: https://www.pca.state.mn.us/pollutants-and-contaminants/perchloroethylene-tetrachloroethylene-pce-or-perc

Moraga , P., 2021. *Geospatial Health Data: Modeling and Visualization with R-INLA and Shiny.* Available at: https://www.paulamoraga.com/book-geospatial/sec-geostatisticaldatatheory.html

Moran, M., Zogorski, J. & Squillace , P., 2007. *Chlorinated Solvents inGroundwater of the United States.* Rapid City(South Dakota): s.n.

Moreno, P., Aral, H. & Vecchio-Sadus, A., 2009. *ENVIRONMENTAL IMPACT AND TOXICOLOGY OF SULPHATE.* Available at: https://www.researchgate.net/publication/282293070_ENVIRONMENTAL_IMPACT_AND_TOXICOLOGY_OF_SULPHATE

National Research Council, 1991. *Spatial Statistics and Digital Image Analysis.* Washington, DC: The National Academies Press.

Olea, R., 2018. *A practical primer on geostatistics.*

Panagiotou, C., Kyriakidis, P. & Tziritis, E., 2022. *Application of geostatistical methods to groundwater salinization problems: A review.* Available at: https://doi.org/10.1016/j.jhydrol.2022.128566

Pierri, D., 2021. *Actual decay of tetrachloroethene (PCE) and trichloroethene (TCE) in a highly contaminated shallow groundwater system.* Available at: https://pdf.sciencedirectassets.com/777793/1-s2.0-S2666765721X00038/1-s2.0-S2666765721000612/main.pdf?X-Amz-Security-Token=IQoJb3JpZ2luX2VjEA0aCXVzLWVhc3QtMSJHMEUCIQCgLit%2F1rTWgQRPrD00uRyJ2l3q3lMbodi3wLISN%2BKnLwIgCqMHoFhqPe%2Bbr87Iav7TPcq5bBzCbmT%2B4MqO

Popp, D., 2023. *European Parliament.* Available at: https://www.europarl.europa.eu/news/en/press-room/20230626IPR00824/reducing-pollution-in-eu-groundwater-and-surface-waters

Scialli, A., DeSesso, J. & Breckenridge, C., 2014. Developmental Toxicity Studies with Atrazine and its Major Metabolites in Rats and Rabbits. *Wiley Periodicals*, 13 january, Volume 101, pp. 199-214.

Socchera, E. & Minutolo, A., 2022. *ACQUE SOTTERRANEE - Il necessario è invisibile agli occhi.,* s.l.: LEGAMBIENTE.

Taghavi, N., Niven, R., Paull, D. & Kramer, M., 2022. *Groundwater vulnerability assessment: A review including new statistical and hybrid methods.* Available at: http://dx.doi.org/10.1016/j.scitotenv.2022.153486

Tamà, G., 2013. *Progetto definitivo di riorganizzazione con inserimento di nuovi codici C.E.R. ed aumento della capcità produttiva di un impianto esistente (autorizzato) di recupero di rifiuti non pericolosi in regime ordinario..* Available at: https://www.provincia.vicenza.it/doc-via/2014/NUOVA%20EUROP%20METALLI%20-%20Aumento%20capacita%20imp.%20rec.%20rifiuti%20-%20CARRE%27/progetto%20definitivo/1D17%20-%20Carte%20regionali%20-%20Geologica%20-%20Isofreatica%20-%20Piezometrica%20.pdf/view

Tariq Bashir, M., Ali, S. & Bashir, A., 2012. *Helath Effects from Exposure to Sulphates and Chlorides in Drinking Water.* Available at: https://www.researchgate.net/publication/242344864_Health_Effects_from_Exposure_to_Sulphates_and_Chlorides_in_Drinking_Water

Tomer, V., 2013. *Vegetable Processing At Household Level: Effective Tools Against Pesticide Residue Exposure.* Available at: https://www.researchgate.net/publication/315305060

Van Parys, s.d. *Mean, median, and mode are all measures of central tendency and represent a "typical" data point from your dataset.* Available at: https://ledidi.com/academy/measures-of-central-tendency-mean-median-and-mode

Vezzil, A. et al., 2018. *PAESC DEI COMUNI DELLA VALLE DELL'AGNO,* Valdagno: s.n.

Vincenzi , M., 2019. *Impianto di recupero rifiuti non pericolosi. Relazione di compatbilità idraulica.,* Creazzo: Agno Chiampo Ambiente s.r.l..

Wang, H. & Zhang, Q., 2019. *Research Advances in Identifying Sulfate Contamination Sources of Water Environment by Using Stable Isotopes.* Available at: https://www.mdpi.com/1660-4601/16/11/1914

WHO , 1996. Health criteria and other supporting information. In: *Guidelines for drinking-water quality.* Geneva: s.n.

WHO , 2004. *Sulfate in Drinking-water,* s.l.: World Health Organization .

WHO, 2020. *Livestock and environment statistics: manure and greenhouse gas emissions,* Rome : s.n.

WHO, 2022. *Pesticide residues in food.* Available at: https://www.who.int/news-room/fact-sheets/detail/pesticide-residues-in-food

World Health Organization, 1998. *Nitrate and nitrite in Drinking-water,* Geneva: WHO.